ÉCOLE POLYTECHNIQUE DE BRUXELLES
UNIVERSITÉ LIBRE DE BRUXELLES

Modelling of contact lines on heterogeneous substrates : stick-slip and contact angle hysteresis

Thesis presented by Metin HATIPOGULLARI
with a view to obtaining the PhD Degree in Engineering Sciences (”Docteur en Sciences de l’ingénieur et technologie”)
Année académique 2019-2020

Supervisor : Professor Pierre COLINET
Transfers, Interfaces and Processes (TIPs)

Thesis jury :

Pierre COLINET (Université libre de Bruxelles)
Joël DE CONINCK (Université de Mons)
Frédéric DEBASTE (Université libre de Bruxelles)
Serafim KALLIADASIS (Imperial College London)
Pierre LAMBERT (Université libre de Bruxelles)
Thierry ONDARÇUHU (Institut de Mécanique des Fluides de Toulouse)
David SEVENO (Katholieke Universiteit Leuven)

ÉCOLE POLYTECHNIQUE DE BRUXELLES
UNIVERSITÉ LIBRE DE BRUXELLES

Thèse présentée en vue de l'obtention du

Grade académique de Docteur en Sciences de l'Ingénieur et Technologie

Délivré par : *l'Université Libre de Bruxelles (ULB)*

Présentée et soutenue par:

Metin Hatipogullari

Modelling of contact lines on heterogeneous substrates: stick-slip and contact angle hysteresis

JURY

Pierre COLINET	Université libre de Bruxelles
Joël DE CONINCK	Université de Mons
Frédéric DEBASTE	Université libre de Bruxelles
Serafim KALLIADASIS	Imperial College London
Pierre LAMBERT	Université libre de Bruxelles
Thierry ONDARÇUHU	Institut de Mécanique des Fluides de Toulouse
David SEVENO	Katholieke Universiteit Leuven

Unité de Recherche:

Service de Transferts, Interfaces et Procédés (TIPs)

Directeur de Thèse et Promoteur:

Prof. Pierre Colinet

ABSTRACT

This thesis highlights generic aspects of contact angle hysteresis and stick-slip motion, encountered in most practical wetting situations.

First, we study the scaling relation between the heterogeneity strength and the amplitude of the contact angle hysteresis it induces in the model configuration of a chemically heterogeneous microchannel. A key parameter which determines the qualitative features is the heterogeneity wavelength. In particular, we identify a near-threshold behavior where the quadratic scaling between the heterogeneity amplitude and the resulting hysteresis, already known for a dilute system of wetting defects, is explained by the closeness to the threshold, and a macroscopic limit without observable stick-slip where this scaling is linear.

In the second part, we adapt the description to the configuration of a meniscus around a wavy fibre. This adaptation brings the generic results of the first part in the reach of experiments. A comparison with experiments is achieved at the level of the individual topography-induced jumps.

In the third part, we expand the formulation to treat the quasi-steady interface shape contact line dynamics and study how the the presence of stick-slip motion at the observable or unobservable scale modifies the scaling relation between the contact line velocity and contact angle. We recover the known result that the scaling exponent depends on the nature of the externally controlled parameter, identify the causes of this dependency in the corresponding static limits, and predict the disappearance of this dependency above a critical velocity which decreases with the heterogeneity wavelength.

Finally, we show trough examples how the modelling framework which permits capturing contact angle hysteresis and stick-slip motion in a minimalistic way can be adopted to treat configurations with a finite amount of contact points, or the 3D problem of a drop with a deformed contact line. We discuss the arising configuration-specific effects, also in configurations of biomimetic interest.

Keywords: *Wetting*, *Spreading*, *Contact angle hysteresis*, *Stick-slip*, *Cox-Voinov*.

RÉSUMÉ

Cette thèse met en évidence les aspects génériques de lhystèrèse de l'angle de contact et du mouvement du type stick-slip, rencontrés dans la plupart des situations pratiques impliquant mouillage.

Nous étudions d'abord les lois de puissance entre la force de l'hétérogénéité et l'amplitude de l'hystérésis de l'angle de contact qu'elle induit dans la configuration modèle d'un microcanal chimiquement hétérogène. Un paramètre clé qui détermine les caractéristiques qualitatives est la longueur d'onde de l'hétérogénéité. En particulier, nous identifions un comportement proche du seuil où la relation est quadratique, comme déjà connue pour l'hystérésis induite par des défauts de mouillabilité peu espacés, qui s'explique par la proximité du seuil et une limite macroscopique sans stick-slip observable où la relation est linéaire.

Dans la deuxième partie, nous adaptons la description à la configuration d'un ménisque autour d'une fibre ondulée. Cette adaptation amène les résultats génériques de la première partie à la portée des expériences. Une comparaison avec les expériences est réalisée au niveau des sauts individuels induits par la topographie.

Dans la troisième partie, nous développons une formulation pour traiter la dynamique de la ligne de contact en supposant une forme d'interface quasi-statique et étudions comment la présence du mouvement de type stick-slip à l'échelle observable ou non observable modifie la loi de puissance entre la vitesse de la ligne de contact et l'angle de contact. Nous retrouvons le résultat connu que la loi de puissance dépend de la nature du paramètre macroscopique qui est modifié de manière externe pour controler le mouvement de la ligne de contact, identifions les causes de cette dépendance dans les limites statiques correspondantes et prévoyons la disparition de cette dépendance au-dessus d'une vitesse critique qui diminue avec la longueur d'onde de l'hétérogénéité.

Enfin, nous montrons à travers des exemples comment le cadre de modélisation permettant de capturer de manière minimaliste l'hystérésis de l'angle de contact et le mouvement stick-slip peut être adapté pour traiter des configurations avec une quantité finie de points de contact, ou le problème 3D avec une ligne de contact déformée. Nous discutons l'apparition des effets spécifiques aux configurations, aussi dans les configurations d'intérêt biomimétique.

Mots-clés: *Mouillage*, *Étalement*, *Hystérésis de l'angle de contact*, *Stick-slip*.

ACKNOWLEDGEMENTS

I am deeply indebted to my supervisor Pierre Colinet for the continuous support and coaching he provided me from the initial to the final stage of this project. This project would not have been successfully completed without his ideas, patience and gift to transmit his knowledge.

I appreciate the whole Transfers Interfaces and Processes team for providing an inspirational work environment. I am especially grateful to Alexey Rednikov, Sam Dehaeck, Senthil Kumar Parimalanathan and Hosein Sadafi for the numerous discussions we had on many aspects related to this work. I thank the members and ex-members of TIPs with whom I shared good times.

I'd like to give special thanks to Serafim Kalliadasis, Marc Pradas, David Seveno and his team, Carlos Fuentes, Pierre Lambert and Thierry Ondarçuhu for the productive and stimulating collaborations.

I want to thank Joël De Coninck, Serafim Kalliadasis, Thierry Ondarçuhu and David Seveno for agreeing to be part of my thesis jury and in particular Pierre Lambert and Frédéric Debaste for having accepted to be the chair and the reporter.

I acknowledge financial support from the European Space Agency (ESA) and Belgian Federal Science Policy Office (BELSPO) and the Alice and David Van Buuren Fund.

Finally, a big thank-you to my family and friends for the continuous support and constructive distraction they have provided me during the whole process.

TABLE OF CONTENTS

Chapter 1

Introduction

1.1 Context - contact lines in nature, industry and everyday life

Many processes in nature, industry and everyday life involve the contact between gaseous, liquid and solid substances. These substances meet and exchange physical quantities at interfaces. These interfaces, in their turn, meet at three phase contact lines, or in short, *contact lines*. The intriguing behavior of contact lines still poses many generic and fundamental questions, the answers to which will improve the understanding of numerous phenomena [1, 2].

A typical feature of contact lines is that they can stay *pinned*, causing for example droplets to stick on inclined surfaces. In everyday life, we witness raindrops sticking on windows and when applying a dressing to a salad, we count on the sticking of its droplets on the salad leaves. Farmers spraying their crops with pesticides and other agricultural sprays [3] count on the same phenomenon for the effectivity of their treatment and to minimize chemical runoffs [4, 5]. For most industrial processes on the other hand, the sticking of drops of reactants or fuel on walls [6] constitutes a loss at best.

The pinning of contact lines, along with the fact that liquids evaporate fastest at contact lines, leads to the so-called coffee stain effect [7]. The name stems from a spilled coffee drop, which when left to dry, deposits its non-volatile solutes preferably at its contact line, and thereby leaves a circular stain. A better understanding of the contact line physics can lead to strategies to achieve the controlled self-assembly of the solutes [8], or on the contrary to achieve a homogeneous deposition of solutes as desired in inkjet printing of circuits, OLED displays, drying of paint and coatings [9].

On a more general note, the relative importance of contact lines and interfaces over the bulk substances increases as systems become smaller in size. Whereas the motion of large bodies of water is dominated by gravity, at the sub-millimeter scale, forces which act on interfaces dictate the physics. The miniaturisation of flows for pharmaceutical, analytical chemistry and chemical production purposes has intrinsic benefits such as reducing reactant volumes, and reaction times, and has given birth to the fast growing field of microfluidic technologies [10, 11, 12]. In soil science, interfaces and contact lines dominate the penetration of water and oil into the micro-scale pores of rocks [13, 14]. When gravity is absent, surface phenomena are dominant

up to larger length scales, and can be manipulated to move liquids around, for example to feed satellite motors with fuels [15, 1].

Nature contains numerous striking examples where the features of contact line motion are ensured to occur in such a way that it serves the needs of living beings, often inspiring engineering applications. A long list of known instances includes the self-cleaning property of lotus leaves [16], the water-walking ability of insects [17, 18], the anisotropic drop motion on butterfly wings [19], the anti-fogging properties of mosquito eyes [20], the various water collection systems present in plants and animals in dry habitats [21], and the feeding mechanism of shorebirds where they pin a drop inside their beak, and control its motion by opening and closing it [22].

Before describing with more rigour why contact lines get pinned, how the contact line motion can be modelled and understood in such systems, and which are the generic questions mentioned in the first paragraph, let us rehearse in the next sections the required basic concepts, starting from the deformability of liquid-gas interfaces.

1.2 Basic concepts - deformable interfaces and surface tension

At a contact line, three immiscible, or partly miscible, phases make contact with each other. This makes an adequate description of the contact line behavior an inherently multiphase problem. We are interested in cases where one of these phases is a rigid solid. As gases are always miscible with each other, one of the remaining phases must be a liquid and the other one can be a gas or another liquid.

Liquids and gases have no fixed shape and interfaces between them are deformable. In a liquid, molecules feel mutual attraction, but can move around with greater freedom than in solids where they are held together by chemical bonds. In a gas, thermal agitation dominates over these attractive forces, leaving molecules the freedom to occupy all the space available. Let us consider a liquid-gas interface (Fig. 1.1). A liquid molecule in the bulk is surrounded by more attractive neighbors than one at the interface. Therefore, an energetically favorable distribution of the liquid molecules would be one with the least possible amount of liquid molecules at the interface. Or, these cohesive interactions in the liquid and the lack of similar interactions with the gas will favour the deformations of the interface in the direction of minimizing the interface area.

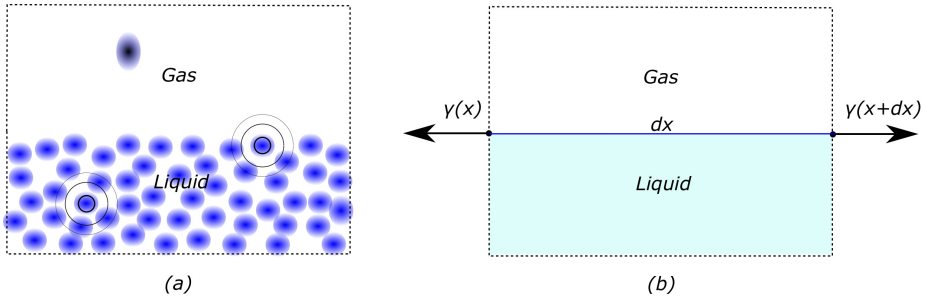

Figure 1.1: Surface tension on flat liquid-gas interface. (a): Physical origin, (b): Successful macroscopic description.

Surface tension is the manifestation of this effect at the macroscopic scale, defined first by Gibbs [23] as a thermodynamic quantity, multiplying the additional (or excess) internal energy term associated with an increase of the extensive parameter which is the area of the surface separating the two phases. Then, the internal energy variation dU of a liquid-gas system can be expressed starting from the first principle of thermodynamics as,

$$dU = \mu_l dn_l + \mu_g dn_g + TdS - pdV + \gamma dA, \tag{1.1}$$

where n_l, n_g, S and V are respectively the number of liquid molecules, the number of gas molecules, the entropy and the total volume, and μ_l, μ_g, T and p are respectively the chemical potential of the liquid, the chemical potential of the gas, the temperature and the pressure, Eq. 1.1 defines the surface tension $\gamma \left[J/m^2\right]$ as the increase in internal energy due to the increase of the interfacial surface area A by one unit. In figure 1.1, $dA = dx$ per unit length in the orthogonal direction. The magnitude of γ can be related to the cohesive energy per molecule, divided by its exposed area [1] and is for example larger for water ($0.072 J/m^2$), where hydrogen bonds enhance cohesion, than

for oils where only van der Waals interactions are present ($\approx 0.02 J/m^2$).

Defining the Helmoltz free energy $F \equiv U - TS$, Eq 1.1 can be rewritten as,

$$dF = \mu_l dn_l + \mu_g dn_g - SdT - pdV + \gamma dA \tag{1.2}$$

Therefore, at constant temperature T, the number of moles $n_l + n_g \equiv n$, and volume V, surface tension is the free energy F per unit interfacial area,

$$\gamma = \left(\frac{\partial F}{\partial A}\right)_{T,V,n}. \tag{1.3}$$

It follows from thermodynamic considerations that interfaces exert forces. The forces arising from surface tension $\gamma\,[N/m]$, which can also be thought of as the interface version of pressure, are termed capillary forces and will be introduced in section 1.3.2. For example, the flat elementary interface drawn in Fig. 1.1 will feel a force $\gamma(x)$ per unit length in the direction orthogonal to the drawing, acting where the interface is cut in the direction tangential to the interface. If the surface tension is uniform along the interface, then this interface element can remain static. If not, the net force will drive a Maragoni flow. In what follows, we will assume that γ (function of the temperature and the chemical composition) is constant. Similarly, if the interface is not flat but curved, the same forces enable it to accommodate in static conditions a pressure difference between the two phases. The static shapes adopted by deformable interfaces is explained by the *Young-Laplace law*.

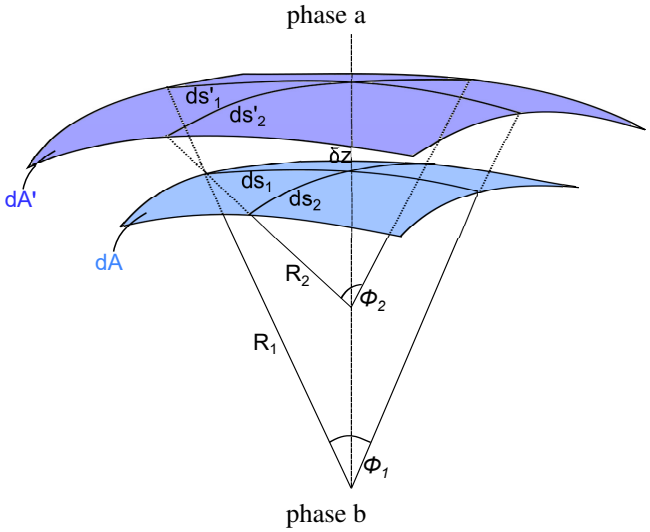

Figure 1.2: Infinitesimal displacement of an infinitesimal interface element over distance δz.

1.3 Statics of deformable interfaces - the Young-Laplace law

1.3.1 A derivation of the Young-Laplace law

The Young-Laplace law can be derived from considerations of force equilibrium or the minimization of surface energy, a version of the latter (from [24]) is given below.

Consider the displacement of an infinitesimal surface element of an interface between immiscible phases a and b. The temperature and number of molecules in both phases stay constant, while the area of the element changes from dA to dA', and the volume of phase a increases by δV (Fig. 1.2). In equilibrium,

$$\delta F = \delta W_p + \delta W_\gamma = 0, \tag{1.4}$$

where δW_p is the work done by pressure forces to change the volume, and δW_γ is the work done by the surface tension to change the interfacial area.

The volume variation between the initial and final surface elements is $\delta V = \delta z dA$. Therefore, the pressure work of the displacement is,

$$\delta W_p = \int (p_b - p_a)\, \delta z dA. \tag{1.5}$$

Similarly, the work of the surface tension forces is given by

$$\delta W_\gamma = \gamma \delta A, \tag{1.6}$$

with,

$$\delta A = dA' - dA, \tag{1.7}$$

the increase in surface area. The right-hand side of Eq. 1.7 can be expressed in terms of the curvature of the principal normal sections. As these sections are orthogonal to each other, the areas dA and dA' are given by the product of the length elements along them, i.e. $dA = ds_1 ds_2$ and $dA' = ds'_1 ds'_2$. These length elements can be expressed as,

$$\begin{cases} ds_1 = R_1 \phi_1 \\ ds'_1 = (R_1 + \delta z)\, \phi_1, \end{cases} \tag{1.8}$$

with similar expressions for ds_2 and ds'_2, leading to

$$\begin{cases} \frac{ds'_1}{ds_1} = 1 + \frac{\delta z}{R_1} \\ \frac{ds'_2}{ds_2} = 1 + \frac{\delta z}{R_2}. \end{cases} \tag{1.9}$$

Substitution of Eq. 1.9 into Eq. 1.7 gives

$$\begin{aligned} \delta A = ds'_1 ds'_2 - ds_1 ds_2 = \left(1 + \frac{\delta z}{R_1}\right)\left(1 + \frac{\delta z}{R_2}\right) dA - dA \\ = \left(\frac{\delta z}{R_1} + \frac{\delta z}{R_2} + \frac{\delta z^2}{R_1 R_2}\right) dA \approx \left(\frac{\delta z}{R_1} + \frac{\delta z}{R_2}\right) dA = \left(\frac{1}{R_1} + \frac{1}{R_2}\right) \delta z dA, \end{aligned} \tag{1.10}$$

where the last approximation is justified as δz is small compared to R_1 and R_2. Now, substitution of Eqs. 1.5 and 1.10 in the equilibrium condition (Eq. 1.4) yields

$$\begin{aligned} \int (p_b - p_a)\, \delta z dA + \int \gamma \left(\frac{1}{R_1} + \frac{1}{R_2}\right) \delta z dA \\ = \int \left((p_b - p_a) + \gamma \left(\frac{1}{R_1} + \frac{1}{R_2}\right)\right) \delta z dA = 0, \end{aligned} \tag{1.11}$$

As Eq. 1.11 must hold for any δz, we conclude that the integrand must be zero, leading to the Young-Laplace equation

$$p_a - p_b = \gamma \left(\frac{1}{R_1} + \frac{1}{R_2}\right). \tag{1.12}$$

The right hand side of Eq. 1.12 is called the Laplace pressure, the curvature pressure or the capillary pressure, and can be rewritten in vectorial form as

$$p_a - p_b = -\gamma \nabla \cdot \vec{n}, \tag{1.13}$$

where $\vec{n}$ is the unit normal on the interface, pointing towards phase b, and $-\nabla \cdot \vec{n}$ is twice the mean curvature H. For an interface specified by a surface $z = h(x, y)$ in Cartesian coordinates the unit normal is given by

$$\vec{n} = \frac{\nabla\left(z - h(x,y)\right)}{\left|\nabla\left(z - h(x,y)\right)\right|} = \frac{-h_x \vec{1}_x - h_y \vec{1}_y + \vec{1}_z}{\left(1 + h_x^2 + h_y^2\right)^{\frac{3}{2}}}, \tag{1.14}$$

in the notation of which we have followed the convention of denoting partial derivatives by subscripts, $\frac{\partial A}{\partial X} = A_X$, and the vectors $\vec{1}_X$ are unit vectors along the coordinate

in the subscript. With the use of Eq. 1.14, the right-hand side of Eq. 1.13 can be explicited as,

$$-\gamma\nabla\cdot\vec{n}=\gamma\frac{\left(1+h_x^2\right)h_{yy}+\left(1+h_y^2\right)h_{xx}-2h_xh_yh_{xy}}{\left(1+h_x^2+h_y^2\right)^{\frac{3}{2}}}. \tag{1.15}$$

For an interface specified by surface in polar coordinates, $z=h(r,\phi)$, substituting $x=r\cos\phi$ and $y=r\sin\phi$ in Eq. 1.15 and simplifying yields,

$$-\gamma\nabla\cdot\vec{n}=\gamma\frac{h_r\left[r^2\left(1+h_r^2\right)+2h_\phi\left(h_\phi-rh_{r\phi}\right)\right]+rh_{rr}\left(r^2+h_\phi^2\right)+rh_{\phi\phi}\left(1+h_r^2\right)}{\left[r^2\left(1+h_r^2\right)+h_{\phi\phi}^2\right]^{\frac{3}{2}}}. \tag{1.16}$$

If p_a and p_b in the left-hand side of Eq. 1.13 are constant, the static interface shape will be one of constant mean curvature. This is however not true in cases where the buildup of hydrostatic pressure in the fluids by gravity needs to be taken into account. This hydrostatic pressure can be taken into account in the right-hand side of Eq. 1.13, as a vertical variation of the pressure. This effect is neglected for typical system sizes much smaller than the capillary length $l_c=(\gamma/\Delta\rho g)^{1/2}$, where g is the gravitational acceleration and $\Delta\rho$ is the difference between the fluid densities. The square of the ratio of the typical system size divided by the capillary length emerges naturally in many models [25, 26, 27] incorporating both effects and is called the Bond number.

1.3.2 Static interfaces of interest and capillary forces

In the general case, as can be seen from Eq. 1.15 or Eq. 1.16, the Young-Laplace equation is a second order partial differential equation, to be posed with four appropriate boundary conditions. A fifth condition is necessary in many cases where the value of the accommodated pressure difference p_a-p_b is not known. This section contains selected examples of solutions of the Young-Laplace equation, which we apply for different wetting configurations. We discuss quantities which are free to be chosen, the amount of which is reduced by symmetries or constraints.

We will also calculate for the example geometries the capillary force, defined as the net force acting on an interface resulting from Laplace pressure and show that this force can be deduced directly from the geometry of the liquid-gas interface at its end points. Considering capillary forces in the presence of substrates, as in later sections, requires care in the proper and complete definition of a system on which the forces act (see for example [28] for a discussion on the subtlety of this point).

1.3.2.1 Spherical interfaces

Any spherical interface is, in the absence of hydrostatic pressure, a trivial solution of the Young-Laplace equation because all points on a spherical cap have the same radii of curvature equal to the radius of the sphere, i.e. $R_1=R_2=R$. Therefore the pressure of the phase at the inner side of the sphere is higher than the pressure of the phase on its outer side by a quantity

$$\Delta p=\frac{2\gamma}{R}. \tag{1.17}$$

Any liquid-gas interface which is a part of a spherical shell satisfies the Young-Laplace law. So does an interface which has the form of a spherical shell delimited by a plane, or in short a spherical cap. This shape is adopted by for example small sessile

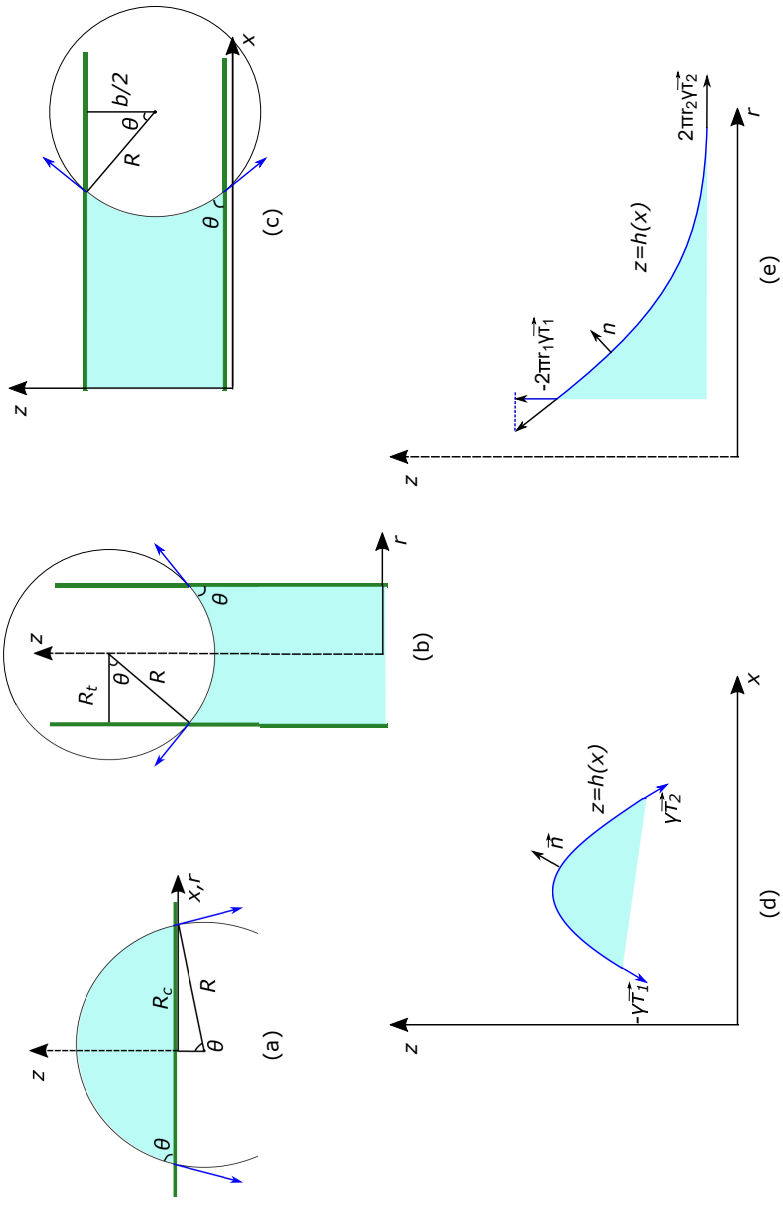

Figure 1.3: Sketches static interfaces of interest and capillary forces. (a): spherical sessile drop; (b): spherical meniscus inside a thin tube (1.3.2.1); (c): circular meniscus inside a microchannel (1.3.2.2); (d) system definition of a 2D interface (1.3.2.4); (e): system definition of an axisymmetric interface (1.3.2.5)

or hanging drops, and by the meniscus of a liquid column inside a thin tube. A sphere is a shape characterized by the location of the middle point and a radius R, which makes four parameters in the three dimensional space.

The spherical sessile drop shown in Fig. 1.3a could be for example described by a volume, a contact radius, the angle it makes with the substrate (which is constant along the contact perimeter), the horizontal position of the apex, the Laplace pressure, etc. A straight-forward choice here is to characterize the drop by a contact radius R_c, the angle θ it makes with the substrate and the two coordinates of its apex. For any choice of these quantities, there exists a static spherical interface with a corresponding value of the volume and Laplace pressure,

$$\Delta p = \frac{2\gamma \sin\theta}{R_c}. \tag{1.18}$$

Similarly, a spherical meniscus inside a thin capillary tube (Fig. 1.3b) is determined by four parameters, i.e. the radius R_t of the tube, the angles the meniscus makes with the tube at two points (which differ from each other the sphere center is not on the axis of the cylinder) and the mean height of the meniscus. If the meniscus makes a constant angle θ with the tube, then the value of the capillary pressure is,

$$\Delta p = \frac{2\gamma \cos\theta}{R_t}. \tag{1.19}$$

1.3.2.2 Cylindrical interfaces

Any cylindrical interface is, in the absence of hydrostatic pressure, a trivial solution of the Young-Laplace equation because all points on a cylinder have the same radii of curvature, namely $R_1 = R$ equal to the radius of the cylinder, and $R_2 = \infty$. Therefore the pressure of the phase at the inner side of the cylinder p_a is higher than the pressure of the phase on its outer side p_b by a quantity,

$$\Delta p = \frac{\gamma}{R}. \tag{1.20}$$

A circle is characterized by the location of the middle point and a radius R, which makes three parameters.

This shape is for example adopted by the meniscus of a liquid squeezed between two plates. Possible quantities to describe such configuration include the angle the meniscus makes with the upper plate, the angle that the meniscus makes with the lower plate, the positions where the meniscus touches the two plates, the distance and angle between the two plates, the volume of the liquid, the pressure inside the liquid, the position of the apex of the meniscus etc. For the meniscus to be circular and thereby static, only three of them can be chosen independently. For a meniscus between parallel plates (Fig. 1.3c), which has the same angle at the two plates, and which is described by the inter-plate distance b, the contact angle θ and the coordinate of the contact line, the volume is determined and the Laplace pressure is given by,

$$\Delta p = \frac{2\gamma \cos\theta}{b}. \tag{1.21}$$

Similarly, a cylindrical sessile drop, described by a contact radius R_c and an angle θ and a lateral translation, will have a Laplace pressure of

$$\Delta p = \frac{\gamma \sin\theta}{R_c}. \tag{1.22}$$

1.3.2.3 Almost flat interfaces

Any flat interface is a trivial solution of the Young-Laplace equation with $p_a = p_b$. This can be seen by choosing $R_1 = R_2 = \infty$ in Eq. 1.12, or by setting all partial derivatives to zero in Eq. 1.15.

For almost flat interfaces, where the interface height h varies over a large typical length scale $\frac{h}{\epsilon}$, with smallness parameter $\epsilon \ll 1$, Eq. 1.15 simplifies to

$$-\gamma \nabla \cdot \vec{n} = \gamma \left(h_{xx} + h_{yy} \right), \tag{1.23}$$

at lowest order. This form of the Laplace pressure is a boundary condition consistent with the lubrication approximation, a framework which gives physical insight into intricate multi-phase problems and in particular interface instabilities[29]. In the lubrication theory, the smallness of ϵ enhances the analytical tractability of flows inside thin films by justifying to neglect the non-linear inertial terms in the Navier-Stokes equation, which describes the momentum conservation inside the liquid. This type of analysis can for example tell which physical effects will dampen or amplify the initially small perturbations of an almost flat (or almost cylindrical) interface. A well-known surface tension driven instability is the Rayleigh-Plateau instability by which a cylindrical liquid jet disintegrates into droplets, leading to a decrease in the interfacial area.

In the absence of hydrostatic pressure, the 2D equivalent of Eq. 1.23, $h_{xx} = 0$, predicts a static parabolic interface shape $h = ax^2 + by + c$ with three coefficients, a, b and c. This shape can be for example adopted by a thin drop. This drop satisfies the Young-Laplace law and is therefore static for any arbitrary choice of (small) contact angle θ, (large) contact radius R_c and apex position. If those quantities are chosen, the volume and the pressure are given by the Young-Laplace equation,

$$\Delta p = \frac{\gamma \tan\theta}{R_c} \approx \frac{\gamma\theta}{R_c}. \tag{1.24}$$

Similarly, a thin drop which is a paraboloid of revolution, $h = \alpha r^2 + \beta r + \gamma$, which has a contact angle θ and a contact radius R_c will have a Laplace pressure of

$$\Delta p = \frac{2\gamma \tan\theta}{R_c} \approx \frac{2\gamma\theta}{R_c}. \tag{1.25}$$

1.3.2.4 Net force on two-dimensional interfaces

Coming back to the case of contact angles of the order of one, for 2D interface shapes $z = h(x)$ (Fig. 1.3d) the curvature at any point on the interface, given by Eq. 1.15, simplifies to

$$-\gamma \nabla \cdot \vec{n} = \gamma \frac{h_{xx}}{(1 + h_x^2)^{\frac{3}{2}}}. \tag{1.26}$$

In the absence of hydrostatic pressure, this quantity is constant along the interface. The interface shape can be found by solving Eq. 1.26 equal to an unknown constant value of the capillary pressure, with two boundary conditions. One family of solutions are the circular interfaces discussed in section 1.3.2.2, which are indeed described by three coefficients.

The net force $\vec{F}$ acting on an interface resulting from Laplace pressure is termed the capillary force, and can be calculated as,

$$\vec{F} = \int_1^2 (p_b - p_a)\, \vec{n} ds, \tag{1.27}$$

where $ds^2 = dx^2 + dz^2$, and 1 and 2 are two points on the interface between which the net force is calculated (Fig. 1.3d). The force is given per unit length orthogonal to the page. Using the Young-Laplace law (Eq. 1.13), we obtain,

$$\vec{F} = \gamma \int_1^2 \left(\vec{\nabla} \cdot \vec{n}\right) \vec{n} ds. \tag{1.28}$$

Now, using the Frenet-Serret equations, the integrand in Eq. 1.28 can be rewritten as [30],

$$\vec{F} = \gamma \int_1^2 \frac{d\vec{\tau}}{ds} ds = \gamma \left(\vec{\tau}_2 - \vec{\tau}_1\right). \tag{1.29}$$

Therefore, the net capillary force acting on an interface can simply be deduced from the tangent vectors at the extremities of the interface as indicated on Fig. 1.3d.

For example, for a liquid squeezed between two identical plates, the Laplace pressure is given by Eq. 1.21. The force in the x-direction is

$$\vec{F} \cdot \vec{1}_x = \frac{2\gamma \cos\theta}{b} \int_0^b dz = 2\gamma \cos\theta.$$

The same result can simply be deduced from the shape of the extremities of the interface on Fig. 1.3c, which using Eq. 1.29 gives

$$\vec{F} = 2\gamma \cos\theta \vec{1}_x.$$

Similarly, for a cylindrical drop, the Laplace pressure is given by Eq. 1.20. The force in the z-direction is

$$\vec{F} \cdot \vec{1}_z = \frac{\gamma \sin\theta}{R_c} \int_{-R_c}^{R_c} dx = 2\gamma \sin\theta,$$

which can also be deduced from the shape of the extremities of the interface. For the parabolic drop discussed in section 1.3.2.3, Eq. 1.20 yields the same force as for the cylindrical drop in the expression above, while multiplying the Laplace pressure with the interface area gives

$$\vec{F} \cdot \vec{1}_z = \frac{\gamma \tan\theta}{R_c} \int_{-R_c}^{R_c} dx = 2\gamma \tan\theta \approx 2\gamma \sin\theta,$$

where last approximation sign is consistent with the framework of almost flat interfaces.

1.3.2.5 Axisymmetric interfaces in general

For interface shapes which are invariant for changes in ϕ, i.e. axisymmetric around $\vec{1}_z$, the curvature at any point on the interface, given by Eq. 1.16 simplifies to,

$$-\gamma\nabla\cdot\vec{n}=\gamma\left(\frac{h_r}{r\sqrt{1+h_r^2}}+\frac{h_{rr}}{(1+h_r^2)^{\frac{3}{2}}}\right). \tag{1.30}$$

The first term in the brackets is the inverse of the second principal radius of curvature R_2^{-1} and the second term is R_1^{-1}. This equation (along with Eq. 1.13) governs the static axisymmetric interface shapes of the form $z=h(r)$.

In the absence of the hydrostatic pressure, this quantity is constant along the interface. The interface shape can be found by solving Eq. 1.30 equal to an unknown constant value of the capillary pressure, with two boundary conditions. One family of solutions are the spherical interfaces discussed in section 1.3.2.1.

Other configurations where the value of the Laplace pressure is typically not known a priori include liquid bridges between solids and (barrel-shaped) drops on fibres. In these cases, also three parameters are free to be chosen. For a barrel-shaped drop on a conical fibre of which the radial position of the two contact points and the volume are given, the Young-Laplace law fixes the contact angles at both sides of the drop, as well as the value of the Laplace pressure. Similarly, for a liquid bridge of which the two contact radii and volume are chosen, the Young-Laplace law fixes the values of the two contact angles.

A case where no unknown pressure terms appear, is the configuration of a fibre which is immersed vertically in a liquid bath. The Young-Laplace equation governs the static shape of the meniscus around a fibre. Far away from the fibre, the liquid bath is horizontal and placing the plane $z=0$ at this height of the liquid bath, we can explicit the right hand side of Eq. 1.13 to obtain,

$$\rho g h=\gamma\left(\frac{h_r}{r\sqrt{1+h_r^2}}+\frac{h_{rr}}{(1+h_r^2)^{\frac{3}{2}}}\right). \tag{1.31}$$

This equation can be solved with two boundary conditions; one to specify the horizontal bath level far away from the bath, and one to specify the contact angle at the fibre. The equilibrium height of the capillary rise is then determined by the Young-Laplace equation.

For axisymmetric interfaces, the net force $\vec{F}$ acting the interface resulting from Laplace pressure can be calculated as

$$\vec{F}=\int_1^2\left(p_b-p_a\right)\vec{n}dA=\gamma\int_1^2\left(\vec{\nabla}\cdot\vec{n}\right)\vec{n}ds=\gamma\int_0^{2\pi}d\phi\int_1^2\left(\vec{\nabla}\cdot\vec{n}\right)\vec{n}rds \tag{1.32}$$

The radial component of this force cancels out by axisymmetry (as $\int_0^{2\pi}\vec{1}_r=0$). We proceed to show that the z-component of the force is directly related to contact angle and contact radius by,

$$\vec{F}\cdot\vec{1}_z=2\pi\gamma\left[r\vec{\tau}\cdot\vec{1}_z\right]_2^1 \tag{1.33}$$

The left-hand side of Eq. 1.33 is calculated by expliciting the force given by Eq.

1.32 using the expression of the mean curvature (Eq. 1.30), where the unit normal is given by,

$$\vec{n} = \frac{\vec{1}_z - h_r \vec{1}_r}{\left(1 + h_r^2\right)^{1/2}}.$$

This leads to

$$\vec{F} \cdot \vec{1}_z = -2\pi\gamma \int_1^2 \left(\frac{h_r}{\left(1 + h_r^2\right)} + \frac{r h_{rr}}{\left(1 + h_r^2\right)^2} \right) ds \tag{1.34}$$

Now, Eq. 1.33 follows by showing that the integrand on the right-hand side of Eq. 1.34 equals

$$\frac{d\left(r\vec{\tau} \cdot \vec{1}_z\right)}{ds},$$

with the unit tangent vector

$$\vec{\tau} = \frac{h_r \vec{1}_z + \vec{1}_r}{\left(1 + h_r^2\right)^{1/2}}.$$

Indeed,

$$\frac{d\left(\frac{r h_r}{\sqrt{1+h_r^2}}\right)}{dr}\frac{dr}{ds} = \frac{\sqrt{1+h_r^2}\left(h_r + r h_{rr}\right) - r h_r^2 h_{rr}\left(1+h_r^2\right)^{-1/2}}{\left(1+h_r^2\right)^{\frac{3}{2}}}$$

$$= \frac{h_r + r h_{rr} + h_r^3 + r h_{rr} h_r^2 - r h_r^2 h_{rr}}{\left(1+h_r^2\right)^2} = \frac{h_{rr} + h_r\left(1+h_r^2\right)}{\left(1+h_r^2\right)^2}.$$

For example, for a spherical drop, the Laplace pressure is given by Eq. 1.18. The net capillary force in the z-direction is

$$\vec{F} \cdot \vec{1}_z = \frac{2\gamma \sin\theta}{R_c} 2\pi \int_0^{R_c} r dr = 2\pi R_c \gamma \sin\theta$$

The same result can simply be deduced from the shape of the extremities of the interface on Fig. 1.3a, which using Eq. 1.33 gives

$$\vec{F} = 2\pi R_c \gamma \sin\theta \vec{1}_z$$

Similarly, for a meniscus inside a thin tube, the Laplace pressure is given by Eq. 1.19. The force in the z-direction is

$$\vec{F} = 2\pi R_t \gamma \cos\theta \vec{1}_z \tag{1.35}$$

which can also be deduced from the extremities of the interfaces using Eq. 1.33. Note that the same force is obtained for the configuration of the meniscus around a fibre described in Eq. 1.31.

1.3.2.5.1 Side note: Jurin's law For the tube configuration, balancing the capillary force given by Eq. 1.35 with the weight of the liquid inside the tube, and neglecting

the volume of the meniscus gives the height H to which the meniscus will rise,

$$H = \frac{2l_c^2 \cos\theta}{R_t},$$

measured from a plane where the liquid makes contact with the gas horizontally. This expression is called Jurin‘s law of capillary rise. For example, capillary forces can lift water up about one meter in a perfectly wetting tube with an internal diameter of 10 microns.

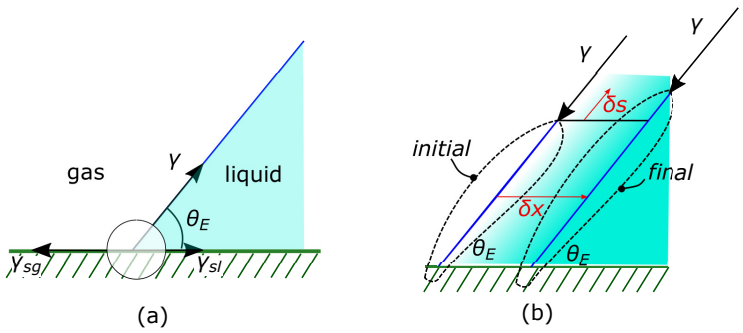

Figure 1.4: Young's law. (a): graphical interpretation, (b): displacement of a liquid wedge.

1.4 Statics of contact lines - Young's law

1.4.1 Interpretation of Young's law

We consider now the situation where a liquid-gas interface is put in contact with a solid substrate, creating two additional interfaces, namely a solid-liquid interface and a solid-gas one, as well as a contact line where all three phases intersect. This contact dictates in mechanical equilibrium the angle at which the liquid-gas interface intersects the solid by Young's law.

Adding up the capillary forces acting on a contact line, as in Fig. 1.4a, and equating the sum of their projections on the solid substrate to zero gives Young's law,

$$\cos\theta_E = \frac{\gamma_{sg} - \gamma_{sl}}{\gamma}, \tag{1.36}$$

where γ_{sl} and γ_{sg} are the solid-liquid and solid-gas interfacial tensions and θ_E is the equilibrium contact angle, by convention measured from the liquid side. As stressed in the reviews [31] and [2], γ, γ_{sg} and γsl adequately describe the energy content of the interfaces at a distance longer than typically 100 Angstrom from the contact line, i.e. outside of a core region where intermolecular forces cause further complications. This is shown with a circle around the contact point in Fig. 1.4a and b, symbolizing a tiny vicinity of the contact line inside of which the intermolecular forces can be felt and break down the used description.

The scope of this work is limited to the macroscopic aspects of drops/menisci on substrates which are rigid, i.e. balancing any normal force component $\gamma \sin\theta_E$ by a reaction force of equal magnitude. Microscopically, trough the statistical mechanics of inhomogeneous fluids [32] and density-functional theory [33] this normal force component is shown to be related to wall-fluid interactions in a tiny vicinity of the contact line. On elastic substrates, Eq. 1.36 is shown [34] to hold for drops of much larger radius than the substrate thickness, while in the opposite limit the substrate deforms like a liquid and the forces in the normal direction contribute to determining the geometry of the lens-shaped drop.

In Eq. 1.36, only the difference $\gamma_{sg} - \gamma_{sl}$ is of importance and not the individual value of these interfacial tensions. For higher values of this difference, solid-liquid contact is favoured more over solid-gas contact and the solid is called more wettable. In the limit situation where this difference tends to γ, $\theta_E \to 0$ and the solid is perfectly

wettable. In the opposite limit, where this difference tends to $-\gamma$, $\theta_E \to \pi$. Such substrate is attributed the property of superhydrophobicity. In this work, we are interested in situations of partial wetting, which fall between these two limits.

Another important question is down to which sizes the macroscopic description provided by Young's law works. In the last decade, concepts arising from Young's law have been successful at explaining phenomena at nanometric scale on atomic force microscopy tips [35] and it has been shown with molecular-dynamics simulations [36] that the force at the contact line on a 15 nm fibre agrees well with Young's law.

1.4.2 A derivation of Young's law

Young's law (Eq. 1.36) can be obtained based on thermodynamic considerations. The first principle of thermodynamics states that the variation of the internal energy of a system of a closed system is given by

$$dU = \delta Q + \delta W.$$

The second principle states that $\delta Q = TdS - Td_iS$, where the second term is absent for reversible processes. Therefore,

$$dU = TdS - Td_iS + \delta W.$$

It is useful to define the Helmoltz free energy as,

$$dF = dU - TdS - SdT = -Td_iS + \delta W - SdT,$$

such that at constant temperature and for reversible processes,

$$dF = \delta W.$$

The applicability of Young's law can be demonstrated for all practical cases (i.e. independently of geometry or external constraints or the presence/absence of body forces), as done with a subtle and elegant argumentation in the review of de Gennes [31], or with a rigorous proof, as presented by Roura et al. [37]. Both of them are considering the free energy of a system which is a planar liquid wedge (Fig. 1.4b), of which the equilibrium contact angle θ_E is defined as the dihedral angle of the wedge for which the free energy of the system is stationary under allowed changes. Keeping the angle constant, we allow for displacements of the contact line δx, and for the elongation of the liquid-gas interface δs, with both quantities a priori unrelated to each other.

The planar liquid wedge represents a part of any system with a contact line, near the contact line. The superimposed curvatures (on zero for the planar wedge) of the liquid-gas interface, as well as of the contact line, are in most practical cases weak compared to curvatures present in the core region (which are of the order $\frac{1}{100A}$) [31]. We assume that the tiny core region around the contact line is unaffected but simply translated from the initial and the final state.

By defining the system in a close enough vicinity of the contact line, the work done by the hydrostatic pressure and the gravitational potential energy can be neglected. These quantities are namely proportional to resp. the height and the square of the height of the wedge (see e.g. [37]) while we will consider terms which are independent of the height of the wedge. Furthermore, for the planar wedge, the capillary pressure

difference between the liquid and the gas is zero. It is shown that considerations [37] result in the cancellation of the $p\delta V$-term with the contribution coming from cutting the liquid phase with the boundary of our system.

Then, the work associated with the changes δx and δs has two contributions,

$$\delta F = \delta W = \delta W_\gamma + \delta W_{ext}. \tag{1.37}$$

Here, δW_γ is due the change in the interfacial areas of the three interfaces. The gas displaces the liquid on the substrate over a distance δx and the liquid-gas interface can get elongated by δs,

$$\delta W_\gamma = (\gamma_{sg} - \gamma sl)\,\delta x + \gamma \delta s. \tag{1.38}$$

Secondly, the boundary of our system, unavoidably, *cuts* the liquid-gas interface and therefore we need to consider the external work δW_{ext} done on our system by the capillary force, δW_{ext}, given by the projection of this force on the two allowed displacements,

$$\delta W_{ext} = -\gamma \cos\theta_E \delta x - \gamma \delta s. \tag{1.39}$$

Now specifying the expressions of the work (Eqs. 1.38 and 1.39) in Eq. 1.37, we obtain

$$\delta F = (\gamma_{sg} - \gamma sl - \gamma \cos\theta_E)\,\delta x + (\gamma - \gamma)\,\delta s \tag{1.40}$$

Thus, the free energy of our system around the contact line is stationary for arbitrary displacements δx and δs, only if the contact angle satisfies Young's equation (Eq. 1.36).

Even though derivations such as the one above show the applicability of Young's law, independently of geometry or from external constraints or from the absence of body forces such as gravity, this law has also been derived by minimizing the total free energy of macroscopic systems, showing the consistency of the macroscopic formulation and usually leading to new insights.

This has for example been done for an axisymmetric drop, independently of external fields by using variational techniques [38, 39], where Young's law results from the transversality condition. It this context, we also note the derivation of the augmented Young's law [40, 41] which is derived by free energy minimization of a system consisting of a 2D or axisymmetric drop whose edges fall under the influence disjoining (Derjaguin) pressure.

1.4.3 Young's law for a spherical drop

Let us now write the free energy of a drop of the shape of a spherical cap and check the consistency of the energy by deriving Young's law. The adopted formulation will be used in further sections to include the effects of the heterogeneity of wetting properties.

The shape of a spherical cap satisfies the Young-Laplace equation in the absence of gravity. Therefore it is consistent to neglect the gravitational potential energy. Furthermore we specify that the drop has a fixed volume V, such that no pdV term enters the equilibrium condition. This constraint makes that, as shown in Fig. 1.4c, moving the contact line over a distance δx requires to adapt the whole liquid-gas interface to the new situation. In such system, the free energy is stationary for,

$$dF = \delta W_\gamma = (\gamma_{sl} - \gamma_{sg})\, dA_{sl} + \gamma dA_{lg} = 0 \implies \frac{\gamma_{sg} - \gamma_{sl}}{\gamma} = \left(\frac{dA_{lg}}{dA_{sl}}\right)_V, \quad (1.41)$$

where it is assumed that all of the solid is contacted by either one of the phases,

$$dA_{sg} + dA_{sl} = 0.$$

The liquid-gas interface area of a spherical drop is given by,

$$A_{lg}(R_c, \theta) = \frac{2\pi R_c^2}{1+\cos\theta} \rightarrow dA_{lg} = 2\pi R_c^2 \frac{\sin\theta}{(1+\cos\theta)^2} d\theta + \frac{4\pi R_c}{1+\cos\theta} dR_c.$$

The solid-liquid contact area is disc-shaped, so $dA_{sl} = 2\pi R_c dR_c$. Substituting both infinitesimal areas into Eq. 1.41 gives,

$$\frac{dA_{lg}}{dA_{sl}} = R_c \frac{\sin\theta}{(1+\cos\theta)^2} \frac{d\theta}{dR_c} + \frac{2}{1+\cos\theta}, \quad (1.42)$$

where $\frac{d\theta}{dR_c}$ should be determined by the fact the volume of the droplet does not change during the process. The volume of the drop is given by,

$$V(R_c, \theta) = \pi R_c^3 \frac{(1-\cos\theta)^2 (2+\cos\theta)}{3\sin^3\theta}. \quad (1.43)$$

Differentiation gives,

$$dV = \frac{\pi R_c^2 (1-\cos\theta)^2 (2+\cos\theta)}{\sin^3\theta} dR_c + \frac{\pi R_c^3}{4\cos^4(\frac{\theta}{2})} d\theta,$$

and therefore,

$$\left(\frac{d\theta}{dR_c}\right)_V = -\frac{4(1-\cos\theta)^2 (2+\cos\theta)\cos^4(\frac{\theta}{2})}{R_c \sin^3\theta}. \quad (1.44)$$

Substituting Eq. 1.44 into Eq. 1.42 and simplifying gives naturally Young's law,

$$\frac{\gamma_{sg} - \gamma_{sl}}{\gamma} = \left(\frac{dA_{lg}}{dA_{sl}}\right)_V = \cos\theta \equiv \cos\theta_E.$$

Fig. 1.5b and c shows numerical example for a 1 microliter drop on a substrate for which the equilibrium angle is given by $\theta_E = \pi/4$. These two conditions fix a unique value of the contact radius R_c as shown in panel (b). The fixed volume constraint is satisfied on a monotonously descending curve (black). This black curve has one single intersection with the horizontal line, which represents the equilibrium contact angle. At this intersection, both the volume condition and contact angle equilibrium conditions are met.

As expected, the equilibrium is a stable. For example, if starting from this intersection, if R_c would be slightly increased (at constant volume), then θ would become smaller than the equilibrium angle. This means that a net force would be acting on the contact line, in the direction which restores the R_c back to its equilibrium position.

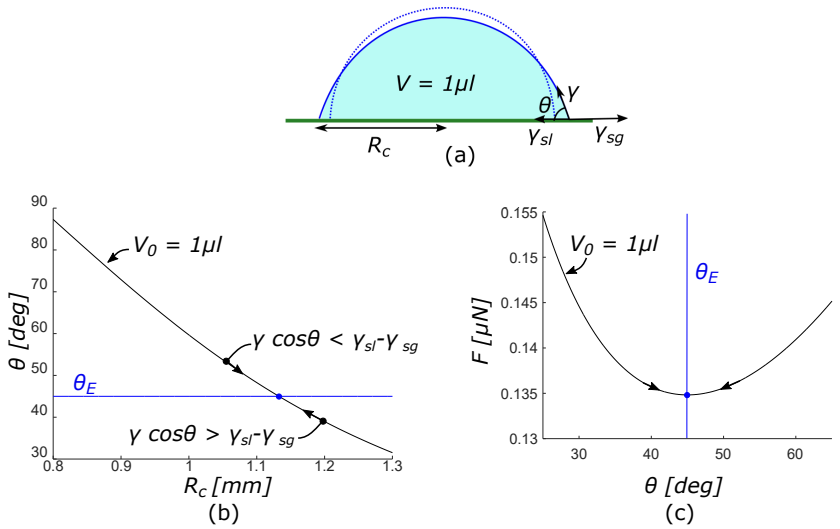

Figure 1.5: Numerical example of a spherical drop on a homogeneous substrate. (a): A drop at fixed volume for which variations of angle and contact radius are linked. (b): Contact angle versus contact radius (c): Free energy versus contact angle, with $\gamma = 0.072 N/m$.

The stability is confirmed in panel (c) by the fact that the equilibrium configuration corresponds to a minimum of the free energy. This free energy is calculated by integrating dF Eq. 1.41, yielding up to a constant,

$$F(R_c, \theta) = \gamma A_{lg}(R_c, \theta) - \gamma \cos\theta_E A_{sl}(R_c). \tag{1.45}$$

The free energy in panel (c) is calculated at the constant volume V of 1 microliter. More specifically, the relation between the two arguments of Eq. 1.45 are explicited from the expression of the volume (Eq. 1.43) as,

$$R_c(V, \theta) = \sin\theta \left(\frac{3V}{\pi (1 - \cos\theta)^2 (2 + \cos\theta)} \right)^{\frac{1}{3}}.$$

1.4.4 Wenzel and Cassie-Baxter relations

Let us first consider the limit case of solid surfaces with heterogeneous wetting properties (and roughness), where the deviation of the ideal case (i.e. a homogeneous and smooth substrate) is characterized by a single parameter which is uniform throughout the substrate.

If the substrate displays some roughness, such that surface area of the solid is anywhere a factor r larger than its horizontal projection, then we can repeat the above calculation, where we replace $dA_{sl} \to r dA_{sl}$ with r a constant larger than one. This constant r finally appears in the final result as,

$$\frac{\gamma_{sg} - \gamma_{sl}}{\gamma} = \frac{1}{r} \left(\frac{dA_{lg}}{dA_{sl}} \right)_V = \frac{1}{r} \cos\theta \implies \cos\theta_E(r) = r \left(\cos\theta_E \right)_{r=1}, \tag{1.46}$$

with $\cos\theta_E(r = 1)$ the equilibrium angle on a smooth substrate with the same wetting properties. Eq. 1.46 is called Wenzel's relation [42]. It predicts that the effect of roughness is to enforce the hydrophilic or hydrophobic character of a bare substrate, by bringing θ_E closer to 0 or π, depending on the sign of $(\cos\theta_E)_{r=1}$.

A similar reasoning can be applied for a smooth but chemically heterogeneous substrate. Consider a substrate which consists of alternations of infinitely small regions of different wettability, characterized by $(\gamma_{sl} - \gamma_{sg})_1$ and $(\gamma_{sl} - \gamma_{sg})_2$, with area fractions f_1 and f_2. Now, we replace

$$(\gamma_{sl} - \gamma_{sg}) \implies f_1 (\gamma_{sl} - \gamma_{sg})_1 + f_2 (\gamma_{sl} - \gamma_{sg})_2 ,$$

where f_1 and f_2 are the probabilities of sweeping wettabilities 1 and 2 when moving the contact line. Defining $\cos\theta_{E1} = \frac{(\gamma_{sg}-\gamma_{sl})_1}{\gamma}$ and $\cos\theta_{E1} = \frac{(\gamma_{sg}-\gamma_{sl})_2}{\gamma}$ yields,

$$\cos\theta_E(f_1, f_2) = f_1 \cos\theta_{E1} + f_2 \cos\theta_{E2}. \tag{1.47}$$

Eq. 1.47 is called the Cassie-Baxter relation, which states that on a substrate with a heterogeneity at tiny a scale, $\cos\theta_E$ can be calculated as a area-weighted average of the $\cos\theta_E$s of the surface constituents.

The relevance of the Cassie-Baxter and Wenzel relations (Eqs. 1.46 and 1.47) is still heavily debated (see e.g. the review on the debate [43]). The question is whether contact angles are really influenced by the properties of the substrate inside the wetted area. For example, for a drop on a substrate, it is evidenced experimentally that the presence of a patch of different wettability inside the wetted area (with the patch not touching the contact line), does not affect the contact angle [44, 45]. This type of substrate clearly violates the hypothesis behind the derivation of the Cassie relation, where the heterogeneity is assumed to be uniformly present all over the substrate, including the contact line position. At the same time, it is a case where the average wettability of the wetted area seems to have no effect at all on the contact angle. We will return to this question in two following sections.

1.4.5 What oversimplified models fail to capture - stick-slip and contact angle hysteresis

The assumption that the substrate is perfectly smooth and chemically homogeneous, as well as the assumption that the effects of substrate roughness and chemical heterogeneity on the contact line motion would be adequately described by assigning scalar properties to the substrate, seem to be oversimplifications of reality. The models of previous sections, which relied on such assumptions, fail to capture the main qualitative features displayed by moving contact lines, contact angle hysteresis, which include stick-slip motion and pinning-depinning. Let us explain these features in this section.

Daily examples of a pinned drop include a liquid column stuck in vertical capillary tube (Fig. 1.6a) and a drop on a a vertical wall or window (Fig. 1.6b). In both cases of static equilibrium, the contact angle θ_1 on the bottom side of the drop is larger than the contact angle θ_2 on the upper side of the drop, such that the resulting net capillary force can balance the weight of the drop. A static equilibrium with $\theta_1 > \theta_2$ is, obviously, not possible if both θ_1 and θ_2 need to be equal to the same equilibrium angle θ_E of the liquid on the substrate.

A similar example is a drop pinned inside a liquid wedge which is an idealization of the beak of a shore bird [46]. Here, the static condition where the pressure p_l is

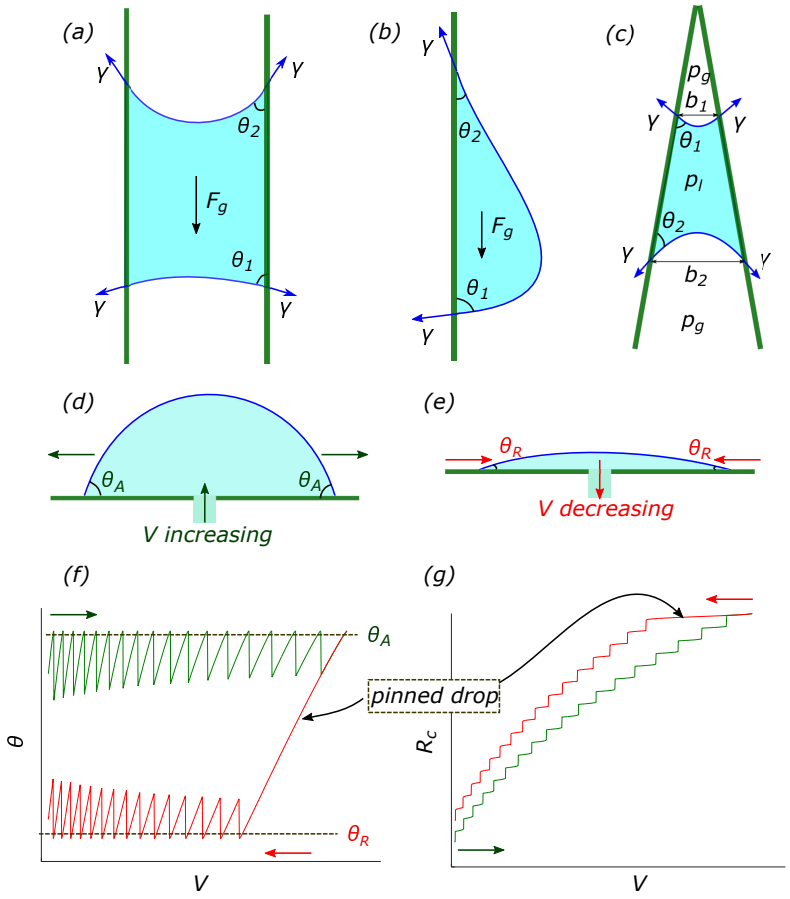

Figure 1.6: Popular examples of the manifestation of contact angle hysteresis. (a): a drop pinned in a capillary tube, (b): drop pinned on a vertical substrate, (c): a drop pinned in a wedge. All these cases of pinning are ultimately explainable by the heterogeneity in the wetting properties (or roughness) of the substrate. (d): A drop advances with an advancing angle θ_A when its volume is increased. (e): The drop recedes with a receding angle θ_R when its volume is decreased. (f) and (g): Contact angle and contact radius versus volume plots for the corresponding process typically show stick a stick-slip behavior and a pinning of the drop when the sign of the variation of V is inverted. These plots are produced with the same heterogeneity shown in Fig. 1.7 later.

uniform in the liquid requires that the radii of curvature of the upper and bottom liquid-gas interfaces should be equal. Or, assuming a circular interface, Eq. 1.21 implies $\frac{b_1}{\cos\theta_1} = \frac{b_2}{\cos\theta_2}$. As $b_1 < b_2$, this necessitates $\theta_1 > \theta_2$. Such static equilibrium cannot be achieved if $\theta_E = \theta_1 = \theta_2$.

Consider the example of a drop placed on a substrate. The models of previous sections (1.4.3 and 1.4.4) predict a single equilibrium angle θ_E, which is independent of for example the drop volume. Therefore, if the volume is slowly increased, such that the system is in equilibrium at all times, the contact angle $\theta = \theta_E$ would stay constant and therefore by volume conservation, R_c would increase. Similarly if the volume is decreased externally, the contact radius R_c would decrease, following the same path.

However, in the real world this experiment would turn out completely different, displaying the typical features shown in the panels (d-g) of Fig. 1.6. The contact line typically advances with an angle θ_A which is larger than the angle θ_R with which it consequently recedes. This difference is termed *contact angle hysteresis* and is for most substrates of the order of tens of degrees, while it can be reduced to a few degrees with careful precautions in substrate preparation [31, 47]. Therefore, in-between its advancing and receding motion, or more specifically when we start to decrease the volume, the drop stays pinned. It does not move appreciably ($\frac{dR_c}{dV} \approx 0$) until the volume is decreased enough to allow for $\theta \to \theta_R$ at the (nearly) fixed R_c. The idea that contact lines stay pinned for the range of contact angles between θ_A and θ_R has for example given rise to the spray retention equation of Furmidge [3]. In this equation the effect of contact angle hysteresis -in opposing drops from sliding due to gravity- appears as a product with the dimensions of a force per unit length of the contact line, $H \equiv \gamma\cos\theta_R - \cos\theta_A$, commonly referred to as *hysteresis force*[2].

Moreover, when the contact line of the drop does move, in many cases it does not move smoothly. Smooth motion at a roughly constant angle (θ_A or θ_R) is typically observed for drops of larger size than any features of the substrate, but higher molecular weight of the liquid also enhances such behaviour (for example alkanes heavier than tetradecane as in contrast to alkanes lighter than nonane in the experiments of [48]). In other cases, or at a finer scale, the motion can be described to be an alternation of stick and slip stages. Panels (f) and (g) of Fig. 1.6 show a calculated example of this case. Let us describe this motion for an advancing contact line. During the stick stage, $\frac{dR_c}{dV} \approx 0$ and θ increases to a critical value θ_A. When this critical angle is reached, a slip stage starts where the contact line jumps in the advancing direction, decreasing by volume conservation θ, such that again a stick stage can follow.

These features are explained treating the wettability of the substrate as a property which varies over the substrate. Namely, panels (f) and (g) of Fig. 1.6 are a numerical example of the model explained in the next section.

1.4.6 Contact line statics on substrates with heterogeneous wetting properties

The sensitivity of contact lines to local gradients of the substrate lies at the core of their intriguing behavior, characterized by contact angle hysteresis, stick-slip motion and pinning-depinning.

Let us rewrite the equilibrium condition (Eq. 1.41), but now with the properties of the solid depending on the spatial coordinates on the solid. Continuing our example configuration of the spherical drop, the term of the free energy related to the wetted area is given up to a constant by,

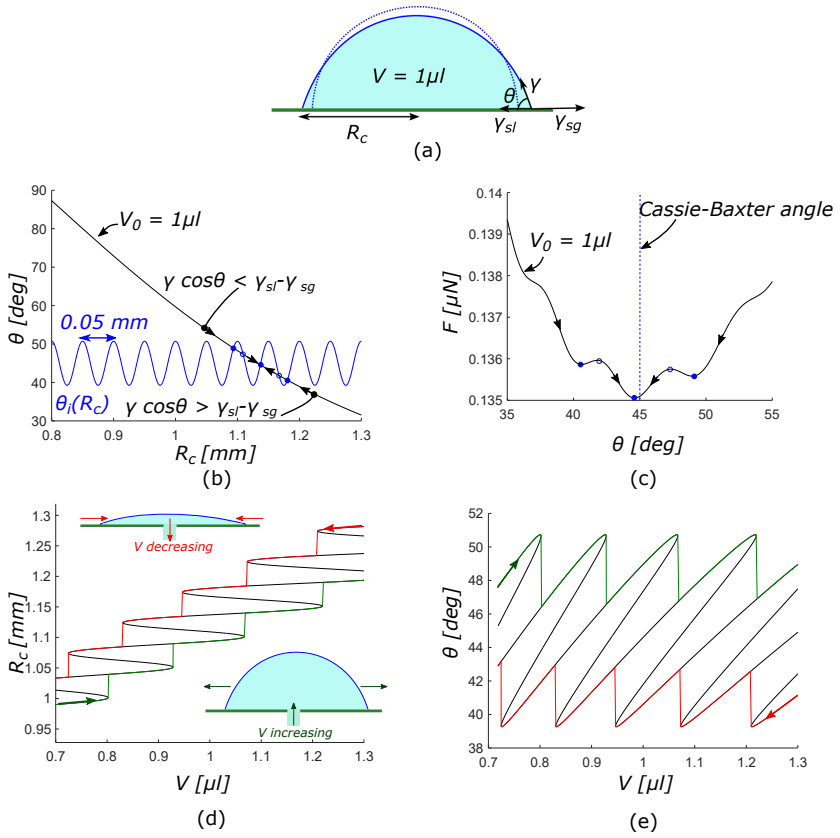

Figure 1.7: Same as Fig. 1.5, but for a drop on a chemically heterogeneous substrate, with now additionally panels (d) and (e) which show how the equilibrium points (black) shift with V, and how tracking it from left to right (green) and right to left (red) result in stick-slip and hysteresis.

$$W_{sl,sg} = \int_{A_{sl}} (\gamma_{sl}(R_c) - \gamma_{sg}(R_c)) = 2\pi \int_0^{R_c} (\gamma_{sl}(R_c) - \gamma_{sg}(R_c))\, 2\pi R_c dR_c,$$

or in differential form by,

$$dW_{sl,sg} = (\gamma sl(R_c) - \gamma_{sg}(R_c))\, 2\pi R_c dR_c. = (\gamma sl(R_c) - \gamma_{sg}(R_c))\, dA_{sl}.$$

The equilibrium condition thus now becomes,

$$dF = \delta W = (\gamma_{sl}(x) - \gamma_{sg}(x))\, dA_{sl} - \gamma dA_{lg} = 0. \tag{1.48}$$

As in Eq. 1.41, it is possible isolate $\frac{dA_{lg}}{dA_{sl}}$, leading now to

$$\frac{\gamma_{sg}(x) - \gamma_{sl}(x)}{\gamma} = \frac{dA_{lg}}{dA_{sl}}, \tag{1.49}$$

As the right-hand side of Eq. 1.49 yields for a spherical drop at the constraint of a fixed volume $\cos\theta$, the equilibrium condition can be written as,

$$\cos\theta = \frac{\gamma_{sg}(R_c) - \gamma_{sl}(R_c)}{\gamma} \equiv \cos\theta_i(R_c), \tag{1.50}$$

where we have defined the intrinsic contact angle θ_i as the local equilibrium angle [49]. This incorporation of the heterogeneous wetting properties of the substrate explains the main qualitative features of contact line motion on real substrates, as can be appreciated by comparing the numerical example in Fig. 1.7 with its counterpart for homogeneous substrates (Fig. 1.5).

Due to the presence of a periodic heterogeneity in $\theta_i(R_c)$ in Fig. 1.7, at the fixed volume V_0 there are multiple configurations $(R_c, \theta_i(R_c))$ which simultaneously satisfy Young's law and the volume constraint. Namely, there are 5 equilibrium configurations, which are alternately metastable and unstable.

The free energy (panel (c)) is now given in integral form up to a constant as,

$$F(R_c, \theta) = \gamma A_{lg}(R_c, \theta) - 2\pi\gamma \int_0^{R_c} \cos\theta_i(R_c) r dr. \tag{1.51}$$

1.4.6.1 Situation at fixed volume

Shuttleworth and Bailey [50] were the first to put forward arguments why the substrate heterogeneity induces a multistability of equilibrium states at fixed drop volume. Johnson and Dettre [51, 52] were the first to concertize and strengthen these arguments with a numerical study. They have studied the case of a spherical drop at constant volume, sitting on a substrate with periodic grooves [51] and on a substrate consisting of alternating circular bands of different wettability [52]. For both cases, they have calculated the free energy of the equilibrium configurations (which satisfy simultaneously Young's law and the volume constraint). This led in both cases to the same physical picture, which also appears in Fig. 1.7c as the 3 metastable and 2 unstable equilibrium configurations. The highest and lowest values of the metastable equilibrium angles at the fixed volume correspond to the highest relative minima of the free energy and also neighbor to the lowest energy barriers (2-3 nJ in our example). This has led to the con-

clusion [52] that the difference between the highest and lowest observable equilibrium angles will be smaller if the drop can overcome some of the energy barriers with the vibrational energy (the precise nature of which was unspecified [53]) it possesses.

Simulations of large drops on substrate with a small-scale heterogeneity [54, 55] have demonstrated that the actual relevance of the Cassie-Baxter type relations (section 1.4.4) is that they accurately predict the value of the most stable contact angle (corresponding to the global minimum of the free energy). In such limit, a free energy plot like Fig. 1.7c becomes nearly indistinguishable from its homogeneous counterpart, Fig. 1.5c, but displays upon closer inspection a large amount of closely adjacent metastable angles, separated by small energy barriers.

Several techniques to provide energy to drops have been demonstrated to lead to a convergence of the contact angle to a value which can be reasonably assumed to be of lower energy. These techniques include vibrating the substrate [56, 57] and the use of sound [58]. The reduction of contact angle hysteresis is also evidenced as a direct effect of an alternating current (AC) electrowetting setup [59], as in contrast to a DC one. These findings however remained qualitative in the sense that no direct connection could be made to the value of the energy barriers crossed by the agitation mechanism.

1.4.6.2 Effect of externally varying the volume

Huh and Mason [53] continued the study of the drop on a substrate with periodic grooves, but differently from [51] investigated the effect of quasi-statically varying the drop volume. This has led to a picture similar to the one shown in Fig. 1.7d and consistent with typical experimental observations.

When the volume V is quasi-statically increased, its effect on panel (a) can be thought of (more or less) as a horizontal shift of the black line to the right. This results in the shape of the static solutions drawn in black in panels (d) and (e), where periodically metastable and unstable branches meet in limit points.

Following the static solutions in the direction of increasing volumes (green curve) results in a periodic alternation of two modes how the system reacts to the externally imposed volume variation. When metastable branches are followed, R_c does not vary much, while θ increases. This is a *stick* stage, where the contact line is *pinned*. When the system reaches a limit point, the contact line needs to perform a sudden advancing jump, i.e. a *slip* stage, to reach the closest by metastable branch. Following the static solutions in the direction of decreasing V necessitates a different path, which has the same features and where the contact angle is smaller. This aspect is referred to as *contact angle hysteresis*.

The study of Huh and Mason [53] provided a plausible theoretical explanation for contact angle hysteresis associated with irreversible jumps of the contact line. A corresponding experimental study followed [60] on drops on substrates of which the roughness is characterized by scanning electron microscopy and profilometry. The experimental results were explained by a combination of jumps due to grooves parallel to the contact line, qualitatively similar to the explanation in [53], and capillary channeling due to grooves orthogonal to the contact line. For advancing motion, the observed advancing angle showed quantitative correspondence with the sum of the contact angle measured on smooth substrates, plus the measured maximal angle of the substrate grooves. For receding motion, axisymmetry was broken and such prediction yielded too high receding angles. Soon after, the Huh's model was adapted to the configuration of a meniscus around a fibre and qualitatively compared to experiments on grooved fibres [61, 62].

Similar models have been deployed for other configurations (see table 1.1); for cylindrical drops [49], for bubbles [63], for contact lines on vertical plates [64] etc., in each case reproducing the qualitative features of typical experiments convincingly well and in a natural way. However no direct comparison was previously been made with experiments on the level of detail of the individual jump events.

More recently, a model of a cylindrical drop on a chemically heterogeneous substrate, which is free to shift laterally has been successful in explaining the hysteretic behavior and stick-slip predicted in a phase-field simulation [65]. A similar model provides a theoretical explanation of the qualitative features of the topography induced contact line jumps observed upon evaporation on wavy smooth substrate[66].

	Title	Year	Ref.	Configuration	External control
a	Effects of surface roughness on wetting (theoretical)	1977	Huh and Mason[53]	Spherical drop on rough substrate	Drop volume
b	An experimental study of some effects of solid surface roughness on wetting	1980	Oliver et al.[60]	Spherical drop on rough substrate	Drop volume
c	Tensiometric studies on wetting	1981	Bayramli et al.[61, 62]	Meniscus around a fibre	Immersion depth
d	Contact angle hysteresis on heterogeneous surfaces	1985	Schwartz and Garoff[64]	Capillary rise on a vertical plate with chemical patches	Immersion depth
e	Capillary rise and hysteresis in periodic porous media	1989	Marmur[67]	Liquid inside porous medium with periodic inclination angle, specific surface and porosity	Imbition height
f	Simulation of Contact Angle Hysteresis on Chemically Heterogeneous Surfaces	1996	Brandon and Marmur[68, 69]	Cylindrical drop on chemically heterogeneous substrate	Drop volume
g	Contact-angle hysteresis on heterogeneous smooth surfaces: theoretical comparison of the captive bubble and drop methods	1998	Marmur[63]	Cylindrical drop and cylindrical bubble on chemically heterogeneous substrate	Drop volume
h	Contact angle hysteresis of cylindrical drops on chemically heterogeneous striped surfaces	2006	Iwamatsu[70]	Cylindrical drop on substrate with chemical patches	Drop volume
i	Wetting on axially-patterned heterogeneous surfaces	2008	Rodriguez et al.[71]	Spherical drop on substrate with chemical patches	Drop volume
j	Dynamics of Fattening and Thinning 2D Sessile Droplets	2016	Pradas et al.[65]	Cylindrical drop (free to shift laterally) on chemically heterogeneous substrate	Drop volume
k	Snap evaporation of droplets on smooth topographies	2018	Wells et al.[66]	Cylindrical drop (free to shift laterally) on wavy substrate	Drop volume

Table 1.1: Overview of methods where statics of contact angle hysteresis is predicted in closed form upon externally varying a parameter.

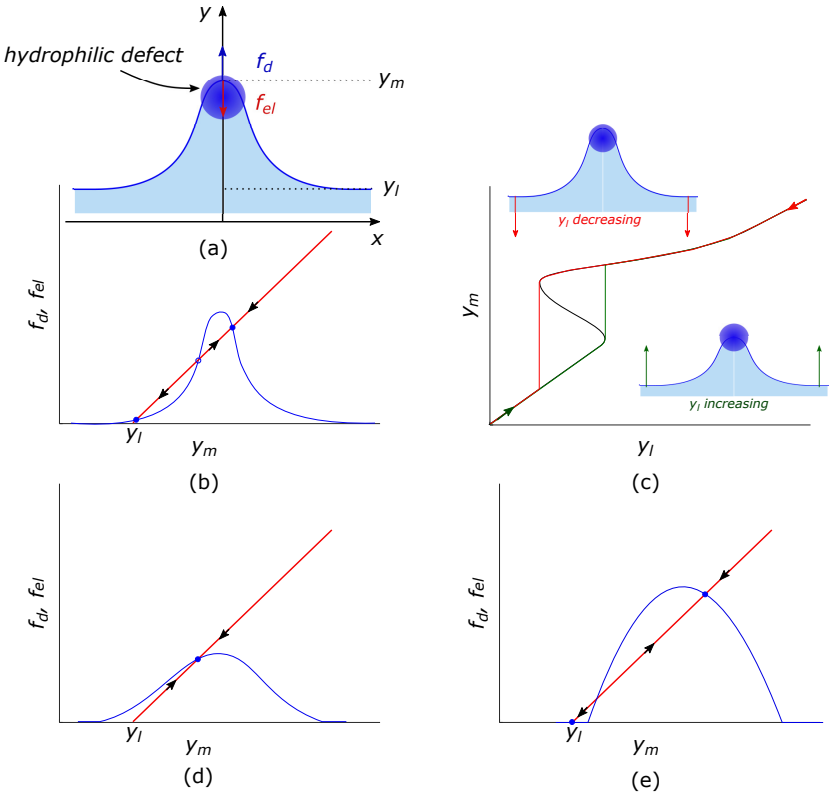

Figure 1.8: Graphical construction of Joanny and de Gennes [72]. (a): liquid wedge from top view, y_l is the position of the unperturbed contact line and y_m is at the height of the defect, (b): graphical force balance, (c): effect of quasi-statically varying y_l, (d): force balance for a weak defect, (e): force balance for a mesa-defect.

1.4.7 Deformed contact lines - Theory of Joanny and de Gennes

The situation is, of course, much more complicated for contact lines which are not circular or straight.

For the situation sketched in Fig. 1.8a, Joanny and de Gennes[72] have derived the elastic energy of a liquid wedge, owing to perturbations of its straightness by a localized force, and shown that the associated elastic restoring force f_{el} can in essence be written in Hookean form,

$$f_{el}\left(y_m, y_l\right) \approx \frac{\pi\gamma\theta_0}{\ln\left(\frac{l}{d}\right)}\left(y_m - y_l\right) \equiv k\left(y_m - y_l\right), \tag{1.52}$$

where l is a microscopic cut-ff and d is a characteristic size of the defect. In the problem of interest, this localized force f_d is exerted by a wettability defect on the contact line, with a main contribution at $y = y_m$,

$$f_d\left(x, y\right) = \int_{-\infty}^{\infty} \gamma\left(\cos\theta_i(x, y) - \cos\theta_0\right) dx \approx f_d\left(y_m\right). \tag{1.53}$$

The implications of the static condition $f_{el}\left(y_m, y_l\right) = f_d\left(y_m\right)$ can be understood

from a graphical construction as in Fig. 1.8b. For the example of a single hydrophilic defect, when the average position of the contact line y_l is close enough to the defect, the contact line will adopt one of the two possible metastable configurations with corresponding values y_m at maximal distortion at the height of the defect. When y_l is varied externally (as can be seen by moving the red line of panel (b) laterally, or the result sketched in panel (c)), stick-slip and hysteretic behavior are predicted.

The graphical force balance also enables to appreciate that not all defects will cause stick-slip and hysteresis. If the gradients in wettability caused by the defect are too small compared to the contact line spring constant k, the force balance will have only one solution (Fig. 1.8d). Such defects are termed weak, or sub-threshold and their existence is experimentally confirmed [35]. On the other hand, defects with sharp edges (Fig. 1.8e), called mesa-defects, will always produce hysteresis.

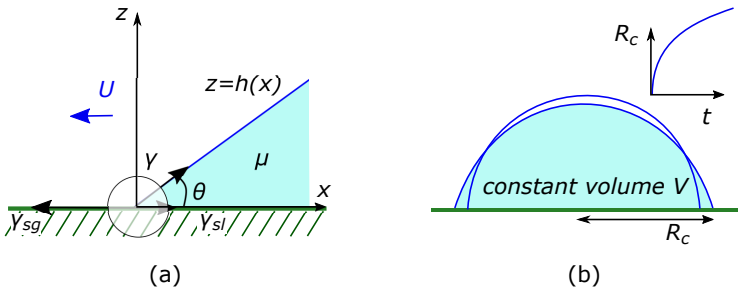

Figure 1.9: (a): Sketch of a liquid wedge moving at a velocity U (b): Spreading of a drop

1.5 Dynamics of contact lines

1.5.1 Scaling arguments based on hydrodynamics

In this section, qualitative scaling arguments[73] are made on the modification of the contact angle θ with a finite contact line velocity U, in the framework of the lubrication (thin-film) approximation. The value of these arguments is that they yield very similar dependencies as the more rigorous derivations, discussed in the next section.

The basic idea is to equate the energy per unit time provided by the capillary forces, $\frac{dE_\gamma}{dt}$, to the energy dissipated through viscosity in the flow, $\frac{dE_\mu}{dt}$, where both energies depend on U and θ.

Consider the liquid wedge, draw in Fig. 1.9a, advancing with a steady velocity U. The height profile of the liquid is described by $h(x,t)$.

Let us first estimate the viscous dissipation due to the flow inside of the liquid. In the lubrication framework, the viscous dissipation inside the film is given by,

$$\frac{dE_\mu}{dt} = \mu \int \left(\int_0^h u_z^2 dz \right) dx, \tag{1.54}$$

where μ is the liquid viscosity and u is the horizontal velocity component. This velocity component is obtained by integrating the x-component of the Navier-Stokes equation, where inertial effects are neglected due to the smallness of the characteristic aspect ratio of the system (ϵ in section 1.3.2.3). In the absence of body forces (which are negligible close enough to the contact line),

$$u_{zz} = \frac{p_x}{\mu} \equiv A(x),$$

where p is the pressure field inside the liquid. Integrating once and applying the condition ($(u_z)_{z=h} = 0$) as the gas viscosity is negligible and the liquid is at constant temperature and pure, gives

$$u_z = A(x)\,(z-h) \tag{1.55}$$

A second integration, with a classical no-slip boundary condition gives the hori-

zontal velocity field in the frame moving with the contact line,

$$u = A(x)\left(\frac{z^2}{2} - hz\right),$$

The volumetric flux q (per unit orthogonal length) can now be calculated as,

$$q = \int_0^h u dz = -A(x)\frac{h^3}{3}. \tag{1.56}$$

Eliminating $A(x)$ from Eq. 1.55 using Eq. 1.56 yields,

$$u_z = -\frac{3q}{h^3}(z - h),$$

and therefore the viscous dissipation (Eq. 1.54) can be rewritten as

$$\frac{dE_\mu}{dt} = 3\mu \int \frac{q^2(x)}{h^3(x)} dx \tag{1.57}$$

To have an estimation of the typical scales of this dissipation rate, let us make the simplifying assumption that the interface is a wedge $h(x) = \theta x$ and $q(x) = Uh(x)$. This is inconsistent in the sense that for such planar interface, the Laplace pressure h_{xx} and its gradient are h_{xxx} are zero, and therefore $A(x) = 0$. The error made is small assuming that most of the dissipation takes place very close to the contact line, where the introduced error is the weakest [73]. Introducing these expressions in Eq. 1.57 yields

$$\frac{dE_\mu}{dt} \approx 3\mu U^2 \int \frac{1}{h(x)} dx \approx 3\mu U^2 \theta^{-1} \int \frac{dx}{x} = 3\mu U^3 \theta^{-1} \ln\left(\frac{l_{mac}}{l_{mic}}\right), \tag{1.58}$$

where l_{mac} is an appropriate macroscopic length scale, such as the length of the wedge, and l_{mic} is a microscopic length scale that needed to be introduced to avoid the dissipation going logarithmically to infinity as $l_{mic} \to 0$. This divergence is referred to as the Huh and Scriven [74] paradox, and would imply the false premise that *not even Herakles could sink a solid*. Another quantity of which classical hydrodynamics predicts the divergence in the same way is the tangential stress acting on the solid substrate,

$$\mu\left(u_z\right)_{z=0} = 3\mu\frac{q}{h^2} \approx 3\mu U^2 \theta^{-1} \ln\left(\frac{l_{mac}}{l_{mic}}\right).$$

Several mechanisms have been proposed to relieve the dynamical singularity near the contact line, which act only in the very near vicinity of the contact line, including slip at the substrate, disjoining pressure, precursor films and diffuse interfaces (a list of proposed mechanisms is given in [2]). More recently, it has been shown [75] that no singularities arise in the same hydrodynamic description if the Kelvin effect is included. This effect also only plays a role in the near vicinity of the contact line and interestingly regularizes the singularity.

Continuing the scaling argument, the energy per unit time provided by the capillary forces, $\frac{dE_\gamma}{dt}$ is estimated as the product of the contact line velocity U and the unbalanced Young's force. If the substrate is assumed to be perfectly wetting, $\theta_E = 0$, or

$\gamma_{sg} - \gamma sl = \gamma$. Therefore, for any finite contact angle θ, the interfacial tensions acting on the contact line result in a net force $\gamma\,(1 - cos\theta)$. The corresponding energy per unit time is estimated for small angles θ as,

$$\frac{dE_\gamma}{dt} \approx U\gamma\,(1 - \cos\theta) \approx U\gamma\frac{\theta^2}{2}. \tag{1.59}$$

Equating Eqs. 1.58 and 1.59 finally yields,

$$\theta^3 = 6\frac{\mu U}{\gamma}\ln\left(\frac{l_{mac}}{l_{mic}}\right) = 6Ca\ln\left(\frac{l_{mac}}{l_{mic}}\right), \tag{1.60}$$

This law has been verified experimentally [76] on perfectly wetting substrates, surprisingly up until angles of 100 degrees, where $\left(\frac{l_{mac}}{l_{mic}}\right)$ was found to be of order 10^4, or $\ln\left(\frac{l_{mac}}{l_{mic}}\right)$ of the order of 10.

1.5.1.1 Tanner's law

Let us apply Eq. 1.60 on the spreading of a drop on a perfectly wetting substrate (Fig. 1.9b), where $U = \frac{dR_c}{dt}$ with R_c the contact radius. The drop has the shape of a paraboloid of revolution (approximating well the shape of a spherical drop for small contact angle), and a constant volume. The spreading rate is given by,

$$\frac{dR_c}{dt} = \theta^3\frac{\gamma}{6\mu\ln\left(\frac{l_{mac}}{l_{mic}}\right)}. \tag{1.61}$$

The drop has a small contact angle θ, and a constant volume V_0. Therefore $\theta \approx \frac{4V_0}{\pi R_c^3}$ and we can rewrite Eq. 1.61 as

$$R_c^9 dR_c = \frac{\gamma}{6\mu\ln\left(\frac{l_{mac}}{l_{mic}}\right)}\left(\frac{4V_0}{\pi}\right)^3 dt, \tag{1.62}$$

where $\left(\frac{l_{mac}}{l_{mic}}\right)$ is considered to be constant as only its logarithm affects the problem. Integrating both sides starting from an initial contact radius 0 gives Tanner's law,

$$R_c = \left(\frac{5\gamma}{3\mu\ln\left(\frac{l_{mac}}{l_{mic}}\right)}\left(\frac{4V_0}{\pi}\right)^3 t\right)^{\frac{1}{10}} \propto t^{\frac{1}{10}} \tag{1.63}$$

1.5.2 Cox-Voinov relation

More rigorous theories have been developed which treat the partial wetting case, leading to similar expressions as Eq. 1.60, but where the factor 6 is replaced by 9. Without entering into the many subtleties arising in these asymptotic treatments of the moving contact line problem (discussed in [2, 77] and the references therein), we summarize below the results of primary relevance to this work.

These more rigorous approaches divide the liquid layer into typically three spatial regions with different orders of magnitudes of the distance x from the contact line. In the intermediate (or overlap [78]) region, independently from the particular geometrical details at the large scale and the microscopic details at the contact line, a stationary

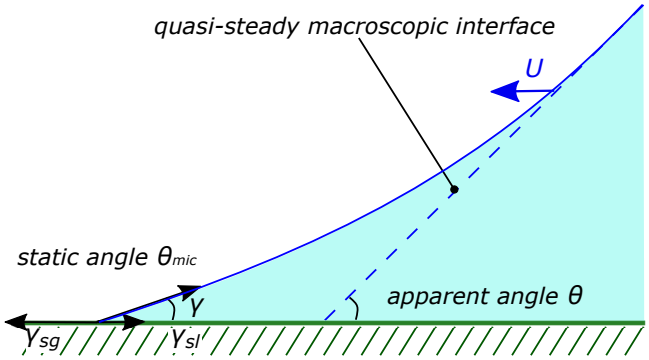

Figure 1.10: Distinction between the apparent (dynamic) contact angle θ and the microscopic (e.g. static) contact angle θ_{mic}. This sketch is horizontally stretched for clarity.

liquid film profile $h(x)$ on a moving substrate requires a balance between viscous and capillary forces, leading to the following lubrication equation, [79]

$$3Ca + h^2 h_{xxx} = 0. \tag{1.64}$$

This third order differential equation has an exact solution [79] which reduces to the famous relation first obtained in different ways and independently by Voinov [80] and Cox [81] (see also e.g. [2]),

$$h_x^3 = \theta_{mic}^3 + 9Ca \ln\left(\frac{x}{l_{mic}}\right), \tag{1.65}$$

or,

$$\theta^3 = \theta_{mic}^3 + 9Ca \ln\left(\frac{l_{mac}}{l_{mic}}\right), \tag{1.66}$$

where θ_{mic} and l_{mic} (with $l_{mic} \ll x < l_{mac}$) come from matching with the microscopic region near the contact line where a relevant process (e.g. Navier slip or disjoining pressure) regularizes the hydrodynamic singularity. Relation 1.66 actually applies for θ up to 135 degrees [81] and the relaxation of the small-slope assumption gives a compatible result [82]. However caution is required for sufficiently large receding velocities ($Ca < 0$) as then the result (Eq. 1.66) ceases to be valid as yielding (non-physical) negative θ (see [83] for a more accurate treatment of what happens in the case of large receding velocities).

In this work, we treat Eq. 1.66 as an effective boundary condition which predicts the velocity dependence of the *apparent contact angle* θ measured at a macroscopic scale (see Fig. 1.10). This apparent contact angle is defined from the extrapolation of the interface profile at the macroscopic scale (taken to be quasi-static at leading order) toward the substrate. The macroscopic contact line position is also an apparent one as it differs from the true contact line position by a distance of the order of the small scale of the problem.

Power laws arising from the Cox-Voinov law (Eq. 1.66) are tested with numerous experiments (reviewed in [2]) and found to accurately describe the spreading of drops of perfectly wetting non-volatile drops ($\theta_{mic} = 0$), where hysteresis is absent. In partial wetting cases, θ_{mic} is typically identified with the contact angle measured at vanishing

speeds, corresponding to an advancing or a receding angle [84, 2]. In chapter 4 of this thesis, we will study the relation between θ and Ca in the presence of stick-slip and hysteresis. An important theoretical prediction by Raphael and de Gennes [85] is that contact line dynamics on heterogeneous substrates results in different scaling laws between the averages of θ and Ca.

1.5.3 Molecular-kinetic theory

Whereas in the Cox-Voinov relation, the unbalanced interfacial tension forces associated with a moving contact line are compensated by viscous dissipation in the flow near the contact line, the molecular-kinetic theory relies on a different dissipative process which takes place in a closer vicinity of a moving contact line. This process is the (individually random) attachment/detachment of liquid molecules from/to the solid substrate, described in the framework of statistical dynamics by an equilibrium frequency κ^o and an average distance λ between the receptive sites on the substrate. A detailed analysis [86, 87] has led to the result,

$$\cos\theta = \cos\theta_{mic} + \frac{2k_BT}{\gamma\lambda^2}\sinh^{-1}\left(\frac{U}{2\kappa^o\lambda}\right), \tag{1.67}$$

where k_B is the Boltzmann constant. For small angles and velocities, this result can be linearized,

$$\theta^2 = \theta_{mic}^2 + \frac{2k_BT}{\gamma\lambda^3\kappa^o}U, \tag{1.68}$$

revealing a dependency of the form $U \propto \theta^2 - \theta_{mic}^2$, which is different than the hydrodynamic result $U \propto \theta^3 - \theta_{mic}^3$. This difference however generally does not imply an experimental distinguishability between the two theories due to the fitting parameters involved (θ_{mic}, λ and κ^o here and θ_0 and $\ln\left(\frac{l_{mac}}{l_mic}\right)$ in the Cox-Voinov relation), as shown in a detailed comparative fitting analysis [88].

1.6 Objectives and overview of the thesis

Contact lines in nature, industry and everyday life typically display pinning-depinning and associated hysteretic effects at the observable or macroscopic scale. The description of contact lines is an inherently multiphase and multiscale problem, which interestingly can be greatly simplified without losing the essential physics responsible for hysteresis and stick-slip, due to the separation of the orders of magnitudes of the time and length scales of the physical processes involved.

Microscopic phenomena near the contact line, whatever their specific details, fix a contact angle at the observable scale. In the statics of contact lines, whatever the specific interactions at a tiny core region, the contact angle observable at the macroscopic scale is related to far field energies of the interfaces as given by the well-established law of Young. But also the dynamics of contact lines, when governed by dissipation near the contact line, is adequately described by the Cox-Voinov relation (or the molecular-kinetic theory) leading to a velocity dependent angle at the macroscopic scale.

The liquid-gas interface shape at the observable scale and under (quasi-)static conditions is given by the Young-Laplace law, which has for some practical configurations closed-form solutions. For these cases, the contact line statics and the hysteretic behavior rooted in it can be fully predicted in closed form. This enables the formulation of minimalistic models for those configurations which capture the essence of stick-slip and contact angle hysteresis, and which can serve as a basis for straight-forward analysis, or for the calculation of many numerical examples to test scaling laws, with the degree of configuration-dependency of the main predictions still an open question.

In chapter 2, such minimalistic static model is formulated for the configuration of a meniscus inside a chemically heterogeneous microchannel, where the results are primarily compared to results obtained in the framework of the theory of Joanny and de Gennes [72] on the configuration of a contact line deformed by a defect. Even though the configurations are very different, both can be interpreted with a graphical force balance, predict the existence of a threshold strength of the chemical heterogeneity below which no hysteretic effects are induced, and lead to the same scaling laws between the amplitudes of the heterogeneity and the induced hysteresis for the case of hysteresis induced by sparsely spaced defects. Another interesting limit behavior is predicted when the heterogeneity wavelength is vanishingly small compared to the microchannel gap size, or similarly to the contact radius in the configuration of a drop. In this limit, stick-slip is unobservable and the contact line advances/recedes at a (nearly) constant angle, given by the maximum/minimum of the statically allowed range.

In chapter 3, a similar minimalistic static model is formulated for the configuration of a meniscus around a wavy fibre which is immersed slowly and vertically in a liquid bath. The predictions of this model are compared quantitatively with experiments at the level of the individual topography-induced jumps, showing good agreement. The interplay between the terms in the free energy during the stick-slip motion is discussed and a scaling law is predicted between the jump length and the energy dissipated during the jump, which is based on the closeness to the threshold. The link with the scaling laws predicted in chapter 2 is discussed.

In chapter 4, we add a piston to the microchannel configuration (2), and show that the stability of a contact line equilibrium (Young's law) depends on whether (a) the piston position or (b) the force on the piston is fixed externally. The quasi-steady dynamics is studied using the Cox-Voinov relation and molecular-kinetic theory to treat the two corresponding cases of a (a) constant piston velocity, and (b) a constant force on

the piston. Interestingly, and as previously predicted by Raphael and de Gennes [85] the two cases lead to different scaling laws between the contact angle and the velocity. With both the Cox-Voinov relation and the molecular-kinetic theory, we recover for both cases (a) and (b) the scaling laws that were predicted in [85] in both cases. We discuss the disappearance of the difference between the two scaling laws, as the intermittency of the contact line motion fades away above a critical contact line velocity, which is lower if the heterogeneity wavelength is smaller. We adapt the formulation to the configuration of a topographical fibre and predict similar results.

Finally, in chapter 5, we show how the minimalistic modelling approach can be extended to treat other configurations with a single contact line, configurations with multiple contact lines, and the 3D case of deformed contact lines on substrates heterogeneous in two directions. For systems with two contact lines (including configurations of biomimetic interest such as the Phalarope beak) we illustrate a mechanism where a jump of one contact line in the advancing/receding direction is accompanied by a jump of the other contact line in the receding/advancing direction, with both jumps rooted in the static solutions and present numerical examples of how this effect influences e.g. the feeding mechanism of the Pharalope bird.

Chapter 2

Contact angle hysteresis in a microchannel: statics

In this chapter, we study contact angle hysteresis in a chemically heterogeneous microchannel by tracking static meniscus configurations in the microchannel upon varying the volume of liquid.

We first construct a graphical force balance similar to a previous approach by Joanny and de Gennes for this system, though here with a straight contact line. It is shown that hysteresis is induced by wettability gradients above a finite threshold value. This is also visualized in a phase-plane plot enabling to easily predict stick-slip events of the contact line and the occurrence of hysteresis.

Above the threshold and for non-overlapping Gaussian defects, we find good agreement with the expressions by Joanny and de Gennes for the hysteresis amplitude induced by a dilute system of defects. In particular, the hysteresis amplitude is found to be proportional to the square of the defect force and to the defect concentration.

For a model sinusoidal heterogeneity, decreasing the ratio between the heterogeneity wavelength and the microchannel gap size, brings the system from a sub-threshold regime, to a stick-slip dominated regime, and finally to a regime with a quasi-constant advancing and receding angle. In the latter case, the hysteresis amplitude is found to be proportional to the defect force.

We also consider an unusual heterogeneity for which the gradients of increasing and decreasing wettability are different. In such situation breaking the left/right symmetry, whether or not hysteresis is observed will depend on the side the liquid enters the microchannel.

2.1 Introduction

Key features of numerous technological innovations across a wide spectrum of applications and their associated industrial processes (coating of substrates is a well-known example) are the dynamics involved with liquid spreading on a solid surface, that is coverage of the surface by displacement, through wetting, of a gas (usually air) by a liquid – see for example the comprehensive reviews in Refs [31, 2, 89]. Contact angle hysteresis (CAH) is common place in wetting processes and it is characterized by a discontinuity between the receding and advancing contact angles [90, 91].

It is widely recognized that substrate heterogeneities are the principal source of CAH [91, 72, 68]. Such heterogeneities are either chemical or topographical or a combination of the two. Theoretical hydrodynamic analysis of contact line dynamics in the presence of chemical-topographical heterogeneities reveals complex dynamics, such as stick-slip motion and liquid motion due to strong heterogeneity gradients (e.g. uphill motion of a droplet) [92, 93, 94, 95, 96, 97, 98, 65]), often in qualitative agreement with experiments.

But despite the several developments and considerable attention that CAH has received for several decades, a large number of issues and problems have not been resolved. In particular, including rationally and systematically CAH in theoretical contact line models and/or numerical codes still eludes us [2, 9]. This is crucial for the control and optimization of technological processes exploiting CAH.

Lack of fundamental understanding of CAH is due in large part to its inherently multiscale nature, a feature that plays a central role in the rapidly growing field of microfluidics [99, 96], as the largest typical lengthscales involved are below the capillary length, thus enabling capillary forces to dominate over body forces. For example, the motion of a gas-liquid interface in microsystems, and how it is affected by CAH and related issues such as pinning-depinning, still lacks fundamental understanding and rigorous characterization.

A number of theoretical efforts have shown that CAH is rooted in the statics of the system [52, 72]. In particular, it has been shown that CAH is related to the rugged free-energy landscape that is induced by the chemical imperfections of the solid, as the associated energy barriers are able to trap the system in metastable configurations (defined as *pairs of contact line position and contact angle*) that depend on its history [52, 100]. This causes the moving contact line (CL) to display hysteresis, even in systems that are either translationally invariant in one direction and can be treated as two-dimensional (2D), in which case the CL is straight [69, 101], or in systems for which the CL has a constant curvature by axisymmetry [100].

An intrinsically three-dimensional (3D) approach was adopted in the theory of Joanny and de Gennes [72] which has formed the basis of many theoretical extensions as well as experimental investigations [2]. In their work, the profile of a CL, deformed by a single chemical defect on a substrate, is calculated such as to satisfy the balance of two forces acting on the CL: (i) the excess of capillary force exerted by the chemical defect, and (ii) the 'elastic restoring force' opposing the deformation of the CL. For a CL close to a 'strong' defect (i.e. exerting an excess capillary force above a certain threshold), this force balance is satisfied for two (meta)stable configurations, causing the system to display hysteresis.

In the present study we analyse the advancing and receding motion of the CL in a 2D microchannel with chemically heterogeneous walls. We compare our results with the main fundamental predictions of Joanny and de Gennes [72], including the existence of a threshold value of the heterogeneity strength, below which hysteresis is absent, and the case of a Gaussian defect, in which the threshold value shows a logarithmic dependence on the system size and heterogeneity wavelength, and vanishes in the limit of sharp edged (*mesa*) defects. It is important to remark, however, that here we are considering a completely different geometry to the 3D system studied in [72].

In particular, one of the goals of our work is to verify whether their theoretical predictions are still valid in our case. To this end, we only consider *static hysteresis*, neglecting the following effects: (i) thermal noise which can assist the system to overcome energy barriers [102, 103, 35, 104] or external vibrations [100] which if strong enough may mitigate hysteresis [52], and (ii) dynamic effects which can also lead to

the occurrence of hysteresis [105].

Another important, but still unresolved issue regarding CAH is the question of linking the properties of the substrate disorder to the hysteresis amplitude, which we denote as H. A decisive first step on this question was was taken in Ref. [72], where the case of a single strong defect was extended to a regime of sparsely spaced strong defects, and the following scaling law was proposed [72, 1, 2]

$$H = \gamma \left(\cos\theta_R - \cos\theta_A\right) \propto \frac{n F_{\max}^2}{\gamma}, \tag{2.1}$$

where $F_{\max}$ is the maximum excess of capillary force exerted by a single defect, and n is the surface density of the defects. The quadratic dependence on $F_{\max}$ and the proportionality with n were verified experimentally and numerically [106, 107, 102, 108]. However, the extension of this expression to dense defects and to other types of heterogeneities is a challenging question that still remains open [107, 109].

Our aim here is precisely to address these issues and provide a quantitative description of CAH. For this purpose we adopt a 2D meniscus in a (2D) microchannel as a model system. To the best of our knowledge, this is the first attempt to address the existence of threshold and scaling laws of hysteresis in 2D systems.

In Section 2.2.1 we introduce the model system, a liquid-gas meniscus in a microchannel with chemically disordered walls and we give the condition for a meniscus in mechanical equilibrium.

Adopting the liquid volume as the control parameter, we offer an example in Section 2.2.2 of how CAH can arise in the system. An alternative interpretation to this phenomenon is given in Section 2.2.3, which involves a graphical force balance, similar to [72].

This similarity is also present in some of the main results. In Section 2.3.1 we show that weak heterogeneities do not produce hysteresis, and evaluate the hysteresis threshold for certain wettability distributions.

In Section 2.3.2 we explain the qualitatively different regimes of hysteresis upon varying the ratio between the heterogeneity wavelength and the microchannel gap size. We comment on the strong dependence of the threshold on the fluid configuration being considered, and argue that it does not exist for a drop fed by a sufficiently slow (quasi-static) liquid injection, for which all regimes of hysteresis are encountered while the drop grows.

For heterogeneities with a strength sufficiently above the threshold, we explore in Section 2.3.3 scaling laws between the parameters of the wettability distribution and H.

Finally, conclusions and perspectives are offered in Section 2.4.

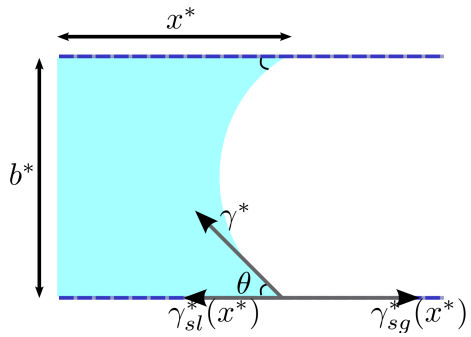

Figure 2.1: Sketch of the profile geometry for a liquid confined inside a chemically heterogeneous microchannel. γ^*_{sl}, γ^*_{sg} and γ^* are the wall-liquid, wall-gas and liquid-gas surface tensions, respectively. The contact angle θ is defined as the angle between the line tangent to the liquid-gas interface at the contact point and and wetted area of the walls.

2.2 Model formulation and theoretical framework

2.2.1 Definition of the system

We consider the 2D setup consisting of a liquid-gas meniscus moving inside a microchannel (Fig. 2.1). A gap of width b^* separates two planar, rigid, topographically flat, but chemically heterogeneous walls. This chemical heterogeneity is characterized by a positional dependence of the interfacial tensions γ^*_{sl} and γ^*_{sg} between the walls and the liquid and the gas, respectively. The liquid-gas surface tension γ^* is assumed constant. We thus impose an intrinsic contact angle θ_i distribution, identical on both walls, as:

$$\cos\theta_i\left(x^*\right) = \frac{\gamma^*_{sg}(x^*) - \gamma^*_{sl}(x^*)}{\gamma^*}, \tag{2.2}$$

where dimensional quantities are denoted with an asterisk.

We assume gravity to be negligible so that the static interface takes a constant curvature (circular arc). Any given pair of the contact line position and contact angle, which we denote as (x^*, θ), fixes the volume of the liquid (per unit length of the contact line):

$$\begin{cases} V^* & = x^* b^* + b^{*2} f\left(\theta\right), \\ f\left(\theta\right) & = \frac{2\theta - \pi + \sin(2\theta)}{8\cos^2\theta}. \end{cases} \tag{2.3}$$

The free energy F^* of the system, per unit length of the contact line and up to a constant, consists of the three interfacial tensions, integrated along the length on which they act:

$$\begin{aligned} F^* = \gamma^* l^* &+ \int_0^{x^*} [\gamma^*_{sl,u}(x^*) - \gamma^*_{sg,u}(x^*)]dx^* \\ &+ \int_0^{x^*} [\gamma^*_{sl,b}(x^*) - \gamma^*_{sg,b}(x^*)]dx^*, \end{aligned} \tag{2.4}$$

where $l^* = (\pi - 2\theta)/2\cos\theta$ is the dimensional liquid-gas meniscus length, and the

subscripts u and b represent the upper and bottom walls, respectively. As we limit our study to identical walls, the two integrals are equal, and

$$F^* = \gamma^* b^* \frac{\pi - 2\theta}{2\cos\theta} - 2\gamma^* \int_0^{x^*} \cos\theta_i(x^*) dx^*. \tag{2.5}$$

To find the extrema of F^* at a fixed volume V_0^*, we minimize the function

$$G^* = F^* + \Lambda[x^* b^* + b^{*2} f(\theta) - V_0^*], \tag{2.6}$$

with respect to x^* and θ, where Λ is a Lagrange multiplier. This calculation actually yields the natural condition

$$\cos(\theta) = \cos(\theta_i(x^*)), \tag{2.7}$$

which states that at equilibrium, the meniscus angle must be equal to the local value of the Young's angle, as expected. In the following, we refer to menisci satisfying Eq. (2.7) as being at *equilibrium configurations*. The volume of such equilibrium configurations is given, in dimensionless form, by:

$$V = \frac{V^*}{b^{*2}} = x + f(\theta_i(x)). \tag{2.8}$$

where we have used b^* as characteristic length scale. Similarly, it is convenient to scale the free energy as:

$$F = \frac{F^*}{b^*\gamma^*} = \frac{\pi - 2\theta}{2\cos\theta} - 2\int_0^{x} \cos\theta_i(x) dx. \tag{2.9}$$

2.2.2 Occurrence of contact angle hysteresis

For homogeneous walls ($\theta_i(x) = \theta_0$), V increases linearly with x [Eq. 2.8]. For non-constant $\theta_i(x)$, a nonlinear variation of V with x occurs, but V might still be monotonously increasing with x if variations of θ_i are weak. For sufficiently disordered walls (the condition will be derived in Section 2.3.1), $V(x)$ increases non-monotonously, enabling the occurrence of multiple equilibrium configurations for a given volume. In Fig. 2.2 we consider a model microchannel with periodically varying wetting properties, illustrating the latter case. Specifically, we take $\cos(\theta_i(x)) = 0.2\sin(\frac{2\pi}{0.02}x)$.

For $V = 0.2$, the contact line will adopt one out of 7 equilibrium configurations, depending on the history of the system. This odd number of configurations corresponds alternatingly to minima (metastable configurations) and maxima (unstable configurations) of the free-energy curve, with the outermost configurations being metastable [see Figure 2.2 (c)]. These four metastable menisci are drawn in 2.2 (d). The difference between maxima and neighboring minima can be interpreted as energy barriers which trap the CL in a given metastable configuration [52, 110]. The magnitudes of these energy barriers are smallest for the metastable configurations with minimal and maximal θ, in agreement with previous results on an axisymmetric drop [52, 110].

Therefore, by imposing that the volume is increasing or decreasing, we obtain the advancing and receding trajectories of the meniscus, respectively, shown as green and red lines in Fig. 2.2 (a). These trajectories are found with the assumption that the system has no ability to overcome energy barriers. For certain values of V, the curve

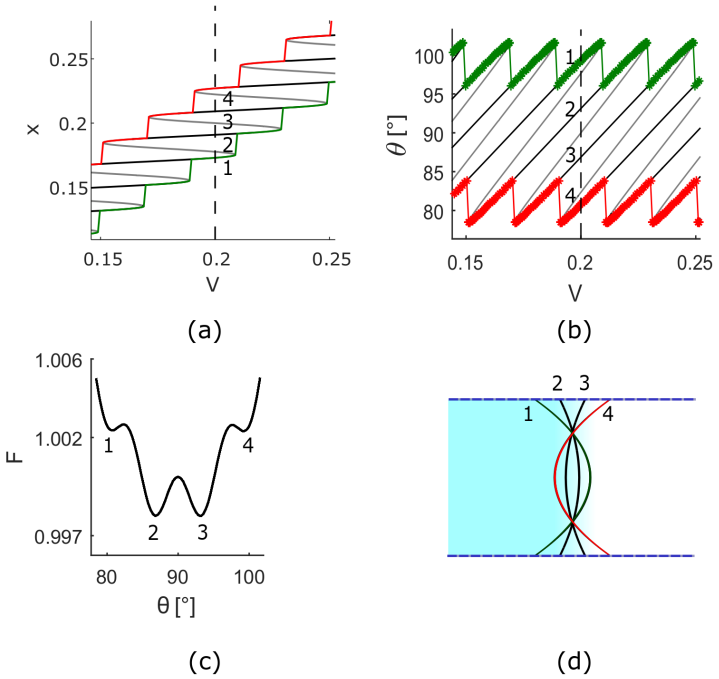

Figure 2.2: Example of how contact angle hysteresis occurs in a 2D microchannel with a chemical pattern given by $\cos\theta_i(x) = 0.2\sin\left(\frac{2\pi}{0.02}x\right)$. (a) Black and gray: metastable and unstable equilibrium configurations given by Eq. (2.8), green: presumed advancing trajectory, red: presumed receding trajectory; (b) The corresponding contact angles; (c) Free energy as a function of the actual contact angle for V = 0.2 (indicated with a dashed line in (a) and (b) Four minima are indicated with numbers; (d) Sketch of the four metastable configurations with V = 0.2, rescaled in the direction orthogonal to the substrate to distinguish clearly the four menisci.

corresponding to equilibrium configurations [black and gray curve in Fig. 2.2 (a)] has a limit (critical) point. At these values of the volume, say V_c, a saddle-node bifurcation takes place, where the local minimum of the free energy F (black) collides with a neighboring maximum (gray) and annihilate each other. At these points, the CL suddenly jumps to the closest available metastable state giving rise to slip motion.

The corresponding trajectory followed by θ (Fig. 2.2 (b]) displays the typical experimentally observed sawtooth shapes [111, 112] associated with the stick-slip mechanism [69, 95, 65]. As expected, the advancing contact angle (θ_A) is larger than the receding contact angle (θ_R).

To quantify the global differences between θ_R and θ_A we define the following

quantities:

$$\langle \cos\theta_R \rangle = \frac{1}{\Delta V} \int \cos\theta_R \, dV, \tag{2.10}$$

$$\langle \cos\theta_A \rangle = \frac{1}{\Delta V} \int \cos\theta_A \, dV, \tag{2.11}$$

$$H = \frac{H^*}{\gamma^*} = \langle \cos\theta_R \rangle - \langle \cos\theta_A \rangle, \tag{2.12}$$

where $\cos\theta_R$ and $\cos\theta_A$ correspond to the solutions tracked upon respectively decreasing and increasing V, and where the choice of ΔV depends on the situation considered. For example, in the case of a periodic heterogeneity, it corresponds to an integer amount of wavelengths. In addition, we will use the Cassie-Baxter contact angle θ_{CB}, which is given by the average value of $\cos\theta_i(x)$ over the whole microchannel with length L_x (or over a period of the heterogeneity $\theta_i(x)$ in the periodic case).

$$\cos\theta_{CB} = \frac{1}{L_x} \int \cos\theta_i \, dx \tag{2.13}$$

2.2.3 Graphical force balance

The phenomenon of CAH can also be interpreted by looking at the interplay between the two forces acting on the horizontal direction of the contact line, namely the spring-type elastic response of the contact line and the force due to the chemical heterogeneities [72].

However, it is important to note that the contact line in our 2D system is straight in the spanwise direction and so the spring-like behaviour is due to deformations of the meniscus in the cross-stream direction, as shown below, and not to corrugations of the contact line in the spanwise direction as as in [72].

We will see here that the occurrence of hysteresis generically is connected to the multiplicity of solutions (x, θ) for the balance between these forces at a fixed value of V.

The presence of the solid implies a force f_s^* (per unit length of the contact line), in the positive x-direction:

$$f_s^* = 2\left(\gamma_{sg}^* - \gamma_{sl}^*\right) = 2\gamma^* \cos\theta_i = \gamma^* f_s. \tag{2.14}$$

At equilibrium, this force is balanced by the *restoring force* f_r^* due to the deformation of the meniscus

$$f_r^* = -2\gamma^* \cos\theta = \gamma^* f_r. \tag{2.15}$$

Clearly, equilibrium implies $f_s^* + f_r^* = 0$, i.e. $\cos\theta = \cos\theta_i(x)$ as obtained in Eq. 2.7. Let us now define the deformation of the meniscus by

$$\Delta x = x_V - x, \tag{2.16}$$

where x_V is the mean position of the meniscus, defined as the position of a straight liquid/gas interface with the same liquid volume.

Hence, Δx is geometrically related to θ by:

$$\Delta x = f(\theta), \tag{2.17}$$

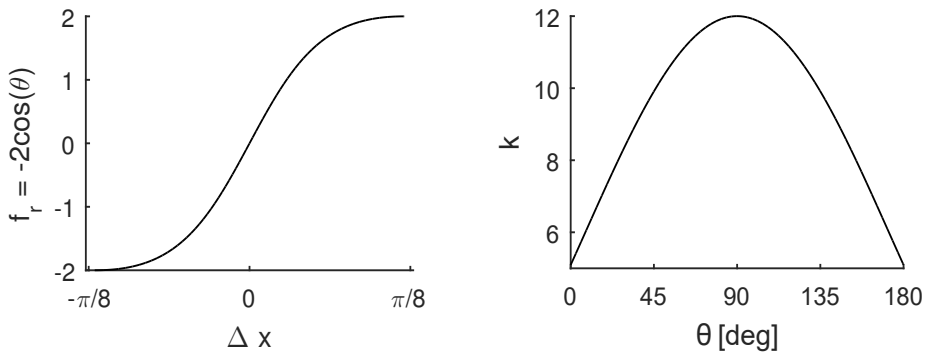

(a) (b)

Figure 2.3: Spring approximation of the meniscus. (a) The restoring force in dimensionless form as a response to a dimensionless deformation of the contact line, where θ is a plotting parameter varied from 0 to π; (b) Meniscus stiffness as a function of the actual angle.

where $f(\theta)$ is given by Eq. (2.3). The restoring force $f_r = -2\cos\theta$ is an increasing function of the deformation Δx, and can be written as:

$$f_r = k(\theta)\Delta x. \tag{2.18}$$

Therefore, we can interpret the meniscus as a spring with stiffness k that depends only on θ (see Fig. 2.3), and is given by

$$k(\theta) = \frac{-2\cos\theta}{f(\theta)} = \frac{16\cos^3\theta}{\pi - 2\theta - \sin(2\theta)}. \tag{2.19}$$

Combining Eq. (2.14) and (2.18), the force balance then reads

$$k(\theta)(x - x_V) = 2\cos\theta_i(x). \tag{2.20}$$

Fig. 2.4 illustrates this force balance for the case of a single Gaussian-shaped defect:

$$\cos\theta_i(x) = \cos\theta_0 + A_0 \exp\left(-\frac{(x - x_d)^2}{2\sigma^2}\right). \tag{2.21}$$

The complete qualitative agreement of Fig. 2.4 with the graphical construction proposed by Joanny and de Gennes [72], despite the different nature of the spring constant, not only shows the robustness of this view, but also that the occurrence of hysteresis is generically associated with the existence of multiple static configurations upon varying an experimentally controllable parameter such as the liquid volume.

We note, however, that in general, the curves representing f_r are not just straight lines as the stiffness depends on the actual contact angle ($\theta = \theta_i(x)$ in Eq. 2.20). By assuming a weak heterogeneity (i.e. $\cos\theta_i(x) = \cos\theta_0 + \Delta\cos\theta_i(x)$ with $|\Delta\cos\theta_i(x)| \ll 1$), the force balance may be linearized by noting that

$$x - x_V = -f(\theta_i(x)) \simeq -f(\theta_0) + f'(\theta_0)\Delta\cos\theta_i(x)/\sin(\theta_0), \tag{2.22}$$

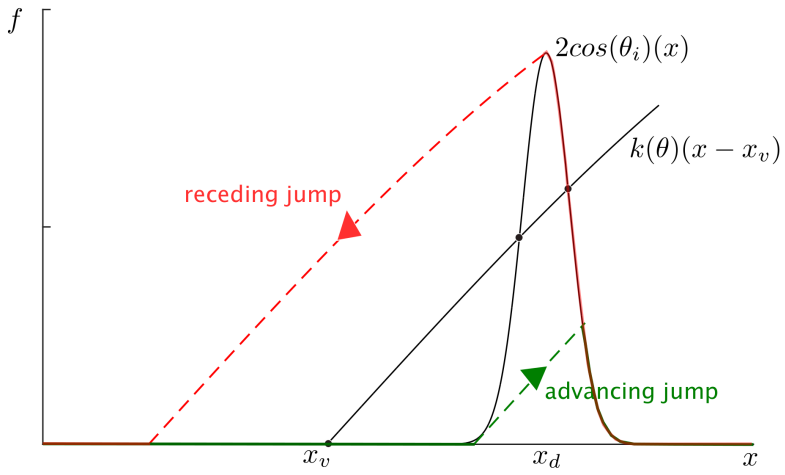

Figure 2.4: Example of graphical force balance with $\theta_0 = \frac{\pi}{2}$, $A_0 = 0.9$ and $\sigma = 0.01$. For a range values of x_V in the vicinity of the defect, up to three solutions are obtained for x (indicated with black dots). In this range, a different path of solutions is followed by the advancing CL (green) and receding CL (red). Both directions require a jump which is indicated with a striped line.

which is recast as

$$\frac{\sin(\theta_0)}{f'(\theta_0)}(x - \tilde{x}_V) = \Delta \cos\theta_i(x), \tag{2.23}$$

with

$$\tilde{x}_V = x_V - f(\theta_0). \tag{2.24}$$

Depending on the particular situation being considered, such a linearized force balance may be sufficient to describe the hysteresis behaviour.

2.3 Results

2.3.1 Hysteresis threshold and phase-plane plots

As is evident from Fig. 2.2, to have a multiplicity of equilibrium configurations for a given volume, there must be at least one critical contact line position x_c, where a saddle-node bifurcation takes place.

At one of these points, the meniscus jumps either forward in an advancing path or backwards in a receding path, as the volume varies. We note that alternatively, we can see these critical points as maxima and minima, respectively, of $V(x)$. Making use of Eq. (2.3) we can hence write:

$$V'(x_c) = 1 + \left.\frac{\partial f(\theta_i)}{\partial \theta_i}\frac{\partial \theta_i}{\partial x}\right|_{x=x_c} = 0, \tag{2.25}$$

where $V'(x_c) = \left.\frac{dV}{dx}\right|_{x=x_c}$. Denoting $\hat{\theta}_{ic} \equiv \theta_i'(x = x_c)$ and rearranging the above equation, we get

$$\hat{\theta}_{ic} = -\frac{1}{\frac{\partial f(\theta_i)}{\partial \theta_i}} = \frac{2\cos^2\theta_i}{(\frac{\pi}{2} - \theta_i)\tan\theta_i - 1}. \tag{2.26}$$

Therefore, at critical points, the *wettability gradient* $\hat{\theta}_{ic}$ exhibits a *generic* behaviour that does not depend on the particular form of $\theta_i(x)$ but only on the given value of θ_i. The points where the curve of $\theta_i'(x)$ versus $\theta_i(x)$ crosses the generic curve $\hat{\theta}_{ic}(\theta_i)$ correspond to the critical values of x at which jumps occur (either forward or backward). Thus, for a given distribution $\theta_i(x)$, visualizing both curves in a *phase-plane plot* will enable predicting whether and where the CL will jump.

As θ_i is physically limited between 0 and π, we have that $\hat{\theta}_{ic}(\theta_i)$ is limited between -2 (for $\theta = 0$ and π) and -6 (for $\theta = \frac{\pi}{2}$). Importantly, the negative sign of $\hat{\theta}_{ic}$ implies that an advancing (receding) meniscus can only start jumping from a position at which the wettability is increasing with increasing x (decreasing with decreasing x).

Another point to remark is that hysteresis occurs only if the strength of a (smooth) heterogeneity is above a finite *threshold* (a similar observation was reported in [72], albeit in a different physical system). If the condition $\theta_i'(\theta_i) = \hat{\theta}_{ic}(\theta_i)$ is not satisfied for any x, then no stick-slip occurs and the same path of static solutions is followed during advancing and receding. These behaviours are illustrated in the following.

2.3.1.1 Smooth heterogeneities

We consider two examples for $\theta_i(x)$, namely a single Gaussian-shaped defect with amplitude A_0, width σ, and located at x_d:

$$\theta_i(x) = \theta_0 + A_0 \exp\left(-\frac{(x - x_d)^2}{2\sigma^2}\right), \tag{2.27}$$

and a periodic heterogeneity with amplitude A_0 and wavelength λ:

$$\theta_i(x) = \theta_0 + A_0 \sin\left(\frac{2\pi x}{\lambda}\right). \tag{2.28}$$

As just remarked, if condition (2.26) cannot be satisfied, a multiplicity of static solutions and hysteresis cannot occur. This is the case when $\theta_i'(x)$ is not negative

enough, which is certainly true if $\min(\theta_i'(x)) > -2$. For the Gaussian defect (2.27) this condition leads to the relation $\frac{|A_0|}{\sigma} < 2\sqrt{e}$, and for the sinusoidal heterogeneity to $\frac{|A_0|}{\lambda} < 1/\pi$.

On the other hand, condition (2.26) is certainly satisfied if $\min(\theta_i'(x)) < -6$, which leads to the conditions $\frac{|A_0|}{\sigma} > 6\sqrt{e}$ for the Gaussian defect, and $\frac{|A_0|}{\lambda} > 3/\pi$ for the sinusoidal heterogeneity (2.28). For values of $\frac{|A_0|}{\sigma} \in (2\sqrt{e}, 6\sqrt{e})$ (or $\frac{|A_0|}{\lambda} \in (1/\pi, 3/\pi)$) hysteresis may or may not occur, depending on the background contact angle θ_0. In that respect that condition 2.26 is more difficult to satisfy for a CA of $\frac{\pi}{2}$, because this is the angle around which $\hat{\theta}_{ic}$ is most negative.

We hence conclude that the quantity $\frac{|A_0|}{\sigma}$ (or $\frac{|A_0|}{\lambda}$) determines whether hysteresis occurs or not, i.e. it is the gradient of wettability that matters. In particular, for a given defect amplitude A_0, hysteresis will always be observed at sufficiently small defect size (compared to the microchannel gap).

Fig. 2.5 depicts a comparison between two cases that are below and above the threshold for a single Gaussian defect [see panel (a)]. As is evident from the phase plot [Fig. 2.5 (b)], the system starts at the origin, and moves clockwise along a closed trajectory for an advancing CL (increasing x), or anticlockwise for a receding CL (decreasing x).

If the defect is weak (dashed line), the phase plot does not intersect the generic line $\hat{\theta}_{ic}(\theta_i)$. On the other hand, for the stronger defect (full line), there are two intersections on the phase plot, which correspond to the minimum (left) and maximum (right) of $V(x)$ (cf. 2.5(c)). These are the points at which the receding and advancing jump start, respectively. The ending points of the jumps are found with the assumption of the constant volume, corresponding to a case where the externally imposed volume variation is of negligible rate compared to the velocity of the jumps.

For values of the volume in between the values corresponding to the jumps, multiple equilibrium states exist and the system will choose one depending on whether the volume has been increasing or decreasing [Fig. 2.5 (c). More specifically, the advancing CL follows the branch corresponding to lower x, while the receding CL follows the branch corresponding to higher x. The middle branch is unstable as it corresponds to maxima of the free energy (as in Fig. 2.2).

The contact angles corresponding to the two branches are shown in Figure 2.5 (d), revealing that when increasing V (green), the CL first sticks on the hydrophobic defect, causing θ to increase progressively, and then slips, corresponding to a sudden decrease of θ. When decreasing V (red), the CL almost directly slips over the hydrophobic defect, corresponding to a sudden increase of θ, and then sticks, causing θ to decrease progressively. Both for the hydrophobic case considered here, and for a hydrophilic defect, jumps correspond to a decrease of θ when increasing V, and to an increase of θ when decreasing V.

For the periodic heterogeneity given by Equation (2.28), we observe a similar behaviour in terms of the threshold-dependence of hysteresis. We will consider this case in more detail in Section 2.3.2.

2.3.1.2 Sharp heterogeneities

We now consider sharp-edged defects, or *mesa defects* adopting the term coined by Joanny and de Gennes [72]. In the limit case of *symmetric* mesa defects – i.e. defects involving both a steplike increase and decrease in wettability, as shown in Fig. 2.6 – $\theta_i'(x)$ will reach both plus and minus infinity, crossing the generic curve $\hat{\theta}_{ic}$ in between.

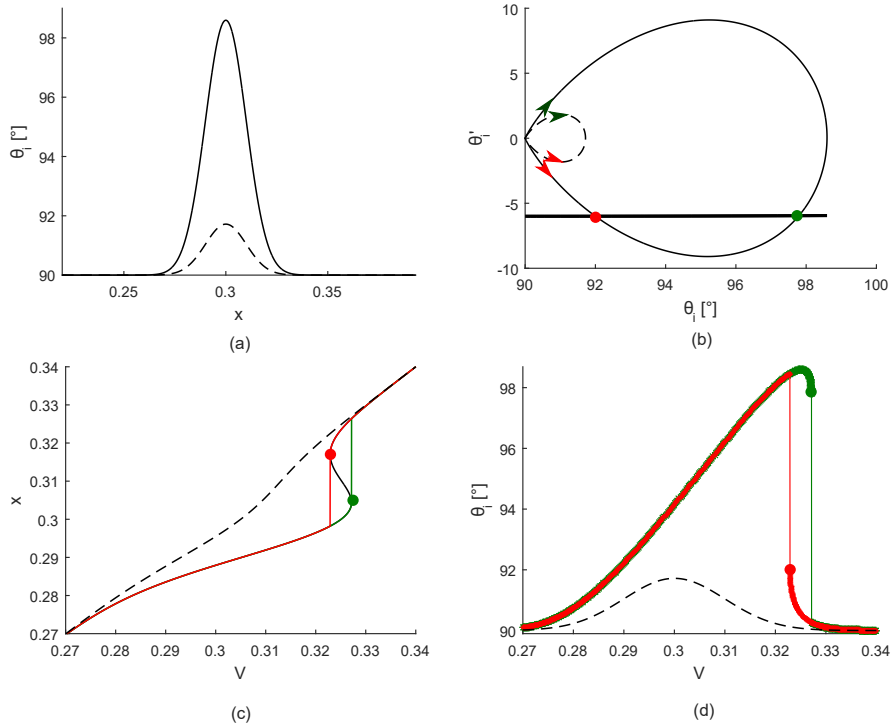

Figure 2.5: Comparison of behavior above ($A_0 = 0.15$, full lines) and below ($A_0 = 0.03$, dashed lines) threshold for a single defect [Eq. (2.27)] with $\sigma = 0.01$ and $\theta_0 = \frac{\pi}{2}$). (a) Intrinsic contact angle distributions. (b) Phase plots of both distributions, the thick line represents $\hat{\theta}_{ic}$ (it is a curve which appears straight with the relevant axes.) The green (red) arrow and dot represent respectively the sense of circulation and the start of the jump for an advancing (receding) CL; (c) CL position followed in advancing (green) and receding (red) trajectory above the threshold, and below the threshold (dashed); (d) Contact angle corresponding to these trajectories.

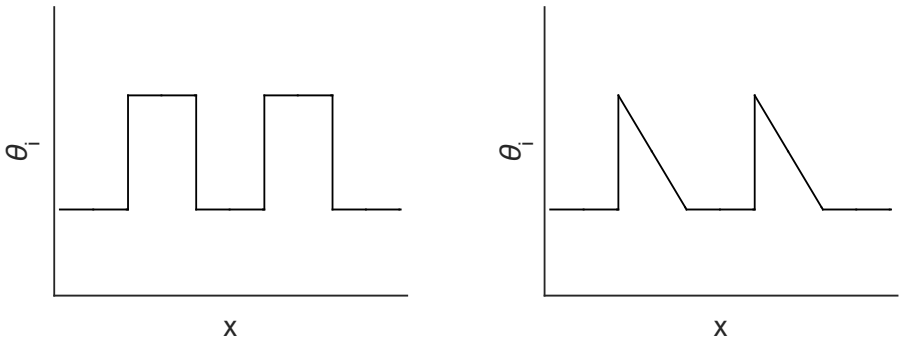

Figure 2.6: Examples of sharp edged heterogeneities. (a) Symmetric, involving the same steps of increasing and decreasing wettability; (b) Non-symmetric, having a different slope for increasing and decreasing wettability.

Hence such defects, featuring infinitely large wettability gradients, always generate hysteresis, as was predicted by Joanny and de Gennes [72].

Asymmetric heterogeneities, however, of which the intrinsic CA decreases too slowly with increasing x ($\min(\theta_i'(x)) > -2$), do not generate hysteresis, even if the increases of CA are step-like. We illustrate this with the example of a triangular heterogeneity with amplitude A_0 and wavelength λ given by:

$$\theta_i(x) = \theta_0 + \frac{2A_0}{\pi} \arctan\left(\cot\left(\frac{\pi x}{\lambda}\right)\right) \tag{2.29}$$

and shown in Fig. 2.7(a). Any negative value of A_0 implies step-like decreases of the intrinsic CA with increasing x, which give rise to hysteresis. For a positive value of A_0 however, no hysteresis will occur if $(\min(\theta_i'(x)) > -2) \equiv -\frac{2A_0}{\lambda} > -2$, or $0 < A_0 < \lambda$. Figure 2.7 is an example of such a case. On the contrary, the same heterogeneity with an inversed sign of A_0 does generate hysteresis (Fig. 2.8). For this heterogeneity, inverting the sign of A_0 is equivalent to inverting the sign of the coordinate x. Therefore the situation in Fig. 2.8 can be obtained in exactly the same microchannel as in Fig. 2.7, by simply placing the liquid inlet at the right-hand side. Hence, for a microchannel with this particular type of heterogeneity, whether or not the system will suffer hysteresis and stick-slip, will depend on the side from which the liquid enters.

This analysis shows that the existence and nature of the threshold does not only depend on the wetting properties of the substrate $\theta_i(x)$, but also on the particular liquid configuration. However, recall that all lengths, and hence the typical length scale of the heterogeneity,) are normalised with the gap width separating the two plates of the microchannel.

As a result the weak Gaussian-shaped defect corresponding to the dashed lines in Fig. 2.5 would be a strong defect in a microchannel with a gap size that is five times larger. This points to the importance of the overall length scales, something that deserves more attention and was not considered in the work by Joanny and de Gennes [72], nor was it discussed in the more recent review by Bonn *et al.* [2].

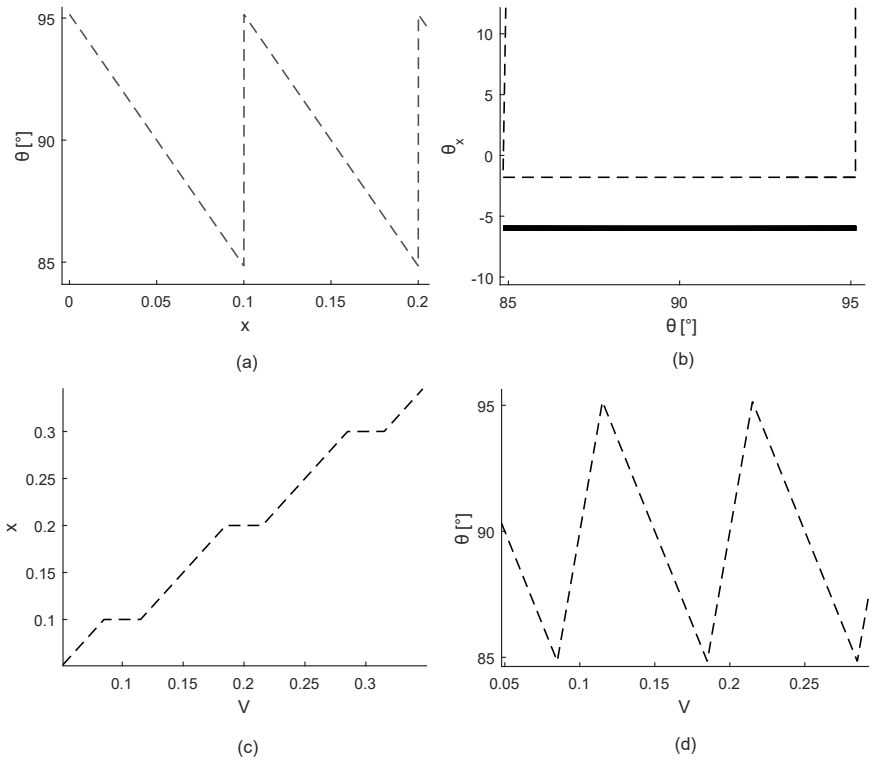

Figure 2.7: Sub-threshold triangular heterogeneity (Eq. 2.29 with $A_0 = 0.09$, $\theta_0 = \pi/2$ and $\lambda = 0.1$). (a) Intrinsic contact angle distribution. (b) Phase-plane plot, the thick line represents $\hat{\theta}_{ic}$; (c) CL position as a function of volume (same for advancing and receding); (d) Contact angle corresponding to this trajectory.

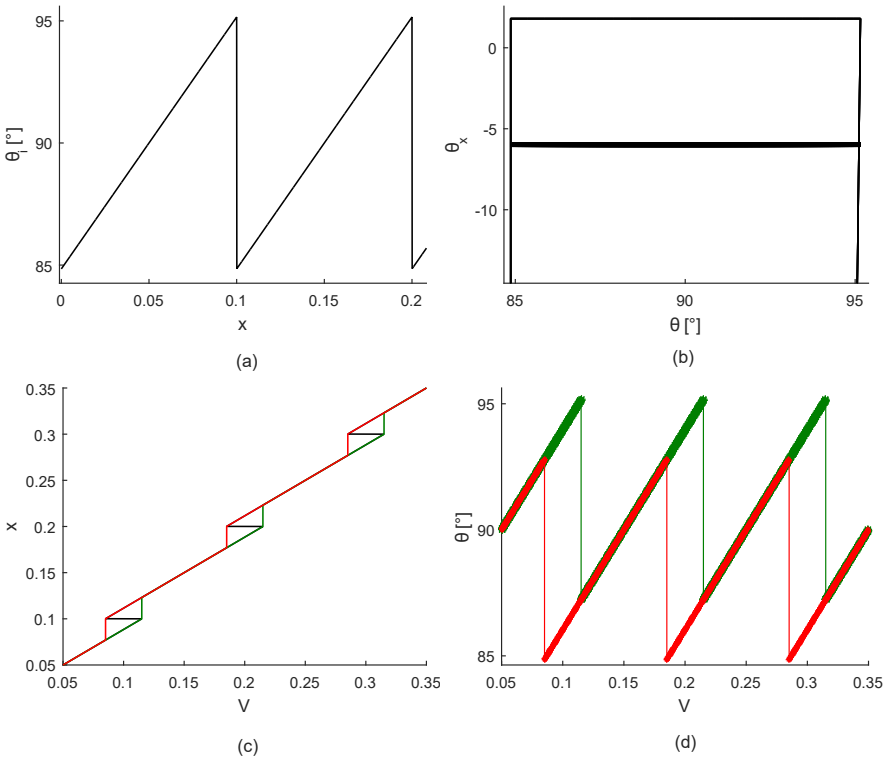

Figure 2.8: Triangular heterogeneity which generates hysteresis (Eq. 2.29 with $A_0 = -0.09$ and $\lambda = 0.1$). (a) Intrinsic contact angle distribution; (b) Phase-plane plot, the thick line represents $\hat{\theta}_{ic}$; (c) CL position as a function of volume for (black: all static solutions, green: followed during advancing, red: followed during receding); (d) Contact angle corresponding to these paths.

2.3.2 From large to small heterogeneity length scale: the macroscopic limit.

Here we discuss qualitatively the effects on hysteresis of the ratio λ between the characteristic lengthscale of the heterogeneity and the gap size of the microchannel (which is constraining the liquid-vapor interface in this configuration), by looking at a periodic distribution of the spreading coefficient of the walls as a model prototype.

$$\cos\theta_i(x) = A_0 \sin\left(\frac{2\pi}{\lambda}x\right) \tag{2.30}$$

This heterogeneity is different to that given by Eq. 2.28, because we had imposed for simplicity a distribution for $\theta_i(x)$, as opposed to the spreading coefficient which is proportional to $\cos\theta_i(x)$ and which gave simple analytical result for the value of the threshold, whereas here we want to obtain a scaling law for the hysteresis force. The results for this case are presented in Fig. 2.9.

For a given value of A_0 and when λ is sufficiently high (see first column of Fig. 2.9) the system is in a sub-threshold regime (i.e. the gradient $|A_0|/\lambda$ is too small). Although the contact angle varies with volume, hysteresis is absent. In particular, we observe that for each volume we find a unique static configuration (x, θ), the phase-plane plot of the heterogeneity does not intersect the generic curve $\hat{\theta}_{ic}$, and the advancing and receding CL follow the same path, in clockwise and anticlockwise directions, respectively. The CA takes all possible values imposed in the distribution 2.30 in both the advancing and receding directions. Hence in this regime, advancing CAs lower than the Cassie-Baxter angle (here equal to 90 deg) are possible, and receding CAs higher than the Cassie-Baxter one, are possible.

If we decrease λ by a factor three (second column of Fig. 2.9) by, e.g., increasing the gap width by the same factor, the system is then in a regime in which hysteresis occurs. We find that for most volumes there exists a unique static configuration (x, θ), but in certain ranges three static solutions are found. At these points, the branch followed by the system will depend on whether the CL advances or recedes. The contact angle of an advancing CL is on average higher. At the intersections between the phase plot of the heterogeneity and the generic curve $\hat{\theta}_{ic}$, the contact line jumps (slips) to a point which has the same volume if we assume that such jumps occur instantaneously compared to the rate of volume variation. In the phase-plane plot, an advancing CL follows a different path than a receding CL.

A further decrease in λ (third column of Fig. 2.9) increases the number of static solutions (x, θ) for a given volume. The path followed by an advancing CL is now totally different than the one followed by a receding CL. When λ decreases, gradually, jumps get smaller and occur more frequently. The contact angles follow sawtooth shapes which get further separated. The advancing CAs are at all times higher than the Cassie-Baxter angle, while the receding CAs are lower. The bows followed in the phase diagram are separated further.

In the limit $\lambda \to 0$, which we refer to hereafter as the *macroscopic limit*, the number of static solutions (x, θ) at any given volume starts becoming arbitrarily high. This situation is represented for $\lambda = 0.001$ in the fourth column of Fig. 2.9. The CL advances with a nearly constant contact angle, corresponding in this case to the maximum of the imposed distribution, and recedes with a nearly constant contact angle (which is the minimum of the imposed distribution). The sawtooth amplitude of the contact angle is below 0.3 deg and hysteresis is maximum.

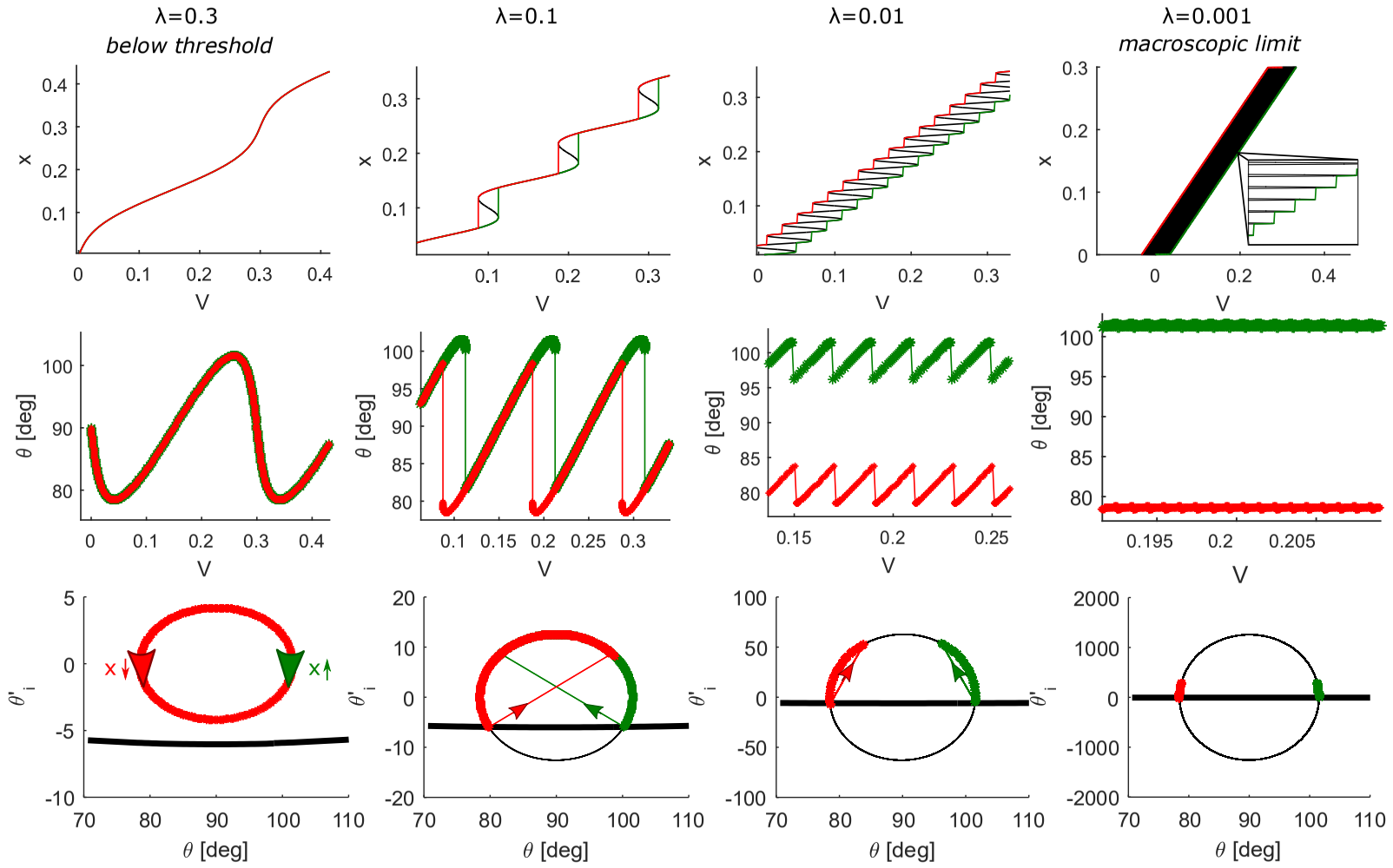

Figure 2.9: Qualitatively different regimes of hysteresis for the microchannel (assuming the system has no ability to overcome any energy barriers) caused by a model periodic heterogeneity given in Eq. (2.30) with $A_0 = 0.2$. The columns represent different values of λ, from left to right: 0.3, 0.1, 0.02 and 0.001. On the upper row: Black: equilibrium configurations, green: presumed advancing path, red: presumed receding path; on the middle row: the contact angle of the equilibrium configurations encountered in the advancing (green) and receding (red) path. Lower row: phase plots of the distribution in black, the thick line represents $\hat{\theta}_{ic}$, for an advancing contact line (green), the system moves in a clockwise fashion, while for a receding contact line (red), the motion is counterclockwise, as indicated with the large arrows. The small arrows (with the same color code) indicate jumps.

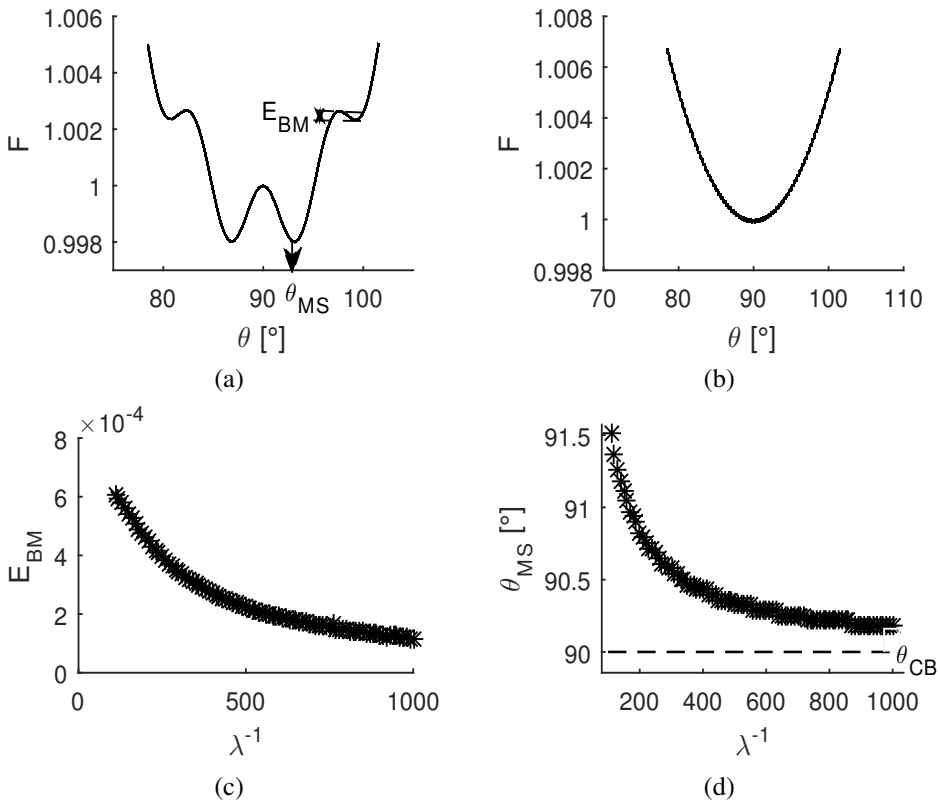

Figure 2.10: Change of rugged energy landscape upon varying λ in Eq. 2.30 with $A_0 = 0.2$ with a fixed volume $V = 0.2$. (a) and (b): Energy landscape $F = \frac{F^*}{\gamma^* b^*}$ as a function of actual contact angle for resp. $\lambda = 0.02$ and $\lambda = 0.001$. The most stable contact angle θ_{MS} and the maximal energy barrier E_{BM} to reach it are indicated with arrows on (a). As the energy landscape is symmetric about 90 deg, these quantities are measured from the right side; (c) The maximum energy barrier to reach the most stable contact angle versus λ^{-1}. (d): Most stable contact angle versus λ^{-1}. The dotted line represents the Cassie-Baxter angle.

In the above analysis, we have assumed that the system has no ability to overcome energy barriers, which are also affected by varying λ. A lower value of this parameter increases the amount of extrema in the energy landscape for a fixed volume (Fig. 2.10, (a) and (b)). We define the maximum energy barrier E_{BM} which needs to be overcome in order to attain the most stable contact angle θ_{MS}, as indicated on Fig. 2.10(b).

E_{BM} is found to decrease with λ^{-1} and reaches a value of the order 10^{-4} for $\lambda = 0.001$ (Fig. 2.10(c)). The most stable angle [Figure 2.10 (d)], approaches the Cassie-Baxter angle (90 deg). This result was previously reported in Refs [113, 55] for a configuration of a drop much larger than the heterogeneity wavelength.

2.3.3 Scaling laws of the hysteresis force

2.3.3.1 Near threshold behavior

Let A_{0c} be the threshold value for the amplitude of the chemical defect. For $A_0 = A_{0c}$, at a certain contact line position, say x_0, we have that the volume satisfies:

$$V'(x_0) = V''(x_0) = 0. \tag{2.31}$$

Consider the deviations from this point for the quantities:

$$\begin{cases} A_0 = A_{0c} + \mu, \\ x = x_0 + \tilde{x}. \end{cases} \tag{2.32}$$

By using (2.31), we expand the volume for $\mu \ll 1$ and $\tilde{x} \ll 1$ as

$$V = x + f(\theta_i(x, A_0)) \approx V_0 + c_1\mu + c_2\mu\tilde{x} + c_3\tilde{x}^3. \tag{2.33}$$

The extrema of V are then given by

$$\frac{dV}{dx} = 0 = c_2\mu + 3c_3\tilde{x}^2, \tag{2.34}$$

the solutions of which, assuming $c_2c_3 < 0$, are

$$\tilde{x}_\pm = \pm\left(-\frac{c_2\mu}{3c_3}\right)^{1/2} \propto \mu^{1/2}. \tag{2.35}$$

Inserting the above values into Eq. 2.33, we obtain:

$$V_{\max} - V_{\min} \propto \mu^{3/2}, \tag{2.36}$$

where $V_{\max} = V(x_+, A_0)$ is the relative maximum of the volume at which the CL jumps in an advancing path, and $V_{\min} = V(x_-, A_0)$ is the relative minimum of the volume, at which the CL jumps in a receding path. The magnitude of the jumps of the force scales as

$$\begin{aligned} \delta f \;\propto\; \cos(\theta_i(x_-, A_0)) \;&-\; \cos(\theta_i(x_+, A_0)) \\ \propto\; \theta_i(x_+, A_0) \;&-\; \theta_i(x_-, A_0) \\ \propto\; x_+ - x_- \;\propto\; \mu^{1/2}. & \end{aligned} \tag{2.37}$$

According to definitions (2.10)-(2.12), the hysteresis H is directly related to the area between the curves of $\cos(\theta_R)$ and $\cos(\theta_A)$ versus V. Combining (2.36) and (2.37) we thus find that close enough to the threshold, the hysteresis amplitude scales as

$$H \propto \mu^2 \propto (\delta f)^4. \tag{2.38}$$

In the following, we explore numerically the emergence of scaling laws. We first focus on the case of hysteresis caused by an array of wetting defects, where we focus on the dilute limit at which we have a minimum number of equilibrium configurations for a given volume.

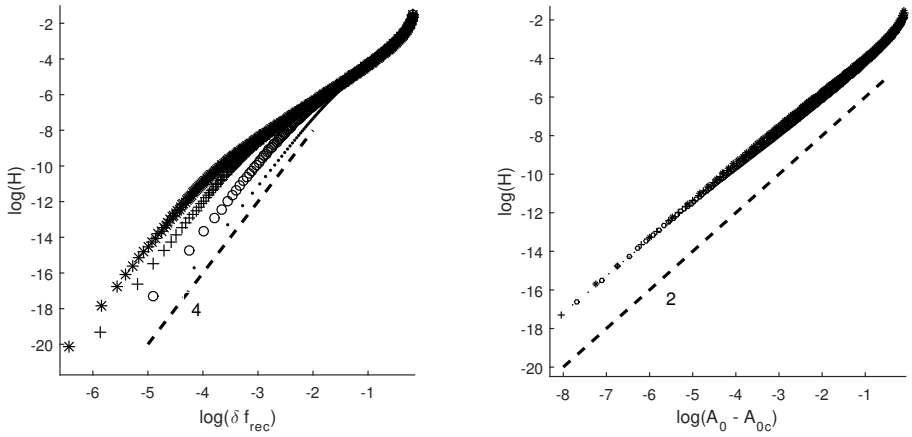

(a) (b)

Figure 2.11: For a single, wetting defect, logarithmic plots of the dimensionless hysteresis force $H =< cos\theta_R - cos\theta_A >$ for $\theta_0 = \pi/2$ for four values of σ : 0.01 $(*)$, 0.005 $(+)$, 0.002 (o), and 0.001 $(.)$, as a function of (a) the defect amplitude, and (b) the fluctuation δf_{rec} of $\cos\theta_R$ during the jump. The dashed lines with slopes two and four are drawn to guide the eye.

2.3.3.2 Dilute system of wetting defects

Consider a single Gaussian-shaped defect:

$$\cos\theta_i(x) = \cos\theta_0 + A_0 \exp\left(-\frac{(x-\frac{L_x}{2})^2}{2\sigma^2}\right), \tag{2.39}$$

where we fix $\theta_0 = \frac{\pi}{2}$. We assume $A_0 > 0$, i.e. a defect which is more wettable than the rest of the surface, and vary the amplitude A_0 over 400 values, logarithmically spaced in the interval between 0.001 and 0.99, for four values of the defect width σ. The computational domain L_x is fixed to a dimensionless length of unity and discretized in sections of $\Delta x = 10^{-5}$. With this length the whole pinning-depinning process is captured for all calculated defects. For each value of σ, a threshold amplitude A_{0c} is calculated numerically as the minimum A_0 for which the phase plot of the heterogeneity intersects the generic line (Section 2.3.1).

Fig. 2.11(a) shows that hysteresis depends only slightly on the width of the defect. The effect of defect amplitude A_0 on the hysteresis is twofold. A larger A_0 does not only imply a larger difference between the CA on the defect and the background angle, but also larger jumps (see the graphical force balance in Fig. 2.4), hence a larger range of V during which the CA differs from the background angle. Near the threshold (see Eq. 2.38) but also far from it, the hysteresis is found to scale as:

$$H \propto (A_0 - A_{0c})^2, \tag{2.40}$$

where A_{0c} is the threshold amplitude depending on σ, which is 0.04945 and 0.00495 for the broadest and sharpest defect, respectively. As the maximum excess force $F^*_{s,max}$ exerted on the contact line by the defect is proportional to $\gamma^* A_0$, we may write

for the dimensional hysteresis force H^*

$$H^* = \gamma^* H \propto \frac{F_{s,max}^{*2}}{\gamma^*}, \tag{2.41}$$

where A_{0c} has been assumed negligibly small against A_0, e.g. in the macroscopic limit $\sigma \to 0$. This scaling law is in agreement with previous theoretical and numerical predictions [72, 108] and experiments [106], though in different configurations to the one studied here.

It is important to emphasise that in fact, the hysteresis caused by the wetting defect is mainly due to the increase of $\langle \cos\theta_R \rangle$ when A_0 increases, while $\langle \cos\theta_A \rangle$ stays nearly constant (see also the graphical force balance in Fig. 2.4). This is consistent with experimental findings [102, 114, 112] on surfaces with controlled chemical defects and can be understood by the fact that a wetting defect primarily affects [90] or more specifically pins [112] the CL in the receding direction. Fig. 2.11 (b) shows that close enough to the threshold, the hysteresis amplitude scales with the fluctuation of the force caused by a jump to the power four, also in agreement with Section 2.3.3.1. Further from threshold, no clear scaling behaviour can be observed.

We note that as we quantify averaged hysteresis, the absolute value of H depends on the domain size. An increasing system size indeed enhances the dilution of the effects of the defect by the homogeneous background. This can be avoided by considering an array of such defects. We thus impose an array of N equally spaced and identical wetting defects.

$$\cos\theta_i(x) = \cos\theta_0 + A_0 \sum_{i=1}^{N} \exp\left(-\frac{(x - x_{di})^2}{2\sigma^2}\right), \tag{2.42}$$

where $x_{di} = i\frac{L_x}{N+1}$. Fig. 2.12 shows that for low enough N, the hysteresis force is directly proportional to N, which is in agreement with experiments [107] and the proposed scaling law for the hysteresis caused by a dilute system of defects [72, 1, 2]

$$H^* = \gamma^* \left(\cos\theta_R - \cos\theta_A\right) \propto \frac{n(F_{max}^*)^2}{\gamma^*}. \tag{2.43}$$

The effects of the individual defects are simply additive as long as they are independent (non-overlapping). As the density of defects N is increased however, this proportionality no longer holds as the stick-slip of the CL on a defect is affected by the neighboring defects. More specifically, the jumps of the CL do not end anymore on homogeneous parts between defects, but on other defects. This *shadowing* effect increases with N, decreasing the slope on the plot. For N above 150, the defects start overlapping and hysteresis even starts decreasing as the substrate becomes less heterogeneous, though with a shifted background value.

2.3.3.3 Periodic heterogeneity

In our last example, we consider a periodic heterogeneity of the form:

$$\cos(\theta_i(x)) = A_0 \sin\left(\frac{2\pi}{\lambda}x\right). \tag{2.44}$$

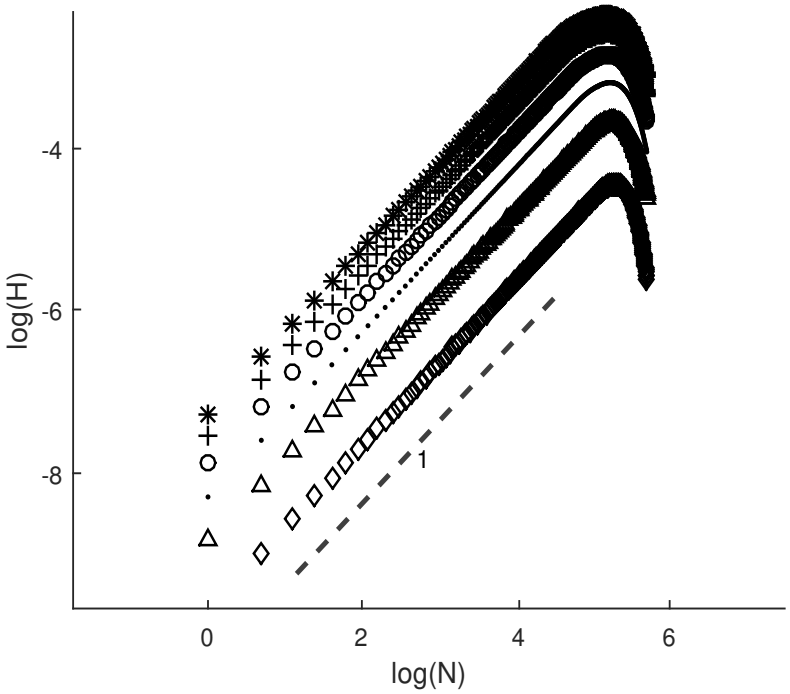

Figure 2.12: Logarithmic plot of the dimensionless hysteresis force $H =< cos\theta_R > - < cos\theta_A >$ for an array of equally spaced, identical wetting defects with width $\sigma = 0.01$ as a function of the amount of defects for six values of A_0 : 0.075 ($\diamond$), 0.1 ($\triangle$), 0.125 (.), 0.15 (o), 0.175 ($+$) and 0.2 ($*$).

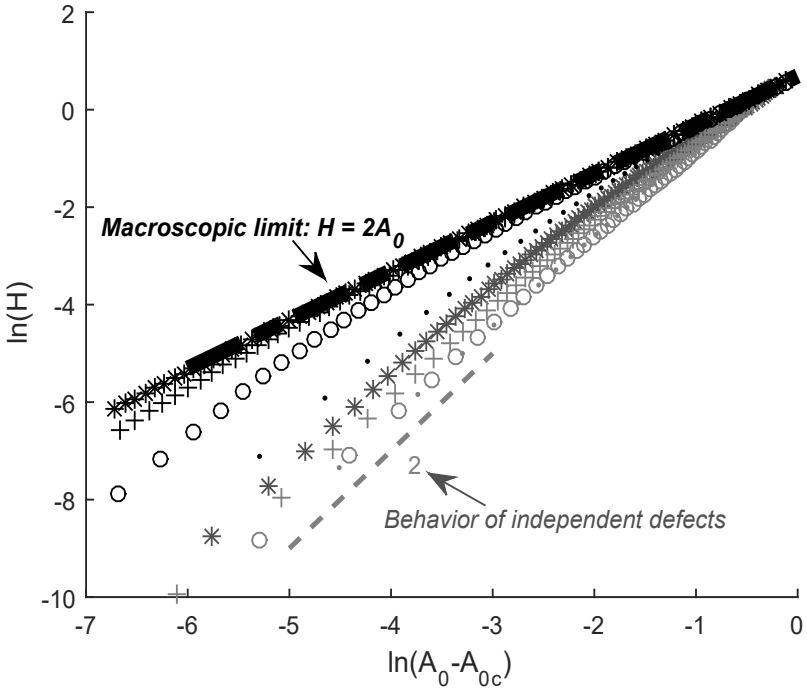

Figure 2.13: Logarithmic plot of the dimensionless hysteresis force $H =< cos\theta_R > - < cos\theta_A >$ as a function of the heterogeneity amplitude for a periodic heterogeneity with $\theta_0 = \pi/2$ and 8 values of λ. Black symbols correspond to small wavelengths: $\lambda = 1.\ 10^{-4}$ $(*)$, $8\ .\ 10^{-4}$ $(+)$, $5.80.\ 10^{-3}$ (o), $4.44.\ 10^{-2}$ and $(.)$. Gray symbols correspond to large wavelengths: $\lambda = 0.1$ $(*)$, 0.178 $(+)$, 0.316 (o) and 0.562 $(.)$. The black dashed line (collapsing with data) corresponds to the macroscopic limit. The gray dashed line with slope two is drawn as visual aid.

The computational domain has a length of 20λ. We vary A_0 over 100 logarithmically spaced values between the threshold value and 0.89, and λ over 8 logarithmically spaced values, between 10^{-4}, which is indistinguishably close to the macroscopic limit, and 0.578. The ranges of V over which the contact angles are integrated (in Eq. 2.10 and 2.11) start and end with a value at the CL jumps.

The threshold amplitude A_{0c} is 0.302 for the highest λ and 9.56×10^{-5} for the lowest, satisfying A_{0c}/λ constant. We find that the scaling exponent depends on the wavelength λ as follows. For the lowest values of λ the hysteresis force is proportional to the defect force. For broader heterogeneities, the scaling exponent increases with λ and reaches a value of around two when λ is of the order of one (see Fig. 2.13). We then write:

$$H^* \propto F^*_{s,max}, \tag{2.45}$$

for $\lambda \to 0$. The linear behavior corresponds exactly to the macroscopic limit ($\lambda = \frac{\lambda^*}{b^*} \to 0$), in which the advancing and receding angle are nearly constant and equal to the minimum and maximum of the imposed distribution ($H \to 2A_0$), respectively. Also, for this infinitely sharp heterogeneity, the threshold amplitude vanishes ($A_{0c} \to$

0). This limit is plotted in black dashed lines and collapses with the data for sufficiently low λ, and at sufficiently high $A_0 - A_{0c}$ (although A_0 has an upper bound $A_0 = 1$, see Equation 2.44. This suggests that the value of λ below which this limit is reached depends on A_0.

Away from this limit, i.e. for higher λ), the system is in a regime of observable stick-slip (see Section 2.3.2) where the difference between the advancing and receding angle depends on V. The exponent larger than one found for this regime is due to the same effect as in the case of a single defect (section 2.3.3.2): an increase of the amplitude of the heterogeneity A_0 increases both the difference between the advancing and receding angle at the value of V at which the jumps occur, and the range of V during which these angles differ.

2.4 Conclusions and perspectives

We have analyzed in detail stick-slip motion and CAH of a liquid-gas meniscus in a chemically heterogeneous microchannel of fixed gap width by tracking stable and metastable states upon varying the liquid volume and for a wide range of heterogeneity distributions. To the best of our knowledge, this is the first time that such a study has been undertaken. Our goal has also been to examine to what extent previous results of wetting hysteresis hold in the present configuration.

We showed that the stick-slip mechanism can be studied using phase-plane plots of the heterogeneity. Weak heterogeneities do not produce hysteresis, a threshold for the heterogeneity strength is required. For values of the heterogeneity strength sufficiently above the threshold, we find good agreement with the previously reported expressions for the hysteresis amplitude for a diluted system of defects, even though the geometry and approach used here are notably different.

For a model sinusoidal heterogeneity, we have found that the ratio between the heterogeneity wavelength and the liquid-gas interface length is a key parameter determining the qualitative aspects of the hysteresis. More specifically, decreasing gradually this ratio brings the system from a sub-threshold regime (i.e. no hysteresis), to a stick-slip dominated regime, and ultimately to a regime with a nearly constant advancing and receding angles. In the latter regime, which we referred to as the macroscopic limit, the hysteresis amplitude is shown to be proportional to the defect force.

Finally there are a number of interesting questions closely related to the analysis presented here. For example, extension of the static approach to investigate a microchannel configuration with non-identical upper and lower walls (as in chapter 5), but also account for the influence of thermal noise, especially in the macroscopic limit, where the energy barriers which keep the system in metastable states are relatively low [104]. Moreover, noise can induce dynamic/state transitions in rugged energy landscapes and further hysteresis effects (noise-induced hysteresis) [115, 116].

Of particular interest will also be the corresponding dynamic study, addressing the question of how the hysteresis is amplified by the absolute velocity of the CL in each of the qualitatively differently different regimes of hysteresis. Such study is presented in chapter 4. Extension of the present analysis to more realistic three-dimensional configurations, though possible in principle, would require considering an infinite-dimensional generalization of the approach, which is not expected to be treatable other than numerically.

Chapter 3

Contact line stick-slip motion on micrometer-size wavy fibres

In chapter 2, by studying the statics of contact line motion in a two-dimensional chemically heterogeneous microchannel, we have gained insights on generic aspects of stick-slip and contact angle hysteresis. Considering such highly idealized setup facilitated the performed analysis, but came at the price of hindering a direct quantitative comparison with experiments.

Fortunately, the opportunity arose to collaborate with Dr. Carlos A. Fuentes (KU Leuven) and co-workers, who performed tensiometric and goniometric experiments to study on the dynamic wetting behaviour of axisymmetric sinus-shaped fibres (wavy fibres) immersed perpendicularly in a liquid bath. This setup is in terms of modeling very analogous to the one studied in chapter 2 and therefore provided the chance to directly test quantitative predictions of stick-slip motion and of associated scaling laws.

Immersion and retraction of the fiber resulted in the observation of a stick-slip motion of the meniscus depending on both the fibre surface curvature and its intrinsic wettability. The model predicts that the behaviour of the seemingly pinned and then jumping contact line, with associated changes in apparent contact angles, can be explained by the interplay between a constant local contact angle and the movement of the bulk liquid, leading to the storage of energy which is suddenly released when the contact line passes a given point of fibre curvature.

3.1 Introduction

The architecture of complex-shaped fibres affects the motion of the contact line and the evolution of its associated menisci when a fibre is immersed into a liquid. Understanding and predicting the motion of the contact line is critical in the design of complex-shaped fibres for many engineering applications as well as for surface science. While wetting on classic circular cylinders has been well studied, singularities during the wetting process of complex-shaped fibres are not yet well understood.

Wetting forces and analysis of meniscus shape formed around fibres immersed perpendicularly into a liquid have been traditionally used to study the wettability of single fibres, which is essential in several technological applications, such as fibre reinforced composite design [117, 118, 119] and coating of textile fibres [120].

The measurement of the capillary force exerted by a liquid on a fibre, from which a contact angle can be calculated, is known as the Wilhelmy method (tensiometry) [121]. This pull or push force is produced by the weight of displaced liquid above or below the reference horizontal free surface [122]. An advancing meniscus is formed when the fibre is immersed into a liquid, while a receding meniscus is observed when the fibre is withdrawn from the liquid. In general, both situations correspond to different apparent contact angles and not to a single value, as theoretically predicted by Youngs equation for an ideal surface.

This so-called hysteresis is related to the pinning of the contact line at physical or/and chemical heterogeneities [123, 124]. Moreover, the value of the experimentally measured contact angle is also influenced by the velocity of the advancing and receding fronts [119, 125, 87].

Almost all the models previously described for measuring the wettability of fibres have been developed for the characterization of the menisci on perfect circular cylinders, while fibres with more complex shapes have received less attention [126, 127]. Irregular natural fibres [128] and the recent development of complex-shaped fibres for industrial applications, such as hollow glass [129] and expanded/ablated fibres [130] for improving composite interfaces, call for new studies focusing on the particular features (e.g. diameter change along the fibre length) encountered during the motion of the contact line on fibres with non-circular and variable cross sections [126, 131, 132]. An analysis of the meniscus shape on such complex-shaped fibres needs the development of new experimental techniques and the validation or improvement of traditional theoretical models.

In this chapter, the dynamic wetting behaviour of an axisymmetric sinus-shaped fibre (wavy fibre) immersed vertically in a large liquid volume has been investigated. Fibres were computer-designed and 3D printed down to micrometre dimensions with Nanoscribe Photonics GT equipment, and the Wilhelmy method was used in parallel with meniscus shape analysis; these two independent techniques were being cross-validated by direct comparison of resulting contact angles. This methodology enabled monitoring the profile of the fibre and the liquid meniscus while the fibre was being immersed, and to correlate the contact angle variations with the motion of the contact line.

The immersion and withdrawal of the fibre resulted in stick-slip motion of the meniscus [127, 110, 133, 48, 134], which is predicted by a quasi-static model directly inspired by an analysis of the impact of chemical heterogeneities on stick-slip behaviour and hysteresis in a microchannel (cf. chapter 2). Here, static model solutions are tracked upon varying the immersion depth in upward and downward direc-

tions, explaining why two different paths for the contact line position are observed, with pinning-depinning events occurring in both cases.

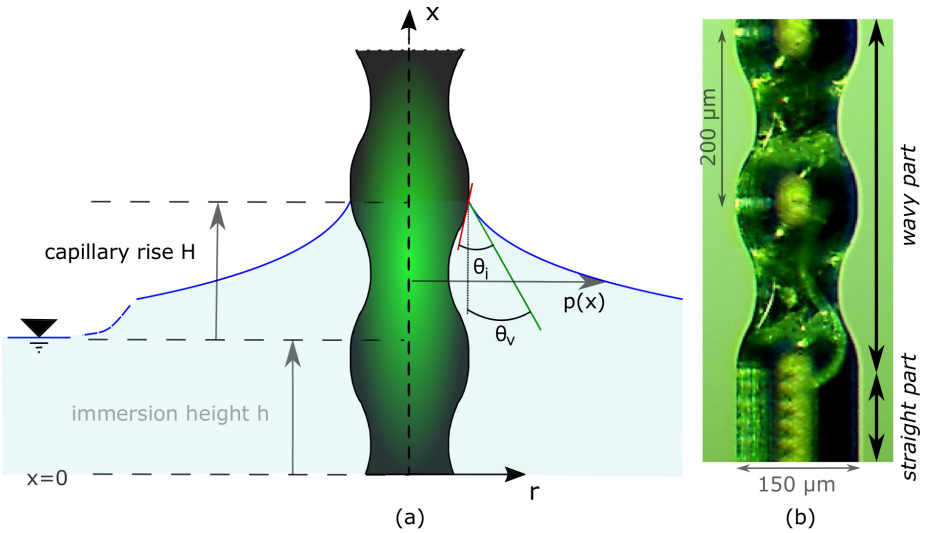

Figure 3.1: (a): Equilibrium configuration of an axisymmetric wavy fibre, immersed vertically into a liquid. x is the axial coordinate attached to the fibre. The level of the liquid bath is at $x = h$. The contact line is at $x = h + H$ (with H the capillary rise) where the meniscus makes an angle θ_i with the fibre and θ_V with the vertical. (b): Optical microscopy of a 150/100 (outer diameter/inner diameter dimensions in microns) fibre.

3.2 Theoretical framework

Consider an axisymmetric fibre (Fig. 3.1). Its topology (waviness) is specified by a distribution of radii $r(x)$ and its wettability by a distribution of intrinsic contact angles, defined [110] as

$$\cos\theta_i\,(x) = \frac{\gamma_{sg}(x) - \gamma_{sl}(x)}{\gamma}, \tag{3.1}$$

with γ the liquid-air surface tension [N/m] and $\gamma_{sg}(x) - \gamma_{sl}(x)$ the difference between the solid-air and solid-liquid surface tensions. In most parts of this study (more specifically before section 3.3.3, where we specify another form) we assume in our model that the fibre is chemically homogeneous, with a wettability characterized by the receding angle, experimentally measured on the straight parts of the fibre.

Immersing the fibre vertically in a liquid bath leads to capillary rise ($H > 0$) or depression ($H < 0$) of the meniscus on it. For a radius much smaller than the capillary length l_c $\left(= \sqrt{\frac{\gamma}{\rho g}}\right)$ of the system, the equilibium height H of the capillary rise/depression can be calculated by adapting the formula existing for a straight fibre [135] to the case of an heterogeneous fibre considered here. For each given contact line position. At equilibrium, at each contact line position x_{CL}, one readily obtains

$$H(x_{CL}) \approx r(x_{CL})\cos\theta_V(x_{CL}\left(\ln\frac{4l_c}{r(x_{CL})\,(1+\sin\theta_V(x_{CL}))} - C\right), \tag{3.2}$$

where C is the Euler constant (0.57721 ...), $r(x_{CL}$ is the local radius, and $\theta_V(x_{CL})$ is the (equilibrium) contact angle measured with respect to the vertical axis, i.e.

$$\theta_V(x_{CL}) = \theta_i(x_{CL}) - \arctan r'(x_{CL}). \tag{3.3}$$

In the studied range of r and θ_V, Eq. 3.2 is found to approach the solution of the Young-Laplace ordinary differential equation (Eq. 3.8 below), with an error below 0.15

$$h(x_{CL}) = x_{CL} - H(x_{CL}). \tag{3.4}$$

3.2.1 Occurrence of stick-slip and hysteresis

Importantly, h is actually the experimentally controlled parameter and takes the same role that V took in the analysis of hysteresis in a microchannel (chapter 2). h is a single-valued function of x_{CL} and simply given by Eq. 3.4. Yet, the opposite is not true as the functions $r(x_{CL})$ and/or $\theta_i(x_{CL})$ can cause $h(x_{CL})$ to be increasing non-monotonously, thereby making $x_{CL}(h)$ multi-valued. In such cases, the contact line can be at one of several equilibrium positions x_{CL} at a given value of h.

Forcing h to increase or decrease then results in x_{CL} following it in the same direction, but with sudden jumps which over a length which is of the order of the wavelength of the fibre. The jumps are well-captured in the movie clips in the supplementary material of [136]. They occur both for in the advancing (immersing) and receding (retracting) directions, but at slightly different locations for the two cases.

These sudden jumps in the contact line position can be explained by the statics of capillary rise on a sinusoidal fibre starting from a liquid reservoir level h, the experimentally controlled parameter, which is increased or decreased when immersing or withdrawing the fibre respectively. Fig. 3.2 shows a schematic representation of the receding process (the explanation of the advancing process is analogous).

If we start an experiment with the uppermost drawn configuration of the liquid/air interface, decreasing the liquid bath level h results in the contact line descending on the fibre. This situation continues until the configuration of the liquid/air interface corresponds to $h = h^*$ and $x_{Cl} = x_1$ (drawn in black in Fig. 3.2 a). From this configuration on, displacing the contact line downwards would require increasing h. The configurations of the liquid/air interface, with $x_{CL} < x_1$ but $h > h^*$, are drawn in dashed lines in Fig. 3.2 a. Although they start at a lower position on the fibre, their apparent angles θ_V are high enough (due to the local waviness of the fibre) such that these interfaces already become flat at an immersion height $h > h^*$, which is violating the experimental constraint that h must decrease. The contact line then jumps from a position x_1 to x_2 at a constant immersion depth $h = h^*$.

This model explains the observed jumps and hysteresis upon experimentally varying the liquid bath level h in a qualitatively similar way as the explanation of the jumps and hysteresis for a moving liquid wedge over a chemical defect upon varying the contact line position far from the defect [72], a drop on a chemically heterogeneous substrate upon varying its volume [110], and a liquid in a chemically heterogeneous microchannel upon varying its volume (chapter 2).

3.2.2 Capillary force and free energy

We calculate for each possible contact line position the force that would be measured by a tensiometer as

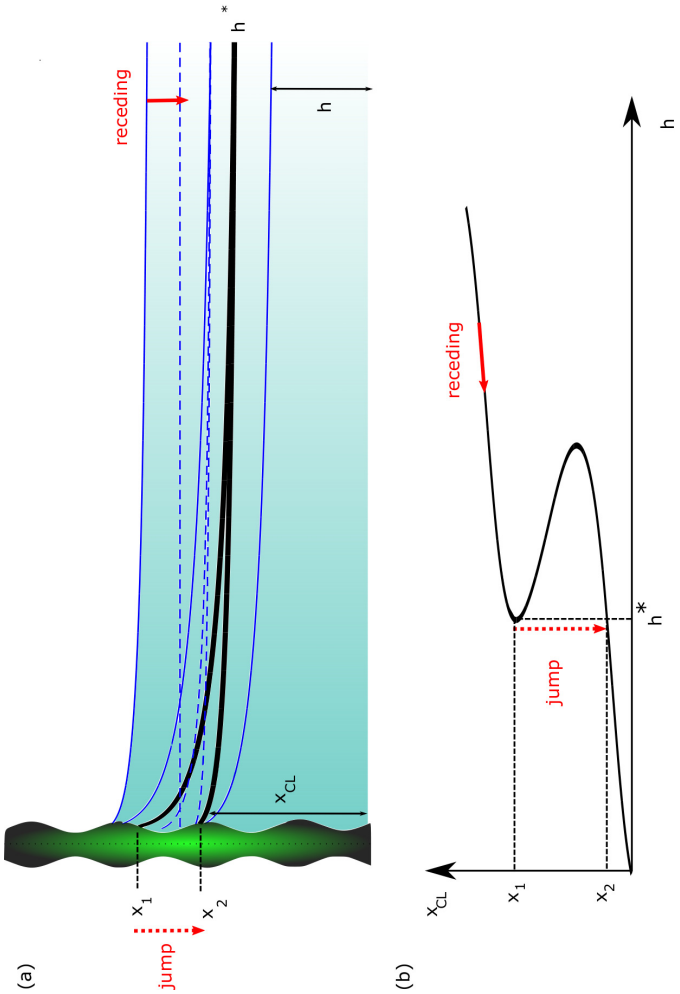

Figure 3.2: Explanation of the jump observed when a sinus-shaped fibre is withdrawn. (a): For different contact line positions, static menisci with the same contact angle θ_i measured locally on the fibre are drawn (equal to the receding angle measured on the straight part of the fibre). When the meniscus is receding (decreasing h), at the immersion height $h = h^*$, a jump of the contact line position occurs from x_1 to x_2, skipping the menisci drawn in dashed lines as they correspond to $h > h^*$. (b): Corresponding graph of the contact line position x_{CL} versus the experimentally controlled immersion height h. Following the graph from right to left requires the contact line to jump.

$$F(x_{CL}) = 2\pi\gamma r(x_{CL})\cos\theta_V(x_{CL}) - \pi\rho g\int_0^{x_{CL}} r^2(x)dx, \tag{3.5}$$

The free energy G of the system is given by the integration of the interfacial tensions along the surfaces on which they act, as well as the gravitational potential energy of the meniscus.

$$G = \gamma A_{lg} + \int \gamma_{sa} dA_{sa} + \int \gamma_{sl} dA_{sl} + \rho g \int x dV_{meniscus}. \tag{3.6}$$

The liquid-gas interface area A_{lg} is calculated is calculated as a revolution integral.

$$2\pi\gamma \int_{r(x_{CL})}^{+\infty} \left(p\sqrt{1+\left(\frac{dp}{dx}\right)^{-2}} \right) dp \tag{3.7}$$

where $p(x)$ is the profile of the meniscus as a function of the axial coordinate as defined in Fig. 3.1). This profile is obtained by solving the Young-Laplace equation (Eq. 3.8 below).

$$x'' = (1+x'^2)\left(l_c^{-2} x\sqrt{1+x'^2} - \frac{x'}{p} \right), \tag{3.8}$$

Here, which primes denote derivation with respect to p and all lengths are scaled with the radius $r(x_{CL})$.

This ordinary differential equation is closed by imposing an angle (relative to the vertical) at the fibre,

$$x'(p=1) = -\cot\theta_V, \tag{3.9}$$

and a flat interface far away from the fibre

$$x'(p\to\infty) = 0. \tag{3.10}$$

Convergence is achieved after taking a domain size of $50 l_c$ and imposing Eq. (3.10) at the domain edge.

The second and third term of Eq. 3.6 can be rewritten by introducing the intrinsic contact angle θ_i by Young's law.

$$\begin{aligned}
\int \gamma_{sa} dA_{sa} + \int \gamma_{sl} dA_{sl} = 2\pi\gamma \int_0^{x_{CL}} \left(r(x)\gamma_{sl}(x)\sqrt{1+\left(\frac{dr}{dx}\right)^2} \right) dx + \\
2\pi\gamma \int_{x_{CL}}^{L_{fibre}} \left(r(x)\gamma_{sg}(x)\sqrt{1+\left(\frac{dr}{dx}\right)^2} \right) dx \\
= -2\pi\gamma \int_0^{x_{CL}} \left(r(x)\cos\theta_i(x)\sqrt{1+\left(\frac{dr}{dx}\right)^2} \right) dx \\
+2\pi\gamma \int_0^{L_{fibre}} \left(r(x)\gamma_{sg}(x)\sqrt{1+\left(\frac{dr}{dx}\right)^2} \right) dx
\end{aligned} \tag{3.11}$$

The last term of Eq. 3.11 is simply constant in the considered problem.

Finally, the volume of the meniscus in the gravitational potential energy term of Eq. 3.6 is caluclated as

$$\int dV_{meniscus} \int_h^{x_{CL}} (p^2 - r^2(x))dx. \tag{3.12}$$

Substituting Eqs. 3.7, 3.11 and 3.12 into Eq. 3.6, the free energy ΔG up to a constant can be calculated as

$$\begin{aligned} \Delta G = 2\pi\gamma \int_{r(x_{CL})}^{+\infty} \left(p\sqrt{1+\left(\frac{dp}{dx}\right)^{-2}} \right) dp \\ -2\pi\gamma \int_0^{x_{CL}} \left(r(x)\cos\theta_i(x)\sqrt{1+\left(\frac{dr}{dx}\right)^{2}} \right) dx \\ +\rho g\pi \int_h^{x_{CL}} (x-h)(p^2 - r^2(x))dx. \end{aligned} \tag{3.13}$$

For a given fibre, which is characterized by $r(x)$, $\theta_i(x)$ and l_c, Eq. 3.13 depends on x_{CL} and θ_V (which enters as a boundary condition of the meniscus profile, i.e. Eq. 3.9). The first term makes the system favour configurations in for which the liquid-air interface is minimal (i.e. $\theta_V \rightarrow 90$ deg). The second term only depends on x_{Cl} and describes the energy cost/gain by wetting the fibre area, depending on whether the fibre is wettable (sign of $\cos\theta_i$). The third describes the energy cost/gain due to elevating/depressing liquid above/below the reservoir level, depending on the sign of $\cos\theta_V$.

In the following, we will consider two cases where one of the two degrees of freedom (which are x_{CL} and θ_V) is eliminated.

- Assuming capillary equilibrium (the equality between the contact angle with respect to the fibre and the intrinsic contact angle at that contact line position), we will look at the interplay between the different terms of the free energy during the stick-slip process described in section 3.2.1.
- Under the constraint of an imposed immersion depth h, we will look if the configuration(s) at capillary equilibrium indeed correspond(s) to extrema of the free energy, as was analytically proven in simpler, i.e. a drop on a chemically heterogeneous substrate [110] and a liquid in a microchannel with chemically heterogeneous walls (chapter 2).

3.3 Results

3.3.1 Energy dissipation during the jump

The effect of the jump on the free energy of the system is evaluated by the analysis of the force trace during wetting of the fibre (Eq. 3.5), as can be seen in Fig. 3.3a. The calculated force trace shows that the work gained by dipping the fibre over one wavelength (area under the green curve) is smaller than the work required to withdraw the fibre over one wavelength (area under the red curve). More specifically, an advancing-receding cycle over one wavelength dissipates 1.76 nJ of energy.

Fig. 3.3b shows a clearer picture on how this 1.76 nJ is dissipated in an advancing-receding cycle over one wavelength, using Eq. 3.13. Starting from $h = 100\mu$m, one random position in the single-valued range of h where the free energy value corresponds to 9.30 nJ, dipping the fibre (increasing h) results in a global reduction of the free energy of the system as the fibre is wettable. When $h = 300\mu$m is reached (i.e. after 200 μm, one wavelength), after the in-between advancing jump at $h = 243\mu$m, the free energy of the system is 5.38 nJ. Then, the free energy of the system was reduced by 3.9 nJ, of which 1.09 nJ is dissipated during the advancing jump. To go back to $h = 100\mu$m, the system requires 4.59 nJ, of which 0.67 nJ will be dissipated during the receding jump at $h = 138\mu$m.

As can be seen from Fig. 3.2a, in the receding process, before the jump, the liquid-air interface area continuously increases while θ_V decreases. Thus, in this range of h values, the system stores the work that is provided to decrease h in its liquid-air interface and as gravitational potential energy. Immediately after the jump, the contact line is at $x_{CL} = x_2$ with a lower liquid-air interface area and gravitational potential energy. This means that during the jump, at $h = h^*$, part of the stored energy is used to dewet the fibre from x_1 to x_2, while 0.67 nJ still needs to be dissipated as the system cannot keep storing it at the equilibrium state that the system attains immediately after the jump.

Fig. 3.3b also shows that although multiple equilibrium configurations exist in a range of h values, still one of them has a lower free energy than the others. In this range, the free energy as a function of x_{CL} (drawn for an arbitrary height $h = 150\mu$m in Fig. 3.3c) shows that both the advancing and receding solutions (presented as dots) are local minima of the free energy, with a local maximum in between which acts as an energy barrier to trap the system in a metastable configuration. This result, proven analytically in the configuration of a drop on a chemically heterogeneous substrate [110] and a liquid in a microchannel with chemically heterogeneous walls (c.f. chapter 2), is recovered here numerically for this configuration.

For the situation drawn in Fig. 3.3c, the system is trapped in the receding configuration (red dot). This local minimum is separated from the advancing configuration (green dot) by a local maximum. In order to move from one metastable to the other, the system would have to overcome the barrier of 0.04 nJ, and then the advancing jump will take place and dissipate 0.54 nJ, reaching the minimum energy configuration indicated with the green dot. This energy barrier can for example be overcome by vibrational noise [57, 137]. But in absence of this situation, the system will proceed to recede along the red track in Fig. 3.3b, until the receding jump takes place at $h = 138\mu$m.

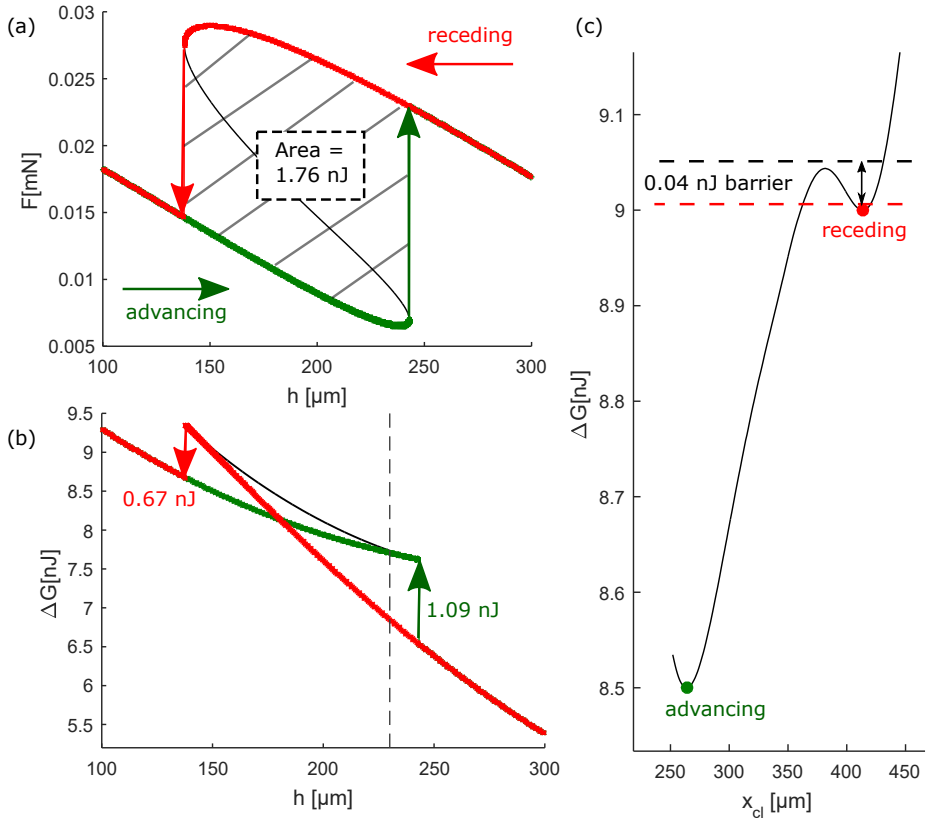

Figure 3.3: Energy dissipated in the jumps; (a): Force exerted on the fibre (Eq. 3.5) versus immersion depth . Black: all static solutions, Green: subset of stable static solutions, tracked upon increasing h (advancing), Red: stable solutions tracked upon decreasing h (receding). (b): With the same colour code, free energy of equilibrium configurations (contact angle θ_i is equal to its equilibrium value, which is a constant) as a function of h, the vertical dotted line corresponds to an arbitrary constant immersion height of 150μm. (c) free energy as a function of x_{CL} at h equal to 150 μm, where the contact angle is now a free parameter. The red and green dot correspond to the equilibrium configurations encountered in the receding and advancing path respectively.

3.3.2 Scaling relation between jump length and dissipated energy

As demonstrated in section 3.2.1, the jumps of the contact line are induced by the topography of the fibre. Here, we characterize these jumps by the energy they dissipate (c.f. section 3.3.1) and the vertical length over which they occur. Both these quantities obviously vanish when there are no jumps (e.g. a perfectly cylindrical fibre) and increase as the fibre becomes more *wavy*. In this section we will explore the scaling relation between these two quantities numerically, analytically and experimentally.

In order to vary these two quantities, a parameter needs to be varied in their cause, i.e. the topography of the fibre. A sinus-shaped fibre (c.f. Fig. 3.1) is characterized by three length scales. We fix the wavelength at 200 microns, the maximal diameter of 150 microns and vary the minimal diameter D_{min}.

3.3.2.1 Near threshold behavior

A perfectly cylindrical fibre (i.e. minimal diameter D_{min} also 150 microns in the form described above), does not induce jumps (stick-slip). A slightly wavy fibre (e.g. $D_{min} = 145$ micron does not induce jumps either. In fact, whether a topography induces hysteresis and jumps has a binary answer which is only positive for D_{min} below a certain threshold value. (c.f. [72] and section 2.3.1).

In section 2.3.3.1 of chapter 2, we have shown for the microchannel configuration that near the threshold, the hysteresis force scales with the square of the defect force. Here, we repeat the same argument to obtain an experimentally verifiable outcome, i.e. a scaling relation between the length over which a depinning jump occurs and the energy dissipated during the jump.

Let D^*_{min} be the threshold value for the lowest diameter of the fibre. For $D_{min} = D^*_{min}$, at a certain contact line position, say x_0, we have that the immersion depth satisfies:

$$h'(x_0) = h''(x_0) = 0. \tag{3.14}$$

Consider the deviations from this point for the quantities:

$$\begin{cases} D_{min} = D^*_{min} - \mu, \\ x_{CL} = x_0 + \tilde{x}. \end{cases} \tag{3.15}$$

By using (3.14), we expand the immersion depth for $\mu \ll 1$ and $\tilde{x} \ll 1$ as

$$h = x_{CL} - H(x_{CL}, D_{min}) \approx h_0 + c_1\mu + c_2\mu\tilde{x} + c_3\tilde{x}^3. \tag{3.16}$$

The extrema of h are then given by

$$\frac{dh}{dx} = 0 = c_2\mu + 3c_3\tilde{x}^2, \tag{3.17}$$

the solutions of which, assuming $c_2c_3 < 0$, are

$$\tilde{x}_\pm = \pm\left(-\frac{c_2\mu}{3c_3}\right)^{1/2} \propto \mu^{1/2}. \tag{3.18}$$

Inserting the above values into Eq. 3.16, we obtain:

$$h_{\max} - h_{\min} \propto \mu^{3/2}, \tag{3.19}$$

where $h_{\max}$ is the relative maximum of the immersion depth at which the contact line jumps in an advancing path, and $h_{\min}$ is the relative minimum of the immersion depth, at which the CL jumps in a receding path. The magnitude of the jumps of the force scales as

$$\delta f \propto \mu^{1/2}.$$

The dissipated energy H^* is given by the area between the curves of the receding and advancing forces versus h. Combining (3.19) and (3.20), we thus find that close enough to the threshold, the dissipated energy scales as

$$H^* \propto \mu^2 \propto (\tilde{x}_{\pm})^4. \tag{3.20}$$

3.3.2.2 Comparison with experiments

Experiments where performed in KU Leuven by Dr. Carlos A. Fuentes and his coworkers on four 3D-printed fibres with different minimal diamter D_{min}, i.e. 80, 100, 120 and 140 microns. The liquid is water and the dipping velocity is 0.5 mm/min (For more information on the experimental aspects, please see [136]).

The experimental displacement of the contact line after the jumps increases with the wave ratio (ratio of smallest to largest diameter of the fibre) as shown in Fig. 3.4a. The black dots correspond to 57.5 μm, 90.9 μm, 128.0 μm and 137.0 μm of displacement for the fibres with diameters of 140 μm, 120 μm, 100 μm, and 80 μm at the lowest amplitude respectively. The latter three fibres correlate well with the predictions of the model (full red line) which is based on tracking the static solutions while decreasing (receding). We first proceed with the analysis of the wetting behaviour of these three fibres and come back to the situation of $D_{min} = 140\mu$m fibre later.

For the fibres with D_{min} equal to 120, 100 and 80 μm, the energy dissipated in the jumps is calculated from the tensiometer force trace (e.g. the trace of 150/80 is given later in Fig. 3.5) as the area $\int (F_R - F_A)\, dh$ between the receding and advancing force. First the area is measured between the traces corresponding to the wavy portion of the fibres, and divided by the wavelength, in order to obtain the average dissipated energy over a wavelength. Secondly, the dissipation due to the (uncontrolled) contact angle hysteresis is measured from the horizontal portion of the force trace, corresponding to the perfectly cylindrical portion of the fibre (c.f. Fig. 3.1). The energy dissipated in one advancing and one receding jump can be then calculated by subtracting the dissipation due to the uncontrolled contact angle hysteresis (e.g. 3.03 nJ for 150/80 in Fig. 8). The experimental values of the dissipated energy increase with the wave ratio from 0.26 nJ to 1.00 nJ to 1.51 nJ for the three fibres of interest, from left to right in Fig. 3.4b (black dots).

The procedure described above relies on the assumption that the total dissipated energy is equal to the dissipation due to contact angle hysteresis (nanoscale wetting heterogeneity) plus the energy dissipated during the jump events. The reasonable match between the experimental values and the model prediction (red line in Fig. 3.4), where the latter is calculated in the absence of a small-scale heterogeneity, verifies that this assumption can be taken here as a good approximation.

Both the experimental and numerical data suggest that the dissipated energy scales with jump distance to the fourth power (Fig. 3.4c). This scaling is especially accurate for low values of the jump length and dissipation, i.e. closer to the threshold of hysteretic behaviour, and therefore in agreement with the derivation of section 3.3.2.1. It is

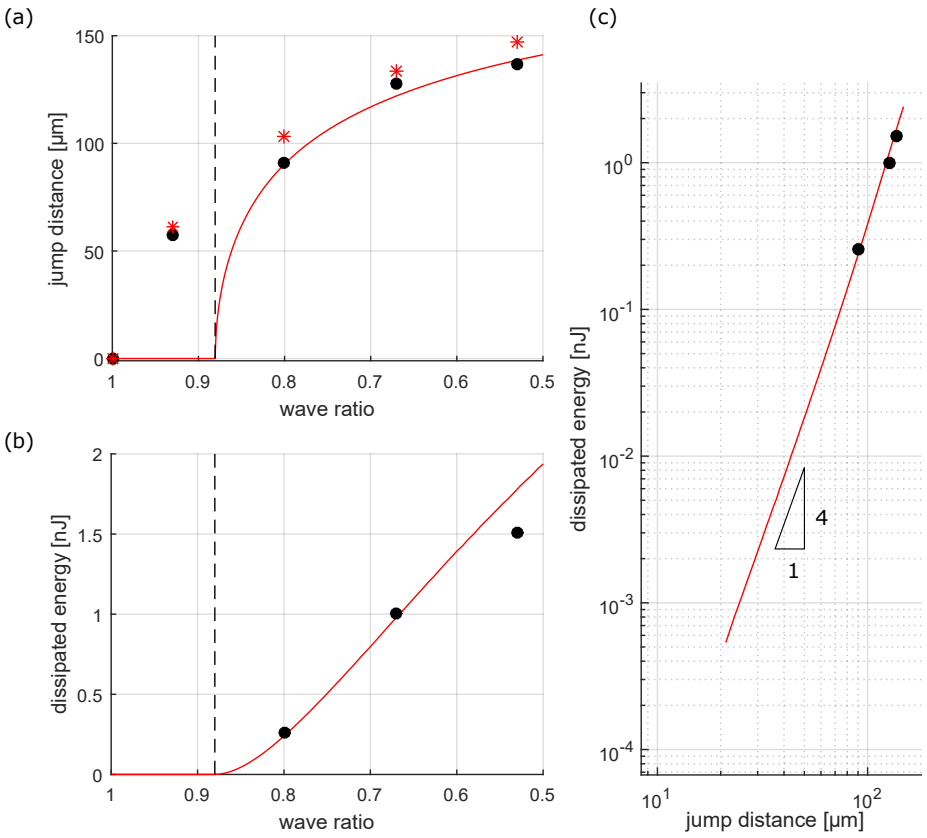

Figure 3.4: (a): Vertical receding jump distance as a function of the wave ratio (ratio between the lowest and largest radius) from experiment (black dots), model (red line) and corrected model data (red stars, assuming jumps when $\frac{\dot{x}}{\dot{h}} > 1.5$. Here $\dot{x}$ is the instantaneous contact line velocity and $\dot{h}$ is the constant and imposed velocity of the liquid bath. The vertical dashed line represents the location of the threshold wave ratio (0.88) (b): Energy dissipated over one wavelength as a function of wave ratio. (c): Energy dissipated as a function of jump length.

different than the quadratic scaling that Shanahan [133] has predicted when the length scale of the pinning sites is much smaller than the system size (in that case the drop radius). The latter condition is typically satisfied *far away* (c.f. section 2.3.2) from the threshold, while here the system is rather *close* to its threshold.

The threshold for a jump to take place is shown as a vertical dashed line in Fig. 3.4a and 3.4b, at a wave amplitude of 0.88, corresponding to $D_{min} = D^*_{min} = 132\mu$m. For $D_{min} > D^*_{min}$ only one equilibrium configuration exists at each fixed immersion depth h and $\frac{dx}{dx_{CL}} > 0$ for each x_{CL}. This is the case for fibres which are not wavy enough, as in the case of the fibre with $D_{min} = 140\mu$m. For this situation the model predicts that the meniscus can contact the whole fibre in a continuous way without the necessity of jumping.

The apparent inconsistency with the experimental observation of a jump (see Figs. 3.4a and 3.4b) is hypothetically caused by quasi-static acceleration/deceleration events[136]. More specifically, the slope of the static x_{CL} versus h curve (such as plotted in Fig. 3.1b for another fibre) is equal to one in average but not equal to one everywhere. Therefore, when a constant bath velocity $\frac{dh}{dt}$ is imposed experimentally, the contact line will still accelerate and decelerate and this can be confused with the slip jumps.

A possible way to distinguish between an acceleration/deceleration event and a real jump would be to *pause* the position of the bulk liquid h during a jump. If a jump over the same portion of the fibre is still observed, then the observed jump is a real depinning jump, while if the jump is paused as well, then it corresponds to a quasi-static acceleration/deceleration event. Another way is to perform experiments with different (still sufficiently low) immersion speeds. If the results for the different immersion speeds collapse in any plot with the immersion height h on the horizontal axis, then again, the observed acceleration/deceleration is not a real jump. The use of high speed cameras could also help to observe more accurately the position at which a jump is produced.

3.3.3 Advancing-receding cycle

In this section, a full advancing-receding cycle is modelled by the incorporation of a small-scale heterogeneity as the responsible for the observed contact angle hysteresis. In contrast with previous sections where the angle with respect to the fibre θ_i was constant, we now impose a distribution of intrinsic contact angles $\theta_i(x_{CL})$.

$$\cos\theta_i(x_{CL}) = \frac{\cos\theta_R + \cos\theta_A}{2} + \frac{\cos\theta_R - \cos\theta_A}{2}\sin\left(\frac{2\pi x_{CL}}{\lambda}\right) \qquad (3.21)$$

Here, $\theta_A = 77$ deg and $\theta_R = 45$ deg correspond to their experimentally measured values on the perfectly cylindrical parts of the fibre (c.f. Fig. 3.1a) and $\lambda = 0.5\mu$m. As in section 2.3.2, a periodic distribution with a wavelength λ much smaller than the length scale of the experiment (i.e. the fibre dimensions) induces a nearly continuous range of metastable apparent angles θ_V at fixed h, while at the same time implying a constant θ_V when h is varied continuously, namely one of the limiting values, θ_A or θ_R, depending on whether h is increased or decreased.

The prediction of this model for the $D_{min} = 80\mu$m fibre compares very well with the measured tensiometer trace (black dots in Fig. 3.5). For the cylindrical portion of the fibre ($h < 100\mu$m), the static solutions (gray) appear one nearly continuous range of F per fixed h at the scales of the graph. They are however discontinuous at the

sub-micron scale of λ. The green/red line is the subset of equilibrium solutions which is tracked upon increasing/decreasing h. These traces display jumps with a periodicity λ equal to the wavelength of the small-scale heterogeneity (shown in the inset). On the experimentally captured scale, these jump lead to a force which stays constant as a function of h.

For the wavy portion of the fibre, the static solutions appear as multiple (from one up to three) ranges of F at fixed h. Besides the small-scale jumps which keep the angle with respect to the fibre remains nearly constant, the tracking now also requires jumps on the scale of the wavelength of the printed structure.

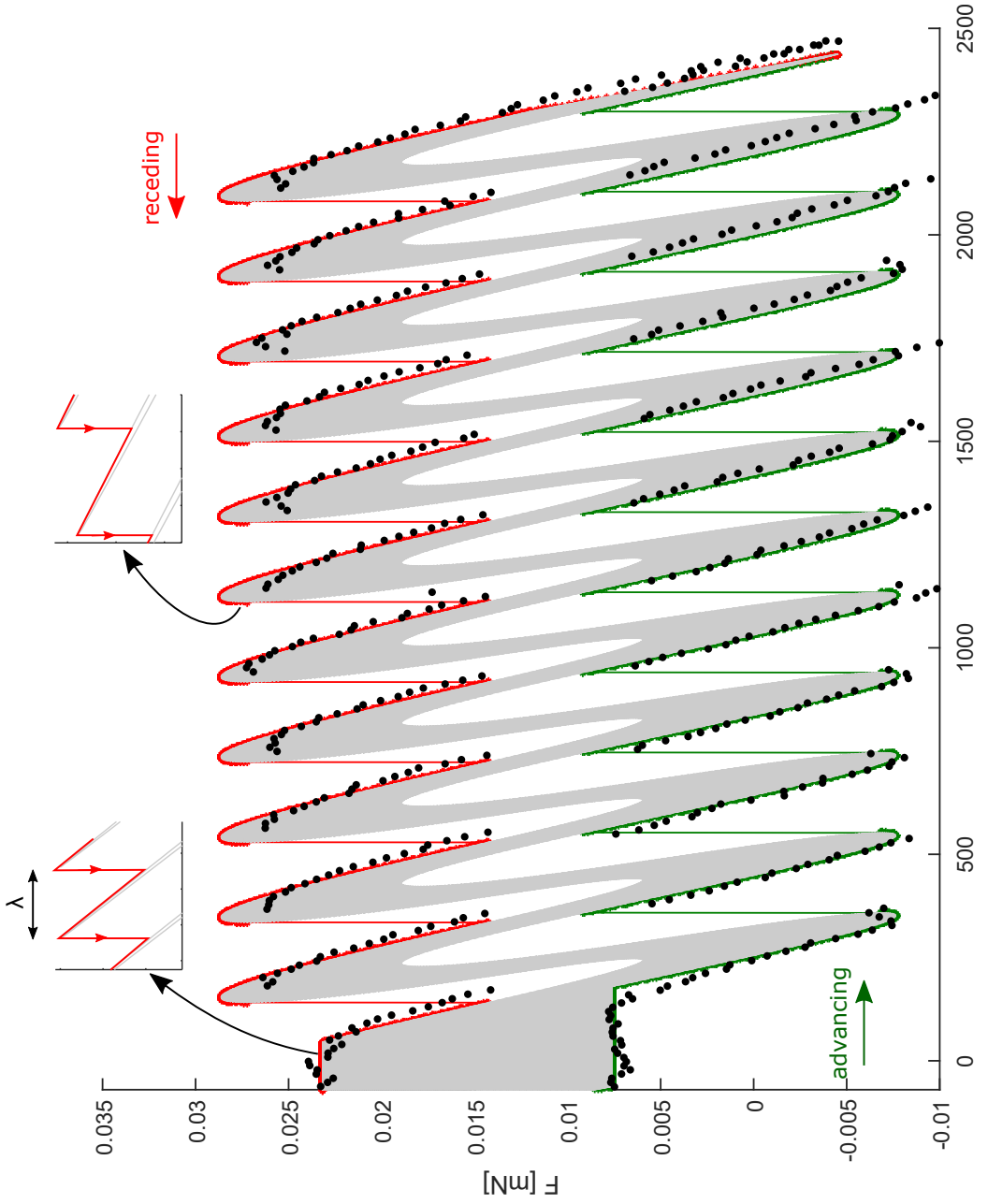

Figure 3.5: Force predictions of the model (gray: all static solutions, green: advancing, red: receding) compared to tensiometer raw data (black dots), where a chemical heterogeneity leading to contact angle hysteresis has been incorporated into the model.

3.4 Concluding remarks

3.4.1 Summary

The observation of liquid advancing and receding fronts on 4 different wavy fibres highlighted a stick-slip motion of the meniscus, the contact line jumping at well-defined positions depending on both the fibre surface topology and its intrinsic wettability.

The stick-slip motion during the immersion and withdrawal of a wavy fibre in a liquid bath is described well by the proposed static model of capillary rise, assuming a distribution of radii along the fibre, and tracking the static solution upon increasing or decreasing the experimentally controlled immersion depth.

Furthermore, the relation between the geometry of the fibre and the jump length of the contact line can be clearly established, in agreement with our theoretical predictions. Deviations between experimental and model data for high wave amplitude fibres can be explained by acceleration/deceleration events that take place during the motion of the contact line on the curved surfaces.

In summary, the behaviour of the seemingly pinned and then jumping contact line, with associated big changes in apparent contact angles (i.e. angles measured with respect to a vertical reference θ_V), can be understood by the interplay of a constant local real contact angle of the material, θ_i, and the movement of the bulk liquid. This leads to storage of energy which is suddenly released when the contact line passes a given point of fibre curvature.

The analysis presented here is limited to sinusoidal wavy fibres but it can be extended to study the wetting behaviour of fibres with more complex shapes and at different dimensions scales, possibly helping to interpret the effect of roughness.

3.4.2 Link with scaling laws predicted in chapter 2

In chapter 2, we have explored the scaling laws between the strength of wettability defects and the magnitude of the hysteresis they induce. Two different laws were identified.

First, near the threshold and for non-overlapping Gaussian-shaped chemical defects, the hysteresis amplitude has been found to be proportional to the square of the defect force. This numerical result is also in agreement with literature as well as a theoretical derivation, analogous to the one done here in section 3.3.2.1 to explain the observed scaling law between jump length and energy dissipation.

Second, for a model sinusoidal heterogeneity, in the limit of the heterogeneity wavelength being much smaller than the microchannel gap size, the hysteresis amplitude has been found to be proportional to the defect force.

It may seem contradictory at first sight that in this chapter we study sinusoidal fibres, but find agreement with the law which applies for the case of well-separated defects.

For all fibres studied in here, there are between one and three equilibrium configurations per h, which is the same number of equilibrium solutions that exist for sparsely spaced smooth defects. This corresponds to a regime which is just above the threshold and the nearness to the threshold explains the observed scaling laws.

On the other end of the spectrum, in the *macroscopic limit* (c.f. section 2.3.2), there are an arbitrary high amount of equilibrium configurations per fixed h or V. This regime was not explored with the fibres studied here, for which the wavelength and maximal diameter were fixed.

In Fig. 3.6 we show the scaling relation between the jump length and dissipated energy for another set of sinusoidal fibres for which both regimes can be observed. Now, we keep the maximal and minimal diameters constant at respectively 150 and 100 microns and vary the wavelength Λ. The equilibrium contact angle θ_0 is taken to be 90 deg, in order to be able to consider vanishingly small Λ while keeping $\theta_V > 0$.

As in the previously discussed case (c.f. section 3.3.2), for Λ above a certain threshold value, no jumps occur. For Λ slightly below the threshold, the jump length and dissipated energy both decrease with Λ and show agreement with the near-threshold scaling relation with power four (D_{min} can be directly replaced by Λ in the derivation of this scaling law in section 3.3.2).

Now in contrast to section 3.3.2, another regime appears far from the threshold. More specifically, for $\Lambda \to 0$, the jump length and dissipated energy over a period vanish too. In this limit, these quantities increase with Λ and show now agreement with the properties of the macroscopic limit, i.e. the jumps happen over a whole wavelength and hysteresis is maximal.

3.4.3 Procedure to reconstruct fibre topography or chemical heterogeneity from tensiometric measurements

Can the modelling approach used in this chapter be turned around to deduce the axial distribution of the fibre radius and the static contact angles starting from a tensiometric measurements? We start the procedure with static advancing and receding data from tensiometric measurements, as pairs of immersion height h and capillary force F, where

$$h = x_{CL} - r(x_{CL}) \cos\theta_V(x_{CL}) \left(\ln \frac{4l_c}{r(x_{CL})\,(1+\sin\theta_V(x_{CL})} - C \right), \qquad (3.22)$$

and

$$F = 2\pi\gamma r(x_{CL}) \cos\theta_V(x_{CL}), \qquad (3.23)$$

where the angle $\theta_V(x_{CL})$ is related to the local equilibrium angle $\theta_i(x_{CL})$ and the local inclination of the fibre $r'(x_{CL})$ through Eq. 3.3. The characterisation of the fibre requires the determination of three unknowns (x_{CL}, r and θ_i) for each measurement point.

This section contains two examples of such inverse procedure both of which involve simplifying assumptions depending on the specific case.

3.4.3.1 Wavy fibre with small scale heterogeneity

We consider data mimicking the tensiometric measurement in the advancing and receding directions at a resolution dh = 1 μm of a fibre with sinusoidal topography (minimal diameter 100 μm, maximal diameter 150 μm and wavelength 200 μm) and a small scale sinusoidal heterogeneity (minimal angle 47 deg, maximal angle 77 deg and wavelength 0.1 μm). These measurements corresponds to respectively the green and red lines in Fig. 3.7 (a). The goal of this procedure is to calculate for each measured point the contact line position x_{CL} and the contact radius r.

Combining Eqs. 3.22 and 3.23, the capillary force can be written in Hookean form,

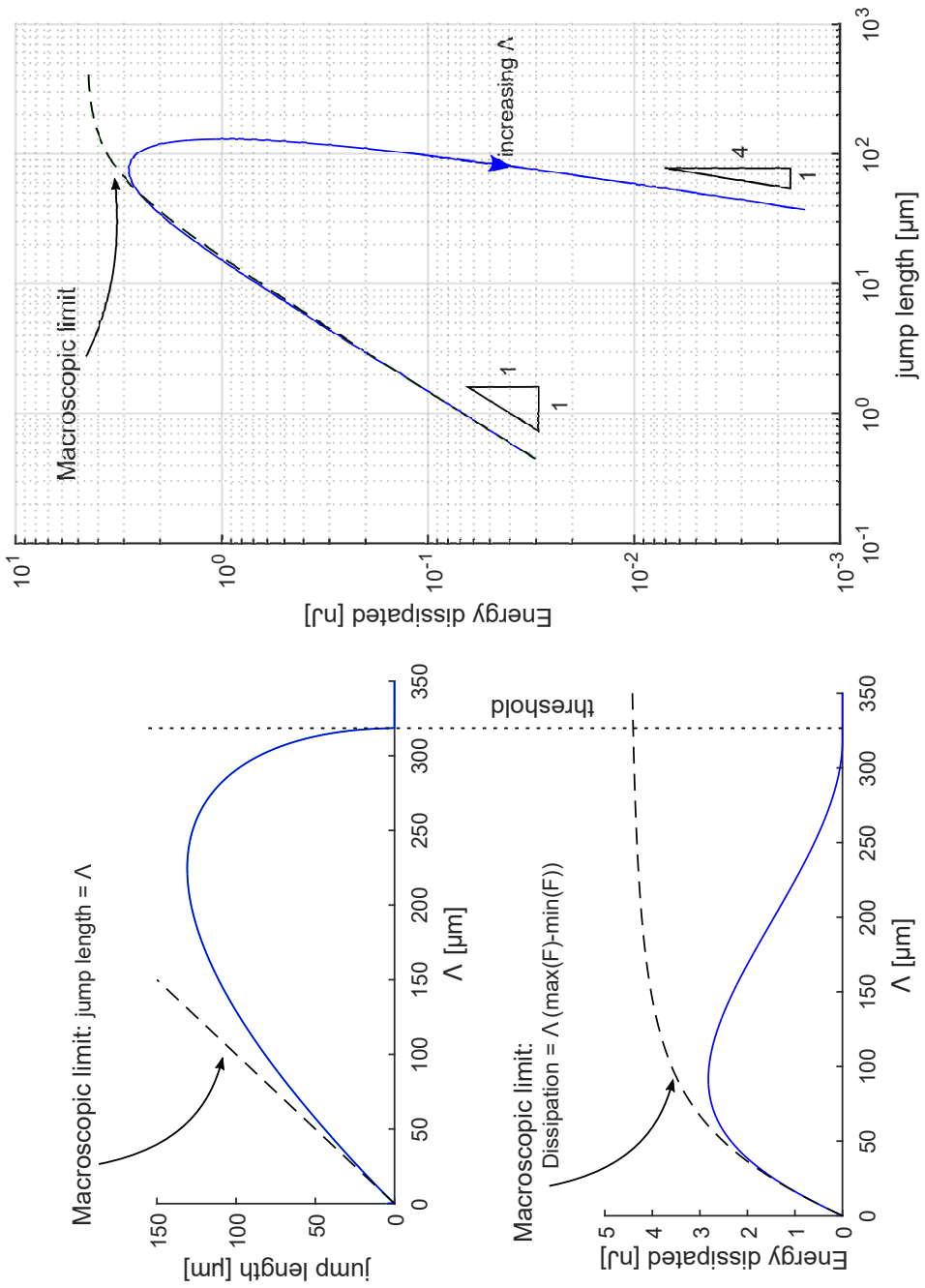

Figure 3.6: Same as Fig. 3.4 but for a set of sinusoidal fibres with minimal and maximal diameter respectively 100 and 150 microns and where the wavelength Λ is varied. The contact angle is now 90 deg.

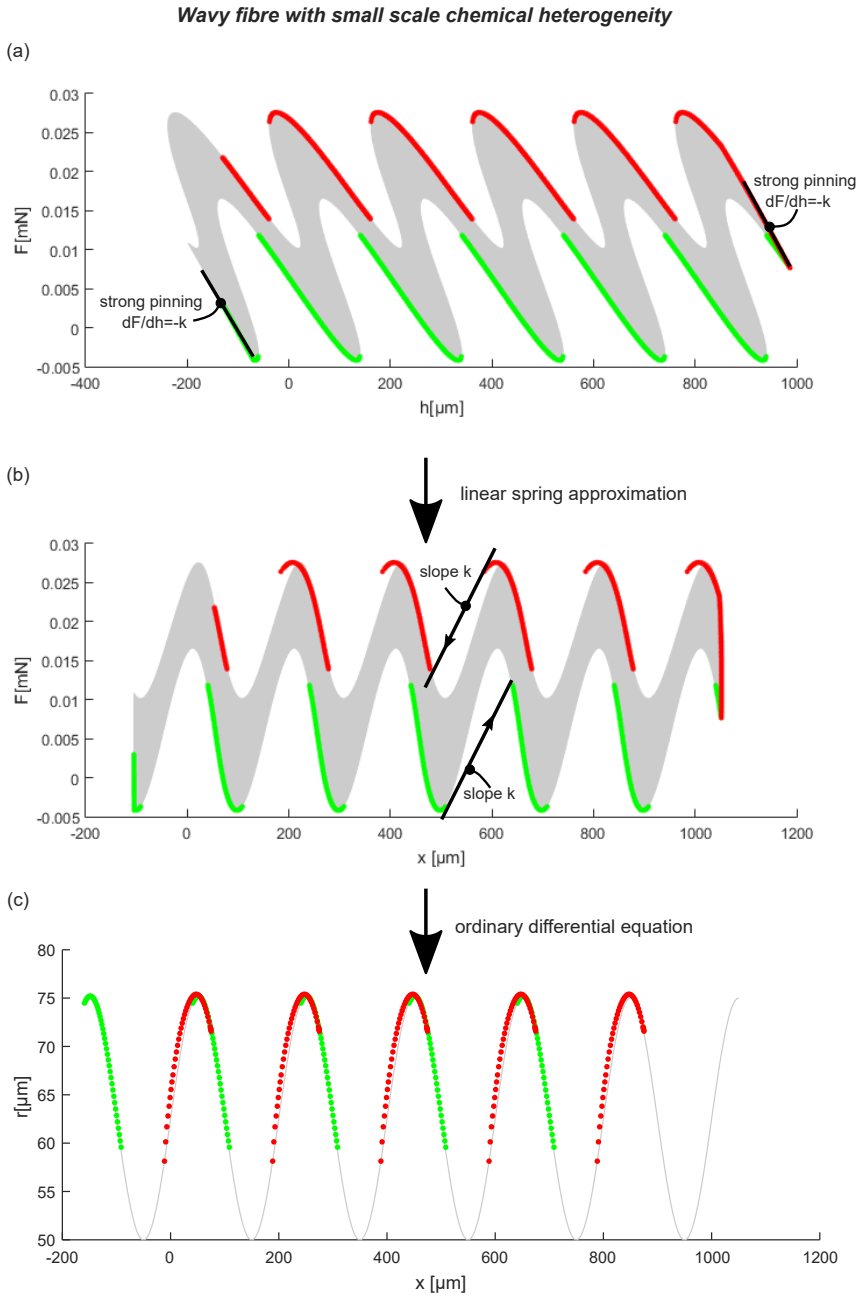

Figure 3.7: Procedure to reconstruct the topography of a wavy fibre with a small-scale chemical heterogeneity from tensiometric measurements. The gray lines are calculated from the a priori inaccessible fibre properties. The green and red lines correspond to the treatment of data accessible from tensiometric measurements, measured resp. in the advancing and receding direction.

$$F = k(x_{CL} - h), \tag{3.24}$$

by defining the spring constant of the meniscus as

$$k \equiv \frac{2\pi\gamma}{\ln \frac{4l_c}{r(1+\sin\theta_V)} - C}.$$

In the rest of the discussion we ignore the logarithmic dependence of k on r and θ_v, treating the meniscus as a linear spring. Treated as a constant, k can be directly measured from the tensiometric graph (Fig. 3.7 (a)) at the onsets of advancing and of receding. Because here, using Eq 3.24, the slope of equilibrium lines in this representation are given by

$$\frac{dF}{dh} = k\left(\frac{dx}{dh} - 1\right) = -k,$$

as the first term vanishes when the contact line is pinned by a small-scale heterogeneity. In the example k is evaluated to be 0.117 N/m at the advancing onset and 0.120 N/m at the receding onset. The calculation is carried on with the mean of the two. The estimation of the spring constant ($k \equiv F/(x_{CL} - h)$ here) from the absolute value of the slope $|dF/dh|$ for a pinned contact line is most accurate for angles θ_v around 90 degrees. For smaller values of θ_v, $|dF/dh| < F/H$ and thus we slightly underestimate the value of our k with this procedure due to the linear spring approximation. See [138] for the verification at the nanoscale of the meniscus spring constant, defined there from the slope $|dF/dh|$. Knowing k, the implicit parameter x_{CL} can now be calculated for each measurement point as

$$x_{CL} = h + \frac{F}{k}. \tag{3.25}$$

This brings us to graphical force balance representation shown in Fig. 3.7 (b), where for each jump the starting and ending point of that jump are connected to each other by a straight line with slope k. Now we can proceed to calculate the contact radius for each measurement point. Combining Eqs. 3.3 and 3.23 yields the ordinary differential equation

$$r'(x_{CL}) = \tan\left[\theta_i - \arccos\left(\frac{F(x_{CL})}{2\pi\gamma r(x_{CL})}\right)\right],$$

where θ_i equals θ_A or θ_R thanks to the small scale of the chemical heterogeneity. This ODE is solved numerically for each curve $F(x_{CL})$ to obtain $r(x_{CL})$. In this example, it is treated as an initial value problem, where the initial values are found by minimizing the discrepancy between the predicted values of r for the regions of x_{CL} for which there are two predictions.

Fig. 3.7 (c) finally shows reasonable visual comparison between the reconstructed topography (green and red) and the true topography which was assumed for data generation (gray), at least for the parts of the fibre over which the contact line has not jumped in both the advancing and receding measurement.

3.4.3.2 Chemically heterogeneous cylindrical fibre

We consider data mimicking the tensiometric measurement in the advancing and receding directions at a resolution dh = 1 μm, this time of a cylindrical fibre with the distribution of equilibrium angles shown in Fig 3.8 (b). Now the goal is to reconstruct

this chemical heterogeneity from the tensiometric data plotted in green and red in Fig. 3.8 (a).

In the absence of fibre topography, the procedure is straightforward without the necessity of making any additional assumptions. The equilibrium contact angle at each measured point can be calculated using Eq. 3.23, after which the contact line position x_{CL} can be explicited from Eq. 3.22. Therefore, the reconstructed parts of the fibre wettability in Fig. 3.8 (b) equal the true values.

The completeness of the reconstruction relies on the on the completeness of the measurement and in principle each contact line position can be measured. Each contact line position for which the equilibrium is stable or metastable can be accessed by varying the value of h starting from which h is imposed to increase or decrease while performing the measurement. Such procedure will become lengthier with decreasing typical wavelength of the heterogeneity, as the latter increases the amount of equilibrium configurations at fixed h.

Each contact line position on which the equilibrium is unstable can be accessed as well. Because those positions will become stable/metastable when the fibre is immersed upside down. In complete analogy to the chemically heterogeneous microchannel configuration (chapter 2), for a chemically heterogeneous fibre it can be shown that the capillary equilibrium is unstable on a contact line position where the wettability gradient $\theta_i'(x_{CL})$ is below a finite negative value (with the convention that x_{CL} increases in the advancing direction). When the fibre is immersed upside down $\theta_i'(x_{CL})$ flips sign, implying that those positions become stable/metastable for a static contact line.

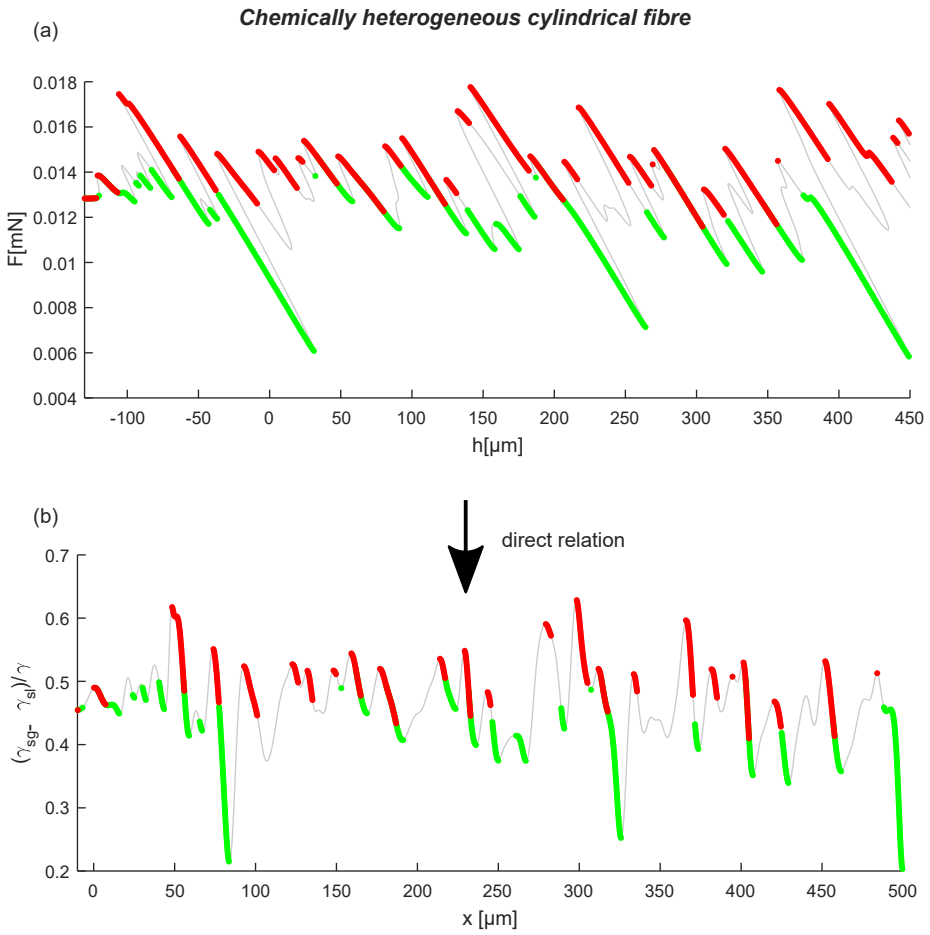

Figure 3.8: Reconstruction of the wettability distribution of a cylindrical fibre from tensiometric measurements. The gray lines are calculated from the a priori inaccessible fibre properties. The green and red lines correspond to the treatment of data accessible from tensiometric measurements, measured resp. in the advancing and receding direction.

Chapter 4

Contact angle hysteresis in a microchannel: dynamics

We study the dynamics of wetting hysteresis in a chemically heterogeneous microchannel assuming a quasi-steady meniscus shape. The meniscus is pushed by a piston either with (a) a constant force or (b) a constant piston velocity. We first show the non-equivalency between (a) and (b) already in their static limit, where the stability of a meniscus at capillary equilibrium for a range of contact line positions depends on whether the force or the piston position is constrained. For the dynamic problem, as theoretically predicted for a different configuration [85], in case (a) the resulting average velocity U of the piston does not depend on the geometric details of the studied configuration and scales with $\epsilon^{1/2}$ where ϵ is the imposed deviation of the force from its static limit, while in case (b) the imposed piston velocity U scales with $\epsilon^{3/2}$, where ϵ is now the average of the resulting deviation of the force from its static limit. For U larger than a critical value (which increases with the heterogeneity wavelength), the scaling law of case (b) tends toward that of case (a). We contrast the corresponding θ - U characteristics with characteristics valid for homogeneous substrates, which follow different scaling laws.

4.1 Introduction

The motion of liquid-gas interfaces over solids is common place in nature and in a wide spectrum of industrial processes. However apart for highly idealized systems, numerous challenges remain in the understanding and modeling of the physics involved, see for example the comprehensive reviews in Refs [31, 2, 89].

One of the most widely adopted theoretical results for the dependence of the contact angle θ on the contact line velocity u^* (although others exist [87]) was obtained independently by Voinov[80] and Cox[81]. It corresponds to the hydrodynamic balance between the curvature gradient of the interface and the viscous force, leading to the *viscous bending* of the interface in a mesoscopic region. This region generally lies between a macroscopically observable region -at a scale l_M^*- and a microscopic region -at a scale l_μ^* where the interface makes an angle θ_μ and the viscous stress singularity [74] is regularized e.g. by relaxing the no-slip condition. Other approaches [2, 75, 139, 89] exist, leading to the same result.

$$\theta^3 - \theta_\mu^3 = 9 \ln(l) \frac{\mu^*}{\gamma^*} u^*, \tag{4.1}$$

The asterisks denote dimensional quantities; γ^* is the liquid-gas surface tension, μ^* is the viscosity of the liquid and $l = l_M^*/l_\mu^*$, with typically $\ln(l) \approx O(10)$. When $u^* = 0$: $\theta = \theta_\mu$, therefore θ_μ is identified with the static equilibrium angle. However on any real substrate, the equilibrium angle displays hysteresis and is typically limited between a value θ_R at the onset of receding motion and a larger value θ_A at the onset of advancing motion. When the *Cox-Voinov relation* (Eq. 4.1) is fitted with experimental data, usually one of these two limiting angles is identified with the equilibrium angle depending on the direction of the contact line motion.

This empirical assumption of the substrate having a spatially uniform equilibrium angle seems to contradict the very reason of the observed hysteresis. Static models have shown that non-uniform wetting properties (dictated by the chemical composition and topography of the solid surface) induce a multiplicity of metastable angles at a fixed value of a macroscopic parameter, such as the volume of a liquid [53, 68, 100, 140], the average position of a liquid wedge [72], or the immersion depth of a partly immersed fiber[141]. When this macroscopic parameter is then varied, the attained metastable angle depends on the sense of the variation and the motion is characterized by abrupt jumps (also called *slip* and *depinning*) occurring on the (in most cases unobservable) scale at which the wetting properties vary.

Contact line dynamics on non-ideal surfaces is a subject of great interest, see for example [142, 93, 143, 96, 65, 144]. Raphaël and de Gennes[85] have studied theoretically the relationship between the capillary force (related to θ) and u^* when the motion is affected by a chemical defect. Two scenarios were shown to be non-equivalent. Applying a constant force, which deviates from its statically allowed range by a quantity ϵ, results in an averaged contact line velocity $u^* \propto \epsilon^{1/2}$. Applying the same u^* as a constant piston velocity does not result to in average the same ϵ, and even the scaling law is different, namely $u^* \propto \epsilon^{3/2}$.

Experiments made by Ström et.al[145] by dipping at constant velocity a polystyrene plate in a liquid (paraffin/silicone oils/PEG) bath have confirmed the $u^* \propto \epsilon^{3/2}$ power law at low capillary numbers. Many other experiments (an overview of which is presented in [146]), where in most cases neither the force nor the reference frame velocity were constant, have found scaling exponents varying from 1 to 5.

Our aim here is to provide a quantitative description of the θ-u^* relation on heterogeneous substrates where hysteresis is present and the contact line motion is intermittent. In particular, we are interested in the non-equivalency between the cases of a motion is driven by (a) a constant force and (b) a constant piston velocity, and in the question if these two situations can become equivalent.

To enable a simple analysis, we adopt a 2D meniscus in a (2D) microchannel as a model system, for which the statics of hysteresis are already well-understood [140]. We model the contact line dynamics using the Cox-Voinov relation while assuming the liquid-gas interface to be quasi-steady, in a sense explained later.

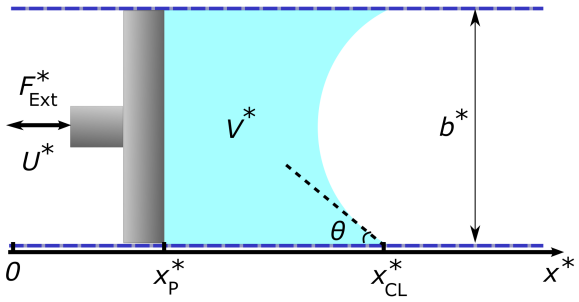

Figure 4.1: Sketch of the considered geometry of a liquid confined inside a chemically heterogeneous microchannel. The contact angle θ is defined as the angle between the line tangent to the liquid-gas interface at the contact point and the wetted area of the walls. We consider two dynamically non-equivalent situations; one where the piston position is controlled by imposing a constant piston velocity U^* and one where a constant external force F^*_{ext} is imposed.

4.2 Model formulation and theoretical framework

4.2.1 Statics: controlled piston position versus controlled external force

We study the 2D setup consisting of a liquid-gas meniscus moving inside a microchannel (Fig. 4.1). A gap of width b^* separates two planar, rigid, topographically flat, but chemically heterogeneous walls. This chemical heterogeneity is characterized by a positional dependence of the intrinsic angle $\theta_i(x^*)$ (identical on both walls). We consider periodic heterogeneities of the form

$$\cos\theta_i(x^*) = \cos\theta_0 + A_0 \sin\left(\frac{2\pi x^*}{\lambda^*}\right), \tag{4.2}$$

We assume gravity to be negligible so that the static interface takes a constant curvature (circular arc). Then, the liquid volume V^* (per unit length of the contact line) is given by

$$V^* = b^*(x^*_{CL} - x^*_P) + b^{*2} f(\theta), \tag{4.3}$$

where x^*_{CL} and x^*_P are the contact line and piston position respectively and

$$f(\theta) = \frac{2\theta - \pi + \sin(2\theta)}{8\cos^2\theta} \tag{4.4}$$

is an increasing function of θ coming from the circular meniscus interface. We scale all lengths with the gap size b^*. As V^* and b^* are constants in the considered configuration, we simplify our formulation by choosing $x_P = \frac{V^*/b^* + x^*_P}{b^*}$. Using Eq. (4.3), this leads to

$$x_P = x_{CL} + f(\theta). \tag{4.5}$$

The differential of the internal energy of the system, dU^* is given by the first principle of thermodynamics,

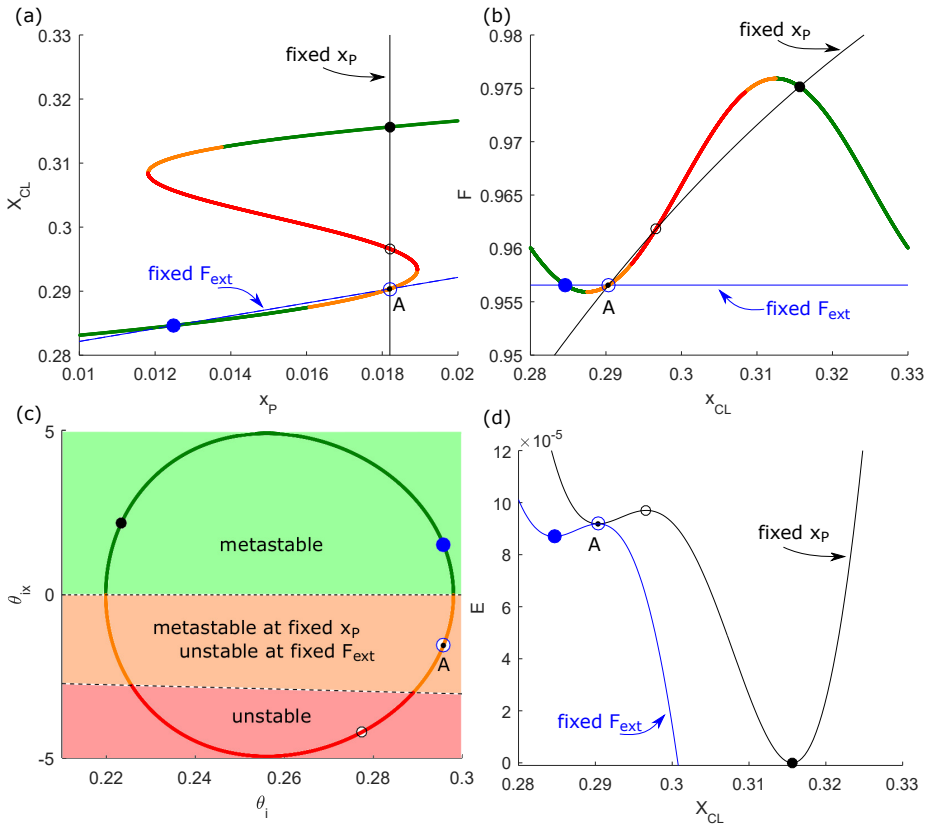

Figure 4.2: Stability of equilibrium solutions for a sinusoidal heterogeneity given by Eq. 4.2 with $\lambda = 0.05$, $\theta_0 = 15$ deg and $A_0 = 0.01$. (a): contact line position versus x_P, (b): graphical force balance, (c): phase plane plot, (d): Free energies as a function of x_{CL} at fixed value of interest of the F_{ext} (blue) and x_P (black).

$$dU^* = \delta Q^* + \delta W^* + \mu_l^* dn_l, \tag{4.6}$$

where the subscript l stands for liquid. The heat δQ^* is given according to the second principle by

$$\delta Q^* = T^* dS^* - T^* d_i S^*, \tag{4.7}$$

where $T^* d_i S^*$ is positive for irreversible processes and zero for reversible ones. The differential of the Helmholtz free energy is then given by

$$dF^* = dU^* - T^* dS^* - S^* dT^* \leq +\delta W^* + \mu_l^* dn_l^* - S^* dT^*. \tag{4.8}$$

The work δW^* has a contribution from the bulk and one from the interfaces,

$$\delta W^* = \delta_{bulk} W^* + \delta W_{int}^*, \tag{4.9}$$

with

$$\delta_{bulk} W^* = (p_l^* - p_g^*) b^* dx_p^* - p_g^* dV l^*. \tag{4.10}$$

The pressure difference between the liquid and the gas is given by the Laplace pressure, which is for a circular interface, $p_l^* - p_g^* = 2\gamma^* \cos\theta / b^*$. The interface contribution can be written, up to a constant, as

$$\delta_{int} W^* = \gamma^* dA_{lg}^* - 2\gamma^* \cos\theta_i(x_{CL}) dx_{CL}. \tag{4.11}$$

where dA_{lg}^*, is given by $b^* l'(\theta) d\theta$ with $l(\theta) = \frac{\pi - 2\theta}{2\cos\theta}$. Combining Eqs. 4.10 and 4.11 in Eq. 4.9 gives

$$\begin{aligned} \delta W^* = 2\gamma^* \cos\theta dx_P - p_g dV_l + \gamma^* b^* l'(\theta) d\theta \\ -2\cos\theta_i(x_{CL}) dx_{CL}, \end{aligned} \tag{4.12}$$

Substituting Eq. 4.12 into Eq. 4.8 and scaling all lengths with γ^* gives at constant T^*, n_l^* and V_l^* the free energy differential

$$dE \leq 2\cos\theta dx_P + l'(\theta)\, d\theta - 2\cos\theta_i\,(x_{CL})\, dx_{Cl}. \tag{4.13}$$

where $E = F^*/(\gamma^* b^*)$ is the dimensionless Helmholtz free energy. In the following, we proceed to particularize this free energy to the two scenario's of interest. We show that they lead to the same equilibrium configurations, the stability of which however depends on the nature of the constrained parameter, i.e. x_P or F_{ext}.

4.2.1.1 Constraint of fixed piston position

If the piston position x_P is fixed and the system is free to adapt x_{CL} and θ, the free energy E of the system, scaled with $b^*\gamma^*$ and up to an additive constant, is given by

$$E = \frac{\pi - 2\theta}{2\cos\theta} - 2\int_0^{x_{CL}} \cos\theta_i(x) dx. \tag{4.14}$$

This determines entirely the static aspects. Note that the static formulation of the problem where x_P is controlled, is exactly the same as the formulation of a problem

without piston ($x_P = 0$) where the liquid volume V^* is controlled, which we have studied in detail in [140]. Below is a summary of the key points. Minimizing this free energy at fixed x_P actually yields the natural condition $\cos\theta = \cos\theta_i(x_{CL})$ (see section 4.2.1.1.1).

This condition enables us to solve for x_P as a function of x_{CL} using Eq. 4.5 while accounting for the substrate heterogeneity (Eq. 4.2), yielding the S-shaped curve shown in Fig 4.2 (a).

The black vertical line (fixed x_P) intersects with three equilibrium solutions. The x_{CL} the system will adopt at that particular x_P will depend on the history of the system, in particular on whether x_P has been increasing (advancing case) or decreasing (receding case) to reach that value. For example, the point denoted A will only be encountered in an advancing experiment and increasing x_P further from this point on will result in an advancing jump of the contact line when x_P reaches the value corresponding to the limit point.

Figure 4.2 (b) shows the process' graphical force balance [72, 140] which additionally enables to physically interpret the stability of the three equilibrium configurations. In this representation, a line at constant x_P ($\cos\theta|_{x_P}$) represents a restoring force [140]. It increases with $x_{CL} - x_P$ and vanishes when $x_{CL} = x_P$. Its intersections with the sinusoidal curve $cos\theta_i(x_{CL})$ yield equilibrium configurations. For example, the first intersection (denoted A) is a metastable equilibrium state. Because starting from A, a positive perturbation of x_{CL} yields to an excess of the restoring force, which in turn decreases x_{CL} back to the point A. The points on the substrate at which (at fixed x_P) the contact line attains a metastable equilibrium are colored in green and in yellow, while on the red part, any equilibrium is unstable.

The stability of the equilibrium states, as well as the spots where the depinning jumps occur on the substrates, are adequately represented in the phase-plane plot (Figure 4.2 (c)). For the process at controlled x_P, the black-white striped line delimiting the orange region from the red one, is of particular importance. It is obtained [140] by expressing the condition of a limit point where the contact line jumps, i.e. $\frac{dx_V(x_{CL},\theta_i(x_{CL}))}{dx_{CL}} = 0$. It also separates the metastable equilibria from the unstable ones (see paragraph 4.2.1.1.1). The sinusoidal heterogeneity considered is represented by an ellipse which intersects twice with this critical line, marking the starting points of depinning jumps as the followed branch of equilibrium states become unstable.

The free energy at the considered fixed value of x_P (black curve in Fig. 4.2 (d)) displays three extrema, which correspond to the equilibrium configurations also shown in panels (a) and (b). They are alternately metastable ($\frac{dx_V(x_{CL},\theta_i(x_{CL}))}{dx_{CL}} > 0$) and unstable ($\frac{dx_V(x_{CL},\theta_i(x_{CL}))}{dx_{CL}} < 0$).

4.2.1.1.1 Stability condition for the capillary equilibrium under the constraint of a fixed piston position

If a constant piston position $x_P = x_{CL} + f(\theta)$ is externally constrained, the free energy of the system is given by Eq. 4.14, which upon directly substituting the constraint can be rewritten as an explicit function of θ only,

$$E(\theta) = l(\theta) - 2\int_0^{x_P - f(\theta)} \cos\theta_i(x)dx, \tag{4.15}$$

where $l(\theta) = \frac{\pi - 2\theta}{2\cos\theta}$ is the dimensionless liquid-gas interface length.

The extrema of this free energy make the first derivative of Eq. 4.15 vanish, i.e.

$$E'(\theta) = l'(\theta) + 2\cos\theta_i\,(x_P - f(\theta))\,f'(\theta) = 0, \tag{4.16}$$

leading to the natural condition for capillary equilibrium,

$$\cos\theta_i(x_{CL}) = -\frac{l'(\theta)}{2f'(\theta)} = \cos\theta, \tag{4.17}$$

where the last equality is shown through algebra. The stability of this equilibrium depends on the sign of $E''(\theta)$, which can be explicitly calculated as,

$$\begin{aligned} E''(\theta) = l''(\theta) + 2\cos\theta_i\,(x_{CL})\,f''(\theta) \\ +2\sin\theta_i\,(x_{CL})\,f'^2(\theta)\theta_i'(x_{CL}), \end{aligned} \tag{4.18}$$

At the extrema of $E(\theta)$, Eq. 4.18 is zero when

$$\theta_i'(x_{CL}) = -\frac{l''(\theta) - 2\cos\theta f''(\theta)}{2\sin\theta f'^2(\theta)} = -f'^{-1}(\theta), \tag{4.19}$$

in which the last equality can be shown trough algebra and the condition $\theta_i'(x_{CL}) = -f'^{-1}(\theta)$ implies $\frac{dx_P(x_{CL},\theta_i(x_{CL}))}{dx_{CL}} = 0$. Furthermore $-f'^{-1}(\theta)$ is always negative in the physical range of θ.

Therefore we conclude that under the condition of a contrained x_P, whether an extremum of the free energy is a minimum or a maximum depends on the sign of $\frac{dx_P(x_{CL},\theta_i(x_{CL}))}{dx_{CL}}$, namely

$$\begin{cases} \frac{dx_P(x_{CL},\theta_i(x_{CL}))}{dx_{CL}} > 0 \rightarrow \textbf{metastable} \\ \\ \frac{dx_P(x_{CL},\theta_i(x_{CL}))}{dx_{CL}} < 0 \rightarrow \textbf{unstable} \end{cases} \tag{4.20}$$

4.2.1.2 Constraint of fixed external force

Non-equivalent is a situation where an external force F_{ext}^* is imposed, which we assume to be directly counteracted by the capillary force, i.e. $F_{ext}^* = 2\gamma^*\cos\theta$. With this assumption, θ is constrained making the liquid-gas interface area constant. However now the system is free to adapt its piston position, with $dx_P = dx_{CL}$, and the dimensionless free energy of the system, up to a constant, is now particularized from Eq. 4.13 as,

$$E = -2\int_0^{x_{CL}} \cos\theta_i(x)dx + F_{ext}x_{CL}, \tag{4.21}$$

where $F_{ext} = F_{ext}^*/\gamma^*$.

Also this free energy has extrema for Young's law, i.e. $\cos\theta = \cos\theta_i(x_{CL})$. For $2\cos(\max(\theta_i)) \leqslant F_{ext} \leqslant 2\cos(\min(\theta_i))$, the system has an infinite amount of pairs of unstable solutions, separated from each by multiples of λ.

However now a different criterion for their stability can be obtained from the second derivative of Eq. 4.21, of which the sign is given by the sign of $\left(\frac{d\theta_i(x)}{dx}\right)_{x=x_{CL}}$. Therefore in this case,

$$\begin{cases} \left(\frac{d\theta_i(x)}{dx}\right)_{x=x_{CL}} > 0 \rightarrow \textbf{metastable} \\ \left(\frac{d\theta_i(x)}{dx}\right)_{x=x_{CL}} < 0 \rightarrow \textbf{unstable} \end{cases} \tag{4.22}$$

Therefore some of the equilibrium configurations which are metastable when x_P is imposed, are unstable when F_{ext} is imposed. Such points ($-\frac{1}{f'(\theta)} < \frac{d\theta_i(x_{CL})}{dxCL} < 0$) are shown in orange in Fig. 4.2, and a particular example is point A. The stability of the contact line in this equilibrium point depends on the nature of the constrained parameter. It is stable if the piston position is constrained, but unstable if the external force is unconstrained.

4.2.2 Dynamics: controlled piston velocity versus controlled external force

When the imposed force exceeds the maximal pinning force the heterogeneity can provide, the contact line will keep on advancing. On the other hand, for a system with a fixed piston position x_P, the contact line will not keep on moving, but reach a static equilibrium somewhere. Our goal here is to compare the steady dynamics of two cases which in their static limit correspond to the two cases discussed in the above paragraph. More specifically, we contrast the case of a constant F_{ext} (out of the range for which static solutions exist) to the case of constant piston velocity U.

In both cases, we model the dynamics of this motion with the Cox-Voinov relation (Eq. 4.1), in which the microscopic angle θ_μ equals the local equilibrium angle $\theta_i(x_{CL})$ and the time is scaled with $[t^*] = \frac{9\ln(l)\mu^* b^*}{\gamma^*}$.

$$\frac{dx_{CL}}{dt} = \theta^3 - \theta_i^3(x_{CL}) \tag{4.23}$$

In section 4.3.2.3, we show that the main results of this study are also obtained for another dynamics relation.

4.2.2.1 Dynamics with fixed piston velocity

For imposed U, θ is calculated by numerically inverting Eq. 4.5 where x_P explicitly depends on time, leading to the non-autonomous differential equation

$$\frac{dx_{CL}}{dt} = (f^{-1}(Ut - x_{CL}))^3 - \theta_i^3(x_{CL}). \tag{4.24}$$

As in [85], we are interested in the average of the resulting deviation from the force from its static limit, which is quantified as

$$\epsilon_{rec} = \frac{\langle\cos\theta(t)\rangle - \cos\theta_{rec,stat}}{\cos\theta_{rec,stat}} \tag{4.25}$$

and

$$\epsilon_{adv} = \frac{\cos\theta_{adv,stat} - \langle\cos\theta(t)\rangle}{\cos\theta_{adv,stat}} \tag{4.26}$$

for the receding and advancing case respectively. The angular brackets denote averaging in time of the periodic response. When $U \rightarrow 0$, we recover the statics of externally controlled x_P, and

$$\cos\theta_{rec,stat} = \frac{\int_{x_{P0}}^{x_{P0}+\lambda} \cos\theta_{rec}(x_P)dx_P}{\lambda}. \tag{4.27}$$

Here $\theta_{rec}(x_P)$ corresponds to the solution of the static problem at constrained x_P. More precisely, as shown in Fig. 4.2 (a), the statics is multi-valued for x_P, and $\theta_{rec}(x_P)$ is obtained upon decreasing x_P. $\cos\theta_{adv,stat}$ is defined in the same way but with the subset of the static solutions tracked upon increasing x_P.

4.2.2.2 Dynamics with fixed external force

Reversing the problem, we will also impose a constant external force F_{ext} on the piston, and calculate the resulting average contact line velocity. In this case, θ is a known constant and Eq. 4.23 is ready to be numerically integrated after separation of variables.

$$dt = \frac{dx_{CL}}{\theta^3 - \theta_i^3(x_{CL})}. \tag{4.28}$$

As in [85], we quantify the deviation of the imposed F_{ext} from the limiting range for which static solutions exists as

$$\epsilon_{rec} = \frac{\cos\theta_{R,dyn} - \max(\cos\theta_i(x))}{\max(\cos\theta_i(x))} = \frac{F_{ext}/2 - \cos\theta_0 - A_0}{\cos\theta_0 + A_0} \tag{4.29}$$

and

$$\epsilon_{adv} = \frac{\cos\theta_0 - A_0 - F_{ext}/2}{\cos\theta_0 - A_0} \tag{4.30}$$

for the receding and advancing cases respectively. The periodic heterogeneity of the walls (Eq. 4.2) will make that the contact line velocity $\dot{x_{CL}}$ (also equal in this case to the piston velocity as θ stays constant) will be periodic in time, with a period T. We are in particular interested in calculating the average velocity U of the piston, defined as

$$U = \frac{\int_0^T \dot{x}_{CL}(t)dt}{T} = \frac{\lambda}{T}. \tag{4.31}$$

with

$$T = \int_0^\lambda \frac{dx}{\theta^3 - \theta_i^3(x)}. \tag{4.32}$$

Note that U does not depend on the wavelength λ of the heterogeneity. The period T_{λ_2} calculated for a wavelength λ_2 equals $\lambda_2/\lambda T_{\lambda_2}$ yielding upon substitution into Eq. 4.31 the same U.

4.2.3 Discussion of the modeling assumptions

Our strongest assumption is that the liquid-gas interface shape is quasi-steady at the time-scale of contact line motion. Here we compare an estimate of the typical time $[t]_{lg}$ needed for the liquid-gas interface to reach its equilibrium shape to the typical time $[t]_{slip}$ of the depinning motion of the contact line.

The liquid gas interface in the vicinity of a substrate (at a typical distance b^*) relaxes to its equilibrium shape in a time which is the geometrical average of the viscous time $[t]_\mu = \frac{b^{*2}\rho^*}{\mu^*}$ [147] and the period of capillary waves $[t]_\gamma = \left(\frac{b^{*3}\rho^*}{\pi\gamma^*}\right)^{1/2}$ [147].

$$[t]_{lg} = ([t]_\mu [t]_\gamma)^{1/2} = \left(\frac{b^{*7}\rho^{*3}}{2\pi\mu^{*2}\gamma^*}\right)^{1/4}, \tag{4.33}$$

The validity of our assumption thus depends on the smallness of the ratio

$$\frac{[t]_{lg}}{[t]_{slip}} = \frac{1}{9\pi^{1/4}\ln(l)t_{slip}}(Oh)^{-3/2}, \tag{4.34}$$

where we have defined the Ohnesorge number $Oh = \frac{\mu^*}{\sqrt{\rho^*\gamma^* b^*}}$ and t_{slip} is the typical dimensionless time-frame where the depinning occurs. None of the parameters in Eq. 4.34 appear in our dimensionless formulation of the dynamics, except from t_{slip} which comes as a simulation result, typically of the order of 10 in the considered situations. Let us consider a millimetric system ($b^* = 1$mm). Then our assumption is less valid for water ($\frac{[t]_s}{[t]_{slip}} = 3.5$), and more valid for more viscous fluids such as glycerol and ethylene glycols ($\frac{[t]_s}{[t]_{slip}} \approx 10^{-4} - 10^{-2}$).

We also assume that the pressure losses inside the channel are negligible. The force F_P^* associated with the pressure drop [148] ΔP^* in a Poiseuille flow in a microchannel is given by

$$F_P^* = b^*\Delta P^* = \frac{12\mu^* U^* V^*}{b^{*2}} = \frac{12V^*\gamma^*(\theta^3 - \theta_i^3)}{9\ln(l)b^{*2}}, \tag{4.35}$$

in which we have substituted the Cox-Voinov relation (Eq. 4.1) for U^*. When the volume V^* is low, i.e. of the order of b^{*2} as drawn in Fig. 4.1, the ratio between F_P^* and the unbalanced Young's force F_Y^* is

$$\frac{F_P^*}{F_Y^*} \approx \frac{\theta^3 - \theta_i^3}{10(\cos\theta_i - \cos\theta)} \approx \frac{\theta^3 - \theta_i^3}{10(\theta^2 - \theta_i^2)} \approx \frac{\theta}{10} \ll 1, \tag{4.36}$$

in which we have used that the angles θ and θ_i are very small. This justifies neglecting the viscous pressure drop inside the channel, at least for not too long liquid plugs.

4.3 Results and discussion

We consider the periodic heterogeneity (Eq. 4.2) with a background intrinsic angle $\theta_0 = 15$ degrees and an amplitude $A_0 = 0.01$. These parameters correspond to a minimal and maximal intrinsic angles of around 12.5 and 17 degrees. The dimensionless heterogeneity wavelength λ determines for the case of controlled x_P the qualitative regime of the hysteresis. We vary λ over decades, from 0.1 for which the wettability gradients are too weak to induce hysteresis, to 5.10^{-4}, close to the macroscopic limit where static hysteresis is maximal.

4.3.1 Qualitative comparison between the two cases

For $\lambda = 0.05$ -producing a wettability gradient slightly above the threshold of hysteresis- panels Fig. 4.3 shows the dynamic trajectories of the receding contact line.

When a sufficiently small piston velocity U is imposed as in panel (a), the contact line stays for most of times close to its static metastable configurations (plotted in black) hindering their visibility in the plot, except during the jumps. The slowest motion (marked with the point S) occurs over a spot where the equilibrium angle is close to its background value θ_0 and $\left(\frac{d\theta_i}{dx_{CL}}\right) > 0$, marked with a *green* color following the color code of Fig. 4.2. From this point on, the contact line starts accelerating. Most of the acceleration occurs over the *red* region and the fastest motion occurs over the *orange* region, where $\left(\frac{d\theta_i}{dx_{CL}}\right) < 0$.

In panel (b), a sufficiently small deviation of the force ϵ is imposed and the trajectory can be qualitatively interpreted as the receding CL staying pinned on the most wettable spot for an amount of time T after which it jumps over a distance λ and the process repeats itself. It is clear from Eq. 4.23 with constant $\theta < \theta_i(x)\ \forall x$ that the fastest receding motion occurs over the least wettable spot and the slowest receding motion occurs over the most wettable spot. In contrast to case (a), here for both these spots, $\left(\frac{d\theta_i}{dx_{CL}}\right) = 0$.

The constant value of ϵ in panel (b) is chosen such that when imposed as a constant, it results in the same average piston velocity U as in panel (a). As the trajectories followed by the contact line in these two cases are qualitatively different from each other, the resulting average force deviation ϵ in case (a) is not the same as the one imposed as a constant in panel (b). More specifically, in panel (a), a constant piston velocity $U = 10^{-4}$ is imposed, resulting in an averaged deviation of the force $\epsilon = 6.8\ 10^{-4}$. In panel (b) a constant force deviation $\epsilon = 1.2\ 10^{-6}$ is imposed, resulting in an averaged piston velocity $U = 10^{-4}$.

These qualitative differences and the intermittency fade away when we go away further from the quasi-static limit, as shown in panels (c) and (d). The trajectory of the fixed force case (d) shows (exactly as in (b)) extrema in contact line velocity on the spots corresponding to the extrema of wettability. On the other hand, for the fixed U case (c), these spots have moved compared to case (a) and have become closer to the spots corresponding to the extrema of wettability (as in (b) and (d)). The quantitative difference decreased as well, namely in (c), $U = 10^{-2}$ is imposed, resulting in $\epsilon = 1.7\ 10^{-2}$. In (d), a constant $\epsilon = 8.6\ 10^{-3}$ is imposed, resulting in $U = 10^{-2}$.

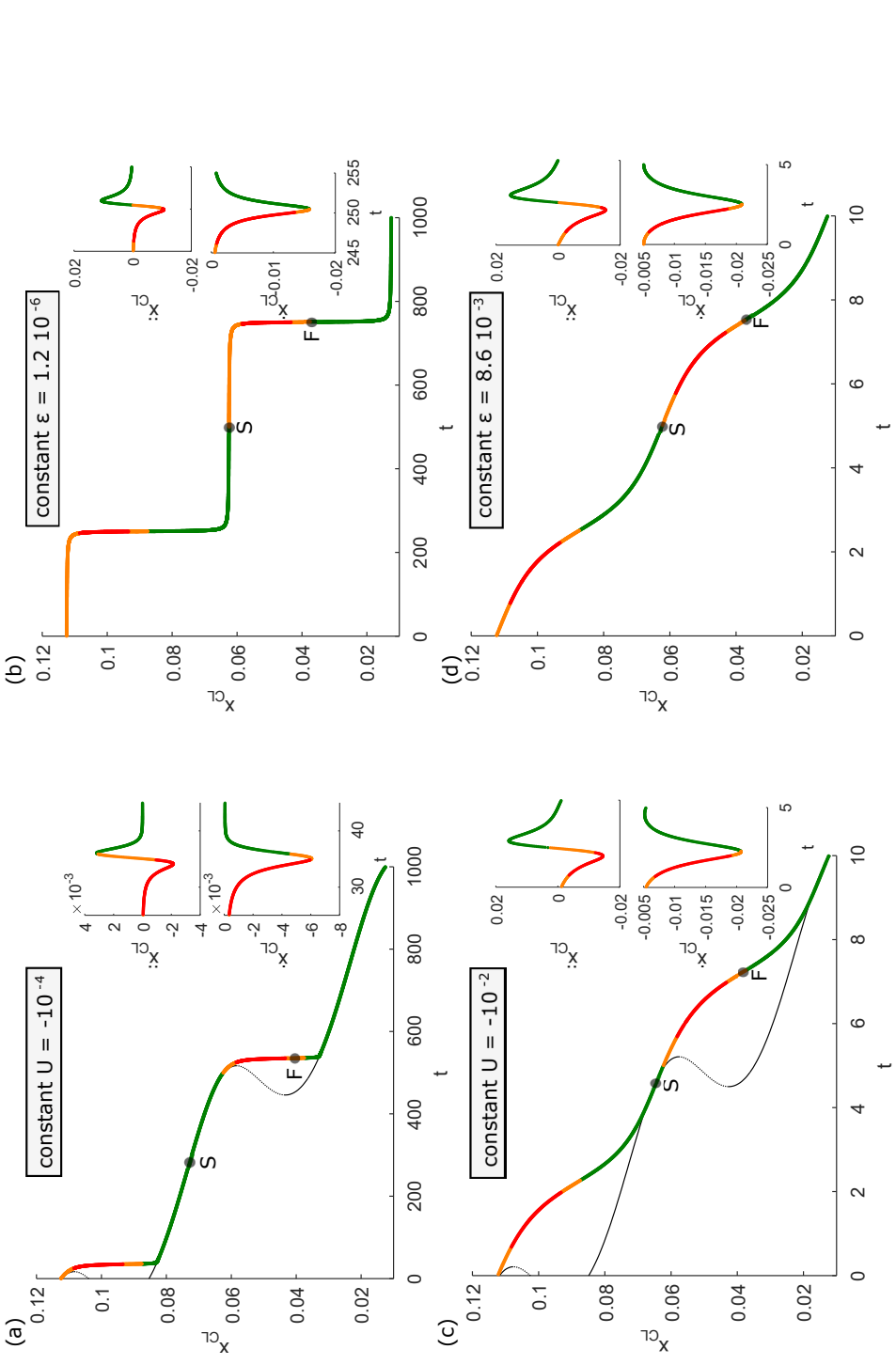

Figure 4.3: Dynamics of the receding contact line for $\lambda = 0.05$ at imposed indicated values. The insets show the contact line velocity and acceleration during the depinning in panels (a) and (b), and during one whole period in panels (c) and (d). The color code (green/orange/red) is the same as in Fig. 4.2 and is determined by the contact line position. The points S and F denote where the contact line moves slowest and fastest respectively. The black curve in panels (a) and (c) shows all static contact line positions x_{CL} corresponding to the piston position that is reached at time t, with dashed parts indicating unstable states.

4.3.2 Scaling laws between force and velocity

Here we study how the presence of wetting heterogeneity changes the scaling law of the form $U \propto \epsilon^{\beta}$.

4.3.2.1 Homogeneous case

First we consider a microchannel with homogeneous walls, characterized by an equilibrium contact angle $\theta_i(x) = \theta_0$. In Eq. 4.23, this implies that the cases of a constant piston velocity and of constant force on the piston are collapsing with each and corresponding to a case where the contact line velocity is constant. For small angles θ and θ_0,

$$\epsilon = \frac{\cos\theta_0 - \cos\theta}{\cos\theta_0} \approx \frac{(\theta-\theta_0)(\theta+\theta_0)}{2-\theta_0^2} = \frac{\delta(\delta+2\theta_0)}{2-\theta_0^2}, \tag{4.37}$$

where in the last equality, we have defined $\delta = \theta - \theta_0$. Similarly Eq. 4.23 can be rewritten as

$$U = \delta\left(\delta^2 + 3\theta_0^2 + 3\delta\theta_0\right). \tag{4.38}$$

Two limit cases can be identified in Eqs. (4.37) and (4.38). For a partial wetting case and sufficiently small contact line velocities (such that $2\theta_0 \gg \delta$),

$$\begin{cases} U \approx 3\theta_0^2\delta \\ \epsilon \approx \frac{2\theta_0}{2-\theta_0^2}\delta \end{cases} \rightarrow U \propto \epsilon \tag{4.39}$$

which is consistent with the treatment of [85] for that case. On the other hand, for a perfectly wetting fluid or for sufficiently large contact line velocities (such that $2\theta_0 \ll \delta$),

$$\begin{cases} U \approx \delta^3 \\ \epsilon \approx \frac{\delta^2}{2-\theta_0^2} \end{cases} \rightarrow U \propto \epsilon^{\frac{3}{2}}. \tag{4.40}$$

The transition between the two behavior occurs around the intersection, where $U \approx \frac{27}{8}\theta_0^3$ and $\epsilon \approx \frac{9}{4}\frac{\theta_0^2}{2-\theta_0^2}$.

4.3.2.2 Heterogeneous case

Fig. 4.4 reveals how these power laws are modified by the presence of a wetting heterogeneity, and how they now depend on the nature of the imposed parameter (fixed F_{ext} or fixed U).

For the fixed F_{ext} case, over the whole range of imposed values, corresponding to ϵ_{rec} from 10^{-6} to 10^{-2}, the behavior is in excellent correspondence with the power law

$$|U| \propto \epsilon^{\frac{1}{2}}, \tag{4.41}$$

which was predicted previously by [85] and is shown in paragraph 4.3.2.2.1 below.

When U is imposed (blue lines), the ϵ, U characteristics do depend on λ. For low enough imposed absolute U, we recover for all λ which cause static hysteresis the power law

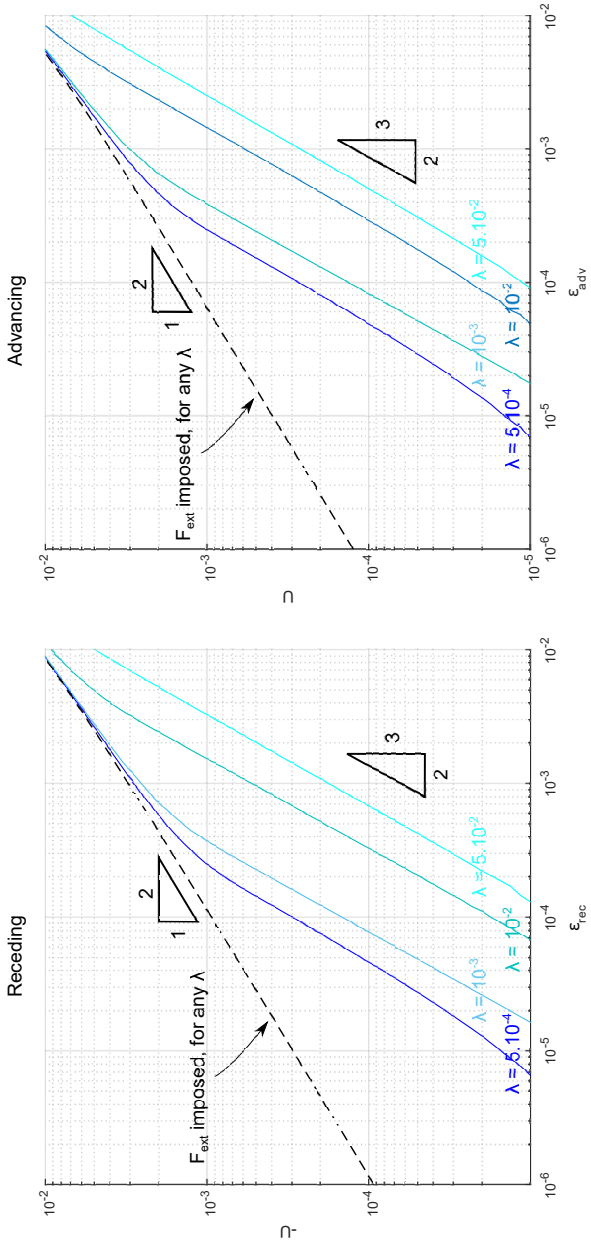

Figure 4.4: Average contact line (and piston) velocity U as a function of deviation of the force with respect to the static limit for the receding case ϵ_{rec}. The blue lines correspond to simulations with imposed constant U for the indicated values of λ which all produce wettability gradients above the threshold of static hysteresis. The black dashed line corresponds to simulations with imposed constant F_{ext} and does not depend on λ.

$$|U| \propto \epsilon^{\frac{3}{2}}, \tag{4.42}$$

which was also predicted by [85]. As the imposed U increases in absolute value, however this power law no longer holds and the curves tend towards the solution of the imposed F_{ext} case (Eq. 4.41). This transition occurs faster for smaller λ, i.e. for heterogeneities closer to the macroscopic limit, which even at the static limit display a behavior of nearly constant θ. The collapse of the curves (imposed F_{ext} and imposed U) signifies that an imposed constant piston velocity U yields an average force, which if imposed as a constant force would yield the same average velocity U of the piston and contact line.

4.3.2.2.1 Scaling law for $U \propto \epsilon^{\frac{1}{2}}$ for a fixed force case Let us consider a periodic heterogeneity of the wetting properties specified by

$$\theta_i(x_{CL}) = \theta_0 + A_0 \sin\left(\frac{2\pi x_{CL}}{\lambda}\right), \tag{4.43}$$

with $A_0 << \theta_0$, such that

$$\theta_i^3(x_{CL}) \approx \theta_0^3 + \theta_0^2 A_0 \sin\left(\frac{2\pi x_{CL}}{\lambda}\right). \tag{4.44}$$

We consider the case of a constant force and thus the contact angle θ, corresponding to the advancing case ($\theta > \theta_0 + A_0$). The average velocity (given by Eqs. (4.31) and (4.32)), specifies to

$$U = \lambda \left(\int_0^{\lambda} \frac{dx}{\theta^3 - \theta_0^3 - \theta_0^2 A_0 \sin\left(\frac{2\pi x_{CL}}{\lambda}\right)} \right)^{-1}. \tag{4.45}$$

Expression (4.45) can be integrated analytically and yields

$$\left(\frac{U}{\theta_0^3}\right)^3 = 1 + \left(\frac{\theta}{\theta_0}\right)^6 - 2\left(\frac{\theta}{\theta_0}\right)^3 - 9\left(\frac{A_0}{\theta_0}\right)^2. \tag{4.46}$$

We define $\delta = \theta - \theta_0$. For $\delta \ll \theta_0$ and $A_0 \ll \theta_0$, we use the approximation

$$\left(1 + \frac{\delta}{\theta_0}\right)^n \approx 1 + n\frac{\delta}{\theta_0} + \frac{n(n-1)}{2}\left(\frac{\delta}{\theta_0}\right)^2, \tag{4.47}$$

yielding

$$U \approx 3\theta_0^2 \sqrt{\delta^2 - A_0^2}, \tag{4.48}$$

where the difference under the square root is always positive in the considered case ($\theta > \theta_0 + A_0$). We define the positive quantity $\omega = \delta - A_0$ and rewrite Eq.(4.48) as

$$U \approx 3\theta_0^2 \sqrt{\omega^2 + 2\omega A_0} \approx 3\theta_0^2 \sqrt{2\omega A_0}, \tag{4.49}$$

where the last approximation sign describes the case $\delta \ll A_0 \ll \theta_0$. On the other hand, an analogous analysis as used to obtain Eq. (4.39) shows that $\epsilon \propto \omega$. Therefore this case obeys the scaling law

$$U \propto \epsilon^{\frac{1}{2}}. \tag{4.50}$$

4.3.2.3 Predictions for the molecular-kinetic theory

In this section, we repeat the analysis of the scaling relation between between the piston velocity U and the deviation of the static force ϵ for contact line dynamics governed by the equation

$$\frac{dx_{CL}}{dt} = \theta^2 - \theta_i^2(x_{CL}), \tag{4.51}$$

instead of the Cox-Voinov relation (Eq. (4.23)). This dimensionless governing equation (4.51) results from the molecular-kinetic theory [87] for small angles θ and θ_i.

Fig. 4.5, obtained upon repeating the calculation behind Fig. (4.4) with the only difference of the particular form of the θ - U relationship (i.e. using Eq. (4.51) instead of Eq. (4.23)). It confirms that also in this case, the same scaling laws apply.

An analysis analogous to the one in section 4.3.2.2.1 can be repeated here to show that in the constant force case, under the same conditions, $U \propto \epsilon^{\frac{1}{2}}$. More specifically it leads to

$$U \approx 2\theta_0\sqrt{\omega^2 + 2\omega A_0} \approx 2\theta_0\sqrt{2\omega A_0}, \tag{4.52}$$

where the last approximation sign describes again the case $\delta \ll A_0 \ll \theta_0$.

The only scenario leading to a scaling law which is different than its counterpart obtained using the Cox-Voinov relation, is the wetting of a homogeneous, perfectly wetting substrate. For this case, Eq. (4.51)-governed dynamics lead to $U \propto \epsilon$. Because here for the homogeneous case, for any θ_0,

$$U \approx \epsilon \cos\theta_0 \propto \epsilon. \tag{4.53}$$

On the other hand, for dynamics governed Eq. (4.23)- it is shown in section 4.3.2.1 that the perfectly wetting case follows $U \propto \epsilon^{\frac{3}{2}}$.

4.3.3 Dynamic angle-contact line velocity characteristics

When the system is forced far enough from the static limit, stick-slip fades and the cases of constant U and constant F_{ext} become equivalent. We now compare the characteristics of the dynamics obtained in this situation to the characteristics of contact line motion when the equilibrium angle is modeled as constant which depends only on the direction of the motion. The latter by definition yields the same jump discontinuity at the zero velocity limit, but does it approximate the dynamics well?

Fig. 4.6 shows for all considered cases the θ-U characteristics. When F_{ext} is imposed (black dashed line), the curve is independent of λ and shows at the zero-velocity limit a jump discontinuity from the lowest to the highest value of the intrinsic angles distribution. Indeed, when F_{ext} corresponds to a θ inside the intrinsic range, the contact line comes to rest at a corresponding metastable equilibrium position. Moving away from this limit, the relation between θ and U satisfies the power law $|U| \propto \epsilon^{\frac{1}{2}}$.

The data corresponding to the conditions of imposed U (full lines) do depend on λ. For each λ the existence and magnitude of the jump discontinuity is understood from the statics [140]. For low enough λ, the behavior tends towards a limit where

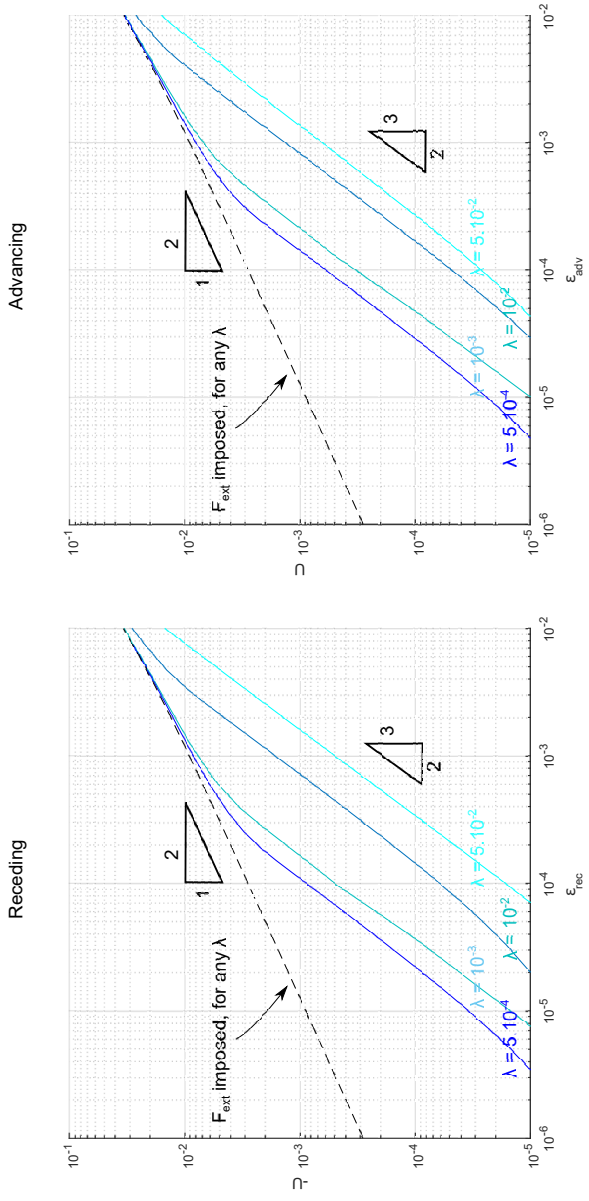

Figure 4.5: Same as Fig. (4.4) but for dynamics governed by the molecular-kinetic theory (Eq. (4.51)) instead of the Cox-Voinov theory (Eq. (4.23)).

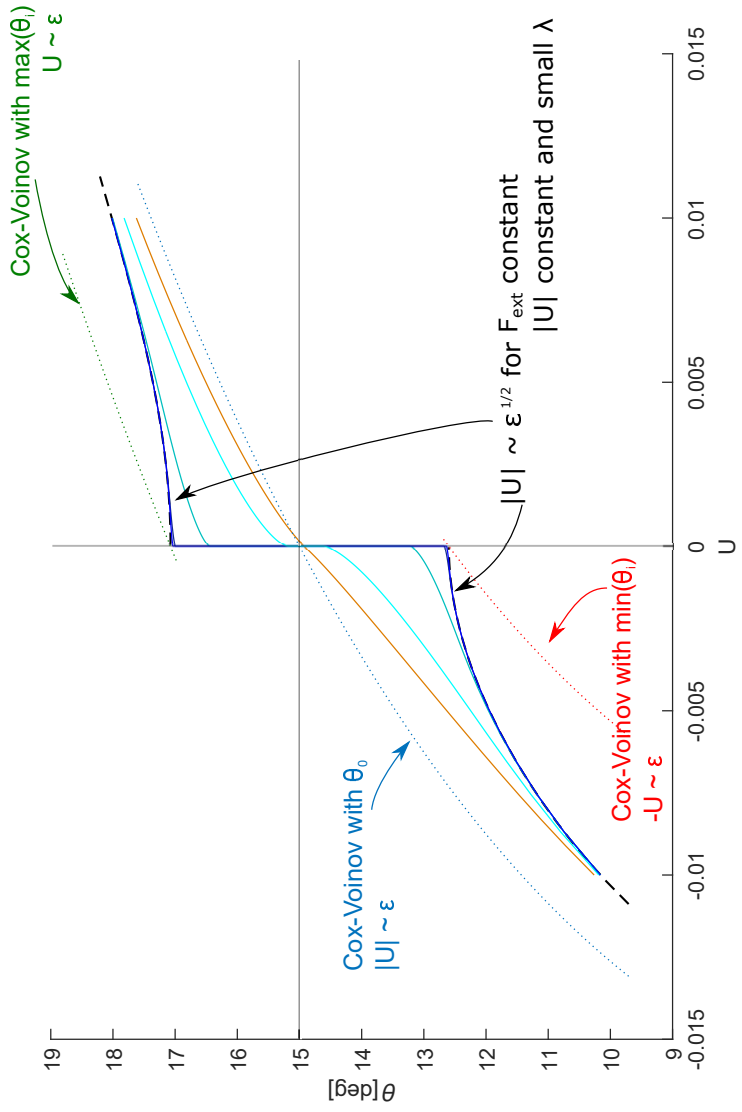

Figure 4.6: Averaged or imposed dynamic contact angle θ as a function of average contact line (and piston) velocity U. The lines have the same color code as Fig. 4.4 with now additionally the brown line corresponding to the case where U is imposed and $\lambda = 0.1$ (a sub-threshold heterogeneity). Three dotted lines correspond to the Cox-Voinov equation (Eq. 4.23) with θ_i constant and indicated.

static hysteresis is maximal ($\lambda = 5.10^{-4}$ and $\lambda = 10^{-3}$). Remarkably, the corresponding curves collapse in this (non-logarithmic) plot with each other and with the line of imposed F_{ext} and also obey $|U| \propto \epsilon^{\frac{1}{2}}$.

We compare this behavior with the Cox-Voinov relation (Eq. 4.23) for homogeneous walls by taking θ_i as a constant, corresponding to the minimum and maximum of its distribution (respectively red and green dotted lines) for respectively the side of receding and advancing velocities. As shown in section 4.3.2.1, in this approximation, $U \propto \epsilon$.

This empirical approximation strongly overestimates the effect of U on θ. Because in this approximation, e.g. in the advancing branch, a given U corresponds to a value of $\theta = (U + \max(\theta_i)^3)^{1/3}$ which is always greater than the dynamic angle $\theta = (U + \langle\theta_i^3\rangle)^{1/3}$ calculated taken the heterogeneity into consideration. Physically, when the walls are heterogeneous, the advancing contact line sees in average more wettable spots and not only its least wettable spots ($\langle\theta_i\rangle < \max(\theta_i)$)).

Now we look at dynamics on walls with a long wavelength heterogeneity, $\lambda = 0.1$. In the controlled x_P case, this heterogeneity is unable to induce hysteresis at the static limit (brown curve on Fig. 4.6) because its wettability gradients are too weak [140].

We compare the dynamics of this sub-threshold heterogeneity with the dynamics on homogeneous walls characterized by the same background angle θ_0 (blue dotted line). This time, the homogeneous angle Cox-Voinov approximation underestimates the effect of U on θ. In the latter approximation, e.g. in the advancing branch, a given U corresponds to a value of $\theta = (U + \theta_0)^3)^{1/3}$ which is smaller than the dynamic angle $\theta = (U + \langle\theta_i^3\rangle)^{1/3}$ calculated taken the heterogeneity into consideration. This means that the advancing contact line spends more time on the less wettable parts of walls than on its more wettable parts, which is consistent with intuition.

4.3.4 Depinning velocities

Lastly, we go deeper in the analysis of the intermittency aspect of the contact line dynamics by quantifying the maximal velocity the contact line reaches while depinning in Fig. 4.7.

Panels (a) and (b) show for respectively the cases of imposed F_{ext} and U the receding contact line velocity for in both cases four different values of the imposed parameter. To improve visibility, the time axis is rescaled with period T which depends for each curve on the value of the imposed parameter. The maximal velocity in all cases is of the order 10^{-2}, which in dimensional units corresponds to e.g. cm/s for water. In both cases ((a) and (b)) the peak velocity increases in absolute value with the magnitude of $|U|$ and ϵ_{rec}, and the intermittency becomes less pronounced as the average velocity increases faster.

In the limit of low $|U|$ and ϵ_{rec}, the peak velocity has a finite value which can be estimated analytically. For the case of imposed F_{ext}, the absolute value of this peak velocity is simply given by $\max\theta_i^3 - \min\theta_i^3$ both for the advancing case (where $\theta = \max\theta_i$) and the receding case (where $\theta = \max\theta_i$). Note that this maximal velocity is independent of λ.

When a vanishingly small U is imposed, the peak velocities for $U \to 0$ can be estimated using a graphical construction (panels (c) and (d) for different λ). The assumption behind this construction is that the jumps happen at constant x_P, which using Eq. 4.5 gives a line on a x_{CL}, θ^3 diagram. In static conditions, the θ and x_{CL} of the system are at each time determined by (one of its) intersection(s) with the black line which is the intrinsic angle distribution (Eq. 4.2) cubed.

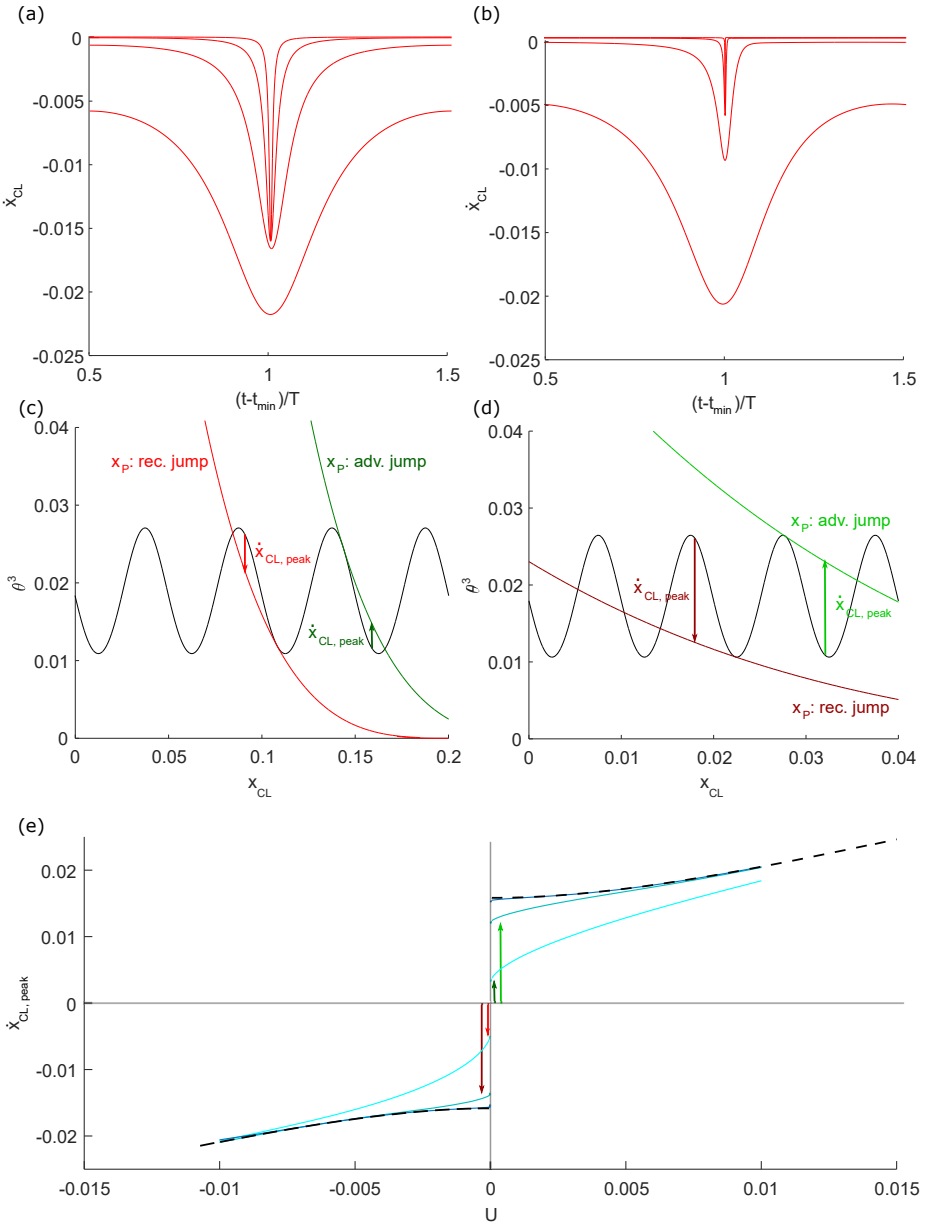

Figure 4.7: Analysis of depinning velocities. (a): F_{ext} is imposed for four values of F_{ext} corresponding to ϵ_{rec} equal to 10^{-5}, 10^{-4}, 10^{-3} and 10^{-2} from uppermost to lowest curve. (b): Same as (a) but for $\lambda = 0.005$ when U is imposed to be 10^{-5}, 10^{-4}, 10^{-3} and 10^{-2} in receding direction. (c) and (d): graphical construction to calculate the peak depinning velocities when imposed U approaches zero for λ respectively 0.005 and 0.01. (e): peak contact line velocity $\dot{x}_{CL,peak}$ as a function of average contact line (and piston) velocity U. The lines have the same color code as Fig. 4.4. The arrows at the jump discontinuity at the zero velocity limit correspond to the arrows in panels (c) and (d).

The intersection of interest depends on the history of the system. If $U > 0$ the line of constant x_P moves from left to right in time and the tracking of intersections shows that x_{CL} follows it with jumps. The green line on panel (c) is drawn for a value of x_P for which such a jump occurs.

During the jump, the instantaneous contact line velocity is given by the vertical distance from the black to the green line. It starts and ends with zero (where these lines touch) and reaches a maximum in between, given by

$$\dot{x}_{CL,peak,|U|\ll 1} = \max(\theta\big|_{x_P}^3(x) - \theta_i^3(x)), \tag{4.54}$$

where x_P is taken at its value where the static jump occurs and x lies in the range between the starting and ending contact line position of the jump. These quasi-static peak velocities are indicated with arrows on panels (c) and (d) for both the advancing and the receding case. When λ is smaller (comparing panel (d) to (c)), the constant x_P line is less steep at the scales of the heterogeneity, and the peak velocity is closer to its maximal value allowed by the heterogeneity, i.e. $\max\theta_i^3 - \min\theta_i^3$ (which is the exact value for the case of imposed F_{ext}).

The arrows on panels (c) and (d) give a jump discontinuity at the zero average velocity limit for the peak contact line velocity (panel (e)). Similarly as with the average dynamic angle on Fig. 4.6, at the limit of large enough imposed U (depending on λ), where the cases of constant F_{ext} and constant U become equivalent, the peak velocities become equal as well.

4.4 Conclusions and perspectives

4.4.1 Summary

We have analyzed in detail the dynamics of stick-slip and wetting hysteresis of a liquid-gas meniscus in a chemically heterogeneous microchannel of fixed gap width. We have modeled the contact line motion with the Cox-Voinov equation where the microscopic angle is taken to be dictated locally by Young's law and assumed that the meniscus shape is quasi-steady.

The meniscus is pushed by a piston under two non-equivalent conditions, either with (a) a constant force on the piston or (b) a constant piston velocity. The statics of case (b) is much richer than that of case (a) and studied in detail previously [140]. Some equilibrium configurations which are metastable in case (b) are unstable in case (a). The key parameter λ which determines the qualitative regime of hysteresis in case (b), does not play the same role in case (a).

The dynamics of stick-slip display qualitative differences as well, e.g. the locations where the contact line is pinned/moves slowest and depins/moves fastest are not the same for (a) and (b). An imposed constant U results in an average ϵ which if it would be imposed to be constant, would not yield the same average U. More specifically, in case (a) the resulting average velocity U of the piston scales with $\epsilon^{1/2}$ where ϵ is the imposed deviation of the force from its static limit, while in case (b) the imposed piston velocity U scales with the resulting average $\epsilon^{3/2}$.

For U larger than a critical value (which increases with the heterogeneity wavelength), the scaling law of case (b) tends toward that of case (a).

We have obtained the same scaling relations with calculations where the contact line dynamics is governed by the molecular kinetic theory.

These results are obtained in a simple model configuration where analysis can be pushed far. The predictions made in this manuscript will also serve as a basis to interpret the results of the extension of the present analysis to wetting on substrates which are disordered in two dimensions.

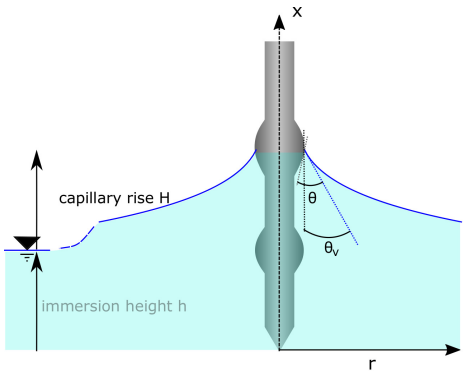

Figure 4.8: Drawing of a meniscus around an axisymmetric tip. The contact angle θ is defined as the angle between the line tangent to the liquid-gas interface at the contact line and the wetted area of the walls. θ_V is the angle between the line tangent to the liquid-gas interface and the vertical at the contact line.

4.4.2 Adaptation to the configuration of an AFM-tip

Probably the experimentally achievable configuration closest to the one dimensional system studied here is that of a meniscus around a thin cylinder (Fig.4.8), characterized by a radius profile $r(x)$. In dimensional form, with the contact line velocity with respect to the tip $u = \dot{x}\sqrt{1+r_x^2}$, the Cox-Voinov relation for this case reads,

$$\dot{x} = \frac{\gamma}{9\mu \ln(l)} \frac{\theta^3(x,t) - \theta_i^3(x)}{\sqrt{1+r_x^2}}. \tag{4.55}$$

The contact angle $\theta(x,t)$ is obtained by numerically inverting at each time-step the expression of the equilibrium capillary rise height [135],

$$H(r(x),\theta_V) = r(x)\cos\theta_V \left(\ln\left(\frac{4l_c}{r(x)(1+\sin\theta_V)} - 0.577\ldots \right) \right) \tag{4.56}$$

Here $\theta_V = \theta - \arctan r_x$. We impose a constant vertical velocity U of the tip with respect to the liquid bath as

$$h(t) = h_0 + Ut = x(t) - H(x,t), \tag{4.57}$$

where h_0 is an initial immersion depth (e.g. 0).

A similar analysis as in this chapter on the scaling relation of the form $U \propto \epsilon^\beta$, where ϵ is the deviation of the force from its static limit and U is the average contact line velocity, results as shown in, Fig. 4.9, also for this configuration in the same scaling laws, consistent with the predictions of [85].

Namely, the cases of constant force and constant tip velocity are dynamically non-equivalent and display exponents β respectively close to $\frac{1}{2}$ and $\frac{3}{2}$.

Fig. 4.9 also shows that for large enough imposed velocities U, the curves of constant velocities approach that of the constant force, showing a region with β close to $\frac{1}{2}$. The smaller the wavelength λ of the heterogeneity, the smaller the value of U above which this transition occurs, very similarly as in the microchannel configuration.

This conclusion brings the scaling laws and the dynamic non-equivalency of the

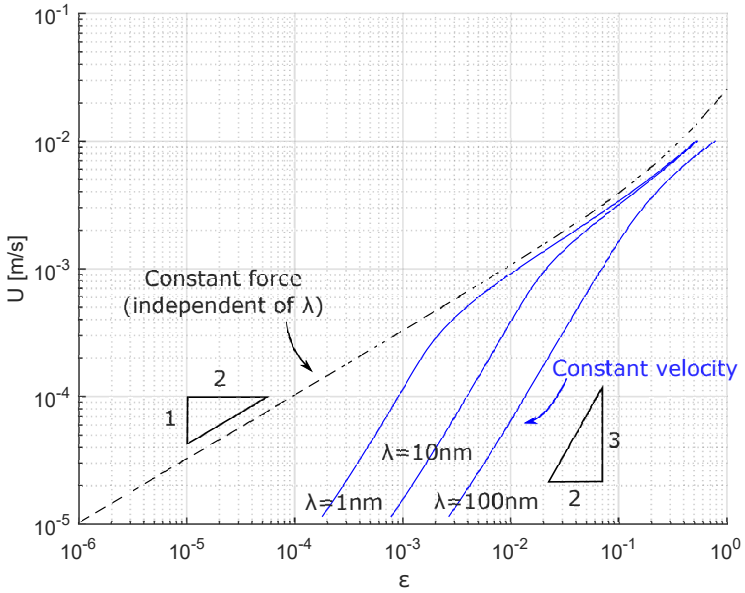

Figure 4.9: Calculation for a tip of radius 100 nm, and 4-ethylene glycol, where the measured values of the advancing and receding angles, θ_A and θ_R are modelled as being induced by a sinusoidal chemical heterogeneity with small wavelength λ.

fixed dipping velocity and fixed force cases analyzed in this chapter in the reach experimental verifiability/falsifiability. This is an aspect we are currently working on in a collaboration with Professor Thierry Ondarçuhu (IMF Toulouse).

Chapter 5

Extension to other configurations and geometry-specific effects

5.1 Introduction

The four previous chapters have demonstrated that the same modelling strategy can be followed in different geometries. In chapter 2, we have made theoretical predictions on the statics of stick-slip and hysteresis in the configuration of a microchannel, which in chapter 3 are adapted to the configuration of a meniscus around a fibre and compared with experiments. The same relation exists in chapter 4 for the dynamics.

In this chapter, we first present the general framework for this modelling strategy and apply it on a selection of configurations. For each of these configurations a static and a dynamic model will be constructed which focus on capturing the stick-slip motions and hysteresis of the contact line and the upon varying an externally controlled parameter σ (such as the liquid volume).

We also highlight qualitative differences between the results of these models for different configurations. Although the different models include the same main ingredients such as the heterogeneity of the wettability, the considered geometry (which will be described by functions G_j), can alter the qualitative features of stick-slip and hysteresis, and even give rise to specific effects.

We will consider five examples which involve a single contact line (sketched in Fig. 5.1) and five examples which involve two contact lines (sketched in Fig. 5.4).

For the single contact line problems, we start by showing how the previously discussed configurations of the chemically heterogeneous microchannel (5.3.1) and wavy fibre (5.3.2) fit in the framework and apply this framework to the geometry of a meniscus in a capillary tube (5.3.3) to get qualitatively similar results. On the other hand, a drop on a substrate (5.3.4) does not display a *threshold* for hysteresis, which was a main feature explaining scaling laws obtained for the former cases. If a voltage is applied to the substrate to enhance its wettability in an electrowetting (5.3.4.2) configuration, the effect of the heterogeneous wetting properties will be a delay in drop response.

A set of the examples which involve a generalization of the approach to treat two contact lines presents a richer dynamics, where the jumps of one contact line in the advancing/receding direction is accompanied by a jump of the other contact line in the receding/advancing direction. We show for the case of a microchannel with non-

identical walls (5.4.1) that both these jumps are rooted in the shape of the static solutions. Qualitatively similar is the stretching of a liquid bridge between non-identical plates (5.4.2).

We present three examples where the geometry or gravity causes one of the contact angle to be systematically larger than the other, thereby favouring the directional transport of liquid. These are a liquid column in a capillary tube with two liquid-air interfaces (5.4.3), a drop on a cone (as a model for the drop collection on the needles of certain species of desert plants) (5.4.4), and a drop between two non-parallel plates (as a model for the feeding mechanism of the Phalarope bird) (5.4.5). For the capillary tube problem (5.4.3), the model predicts a mechanism where the downward transport of the liquid is governed by an interplay between the jumps of the two contact lines. A similar effect is predicted for the configuration of the beak.

All the above examples involve either 2D systems with straight contact lines or axisymmetric systems with circular contact lines.

A further generalization of the approach to treat the dynamics of deformed contact lines on substrates which are disordered in two directions is presented in section 5.5. We focus on the case of drops with small contact angles, a property which greatly simplifies the treatment. The calculation is implemented in the commercial simulation software COMSOL Multiphysics.

The implemented model is tested for three substrates: (a) the perfect wetting case, leading to Tanner's law (5.5.2.1), (b) an axisymmetric substrate, leading to the stick-slip motion of the drop upon externally increasing/decreasing its volume (5.5.2.2), and (c) a heterogeneous substrate on which the drop travels towards a more favorable spot (5.5.2.3).

5.2 Modelling of axisymmetric and 2D cases

We consider an axisymmetric or 2D wetting configuration with n three phase contact lines, where the symmetry enables each of them to be characterized by a contact angle θ_j and contact line position x_{CL_j} (the subscript j is an integer from 1 to n). The system is thus described by $2n$ unknowns.

In this framework, we see these contact line positions and contact angles to be the response of the system. These quantities are in most cases not suited to be controlled externally. Typically contact lines can be made to advance or recede by varying an auxiliary parameter which is better suited for external control, such as the volume of a drop. We denote the externally controlled parameter σ (and consider it as a known).

The configuration is described by n geometrical relations of the form

$$G_j\left(x_{CL_1}\ldots,x_{CL_n},\theta_1,\ldots,\theta_n,\sigma\right)=0. \tag{5.1}$$

This makes n equations in $2n$ unknowns. The remaining equations that are needed to close the system depend on whether the statics or the dynamics are studied. For both cases, we consider that the heterogeneous wetting properties are described by n known distributions of the spatial coordinate x,

$$\cos\theta_{i_j}\left(x\right)=\frac{\gamma_{sg_j}(x)-\gamma_{sl_j}(x)}{\gamma_j}, \tag{5.2}$$

where $\gamma_{sg_j}(x)$ and $\gamma_{sl_j}(x)$ are respectively the solid-gas and solid-liquid interfacial tension distributions of the solid contacted by the jth contact line. In the examples of this chapter, we will impose sinusoidal distribution with a maximal angle θ_A, a minimal angle θ_R and a wavelength λ,

$$\cos\theta_i|_{\sigma=0}\left(x_{CL}\right)=\frac{\cos\theta_R+\cos\theta_A}{2}+\frac{\cos\theta_R-\cos\theta_A}{2}\sin\left(\frac{2\pi x_{CL}}{\lambda}\right). \tag{5.3}$$

5.2.1 Statics

The static problem is closed by stating that the contact angles are dictated locally by Young's law, leading to n equations

$$\cos\theta_j\ =\cos\theta_{i_j}\left(x_{CL_j}\right). \tag{5.4}$$

Combining Eqs. (5.1), (5.2) and (5.4) gives a system of $3n$ equations in $3n$ variables (θ_j, x_{CL_j}, θ_{i_j}) that can be solved for a given σ. For most substrates (depending on the intrinsic angle distribution - Eq. 5.2), this system will have multiple solutions, leading to hysteretic behavior upon externally controlling σ.

We note that this calculation can be greatly simplified in some configurations with one contact line. More specifically, if G can be rewritten to express σ as an explicit function of x_{CL} and θ, then all static solutions can be calculated with this explicit function by varying x_{CL} (as $\theta\ =\ \theta_i(x_{CL})$). The knowledge of all static solutions enables in a next step to follow a branch of static solutions upon varying σ.

5.2.2 Dynamics

The dynamic problem is closed by writing for each contact line the Cox-Voinov relation, for example as

$$\frac{dx_{CL_j}}{dt} = \frac{\theta_j^3 - \theta_{i_j}^3\left(x_{CL_j}\right)}{9\ln\left(l\right)\frac{\mu}{\gamma}}. \tag{5.5}$$

where μ is the dynamic viscosity and l is the ratio between a macroscopic and microscopic length scale (considered as a constant). Here x_{CL_j} increases in the advancing direction. If a substrate with topography is considered, a space-dependent metric factor enters Eq. 5.5, which projects lengths along the substrate on the axis parallel to the substrate.

Eq. 5.5 is an autonomous ODE as the parameter $\sigma(t)$ is externally controlled. At each time step x_{CL_j} are known and a system of n equations 5.1 are solved to determine the n unknowns θ_j, using e.g. a non-linear root-finding scheme with as initial guess the values of the previous time step. Therefore interestingly and especially for cases with more than one contact line, the dynamic problem is computationally less demanding than the static one.

The geometrical relations we consider in this framework are of the form of Eq. 5.1 and have no time-dependency. They typically describe an equilibrium shape of the liquid-gas interface. Therefore to calculate the dynamics in this framework, we invoke the assumption that the liquid-gas interface shape is quasi-steady at the time-scale of the contact line motion.

5.3 Systems with a single contact line

5.3.1 Liquid in a microchannel

This 2D problem, sketched in Fig. 5.1a, is studied in detail in chapters 2 and 4.

The externally controlled parameter σ is the liquid volume (divided by the square of the inter-plate distance) and the geometrical relation relies on the assumption that the meniscus has its circular equilibrium shape.

$$G\left(x_{CL},\theta,\sigma\right)=x_{CL}+\frac{2\theta-\pi+\sin(2\theta)}{8\cos^2\theta}-\sigma=0 \tag{5.6}$$

In this dimensionless equation x_{CL} is the contact line position divided by the inter-plate distance. Eq. 5.6 contains two unknowns, i.e. x_{CL} and θ.

In chapter 2 it is analytically shown for this configuration that the capillary equilibrium condition (Eq. 5.4) corresponds to extrema of the free energy at constant σ and the statics of hysteresis is studied after closing the system with this equilibrium condition (Eq. 5.4) and a given substrate heterogeneity (Eq. 5.2). The resulting system enabled to express σ as an explicit function of x_{CL}. Therefore, all static solutions could be calculated upon varying x_{CL} and the hysteretic behavior was studied upon following these static solutions when σ was varied.

The dynamics of this problem is studied in chapter 4, where the system is closed with the Cox-Voinov relation (Eq. 5.5). At each time-step, x_{CL} is known and θ is calculated from Eq. 5.6.

We note that in the same chapter the simpler problem was studied where θ is externally imposed. There, no configuration-specific relation of the form of Eq. 5.1 was needed to close the system.

5.3.2 Meniscus around a fibre

The statics of this axisymmetric problem (Fig. 5.1b) is studied in detail in chapter 3 and its dynamics is discussed in chapter 4.

Here the externally controlled parameter σ is the immersion height of fibre and the geometrical relation now relies on the assumption that the meniscus has reached its equilibrium capillary rise height H [135].

$$\begin{cases} G\left(x_{CL},\theta,\sigma\right)=x_{CL}-H\left(\theta-r'(x_{CL}),r(x_{CL})\right)-\sigma=0 \\ H(\theta_V,r)=r\cos\theta_V\left(\ln\frac{4l_c}{r(1+\sin\theta_V)}-0.57721\right) \end{cases} \tag{5.7}$$

Here $r(x)$ is the known fibre topography. Eq. 5.7 can be written as one equation in two unknowns, i.e. x_{CL} and θ.

In chapter 3 it is numerically shown for this configuration that the capillary equilibrium condition (Eq. 5.4) corresponds to extrema of the free energy at constant σ and the statics of hysteresis is studied after closing the system with this equilibrium condition (Eq. 5.4) and a given substrate heterogeneity (Eq. 5.2).

The dynamics of this problem is studied in chapter 4, where the system is closed with the Cox-Voinov relation (Eq. 5.5) with a metric factor. At each time-step, x_{CL} is known and θ is calculated from Eq. 5.7.

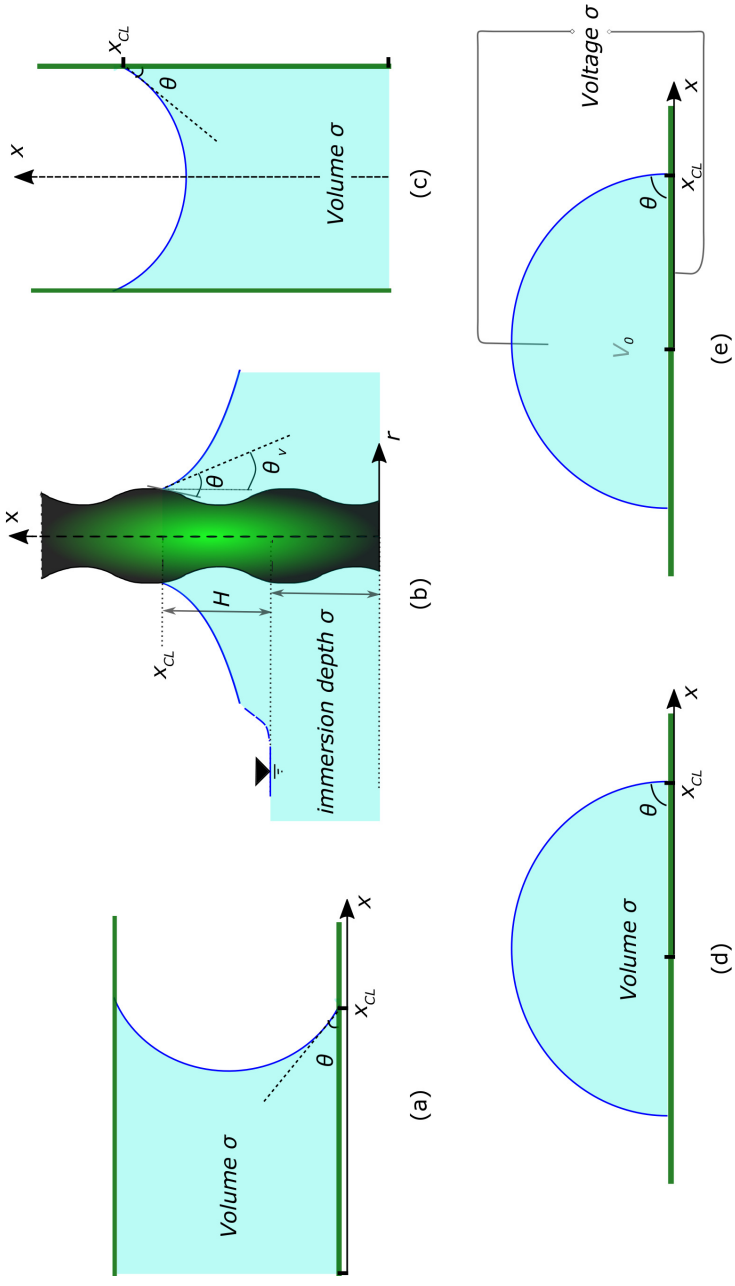

Figure 5.1: Sketches of configurations with one contact line. (a): liquid in a microchannel (5.3.1); (b): meniscus around a fibre (5.3.2); (c): meniscus in a thin tube (5.3.3); (d) sessile drop (5.3.4); (e): electrowetted sessile drop (5.3.4.2)

5.3.3 Liquid column in a capillary tube

We now consider a liquid inside a capillary tube (Fig. 5.1c) of which the inner walls are chemically heterogeneous but perfectly cylindrical with radius r_0.

The externally controlled parameter σ is the liquid volume (scaled with πr_0^3 and the geometrical relation relies on the assumption that the meniscus has its equilibrium shape (which is spherical).

$$G\left(x_{CL},\theta,\sigma\right)=x_{CL}+\frac{3\sin\theta-\sin^3\theta-2}{3\cos^3\theta}-\sigma=0 \tag{5.8}$$

In this dimensionless equation x_{CL} is the contact line position divided by r_0. Eq. 5.8 contains two unknowns, i.e. x_{CL} and θ.

It can be analytically shown for this configuration that the capillary equilibrium condition (Eq. 5.4) corresponds to extrema of the free energy at constant σ.

The free energy F of the system, up to a constant and scaled with $2\pi r_0^2\gamma$, is given by

$$F=\frac{1}{1+\sin\theta}-\int_0^{x_{CL}}\cos\theta_i(x)dx \tag{5.9}$$

To find the extrema of F at a fixed volume σ, we minimize the function

$$L(x_{CL},\theta)=F+\Lambda G\left(x_{CL},\theta,\sigma\right), \tag{5.10}$$

with respect to x_{CL} and θ, where Λ is a Lagrange multiplier and σ is a constant. This calculation yields the natural condition (Eq. 5.4) which states that at equilibrium, the meniscus angle must be equal to the local value of the Young's angle, as expected.

Therefore, as in the previous cases, the statics of hysteresis can be modelled after closing the system with this equilibrium condition (Eq. 5.4) and a given substrate heterogeneity (Eq. 5.2). The dynamics of this problem can be modelled closed with the Cox-Voinov relation (Eq. 5.5) where at each time-step, x_{CL} is known and θ is calculated from Eq. 5.8.

Also similarly to the two previous cases, it can be shown that hysteretic effects only arise if the wettability gradients of the substrate are above a certain threshold.

To have a multiplicity of equilibrium configurations (satisfying the system of Eqs. 5.8, 5.2 and 5.4) for a given volume σ, there must be at least one critical contact line position x_c, where a saddle-node bifurcation takes place.

At one of these points, the meniscus jumps either forward in an advancing path or backwards in a receding path, as the volume varies. We note that alternatively, we can see these critical points as maxima and minima, respectively, of $\sigma(x_{CL})$. Making use of Eq. 5.8 we can hence write:

$$\left.\frac{d\sigma}{dx_{CL}}\right|_{x_{CL}=x_c}=1-\left.\frac{\partial G}{\partial\theta}\frac{\partial\theta_i}{\partial x}\right|_{x=x_c}=0, \tag{5.11}$$

Denoting $\hat{\theta}_{ic}\equiv\theta_i'(x=x_c)$ and rearranging the above equation, we get

$$\hat{\theta}_{ic}=-\frac{3\left(\cos\left(\frac{\theta_i}{2}\right)+\sin\left(\frac{\theta_i}{2}\right)\right)^4}{4+\cos(2\theta_i)}. \tag{5.12}$$

Therefore, at critical points, the *wettability gradient* $\hat{\theta}_{ic}$ exhibits a *generic* behaviour that does not depend on the particular form of $\theta_i(x)$ but only on the given value of θ_i.

As θ_i is physically limited between 0 and π, we have that $\hat{\theta}_{ic}(\theta_i)$ is limited between $-\frac{3}{5}$ (for $\theta = 0$ and π) and -4 (for $\theta = \frac{\pi}{2}$).

We conclude that in this configuration, substrate wettability distributions of the form of Eq. 5.2, of which the gradients are less negative than the threshold value of $-\frac{3}{5}$ everywhere, will not induce hysteric phenomena in the static limit.

5.3.4 Drop on a substrate

We distinguish two versions of the problem of drops on chemically heterogeneous substrates (Fig. 5.1d). The geometry can be 2D (with a cylindrical drop) or axisymmetric (with a spherical drop). The volume of the drop is controlled externally and therefore denoted σ.

For the 2D case, the geometrical relation reads

$$G\left(x_{CL}, \theta, \sigma\right) = x_{CL}^2 \frac{\theta - \sin\theta\cos\theta}{\sin^2\theta} - \sigma = 0. \tag{5.13}$$

Eq. 5.13 contains two unknowns, i.e. base radius x_{CL} and contact angle θ. After closing the system with the equilibrium condition (Eq. 5.4) and a given substrate heterogeneity (Eq. 5.2) the statics of this configuration can be studied. Previous works on the statics of this configuration [68, 69, 70, 149, 100] have predicted hysteresis and stick-slip motion upon varying the volume σ of the droplet, similarly to the work presented in chapter 2. Recently, this behavior has also been observed when the droplet is fed trough a pore [65].

For the axisymmetric case, instead of Eq. 5.13, we write

$$G\left(x_{CL}, \theta, \sigma\right) = x_{CL}^3 \frac{\pi\left(1 - \cos\theta\right)^2\left(2 + \cos\theta\right)}{3\sin^3\theta} - \sigma = 0. \tag{5.14}$$

This configuration is studied in [100] and a variant of it where the substrate is chemically homogeneous but consists of axisymmetric grooves in [53].

5.3.4.1 Qualitative difference with previous configurations: the absence of a threshold

Here we highlight a qualitative difference between the three first configurations and the configuration of a drop on a substrate.

For the cylindrical droplet configuration, the volume σ of the droplet is given by $\sigma = x^2 g(\theta)$, with $g(\theta)$ a geometric factor (which is specified in Eq. 5.13).

A similar analysis as in section 2.3.1 (for the microchannel configuration) and section 5.3.3 (for the capillary tube configuration) would give as a criterion for a jump to occur the expression,

$$\hat{\theta}_{ic} = \frac{-2g(\theta_i)}{x_{CL} g'_{2D}(\theta_i)}, \tag{5.15}$$

where $\frac{g(\theta_i)}{g'(\theta_i)}$ is positive for the physical range of θ_i.

Thus, for this configuration (as well as for its axisymmetric variant) $\hat{\theta}_{ic}$ is an explicit function of x_{CL}, which was not the case for our microchannel and capillary tube.

Whether a defect is strong or weak, will therefore depend on how far it is from the center of the droplet. Any defect which is far enough from the origin ($\hat{\theta}_{ic}$ close enough to zero) will induce hysteresis and therefore no threshold exists for sufficiently large droplets, just like in the macroscopic limit (section 2.3.2) for the microchannel.

Furthermore, Fig. 5.2 shows that, for a given periodic intrinsic contact angle distribution, upon increasing the volume of the droplet, the system passes through the same qualitatively different regimes of hysteresis (introduced in Section 2.3.2) as for the microchannel. We neglect any external noise, which would enable the system to cross energy barriers, and we assume that the droplet center does not shift during the process (see Ref. [65] for details).

Upon increasing the volume $V = \sigma$ (from left to right), the system goes from a sub-threshold regime, through a regime with pronounced stick-slip, and finally to the macroscopic limit, for droplets much larger than the length scale of the heterogeneity. In both this configuration and that of the microchannel, the ratio of the gas-liquid interface length to the typical length scale of the heterogeneity seems to be an important physical parameter which determines the hysteresis behavior.

In particular, a general conclusion seems to be that the advancing and receding contact angles become independent of the particular liquid configuration (drop, meniscus, bubble, $\cdots$) when this ratio becomes sufficiently large. In such macroscopic limit, the hysteresis range is fixed by the maximum and the minimum of the contact angle distribution and stick-slip behavior is unobservable.

This general conclusion supports the use of the common basic way of introducing contact angle hysteresis into static macroscopic models by prescribing given constant values for the advancing and receding angles.

5.3.4.2 Electrowetting of a drop - stick stage at constant volume

As last example of systems with a single contact line, we consider an axisymmetric drop on a chemically heterogeneous surface, of which the wetting properties are modified with an applied electric field (Fig. 5.1e). A review of this phenomenon is presented in refs. [150, 151]. The effect of an applied voltage σ on the wettability of the substrate is described by the Young-Lippmann equation, which is of the form

$$\cos\theta_i\left(\sigma\right) = \left.\cos\theta_i\right|_{\sigma=0} + a\sigma^2, \tag{5.16}$$

where the factor a is a constant, which is of the order of $1V^{-2}$ for the case of an electrolyte droplet placed directly on an electrode surface [150]. The first term in the right hand side is the wettability in the absence of an applied voltage, which we identify with Eq. 5.2.

We consider the geometry of a spherical drop and use Eq. 5.14 where we now assume that the volume is constant throughout the process, and denote it by V_0.

Interestingly, the assumption of constant volume V_0 prohibits the main qualitative features of the stick-slip motion, which the configurations studied in the previous sections have in common. More specifically, during the stick stage, x_{CL} was nearly constant while θ was varying.

On the other hand, now Eq. 5.14 directly relates any advancing motion (increase in x_{CL}) to a decrease in the contact angle θ and any receding motion to an increase in the contact angle.

For a long enough wavelength λ (top row of Fig. 5.3) the stick-slip motions are clearly observable on the scales of the graph. During the stick stage, both x_{CL} and θ stay nearly constant which is a qualitative difference compared to the results of the configurations discussed above. During the slip stages, x_{CL} and θ display jumps of opposite sign, like in the previously discussed configurations where the volume was constant during the jumps.

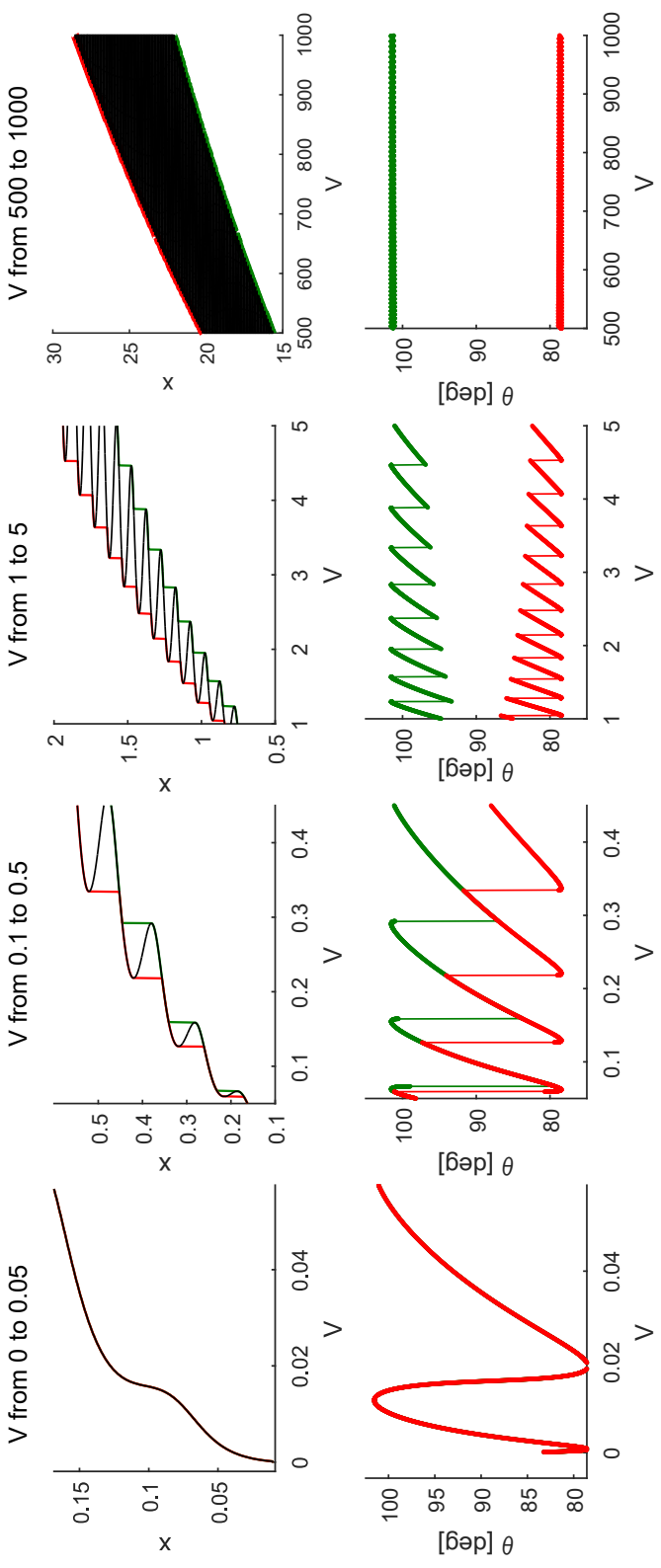

Figure 5.2: Qualitatively different regimes of hysteresis for a droplet (assuming the system has no ability to overcome any energy barriers) caused by a periodic heterogeneity described by Eq. 2.30 with $A_0 = 0.2$ and $\lambda = 0.1$. The columns represent zooms on different ranges of V with qualitatively different behavior. The plotted quantities are the same as in Figure 2.9.

The bottom row of Fig. 5.3 shows the effect of the heterogeneity in the macroscopic limit. Namely, when the sign of the variation of the voltage σ is changed (point denoted A), x_{CL} and θ do not respond to changes of σ until σ has moved over a certain voltage range (reaching point denoted B).

The magnitude of this delay in response can be calculated using the property of the macroscopic limit that advancing motion occurs with $\cos\theta_i|_{\sigma=0} = \cos\theta_A$ and receding motion occurs with $\cos\theta_i|_{\sigma=0} = \cos\theta_R$.

Thus in the macroscopic limit, the points denoted A and B have the same contact angle, which is given by

$$\cos\theta = \cos\theta_A + a\sigma_A^2 = \cos\theta_R + a\sigma_B^2. \tag{5.17}$$

Therefore, the magnitude of the delay is directly related to the contact angle hysteresis by

$$\sigma_A^2 - \sigma_B^2 = \frac{\cos\theta_R - \cos\theta_A}{a}. \tag{5.18}$$

Note that in the previously studied configurations a similar stick stage was present at the onset of changing the sign of variation of e.g. the volume of a drop. There, the contact line stayed pinned for a range of volumes while θ decreased from θ_A to θ_R, with a direct relation between the range of volumes and the contact angle hysteresis (see e.g. [152]).

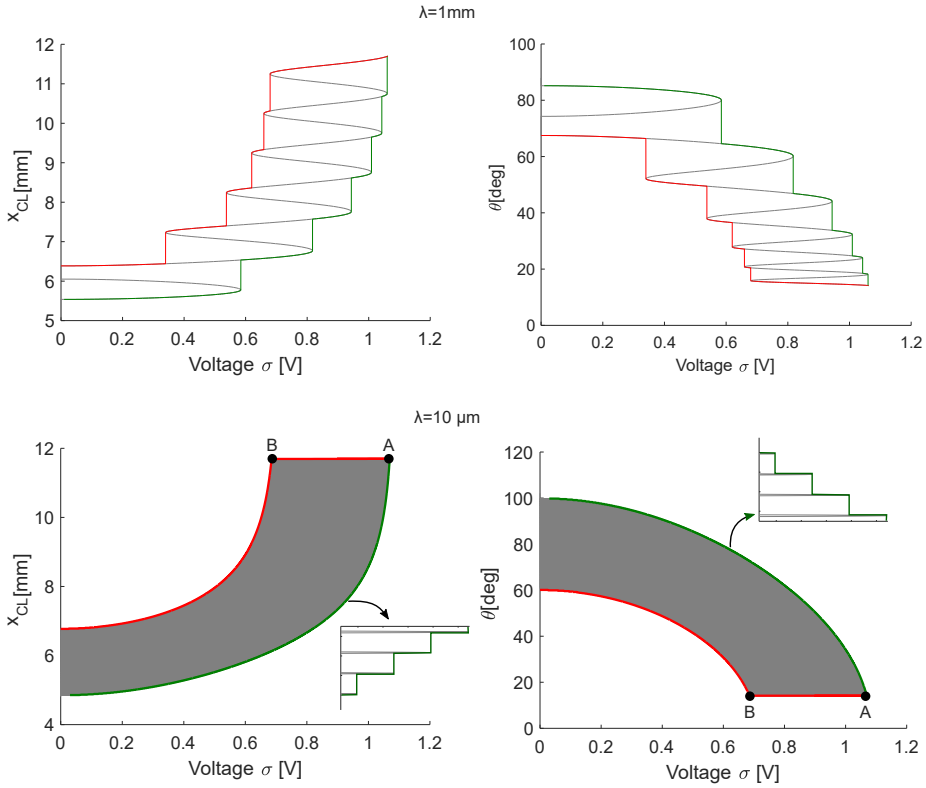

Figure 5.3: Effects of heterogeneous wetting properties for electrowetting configuration, with $a = 1V^{-2}$ and a sinusiudal heterogeneity, i.e. Eq. 5.3 with $\theta_A = 100$ deg, $\theta_R = 60$ deg. Gray: all static solutions. Green: static advancing. Red: static receding.

5.4 Systems with two contact lines

5.4.1 Microchannel with non-identical walls

We consider the 2D microchannel drawn in Fig. 5.4a, where now as in contrast to section 5.3.1, the upper and lower walls are characterized by different wettability distributions. The meniscus profile $p(y)$ is circular and therefore determined by three parameters, i.e. a center point (x_c, y_c) and a radius R.

$$(p - x_c)^2 + (y - y_c)^2 = R^2 \tag{5.19}$$

The upper contact line is at a position x_{CL_1}, where the interface makes an angle θ_1 with the wall and the lower contact line is at a position x_{CL_2}, where the interface makes an angle θ_2 with the wall. This leads to four conditions,

$$\begin{cases} p(y=1) = x_{CL_1} \\ p'(y=1) = \cot\theta_1 \\ p(y=0) = x_{CL_2} \\ p'(y=0) = -\cot\theta_2 \end{cases} \tag{5.20}$$

where all lengths are scaled with the inter-wall distance. Combining Eqs. 5.19 and 5.20, the meniscus profile can be expressed in terms of variables of interest.

$$p(y, x_{CL_2}, \theta_1, \theta_2) = x_{CL_2} + \frac{\sin\theta_2 - \sqrt{1 - \left[(y-1)\cos\theta_2 + y\cos\theta_1\right]^2}}{\cos\theta_1 + \cos\theta_2} \tag{5.21}$$

The first condition in Eq. 5.20 leads to a geometrical relation G_1 which x_{CL_1}, x_{CL_2}, θ_1 and θ_2 need to satisfy in order for the profile to be circular.

$$G_1(x_{CL_1}, x_{CL_2}, \theta_1, \theta_2) = \theta_1 - \theta_2 + 2\arctan(x_{CL_1} - x_{CL_2}) = 0 \tag{5.22}$$

This implies that $x_{CL_1} > x_{CL_2} \rightarrow \theta_1 < \theta_2$ and vice versa. The volume σ is externally controlled and is calculated by integrating the meniscus profile,

$$\sigma = \int_0^1 p(y, x_{CL_2}, \theta_1, \theta_2) dy. \tag{5.23}$$

The integral in Eq. 5.23 can be calculated analytically and leads to our second geometrical relation,

$$G_2(x_{CL_2}, \theta_1, \theta_2, \sigma) = x_{CL_2} + f_2(\theta_1, \theta_2) - \sigma = 0 \tag{5.24}$$

where

$$f_2(\theta_1, \theta_2) = \frac{\theta_1 + \theta_2 - \pi + 2\cos\theta_1\sin\theta_2 - \cos\theta_1\sin\theta_1 - \cos\theta_2\sin\theta_2 + \sin(2\theta_2)}{2\left(\cos\theta_1 + \cos\theta_2\right)^2}. \tag{5.25}$$

Note that when $\theta_1 = \theta_2$, we recover the case of the microchannel with identical walls (section 5.3.1).

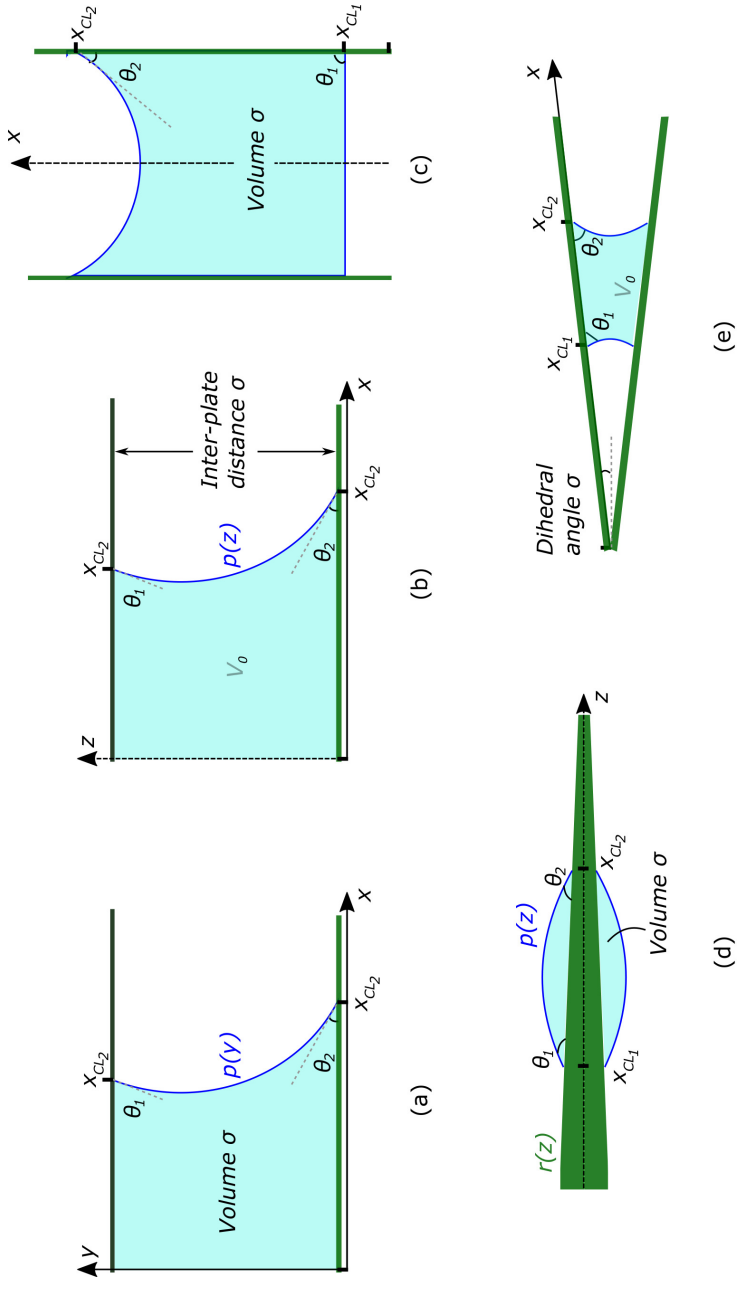

Figure 5.4: Sketches of configurations with two contact lines.(a): microchannel with non-identical walls (5.4.1); (b): stretching of a liquid bridge between non-identical plates (5.4.1); (c): liquid column in a capillary tube with two liquid-air interfaces (5.4.3); (d): drop between two non-parallel plates (as a model for the feeding mechanism of the Pharalope bird) (5.4.5); (e): a drop on a cone (as a model for the drop collection on the needles of certain species of desert plants) (5.4.4).

The two geometrical relations (5.22 and 5.24) contain four unknowns, i.e. x_{CL_1}, x_{CL_2}, θ_1 and θ_2. For given wall heterogeneities of the form of Eq. 5.2, the static problem is closed by capillary equilibrium at both contact lines (i.e. Eq. 5.4) and the dynamics can be studied by writing the Cox-Voinov relation (Eq. 5.5) for both contact lines, where at each time-step x_{CL_1} and x_{CL_2} are known and θ_1 and θ_2 are calculated by solving Eqs. 5.22 and 5.24.

5.4.1.1 Simultaneous jumps in opposite directions

A common feature of the systems with two contact lines considered in this section is that a jump performed by one contact line, is typically associated with a smaller jump in the opposite direction of the other contact line.

In this effect is visible in Fig. 5.5 for a microchannel where the upper wall is homogeneous and the lower wall heterogeneous.

The stick-slip motion on the heterogeneous lower wall (middle panel) is not very different from the stick-slip which occurs in the symmetrical microchannel case (chapters 2 and 4). The statics, calculated here, as well as for the symmetric case, with explicit formulas of x_{CL_2} and plotted in gray, is namely multi-valued for volume σ. And quasi-statically increasing σ necessitates jumps in x_{CL_2}.

Interestingly now, the heterogeneity of the lower wall also induces stick-slip and hysteresis on the homogeneous upper wall (upper panel of Fig. 5.5). The induced jumps here occur in the opposite direction. More specifically, when σ is increased (green), receding jumps occur, while if σ is decreased (red), advancing jumps occur.

These jumps on the homogeneous wall are not an effect caused by the dynamics, but already rooted in the statics. Their occurrence and starting and ending points are predicted by the gray curve. The limit points of the static curves where the jumps start, are both for x_{CL_1} and x_{CL_2} (upper and middle panel) at the same values of σ and correspond to $\frac{d\sigma(x_{CL_2})}{dx_{CL_2}} = 0$. Using Eq. 5.24, it can be shown that at such points $\frac{d\theta_{i_2}}{dx_{CL_2}} < 0$ (i.e. where the contact line on the heterogeneous wall encounters an increasing wettability in the advancing direction). The end points of the jumps are also determined by the statics as they occur at constant volume σ.

On the other hand, the path that the system takes *during* the jumps is not captured by the statics. A dynamic aspect visible in the representation of the bottom panel of Fig. 5.5 is that the jump on the heterogeneous wall in a good approximation precedes the jump on the homogeneous wall.

Dynamically, the jump on the homogeneous wall is induced by the jump on the heterogeneous wall trough volume conservation. During e.g. an advancing jump on the heterogeneous wall, the contact line is accelerated by the heterogeneity (decrease of θ_{i_2} as $\frac{d\theta_{i_2}}{dx_{CL_2}} < 0$). In order to satisfy volume conservation with increasing x_{CL_2} the system responds with an interplay between decreasing θ_2 (which decelerates the advancing jump) and decreasing θ_1 and x_{CL_1}. The interplay between the decreases of the two latter quantities is governed by the Cox-Voinov relation and manifests itself as a receding jump on the homogeneous substrate.

Fig. 5.6 illustrates the occurrence of the same phenomenon for the more complex case of a microchannel with two non-identical heterogeneous walls. The qualitative features of the jumps which are discussed for the above case of Fig. 5.5 are retained.

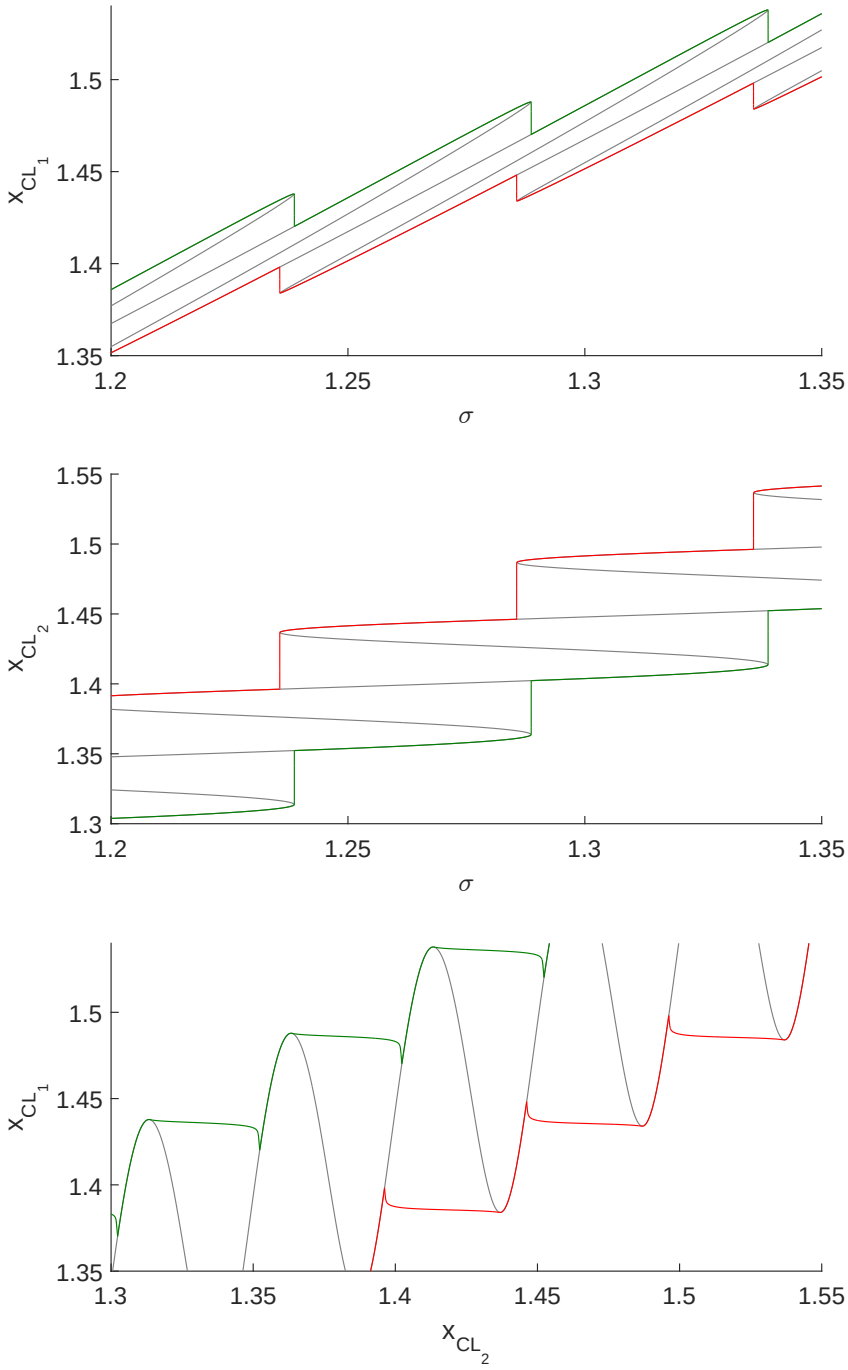

Figure 5.5: Stick-slip in microchannel with homogeneous upper wall (θ_{i_1} of 40 deg) and bottom wall sinusoidally heterogeneous (Eq. 5.3) with θ_A, θ_R and λ resp. 55 deg, 35 deg and 0.05. Gray: static; green and red: advancing and receding (Cox-Voinov with $|\dot{\sigma}| = 10^{-5}$)

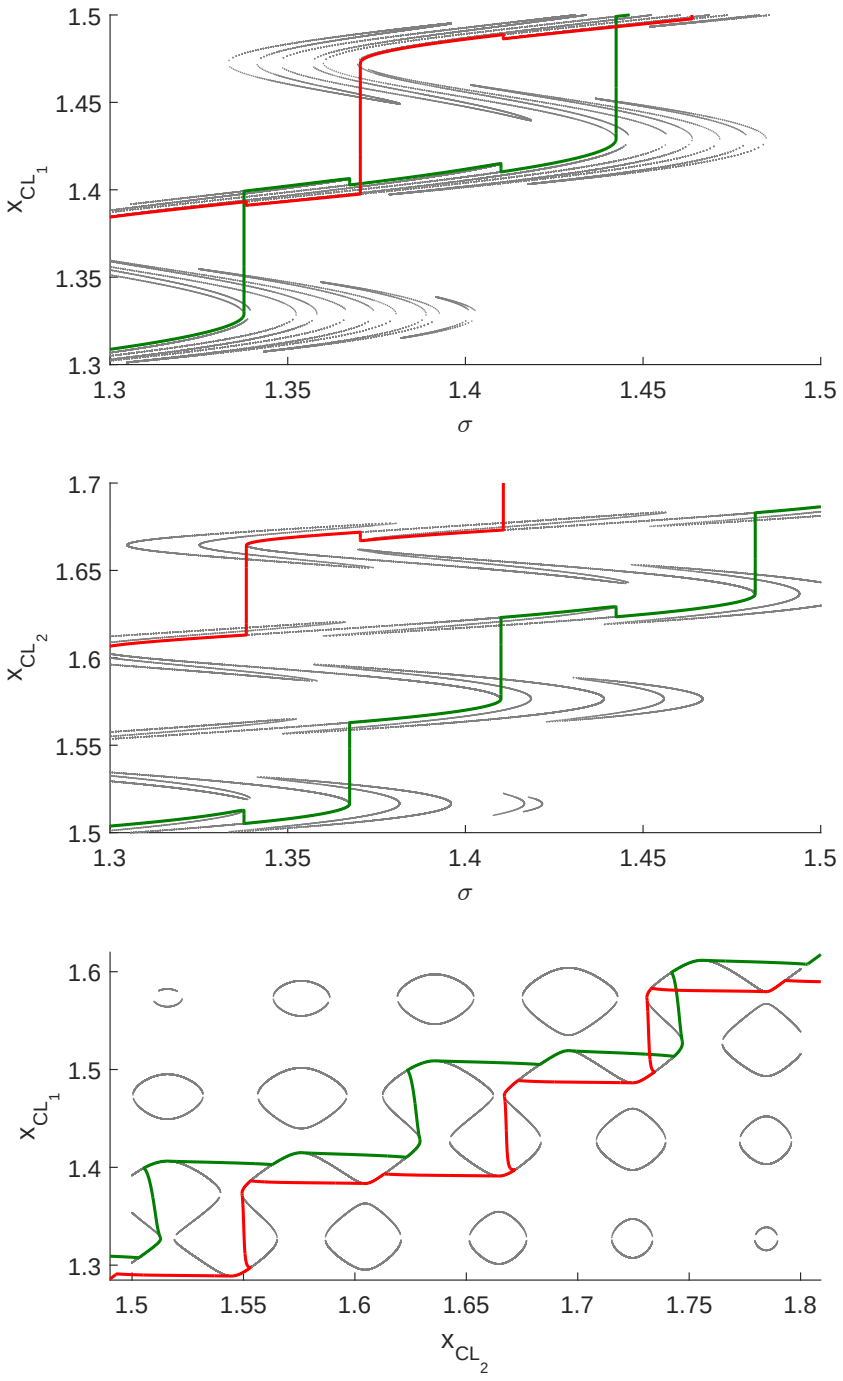

Figure 5.6: Stick-slip in microchannel with non-identical walls with θ_A, θ_R and λ resp. 75 deg, 45 deg and 0.1 for the upper wall, and 55 deg, 25 deg and 0.06 for the lower wall. Same color code as in Fig. 5.5 with the static solutions now gray dots.

5.4.2 Liquid bridge between non-identical plates

We consider the axisymmetric liquid bridge drawn in Fig. 5.4b. As in the previous microchannel example (section 5.4.1), the upper and lower walls are characterized by different wettability distributions. The meniscus profile $p(z)$, where z corresponds to the axis of axisymmetry, is given by the Young-Laplace equation [1],

$$\frac{1}{p\sqrt{1+p'(z)^2}} - \frac{p''(z)}{(1+p'(z))^{\frac{3}{2}}} = \frac{\Delta P}{\gamma}, \tag{5.26}$$

where primes denote derivation with respect to z and the right hand side of this second order ordinary differential equation is the (a priori unknown) value of the constant curvature of the liquid-gas interface. We consider the situation where the inter-plate distance σ is externally controlled and solve Eq. 5.26 with the boundary conditions

$$\begin{cases} p(z=\sigma) = x_{CL_1} \\ p(z=0) = x_{CL_2} \end{cases} \tag{5.27}$$

to obtain a profile $p(z, x_{CL_1}, x_{CL_2}, \frac{\Delta P}{\gamma}, \sigma)$, which thus depends additionally on the unknown curvature $\frac{\Delta P}{\gamma}$. Two geometrical relations are obtained by extracting the contact angles from this profile,

$$\begin{cases} G_1\left(x_{CL_1}, x_{CL_2}, \theta_1, \frac{\Delta P}{\gamma}, \sigma\right) = p'(z=\sigma) + \cot\theta_1 = 0 \\ G_2\left(x_{CL_1}, x_{CL_2}, \theta_2, \frac{\Delta P}{\gamma}, \sigma\right) = p'(z=0) - \cot\theta_2 = 0, \end{cases} \tag{5.28}$$

while the third one comes from assuming a constant liquid volume V_0.

$$G_3\left(_{CL_1}, x_{CL_2}, \frac{\Delta P}{\gamma}, \sigma\right) = \pi \int_0^\sigma p^2\left(z, x_{CL_1}, x_{CL_2}, \frac{\Delta P}{\gamma}, \sigma\right) dz - V_0 = 0 \tag{5.29}$$

The three geometrical relations (Eqs. 5.28 and 5.29) contain five unknowns, i.e. x_{CL_1}, x_{CL_2}, θ_1, θ_2 and $\frac{\Delta P}{\gamma}$. Therefore, as for the previous microchannel example (section 5.4.1), for given wall heterogeneities of the form of Eq. 5.2, the static problem is closed by capillary equilibrium at both contact lines (i.e. Eq. 5.4). The dynamics can be studied by writing the Cox-Voinov relation (Eq. 5.5) for both contact lines, where at each time-step x_{CL_1} and x_{CL_2} are known and θ_1 and θ_2 are calculated using Eq. 5.28 after solving Eq. 5.29.

5.4.3 Liquid column in a capillary tube with two liquid-air interfaces

In Fig. 5.4c, we now consider a variant of the liquid in a capillary tube problem (section 5.3.3), which now has a lower meniscus described by (x_{CL_1}, θ_1) and an upper meniscus described by (x_{CL_2}, θ_2). The inner wall of the tube is chemically heterogeneous but perfectly cylindrical with radius r_0.

The externally controlled parameter σ is the liquid volume (scaled with πr_0^3) and the first geometrical relation relies on the assumption that the meniscus has a spherical shape. Namely,

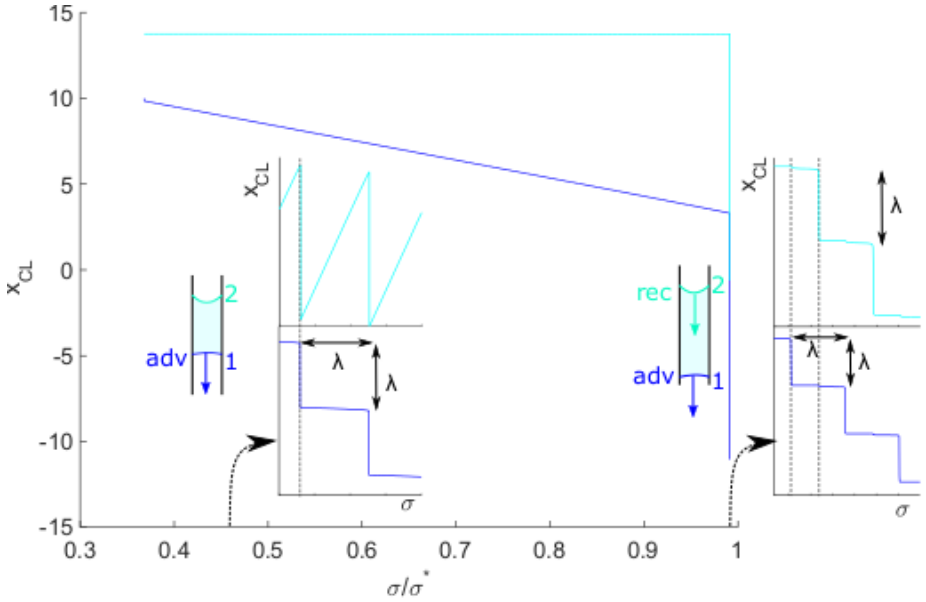

Figure 5.7: Dynamics of a water column growing in a capillary tube at a constant rate of 10^{-8}. The inner walls accommodate a sinusoidal heterogeneity, i.e. Eq. 5.3 with $\theta_A = 75$ deg, θ_R = 25 deg and $\lambda = 0.01$ mm. The insets show the color legend and zooms on the curves at the indicated volumes at the scale of the stick-slip.

$$G_1\left(x_{CL_1}, x_{CL_2}, \theta_1, \theta_2, \sigma\right) = x_{CL_2} - x_{CL_1} + g(\theta_1) + g(\theta_2) - \sigma = 0 \tag{5.30}$$

where and all lengths are scaled by r_0 and

$$g(\theta) = \frac{3\sin\theta - \sin^3\theta - 2}{3\cos^3\theta}. \tag{5.31}$$

The second geometrical relation relies on the vertical force balance,

$$G_2\left(\theta_1, \theta_2, \sigma\right) = \cos\theta_1 - \cos\theta_2 + \frac{\sigma}{2l_c^2} = 0, \tag{5.32}$$

where l_c is the capillary length (i.e. $\sqrt{\frac{\gamma}{\rho g}}$) scaled by r_0. Eq. 5.32 implies $\theta_1 > \theta_2$ with the difference between the angles increasing with the volume σ.

Equations (5.30 and 5.32) contain four unknowns, i.e. x_{CL_1}, x_{CL_2}, θ_1 and θ_2. For given wall heterogeneities of the form of Eq. 5.2, the static problem is closed by capillary equilibrium at both contact lines (i.e. Eq. 5.4) and the dynamics can be studied by writing the Cox-Voinov relation (Eq. 5.5) for both contact lines, where at each time-step x_{CL_1} and x_{CL_2} are known and θ_1 and θ_2 are calculated by solving Eqs. 5.30 and 5.32.

5.4.3.1 Falling of the liquid column

The ability of contact angle hysteresis to support the weight of a liquid column in this configuration is a classical example often used in pedagogical introductions to contact angle hysteresis. In this paragraph, we go deeper on this example and in particular show the emergence of a mechanism involving coupled stick-slip motions of both contact lines, by which the liquid column falls.

As classically known, for a liquid column to be trapped in a tube as drawn in Fig. 5.4c, the tube needs to have heterogeneous wetting properties. As gravity causes the lower contact angle θ_1 to be larger than the upper contact angle θ_2 (Eq. 5.32), they cannot be both equal to the constant equilibrium angle θ_i. In steady conditions, the liquid column will move downwards with at a constant dimensionless velocity $\theta_1^3 - \theta_i^3$, where θ_1 is given by solving a system of two equations in two unknowns, consisting of $2\theta_i^3 = \theta_1^3 - \theta_2^3$ and the force balance (Eq. 5.32). Volume conservation (Eq. 5.30) will give the length of such liquid column.

For a heterogeneous tube, the unbalanced Young's forces can support a liquid volume $\sigma*$ thanks to contact angle hysteresis, which can be calculated by equating $\theta_1 = \theta_A$ and $\theta_2 = \theta_R$ in Eq. 5.32, yielding

$$\sigma* = \frac{\cos\theta_R - \cos\theta_A}{2l_c^2}, \tag{5.33}$$

where θ_A and θ_R are respectively the highest and lowest intrinsic angle of the tube wall. Fig. 5.7 shows the contact line dynamics upon slowly increasing σ from a value well-below $\sigma*$. The liquid is inside a tube with a heterogeneity of a wavelength 100 times smaller than the tube radius.

In a first stage, the upper contact line remains pinned, while the bottom contact line advances in the downward direction. The imposed increase of volume tends to increase both contact angles (Eq. 5.30), while keeping $\theta_1 > \theta_2$ due to the force balance (Eq. 5.32). Therefore the bottom contact angle reaches the advancing angle first and advances.

At the scale of the heterogeneity (see inset), the lower contact line advances with jumps almost as long as the heterogeneity wavelength, which is a property of the macroscopic limit. These jumps are accompanied by (as discussed in example 5.4.1 small jumps of the upper contact line in the receding direction, i.e. downwards as well. In-between jumps, both contact lines are pinned. They very slowly advance at a rate proportional to the imposed volume increase and and to slope of the nearly horizontal shape of the static solutions. This pinned motion brings the upper contact line back to its original position, while being negligible on the scale at which the lower contact line moves.

After the imposed volume σ (almost) reaches its critical value σ^*, the liquid column falls downward at a rate much faster than the imposed rate of volume increase. At this volume, $\theta_1 \approx \theta_A$ and $\theta_2 \approx \theta_R$. At the small-scale the motion is intermittent. Now with advancing jumps of the lower contact line associated with small receding jumps of the upper contact line, and additionally receding jumps of the upper contact line associated with small advancing jumps of the lower contact line. All these jumps contribute to the downwards motion of the liquid column.

Fig. 5.8 shows the same process, but now with a heterogeneity wave-length comparable to the tube radius. Interestingly, the liquid column already falls at a volume σ of around $0.61\sigma^*$.

The lower panel of Fig. 5.8 sheds light on the falling mechanism.

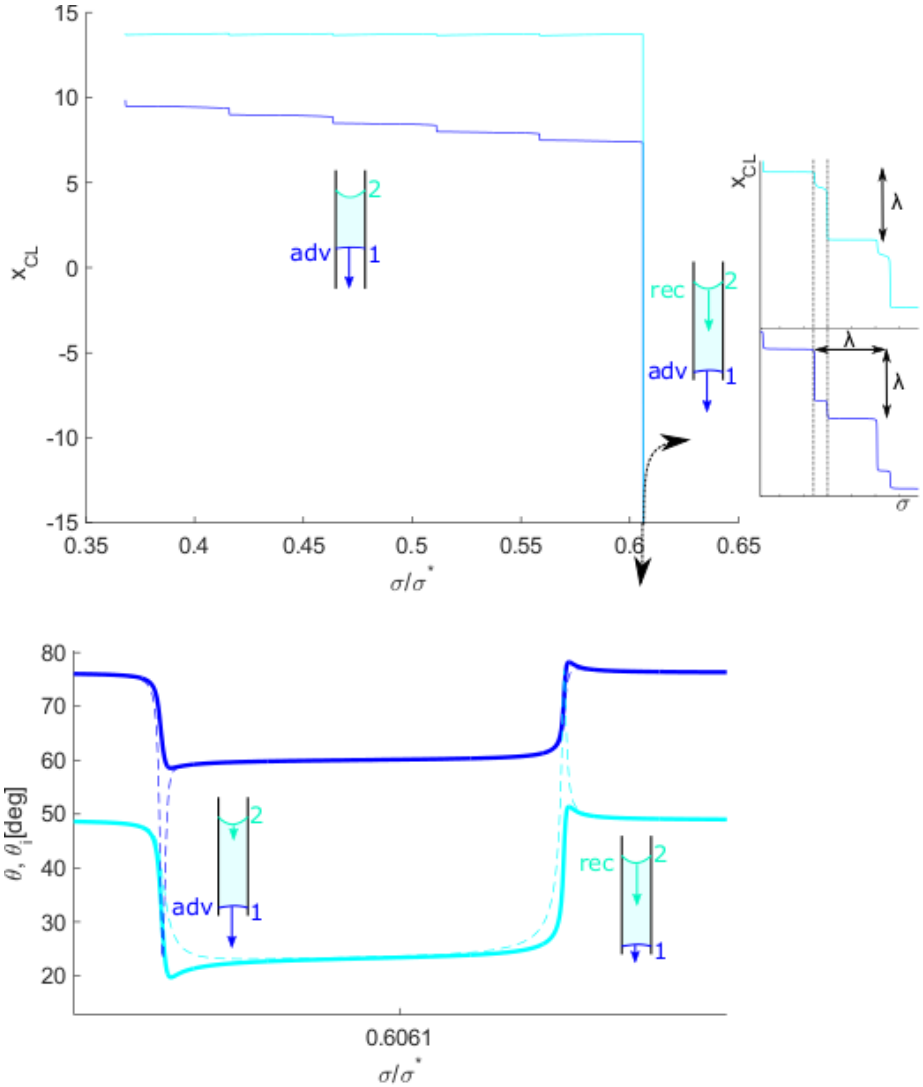

Figure 5.8: Same as Fig. 5.7 but with $\lambda = 0.5$. The lower panel shows the θ (thick lines) and θ_i (dashed lines) during the fall of the liquid column over one wavelength λ.

First, an advancing jump of the bottom contact line takes place, which is induced by the sharp decrease of the equilibrium angle θ_{i_1} (blue dashed line) in the Cox-Voinov relation. As due this advancing jump, x_{CL_2} has moved downwards at (nearly) constant volume σ, the geometry of the systems (as described by Eqs. 5.30 and 5.32) respond by a combination of decreasing θ_1 (which decelerates this advancing jump), directly linked to a decrease in θ_2. Thereby, θ_2 drops below its equilibrium value and the upper contact line recedes in a small jump.

Now, this small receding motion has brought the upper contact line to a position where the wettability of the tube will induce its receding jump. This receding jump of the upper contact line will in its turn induce a small advancing jump of the bottom contact line, moving the bottom contact line closer to a position where it can perform an advancing jump.

5.4.4 Drop around a cone - model for the drop collection on the needles of certain species of desert plants

We consider the axisymmetric configuration of drop around a conical fibre, as drawn in Fig. 5.4d. The fibre has a profile $r(z)$. The contact line on the side where the fibre is thicker is described by (x_{CL_1}, θ_1) and the contact line on the thinner side by (x_{CL_2}, θ_2). As in the previous liquid bridge example (section 5.4.2), the meniscus profile $p(z)$, where z corresponds to the axis of axisymmetry, is given by the Young-Laplace equation (Eq. 5.26).

We consider the situation where the liquid volume σ is externally controlled and solve Eq. 5.26 with the boundary conditions

$$\begin{cases} p(z = x_{CL_1}) = r(x_{CL_1}) \\ p(z = x_{CL_2}) = r(x_{CL_2}) \end{cases} \tag{5.34}$$

to obtain a profile $p(z, x_{CL_1}, x_{CL_2}, \frac{\Delta P}{\gamma})$. As for the liquid bridge problem (section 5.4.2), two geometrical relations are obtained by extracting the contact angles from this profile.

$$\begin{aligned} G_1\left(x_{CL_1}, x_{CL_2}, \theta_1, \frac{\Delta P}{\gamma}\right) = \\ \arctan\left(p'(z = x_{CL_1})\right) - \arctan\left(r'(z = x_{CL_1})\right) - \theta_1 = 0 \end{aligned} \tag{5.35}$$

$$\begin{aligned} G_2\left(x_{CL_1}, x_{CL_2}, \theta_2, \frac{\Delta P}{\gamma}\right) = \\ \arctan\left(p'(z = x_{CL_2})\right) - \arctan\left(r'(z = x_{CL_2})\right) + \theta_2 = 0 \end{aligned} \tag{5.36}$$

For a conical needle as drawn in Fig., the angle $-\arctan r'(z))$ is a positive constant. For this case, Eqs. 5.35 and 5.36 typically lead to $\theta_1 > \theta_2$.

The third geometrical relation is conservation of volume.

$$G_3\left(x_{CL_1}, x_{CL_2}, \frac{\Delta P}{\gamma}, \sigma\right) = \pi \int_{x_{CL_1}}^{x_{CL_2}} \left[p^2\left(z, x_{CL_1}, x_{CL_2}, \frac{\Delta P}{\gamma}\right) - r^2(z)\right] dz - \sigma = 0 \tag{5.37}$$

The three geometrical relations (Eqs. 5.35, 5.36 and 5.37) contain five unknowns, i.e. x_{CL_1}, x_{CL_2}, θ_1, θ_2 and $\frac{\Delta P}{\gamma}$. Therefore, as for the previous liquid bridge example (section 5.4.2), for a given cone heterogeneity of the form of Eq. 5.2, the static problem is closed by capillary equilibrium at both contact lines (i.e. Eq. 5.4). The dynamics can be studied by using the Cox-Voinov relation (Eq. 5.5, with now additionally a metrif factor) for both contact lines, where at each time-step x_{CL_1} and x_{CL_2} are known and θ_1 and θ_2 are calculated using Eqs. 5.35 and 5.36 after solving Eq. 5.37.

5.4.5 Drop between two non-parallel plates - model for the feeding mechanism of the Pharalope bird

In the last example, we consider the 2D problem of a drop sandwiched between two non-parallel plates which make an externally controlled angle α with one another (Fig. 5.4e). We denote $\sigma = \alpha/2$. The meniscus at the narrow end is described by (x_{CL_1}, θ_1) and the meniscus at the broad end described by (x_{CL_2}, θ_2). The plates are flat but chemically heterogeneous.

The first geometrical relation relies on the assumption that the menisci are circular, leading to

$$\begin{aligned} G_1\left(x_{CL_1}, x_{CL_2}, \theta_1, \theta_2, \sigma\right) &= 2\sin\sigma\cos\sigma\left(x_{CL_2}^2 - x_{CL_1}^2\right) \\ &+4\sin^2\sigma\left[x_{CL_1}^2 f\left(\theta_1 - \sigma\right) + x_{CL_2}^2 f\left(\theta_2 + \sigma\right)\right] - V_0 = 0, \end{aligned} \tag{5.38}$$

where,

$$f(\theta) = \frac{2\theta - \pi + \sin(2\theta)}{8\cos^2\theta} \tag{5.39}$$

is the same geometric factor as in the microchannel problem (section 5.3.1). The second geometrical relation relies on the force balance in the absence of gravity [46].

$$G_2\left(x_{CL_1}, x_{CL_2}, \theta_1, \theta_2, \sigma\right) = \cos\left(\theta_2 + \sigma\right) - \frac{x_{CL_2}}{x_{CL_1}}\cos\left(\theta_1 - \sigma\right) = 0 \tag{5.40}$$

Note that eq. 5.40 implies $\theta_1 > \theta_2$ with the difference between the two increasing with the ratio $\frac{x_{CL_2}}{x_{CL_1}}$ (e.g. for drops closer to the corner) and the angle between the plates.

Equations 5.38 and 5.40 contain four unknowns, i.e. x_{CL_1}, x_{CL_2}, θ_1 and θ_2. For given wall heterogeneities of the form of Eq. 5.2, the static problem is closed by capillary equilibrium at both contact lines (i.e. Eq. 5.4) and the dynamics can be studied by writing the Cox-Voinov relation (Eq. 5.5) for both contact lines, where at each time-step x_{CL_1} and x_{CL_2} are known and θ_1 and θ_2 are calculated by solving Eqs. 5.38 and 5.40.

5.4.5.1 Mandibular propulsion

The Phalarope shorebird feeds itself by transporting a drop - inside of which a prey is trapped - from its beak to its mouth by cyclically opening and closing its beak. Some of the important aspects of the mechanisms are elegantly studied in [22, 46].

Fig. 5.9 shows that the statics and dynamics of such transport contain features similar to the ones discussed previously for the microchannel (section 5.4.1) and capillary tube (section 5.4.3) examples.

The upper and middle panels correspond to a calculation of the dynamics where the beak motion is quasi-static. The beak half angle σ varies sinusoidally in time with a sufficiently long period, such that it the jumps of the contact lines happen at nearly constant beak angle.

The process starts with a static initial condition, which happens to be an unstable one, and a beak which is opening (red curve). The contact lines jump towards a stable branch of solutions (which seem to satisfy $\frac{dx_{CL_1}}{d\sigma} > 0$ and $\frac{dx_{CL_2}}{d\sigma} < 0$) and stays pinned there while the beak angle keeps increasing.

When the beak starts closing (green curves) mainly contact line 1 moves towards the mouth, while contact line 2 does not move too much. As in the previous examples, the stick and slip stages of the two contact lines are synchronized. In the stick stages while decreasing the beak angle σ, following the static solutions both contact angles increase. In those stages, contact line 1 advances towards the mouth, while contact line 2 advances away from the mouth. As $\theta_1 > \theta_2$, θ_1 reaches faster a spot on the beak where its angle equals the critical angle for an advancing jump of contact line 1 to occur. The advancing jump of contact line 1 is accompanied by a receding jump of contact line 2 (as discussed in 5.4.1 and 5.4.3). Both these jumps are in the direction towards the mouth. For contact line 1 this jump constitutes the main part of the mouthward motion, while for contact line 2, this jump compensates the motion that occurred in the direction away from the mouth.

Similarly, during closing of the beak (red curves) the opposite happens, with the outcome that contact line 2 recedes towards the mouth, while contact line 1 does not move too much. This process repeats for two more cycles of the beak, with a net mouth-ward motion of the drop in each half-cycle.

In the fourth cycle, the shape of the static solutions induce a different type of transport, where now both contact lines move towards the beak during the opening of the beak. At the end of the fourth beak closing, the contact lines have performed an additional jump, taking the system to another branch of static solutions, of which the left limit point is situated more on the left than the right limit point of the branch of static solutions on the right bottom of it.

Therefore, in the consequent opening of the beak, both contact lines perform a stick-slip motion, where the stick stages last for small ranges of σ and the slip stages are towards the mouth and take the system to a branch of static solutions which enables this process to repeat itself while the beak opens.

This example illustrates that in quasi-static conditions, the knowledge of the static solutions (gray) enables to have a precise control over the drop position, as well as a fast mouth-ward drop motion when desired, by simply choosing the path over which to vary the beak angle. In this example, if σ was decreased to 1 degree in the first cycle, the drop would already have traveled fast to the mouth during the consequent beak opening. Also, in the range of σ between 2 and 4 degrees, the system is always in a stick-stage, which could be avoided depending on the needs.

The bottom panel shows that additional control can be achieved trough dynamics.

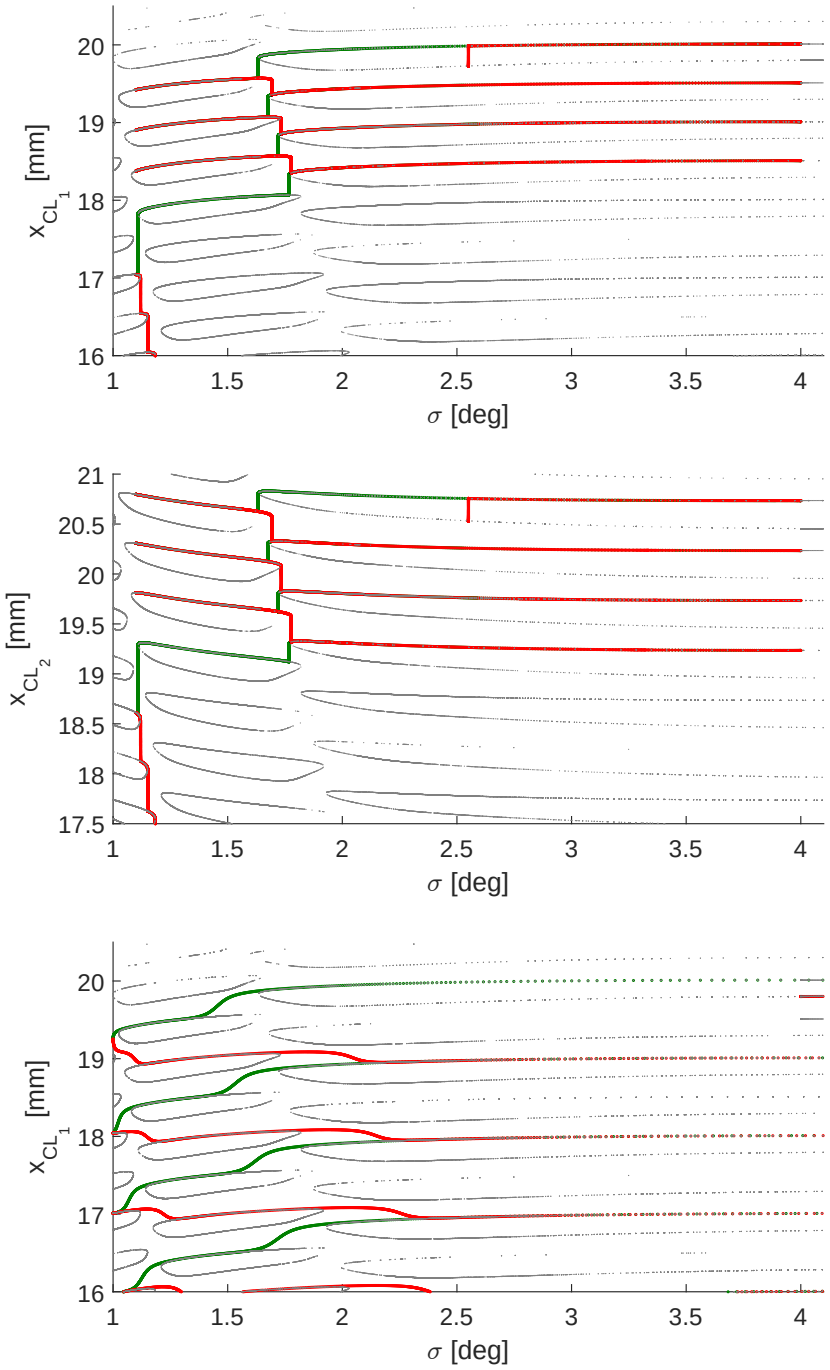

Figure 5.9: Mandibular propulsion (beak heterogeneity given by Eq. 5.3 with θ_A, θ_R and λ resp. 40 deg, 60 deg and 0.5 mm) of a 2mm ^{2} drop. Gray: static solutions. Green and red: solutions of dynamic calculation, while imposed σ is resp. decreasing and increasing. Two upper panels: $T = 100$s, lower panel: $T = 0.1$s.

The only difference with the upper panel is that here the imposed cyclic beak motion occurs faster, such in the time-scale of the contact line jumps, the beak half angle σ varies noticeably. Therefore the jumps do not appear vertical in the graph.

This enables to have control over the ending points of the jumps. For example, when the beak starts opening (red curve) while $x_{CL_1} \approx 18$ mm, the system first follows the same static solutions as in the upper panel. However now the subsequent jump ends in another branch of static solutions than the one that it ended in, in the upper panel.

The above example illustrates how this type of modelling can serve as a convenient design and optimization tool for a tweezer-like device, which offers a precise control over the drop position, yet without compromising the speed of transport. The control is inherent to the fact that the drop always stays immobile at constant beak angle thanks to contact angle hysteresis. Yet the transport can be fast as the drop motion primarily occurs as discrete and fast depinning events. Taking full advantage of both the slow stick and fast slip aspects of such system requires the design and optimization of the wall topography and the choice of the path $\sigma(t)$ to follow. Such optimization is possible with the model discussed in this section, which captures the (quasi-)statics of problem -where the behavior of interest is rooted- while remaining numerically cost-effective. As uncaptured in previous treatments of the problem which modelled hysteresis as a constant advancing and receding angle, here in the example discussed in Fig. 5.9 we show the existence of a qualitatively different trajectory, one with many depinning events and thus a faster drop transport.

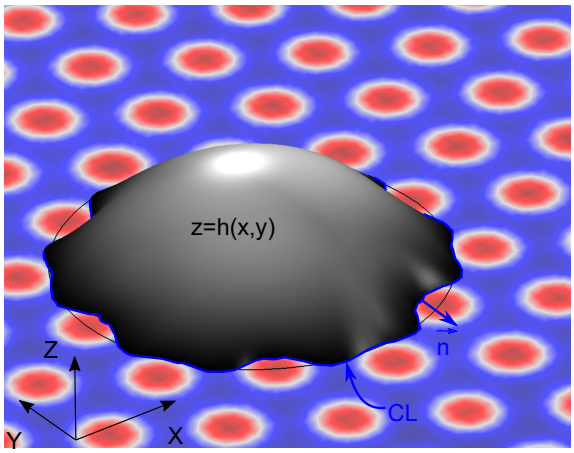

Figure 5.10: Definition of quantities on a figure of a drop on a hexagonal pattern, where red spots are hydrophobic and the blue matrix is hydrophilic. The z-scale is magnified 10 times to improve visibility.

5.5 Extension to the 3D case

5.5.1 Model formulation and solution method

Consider (Fig. 5.10) a drop on a chemically heterogeneous substrate of which the equilibrium wetting properties are described by an intrinsic angle distribution of the form

$$\theta_i(x,y) = \frac{\gamma_{sg}(x,y) - \gamma_{sl}(x,y}{\gamma}, \tag{5.41}$$

where γ_{sl}, γ_{sg} and γ are respectively the solid-liquid, solid-gas and liquid-gas interfacial tensions. The drop is described by a height profile $h(x,y)$ inside a domain D and enclosed by a closed curve CL (i.e. the contact line). The volume of this drop is given by

$$V = \iint_D h(x,y)\mathrm{d}x\mathrm{d}y = \sigma(t) \tag{5.42}$$

and considered to be an externally controlled parameter in this study. The liquid-gas interface area of the drop is given by,

$$A_{lg} = \iint_D \sqrt{h_x^2 + h_y^2 + 1}\mathrm{d}x\mathrm{d}y. \tag{5.43}$$

The free energy G of the drop can be calculated using the definition in Eq. 5.41 as

$$\begin{aligned} G &= \gamma A_{lg} - \gamma \iint_D \cos\theta_i(x,y)\mathrm{d}x\mathrm{d}y \\ &= \gamma \iint_D \left(\sqrt{h_x^2+h_y^2+1} - \cos\theta_i(x,y)\right)\mathrm{d}x\mathrm{d}y, \end{aligned} \tag{5.44}$$

where the first term describes the energy cost of accommodating a liquid-gas interface and the second term describes the energy gained by wetting a wettable area.

We treat the shape of the liquid-gas interface as quasi-steady at the time-scale of the contact-line motion. Under this condition, the liquid-gas interface has a constant curvature by which it sustains a uniform capillary pressure difference between the drop and the surrounding air, $(p_l - p_a)$, given by the Young-Laplace equation,

$$p_l - p_g = -\gamma \nabla \cdot \vec{n}_{lg}. \tag{5.45}$$

Here $\vec{n}_{lg}$ is the outward pointing unit normal on the liquid-gas interface $z = h(x,y)$ in Cartesian coordinates,

$$\vec{n_{lg}} = \frac{\nabla\left(z - h(x,y)\right)}{|\nabla\left(z-h(x,y)\right)|} = \frac{-h_x\vec{1}_x - h_y\vec{1}_y + \vec{1}_z}{\left(1+h_x^2+h_y^2\right)^{\frac{3}{2}}}, \tag{5.46}$$

in the notation of which we have followed the convention of denoting partial derivatives by subscripts, $\frac{\partial A}{\partial X} = A_X$, and the vectors $\vec{1}_X$ are unit vectors along the coordinate in the subscript. The right-hand side of Eq. 5.45 can be now explicited as,

$$-\gamma\nabla\cdot\vec{n_{lg}} = \gamma\frac{\left(1+h_x^2\right)h_{yy} + \left(1+h_y^2\right)h_{xx} - 2h_xh_yh_{xy}}{\left(1+h_x^2+h_y^2\right)^{\frac{3}{2}}}, \tag{5.47}$$

in the notation of which we have followed the convention $\frac{\partial A}{\partial X} = A_X$. We limit our treatment to the case of thin drops only (with h_x, h_y much smaller than one and thus also a small contact angle) and neglect higher order terms in Eq. 5.47, leading to the result that the Laplace pressure is simply given by the surface tension times the Laplacian of h.

$$\nabla\cdot\vec{n_{lg}} \approx -h_{xx} - h_{yy} = -\Delta h(x,y). \tag{5.48}$$

Combining Eqs. 5.45 and 5.48, we obtain,

$$\Delta h(x,y) = C, \tag{5.49}$$

where $C = \frac{p_g - p_l}{\gamma}$ is an unknown constant in our problem, to be varied in order to satisfy the volume condition (Eq. 5.42).

The merit of the approximation of small slopes (also known as the lubrication approximation) here is that C can be determined directly by imposing a volume σ as both Eqs. 5.42 and 5.49 are linear in h. More specifically, to have a static interface shape enclosing a volume σ, we solve

$$\Delta u(x,y) = -1, \tag{5.50}$$

with the boundary condition that the height vanishes at the contact line,

$$u(x,y)|_{CL} = 0. \tag{5.51}$$

Then the sought height profile $h(x,y)$ is given by

$$h(x,y) = u(x,y)\frac{\sigma(t)}{\iint\limits_D u(x,y)\mathrm{d}x\mathrm{d}y} \tag{5.52}$$

such that $h(x,y)$ has the right volume (Eq. 5.42), a constant Laplacian (Eq. 5.50) and a zero height at the contact line (Eq. 5.51).

The contact angle θ across the contact line is then extracted from the calculated profile using,

$$\theta = -\arctan\left(\nabla h \cdot \vec{n}\right) = -\arctan\left(h_x n_x + h_y n_y\right), \tag{5.53}$$

where $\vec{n}$ is the outward unit normal on the contact line (as drawn in Fig. 5.10) with components (n_x, n_y). The distribution of contact angles is then used to calculate the normal velocity of the contact line trough the Cox-Voinov relation where the microscopic angle is identified with the local equilibrium angle $\theta_i(x,y)$ (c.f. chapter 4), which in dimensionless form reads,

$$\vec{v}_{CL} \cdot \vec{n} = \theta^3 - \theta_i^3(x,y), \tag{5.54}$$

where $\vec{v}_{CL}$ is the dimensionless contact line velocity.

This calculation is implemented in the commercial finite-element based simulation software COMSOL Multiphysics[153]. Eq. 5.50 is implemented trough the PDE interface and Eq. 5.54 makes the boundaries of the computational domain move in time trough the inbuilt Langrangian-Eulerian (ALE) method in the Moving Mesh interface.

More specifically Eq. 5.54 gives the normal velocity of the mesh nodes at the edge of the calculation domain, which are connected by quartic curves to form the contact line. At each time-step, the internal mesh nodes of the previous time-step are conformed with the changed boundary (i.e. contact line) trough *Laplacian smoothing*, where mesh points in the deforming frame (x,y) are obtained by solving the Laplace equation

$$x_{XX} + y_{YY} = 0, \tag{5.55}$$

where the X and Y are the coordinates of the (Eulerian) reference frame. An important limitation of this method is that the connectivity of the mesh remains unchanged during the mesh deformations, prohibiting e.g. simulations of the splitting of drops.

5.5.1.1 A static interface shape: an axisymmetric parabolic drop

A trivial and axisymmetric solution of Eq. 5.49, which we use as an initial condition in section 5.5.2 is of the form

$$h(r) = ar^2 + b, \tag{5.56}$$

where $r = \sqrt{x^2 + y^2}$. The constants a and b are determined by specifying a contact angle θ and a contact radius R, leading to

$$h(r) = \frac{R\tan\theta}{2}\left(1 - \left(\frac{r}{R}\right)^2\right). \tag{5.57}$$

The volume of this drop is calculated by shell integration,

$$V(R,\theta) = 2\pi\int_0^R rh(r)\mathrm{d}r = \frac{\pi R^3}{4}\tan\theta. \tag{5.58}$$

Note that this volume diverges for $\theta \to \frac{\pi}{2}$, which is an angle outside of the applicability domain of our approach. The same is true for the liquid-gas interface area of this drop, which is given by

$$A_{lg}(R,\theta) = 2\pi\int_0^R \sqrt{1+h_r^2}r\mathrm{d}r = \frac{2\pi R^2}{3}\left(\frac{1}{\sin^2\theta\cos\theta} - \cot^2\theta\right). \tag{5.59}$$

The dimensionless free energy of the drop is given by

$$F(r,\theta) = A_{lg}(R,\theta) - 2\pi\int_0^R \cos\theta_i(r)r\mathrm{d}r. \tag{5.60}$$

Minimizing this free energy with the constraint of a fixed volume (Eq. 5.58) now yields the condition,

$$\begin{aligned}\cos\theta_i(R) = \frac{1}{3}\left(\frac{8\cos\theta}{1+\cos\theta} - \frac{1}{\cos\theta}\right) &= 1 - \frac{\theta^2}{2} - O\left(\theta^4\right)\\ &= \cos\theta + O\left(\theta^4\right).\end{aligned} \tag{5.61}$$

This leads to the conclusion that in the applicability domain of our approach, the free energy at fixed volume still has its extrema given by Young's formula (see definition of θ_i in Eq. 5.41), which is a natural prerequisite of the analysis of the next section.

5.5.2 Test cases

5.5.2.1 Spreading on a perfect wetting substrate- Tanner's law

The first and most basic case against which we can test our model is that of a parabolic drop which is placed on a perfectly wetting substrate. For this case, the simulated equations have an analytical solution, which the numerical result should converge to.

Namely, using the Cox-Voinov relation (Eq. 5.54), the increase of the radius R is given by,

$$\frac{dR}{dt} = \theta^3. \tag{5.62}$$

The drop has a small contact angle θ, and a constant volume V_0. Therefore, using Eq. 5.58, we find that $\theta \approx \frac{4V_0}{\pi R^3}$. We can hence rewrite Eq. 5.62 as

$$R^9 dR = \left(\frac{4V_0}{\pi}\right)^3 dt. \tag{5.63}$$

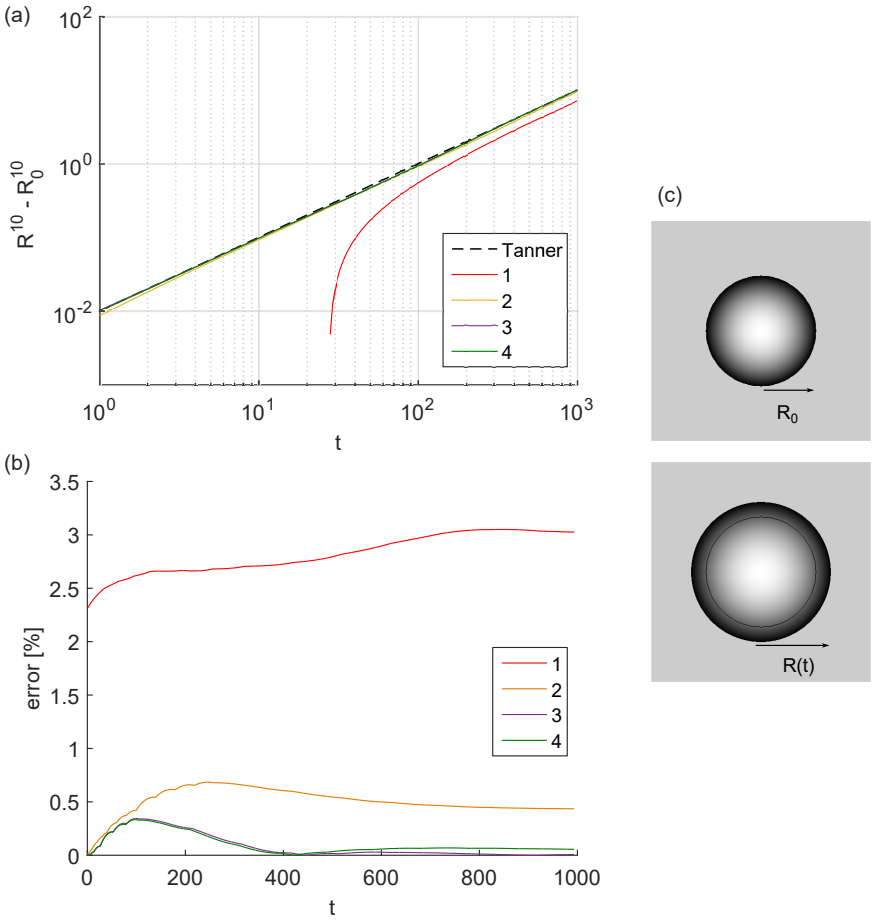

Figure 5.11: Spreading of a drop with constant volume. (a): Testing of Tanner′ law (Eq. 5.64) for four different element orders (in legend). (b) absolute error in percentage, based on the instantaneous difference between $R(t)$ and Eq. 5.64. (c): Two snapshots of the spreading process.

Integrating both sides starting from an initial radius R_0 gives Tanner′s law,

$$R = \left(R_0^{10} + 10 \left(\frac{4V_0}{\pi} \right)^3 t \right)^{\frac{1}{10}} \propto t^{\frac{1}{10}} \tag{5.64}$$

In Fig. 5.11 we compare this prediction to the model results. The initial condition is a parabolic drop (Eq. 5.57) with an initial dimensionless radius of 1 and an initial angle of 0.1 and the volume corresponding to this initial condition is kept constant during the simulation. The calculation domain consists of 40 domain elements and 12 boundary elements.

In panels (a) and (b) we compare the cases of four different element orders, from linear to quartic elements. The results of this calculation do not depend on the element order starting from element order 3 (cubic elements).

We note however that these parameters of the numerical configuration only correspond to a coarse limit of the discretization which enable to achieve convergence for a homogeneous substrate. In general, the discretization for the heterogeneous cases will, obviously, depend on the particular heterogeneity.

5.5.2.2 Axisymmetric substrate - Stick-slip rooted in statics

In this section, we test our method against the case of a drop with increasing/decreasing volume, initially centered on an axisymmetric substrate with a sinusoidal wettability pattern given by,

$$\theta_i(x, y) = 0.1 + 0.01 \cos \left(\frac{2\pi \sqrt{x^2 + y^2}}{0.1} \right). \tag{5.65}$$

Because for this heterogeneity, all the axisymmetric static solutions can be calculated by varying the radius R, using Eq. 5.58, together with the capillary equilibrium condition, for example as $\theta = \theta_i(R, 0)$.

This statics calculation gives the black curves in panels (a) and (b) of Fig. 5.12. They are multi-valued of some ranges of V. It is known that in the static limit (c.f. chapters 2 and 3) the branch of solutions that the system will follow in these ranges, will depend on the sign of the variation of V, with jumps occurring at the limit points of the black curves for both signs. If the variation of V occurs at a finite rate (c.f. chapter 4), the hysteresis loop magnifies for increasing values of this rate.

The green curves in panels (a) and (b) correspond to the advancing case. We start this simulation with a parabolic drop which has a dimensionless radius of 1 and a contact angle equal to the equilibrium angle at this position, i.e. 0.11. We increase the drop volume at a dimensionless rate $V_t = 10^{-5}$ (scaled with $\frac{R_0^2 \gamma}{9\mu \ln(l)}$), which in dimensional form corresponds to the order of μl/min for a millimetric water drop. This steady volume increase results in a stick-slip motion of the drop during which it stays axisymmetric and follows the black curves. This increase of volume is stopped when a volume equal to thrice the initial volume is reached, corresponding to the drop denoted with the letter B in panel (c).

From this point on, the sign of the volume variation is reversed, resulting again in a statics-rooted stick-slip motion (red curves) until the drop named A is reached.

We conclude that the method is able to recover the statics-induced stick-slip on axisymmetric substrates. This test case can thus serve as a common point between the results of well-understood axisymmetric models and this three-dimensional model,

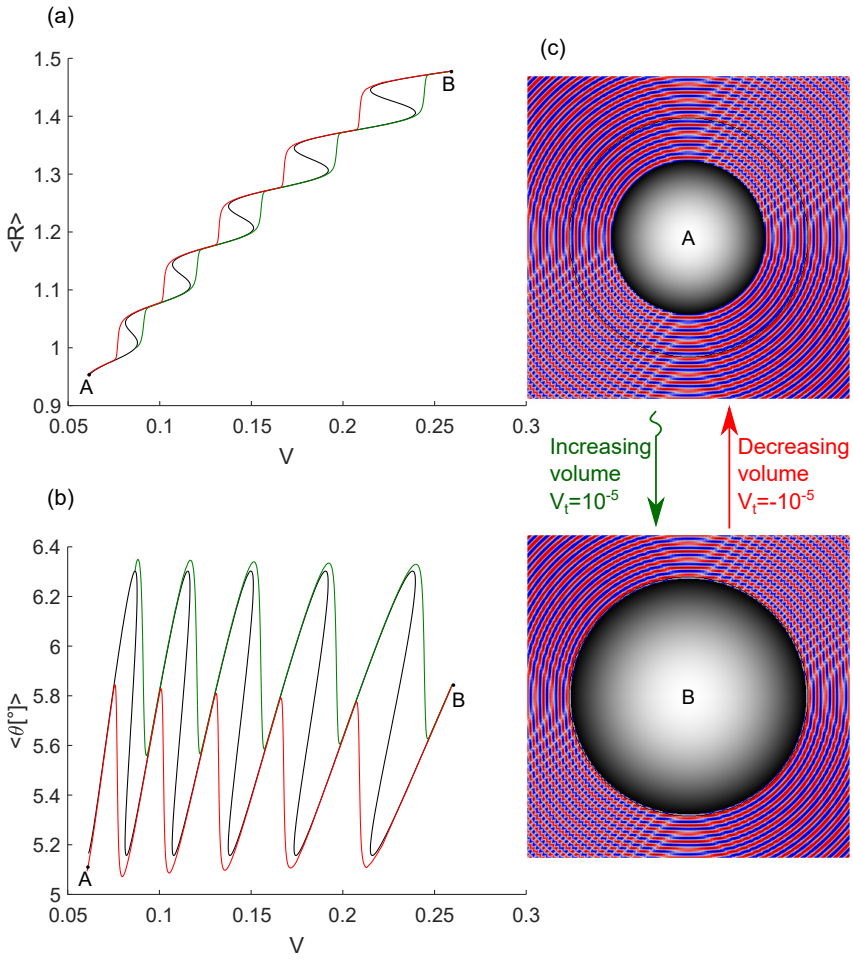

Figure 5.12: Drop on an axisymmetric substrate. (a): Average radius as a function of the volume, where black line are the static solutions calculated by varying R. (b) Contact angle as a function of the volume. (c): The initial and final state (for the receding case).

enabling to study how the results obtained with the former are modified by 3D effects when e.g. the axisymmetry of the wettability pattern is broken, step by step and starting from an understood reference case.

5.5.2.3 Drop on substrate with defects

In this last test case, we place a drop with constant volume on a heterogeneous substrate and simulate its dynamics of moving towards a more favorable spot on this substrate.

The substrate wettability $\theta_i(x, y)$ is an arbitrary one which consists of a hexagonal pattern on which Gaussian-shaped defects are superimposed with randomly selected parameters. The resulting distribution is shown in the color code of panel (a) in Fig. 5.13. The maximal intrinsic angle is 3.7 deg (blue) and the minimal intrinsic angle is 6.8 deg (red).

The black closed curves in panel (a) are the contact line shapes at different time-snaps corresponding to dimensionless times 0, 200, 400, 800, 1600 and 10000, where the time-scale is of the order of ms for a millimetric water drop. The initial and final drop profiles are shown in panel (b). The contact line deformations here are weak compared to the case shown in Fig. 5.10 where the minimal and maximal values of θ_i where 0.5 deg and 9.5 deg.

Initially a parabolic drop with $\theta = 0.09$ is placed on a rather hydrophobic location. The parts of the contact line which touch spots with high intrinsic angles (red) recede, while the parts of the contact line which touch blue, advance. This makes the drop initially move south-west and then further south reaching a final location where the wettability gradients normal to the contact line are in the direction of increasing θ_i. More specifically, from this final location, if a part of the contact line would advance, it would encounter increasing values of θ_i and be prone to recede back to its original location and vice versa.

Panel (c) shows the interplay between the two terms of the free energy (Eq. 5.44) in this process. During its journey, the drop mainly converts energy stored in its wetted area G_{sl} (orange curve) to energy stored its liquid-gas interface (blue curve) and vice versa. Namely, the decreases of one curve correspond to increases of the other curve. However the sum of the two curves is not constant.

This aspect is shown in panel (d). The free energy G, which is the sum of the aforementioned terms monotonously decreases during the process. This means that during each of the energy conversions, a fraction of the energy is dissipated. The net balance at the end of the process is that the energy decrease achieved by contacting a more hydrophilic part of the substrate is higher than the energy increase due to the now higher liquid-gas interfacial area.

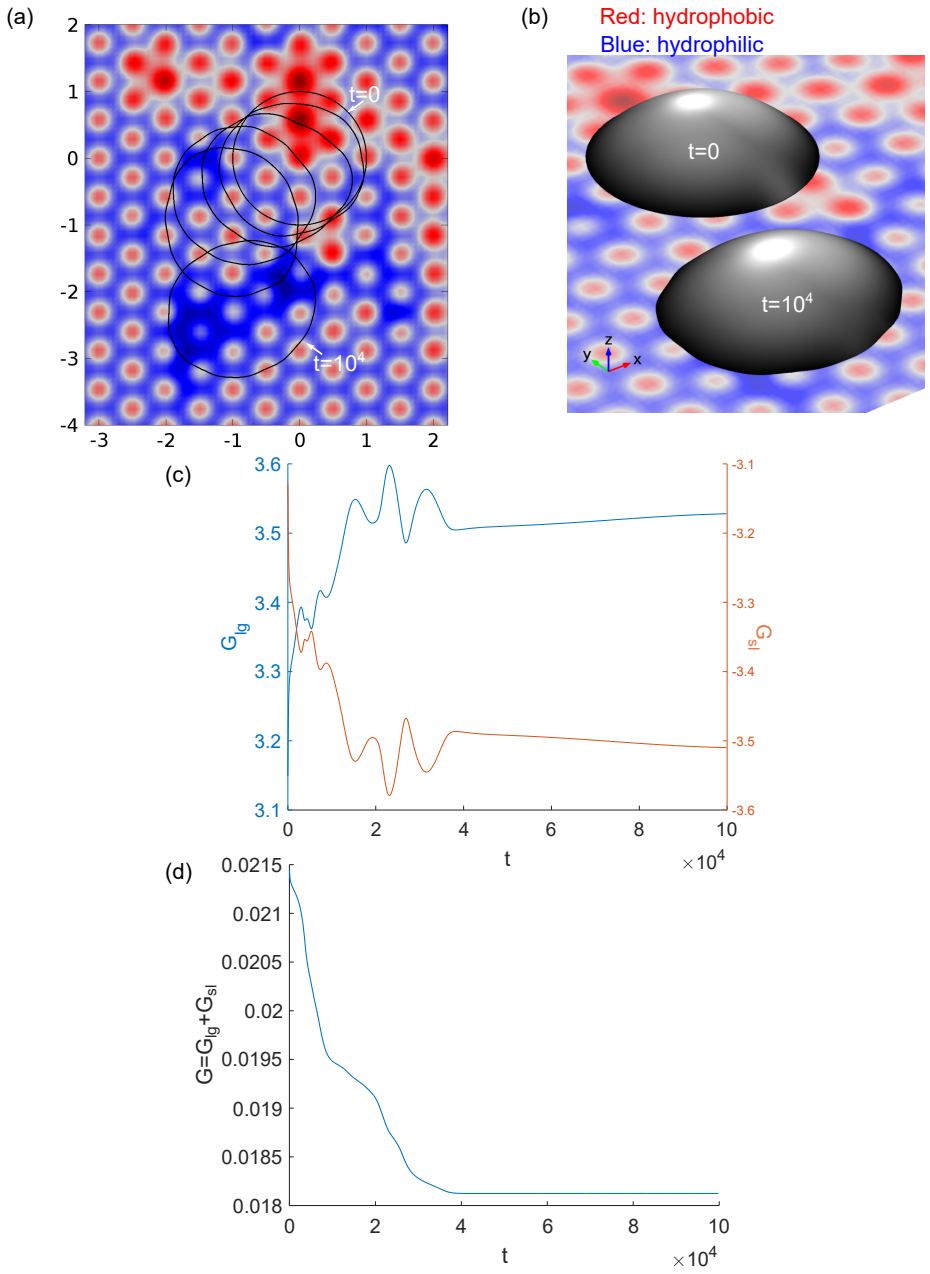

Figure 5.13: Drop on a heterogeneous substrate. (a): Snapshots of the contact line shapes (see text for times) on heterogeneous substrate. (b) 3D image of the initial and final states, where the scale along the z-axis is magnified 10 times to enhance visibility. (c): Two terms of the free energy (Eq. 5.44) scaled with γR_0^2, blue: first term, orange: second term. The time is scaled with $\frac{9\mu R_0 \ln(l)}{\gamma}$. (d) Free energy scaled with γR_0^2.

5.6 Concluding remarks

The modelling framework has been extended to treat the statics and quasi-steady interface shape dynamics in a large variety of 2D and axisymmetric wetting configurations. For most configurations the framework provides models which capture the essence of stick-slip in relatively understandable and numerically not very demanding way.

In each configuration, heterogeneous wetting properties lead to the stick-slip and hysteresis when a parameter σ (such as the volume) is externally varied. The qualitative features of these phenomena depend on the geometry of the configuration, described by the same amount of functions as there are contact lines.

The cases previously treated in this framework have provided a basis to interpret and understand the results of the configurations previously untreated. For example, heterogeneities with wavelengths much smaller than the typical length-scale of the configuration bring forth a limit case of hysteresis. In such macroscopic limit, stick-slip is macroscopically unobservable, and the static advancing/receding angle is equal to the maximum/minimum of the intrinsic angle distribution of the substrate.

But also previously undescribed features have been predicted. For example, in systems which can be idealized to be described by two contact lines connected via volume conservation and a force balance, the contact lines typically display simultaneous jumps. These simultaneous jumps are rooted in the statics, even if one of the contact lines is on a homogeneous substrate.

In particular, the framework yields promising prospects in the understanding of two mechanisms involving contact angle hysteresis utilized by living beings, which recently have started to inspire engineering applications. Namely, the water collection mechanism present in the needles of certain species of desert plants and the feeding mechanism of a certain species of shorebirds.

The description of the contact line dynamics with a quasi-steady liquid-gas interface shape is also generalized to treat the case of drops on substrates which are disordered in two directions. The calculation is implemented in the commercial simulation software COMSOL Multiphysics and least numerically demanding for drops with low contact angles on substrate with not too strong gradients.

The model was tested against three cases corresponding to these conditions.

A drop of constant volume placed on a substrate which it perfectly wets, spreads with a radius R which increases in time as $R \propto t^{\frac{1}{10}}$, and thus follows Tanner′s law. For this case, the numerical result converges towards the analytical one if the order of the finite elements is chosen higher than 3 (cubic elements).

If the drop of constant volume is placed on a substrate with a chemical heterogeneity with a length-scale comparable to the drop radius, the wettability gradient will induce a motion of the drop and bring it to a more wettable spot. During this motion, a back and forth energy conversion with losses happens between the liquid-gas interface and the wetted area, while the total free energy monotonously decreases.

When the volume of a drop on an axisymmetric substrate is increased/decreased, the drop undergoes stick-slip and hysteresis. This behavior is rooted in shape of the static solutions, which for this case can be calculated using explicit formulas. This case connects the studies performed in the previous chapters to a 3D equivalent, where the contact line is allowed to deform.

Chapter 6

General Conclusions and perspectives

Table 6.1 presents an overview of the configurations modelled in this work and serves as a basis to summarize the main results.

Even though the static contact angle on heterogeneous substrates is determined by the contact line position, the latter quantity is not well-suited for external control and hysteresis arises upon externally controlling a macroscopically accessible parameter (as the ones given in the 5th column of table 6.1). This parameter is typically a volume or an immersion height. The qualitative aspects of hysteresis do depend on the nature of this parameter.

- This dependency is illustrated by comparing configurations (a) and (b), where for the same geometry and same heterogeneity, the stability of a contact line equilibrium, given by Young's law, depends on whether the piston position (which is equivalent to the volume in the description in chapter 2) or the force on the piston is externally fixed. The corresponding dynamical studies have shown that close the static limit, the two setups also lead to different scaling laws between the contact angle and velocity.

- Similarly, configurations (e) and (f) can start from the same initial condition, which is a drop at a constant volume on a heterogeneous substrate. If the volume is increased, the classically known stick-slip motion will take place, where in stick-stages the angle increases and in slip-stages the contact radius increases. If on the other hand a voltage is applied, a different stick-slip motion will occur where during stick-stages both quantities stay constant, and in slip-stages, the contact radius increases and the angle decreases, showing larger contact angles during advancing motion than during receding motion.

- The existence of multiple quantities suited for external control and the qualitatively different response of the system to some of them may provide extra possibilities for e.g. prospective applications of precise and programmable manipulation of small volumes of liquids on substrates with known topography. A complete bifurcation diagram with multiple independent variables will show more possibilities of paths rather than only an advancing or receding path as studied in this work.

	Interface	Section(s)	Configuration	External control	# contact points
a	Circular	Chapters 2 and 4; 5.3.1	Meniscus inside microchannel with identical walls	Volume, piston position	1
b		Chapter 4	Meniscus inside microchannel with identical walls	Force on piston	1
c		5.4.1	Meniscus inside microchannel with different walls	Volume	2
d		5.4.5	Meniscus inside planar wedge	Beak angle	2
e	Spherical	1.4.6, 5.3.4	Drop	Volume	1
f		5.3.4.2	Electrowetting of a drop	Voltage	1
g		5.3.3	Liquid column in capillary tube	Volume	1
h		5.4.3	Liquid column in capillary tube	Volume	2
i	Axisymmetric	Chapter 3; 4.4.2, 5.3.2	Meniscus around fibre	immersion height	1
j		5.4.4	Barrel-shaped drop on a conical fibre	Volume	2
k		5.4.2	Liquid bridge between two plates	Interplate distance	2
l	Almost flat	5.5	Thin drop	Volume	$\to \infty$

Table 6.1: Overview of modelled configurations where hysteresis and stick slip result from externally controlling a parameter.

In configurations with a single contact point, the ratio of the typical scale of the heterogeneity to the typical system size is of key importance for many features of the induced hysteresis at the static limit.

- If the heterogeneity wavelength comparatively large, gradients of wettability (or topography) will be smaller than a threshold value below which no hysteretical effects are induced. A threshold is present for deformed contact lines [72] and is explicitly discussed in this work for configurations with a single contact point (a), (g) and (i). For configuration (e) the fact that the interface size increases with the experimentally controlled parameter (the volume) no threshold exists in the same sense as for the configurations mentioned in the previous sentence, although the qualitative features of the sub-threshold regime are present for small drop volumes.

- Systems which are just above this threshold, show the most pronounced stick-slip motion. In this regime, the closeness to the threshold explains the scaling laws between the main characteristics of the stick-slip and hysteresis. It leads to a quadratic scaling between defect amplitude and hysteresis amplitude, as shown for configuration (a), and to a quartic scaling between the jump length and dissipated energy, as shown for configuration (i).

- In the regime described in the above point, the predictions of the model for configuration (i), were successfully compared to tensiometric experiments on 3D-printed wavy fibres, at the level of individual topography-induced stick-slip motion.

- Very small heterogeneity wavelengths lead to a limit situation, persisting in all the configurations given in table 6.1 (also including configurations with multiple contact points). In such macroscopic limit, stick-slip occurs at the scale of the heterogeneity (over a whole wavelength for sinusoidal heterogeneities), and contact lines advance only with an angle corresponding to the maxima of the statically allowed values, and recede only with the minimum statically allowed angle. Therefore, in this limit, the scaling between the heterogeneity amplitude and hysteresis amplitude is linear instead of quadratic, as explained for configuration (a).

This last point justifies the incorporation of contact angle hysteresis into models by prescribing an advancing and a receding angle for many practical cases where no stick-slip is observable. However such approach can only give quantitative results at the static limit as the stick-slip at the unobservable scale does modify scaling relations between the angle and the velocity compared to the relations on homogeneous substrates.

- The different scaling laws which apply in the presence of heterogeneities, previously predicted by [85], were recovered here with quasi-static meniscus simulations for configurations (a), (b), (i) and a variant of (i) where the vertical force on the fibre is externally controlled. The Cox-Voinov relation and the molecular-kinetic theory have led to the same scaling laws.

- The scaling exponent near the static limit depends furthermore on the nature of the externally controlled parameter and has different values for configurations (a) and (b). Far from the static limit, the intermittency of the contact line motion

fades away, and the scaling exponent of configuration (a) tends toward that of (b). For smaller heterogeneity wavelengths, this collapse of (a) with (b) happens at lower velocities.

- The fact that these scaling laws are also predicted for configuration (i), brings them in the reach of experiments on AFM tips.

The minimalistic modelling approach can be extended to treat configurations with n contact points, with a system of equations (which are the boundary conditions of the Young-Laplace law or, more conveniently, its closed form solutions) which link the contact angles, contact line positions and the externally controlled parameter of interest, to be closed with n equations which are either Young's law for each contact point (statics), or a quasi-static mobility law such as the Cox-Voinov relation for each contact point (quasi-steady dynamics). With this approach, we have studied several systems with two contact points. We have also provided an extension of the minimalistic approach to treat the problem of substrates disordered in two directions.

- In all configurations with two contact points, (c), (d), (h), (j) and (k), the stick- and slip-stages at both contact lines are synchronized and jumps occur simultaneously. The jumps of one contact line in the advancing/receding direction are accompanied by jumps of the other contact line in the receding/advancing direction, with both jumps rooted in the static solutions. This feature is even present for menisci inside channels (c), where one of the walls is homogeneous.

- In configurations (c) and (k), the advancing displacement of one contact point, when accompanied by a receding displacement of the other contact line increases the liquid-gas interface area and therefore the free energy of the system. On the other hand, in configurations (d) and (h), such simultaneous jumps result in the displacement of the drop as a whole, to a position which is energetically more favorable, as it decreases the liquid-gas interface area (d), or the gravitational potential energy (h). In both latter cases, in the appropriate conditions a cascade of such simultaneous jumps is predicted, resulting in a fast motion of the drop as a whole.

- A better understanding of the mechanism above can potentially help shedding more light on the feeding mechanism of shore-birds (d), and possibly also the fog-collection mechanism of cactus plants (k), both of which are inspiring engineering applications. The modelling approach presented here furthermore enables to construct bifurcation diagrams of the mandibular propulsion mechanism (d), at least if the beak topography is known. This bifurcation diagram also recovers the known features of the mechanism and can enable to identify optimal paths of opening-closing characteristics.

- The formulation is extended to minimalistically treat cases where the contact line can deform and the heterogeneity is two-dimensional. This model recovers much of the essential physics related to response of contact lines to heterogeneities in the quasi-steady interface shape limit, such as Tanner's law on perfectly wetting substrates, statics-rooted stick-slip on axisymmetric heterogeneities and wettability-gradient induced contact line motion on disordered substrates. The model therefore permits for example to study deviations from configuration (e) when the contact line is allowed to deform, and to tackle generic problems of contact lines on disordered substrates in a minimalistic way.

REFERENCES

[1] P. G. de Gennes, F. Brochard-Wyart, and D. Quéré. *Capillarity and wetting phenomena: Drops, bubbles, Pearls, Waves*. Springer, 2004.

[2] D. Bonn, J. Eggers, J. Indekeu, and J. Meunier. Wetting and spreading. *Rev. Mod. Phys.*, 81(2):739–805, 2009.

[3] C.G.L. Furmidge. Studies at phase interfaces. i. the sliding of liquid drops on solid surfaces and a theory for spray retention. *Journal of colloid science*, 17(4):309–324, 1962.

[4] Mathieu Massinon and Frédéric Lebeau. Comparison of spray retention on synthetic superhydrophobic surface with retention on outdoor grown wheat leaves. *International Advances in Pesticide Application: Aspects of Applied Biology 114, 2012*, pages 261–268, 2012.

[5] Maher Damak, Seyed Reza Mahmoudi, Md Nasim Hyder, and Kripa K Varanasi. Enhancing droplet deposition through in-situ precipitation. *Nature communications*, 7:12560, 2016.

[6] A. B. Thompson and J. K. . Lam. Water run-off in aircraft fuel tanks. *IMA Journal of Applied Mathematics*, 77(1):72–85, Feb 2012.

[7] Robert D Deegan, Olgica Bakajin, Todd F Dupont, Greb Huber, Sidney R Nagel, and Thomas A Witten. Capillary flow as the cause of ring stains from dried liquid drops. *Nature*, 389(6653):827, 1997.

[8] Álvaro G Marín, Hanneke Gelderblom, Detlef Lohse, and Jacco H Snoeijer. Order-to-disorder transition in ring-shaped colloidal stains. *Physical review letters*, 107(8):085502, 2011.

[9] H. B. Eral, D. J. C. M. 't Mannetje ., and J. M. Oh. Contact angle hysteresis: a review of fundamentals and applications. *Colloid Polym. Sci.*, 291:247–260, 2012.

[10] Javier Atencia and David J Beebe. Controlled microfluidic interfaces. *Nature*, 437(7059):648, 2004.

[11] Mathieu Joanicot and Armand Ajdari. Droplet control for microfluidics. *Science*, 309(5736):887–888, 2005.

[12] Chih-kuan Tung, Oleh Krupa, Elif Apaydin, Jr-Jiun Liou, Anthony Diaz-Santana, Beum Jun Kim, and Mingming Wu. A contact line pinning based

microfluidic platform for modelling physiological flows. *Lab on a chip*, 13(19):3876–3885, 2013.

[13] S Majid Hassanizadeh and William G Gray. Thermodynamic basis of capillary pressure in porous media. *Water resources research*, 29(10):3389–3405, 1993.

[14] Noushine Shahidzadeh, Emanuel Bertrand, Jean P Dauplait, Jean C Borgotti, Philippe Vié, and Daniel Bonn. Effect of wetting on gravity drainage in porous media. *Transport in Porous Media*, 52(2):213–227, 2003.

[15] Michael Dreyer, Antonio Delgado, and Hans-Joseph Path. Capillary rise of liquid between parallel plates under microgravity. *Journal of Colloid and interface science*, 163(1):158–168, 1994.

[16] Ralf Blossey. Self-cleaning surfacesvirtual realities. *Nature materials*, 2(5):301, 2003.

[17] David L Hu, Brian Chan, and John WM Bush. The hydrodynamics of water strider locomotion. *Nature*, 424(6949):663, 2003.

[18] Xuefeng Gao and Lei Jiang. Biophysics: water-repellent legs of water striders. *Nature*, 432(7013):36, 2004.

[19] Shichao Niu, Bo Li, Zhengzhi Mu, Meng Yang, Junqiu Zhang, Zhiwu Han, and Luquan Ren. Excellent structure-based multifunction of morpho butterfly wings: a review. *Journal of Bionic Engineering*, 12(2):170–189, 2015.

[20] Timothée Mouterde, Gaëlle Lehoucq, Stéphane Xavier, Antonio Checco, Charles T Black, Atikur Rahman, Thierry Midavaine, Christophe Clanet, and David Quéré. Antifogging abilities of model nanotextures. *Nature materials*, 16(6):658, 2017.

[21] FT Malik, RM Clement, DT Gethin, W Krawszik, and AR Parker. Nature's moisture harvesters: a comparative review. *Bioinspiration & biomimetics*, 9(3):031002, 2014.

[22] Manu Prakash, David Quéré, and John WM Bush. Surface tension transport of prey by feeding shorebirds: the capillary ratchet. *science*, 320(5878):931–934, 2008.

[23] Josiah Willard Gibbs. On the equilibrium of heterogeneous substances. *American Journal of Science*, 96:441–458, 1878.

[24] Leiv Magne Siqveland and Svein Skjaeveland. Derivations of the young–laplace equation. *Unpublished Research*, 2014.

[25] Paul Concus. Static menisci in a vertical right circular cylinder. *Journal of Fluid Mechanics*, 34(3):481–495, 1968.

[26] Omer Atasi, Sepideh Khodaparast, Benoit Scheid, and Howard A Stone. Effect of buoyancy on the motion of long bubbles in horizontal tubes. *Physical Review Fluids*, 2(9):094304, 2017.

[27] Sepideh Khodaparast, Omer Atasi, A Deblais, Benoît Scheid, and Howard A Stone. Dewetting of thin liquid films surrounding air bubbles in microchannels. *Langmuir*, 34(4):1363–1370, 2018.

[28] Antonin Marchand, Joost H Weijs, Jacco H Snoeijer, and Bruno Andreotti. Why is surface tension a force parallel to the interface? *American Journal of Physics*, 79(10):999–1008, 2011.

[29] Legros J. C. Colinet, P. and M. G. Velarde. *Nonlinear Dynamics of Surface-Tension-Driven Instabilities*. Wiley, 2001.

[30] John W. M. Bush. Interfacial phenomena, June 2013.

[31] P. G. de Gennes. Wetting: statics and dynamics. *Rev. Mod. Phys.*, 57:827–863, 1985.

[32] JR Henderson. Statistical mechanics of fluids adsorbed in planar wedges: Finite contact angle. *Physical Review E*, 69(6):061613, 2004.

[33] Antonio Pereira and Serafim Kalliadasis. Equilibrium gas–liquid–solid contact angle from density-functional theory. *Journal of fluid mechanics*, 692:53–77, 2012.

[34] Robert W Style and Eric R Dufresne. Static wetting on deformable substrates, from liquids to soft solids. *Soft Matter*, 8(27):7177–7184, 2012.

[35] M. Delmas, M. Monthioux, and T. Ondarçuhu. Contact angle hysteresis at the nanometer scale. *Phys. Rev. Lett.*, 106(13):136102, 2011.

[36] David Seveno, Terence D Blake, and Joël De Coninck. Youngs equation at the nanoscale. *Physical review letters*, 111(9):096101, 2013.

[37] P Roura and Joaquim Fort. Local thermodynamic derivation of young's equation. *Journal of colloid and interface science*, 272(2):420–429, 2004.

[38] EM Blokhuis, Y Shilkrot, and B Widom. Young's law with gravity. *Molecular Physics*, 86(4):891–899, 1995.

[39] Edward Bormashenko. Young, boruvka–neumann, wenzel and cassie–baxter equations as the transversality conditions for the variational problem of wetting. *Colloids and Surfaces A: Physicochemical and Engineering Aspects*, 345(1-3):163–165, 2009.

[40] EK Yeh, John Newman, and CJ Radke. Equilibrium configurations of liquid droplets on solid surfaces under the influence of thin-film forces: Part i. thermodynamics. *Colloids and Surfaces A: Physicochemical and Engineering Aspects*, 156(1-3):137–144, 1999.

[41] EK Yeh, John Newman, and CJ Radke. Equilibrium configurations of liquid droplets on solid surfaces under the influence of thin-film forces: Part ii. shape calculations. *Colloids and Surfaces A: Physicochemical and Engineering Aspects*, 156(1-3):525–546, 1999.

[42] Robert N Wenzel. Surface roughness and contact angle. *The Journal of Physical Chemistry*, 53(9):1466–1467, 1949.

[43] H Yildirim Erbil. The debate on the dependence of apparent contact angles on drop contact area or three-phase contact line: A review. *Surface Science Reports*, 69(4):325–365, 2014.

[44] CW Extrand. Contact angles and hysteresis on surfaces with chemically heterogeneous islands. *Langmuir*, 19(9):3793–3796, 2003.

[45] Lichao Gao and Thomas J McCarthy. How wenzel and cassie were wrong. *Langmuir*, 23(7):3762–3765, 2007.

[46] John WM Bush, François Peaudecerf, Manu Prakash, and David Quéré. On a tweezer for droplets. *Advances in colloid and interface science*, 161(1-2):10–14, 2010.

[47] RE Johnson and RH Dettre. *Wetting of low-energy surfaces*, volume 49. Marcel Dekker, Inc.: New York, 1993.

[48] Hossein Tavana, Guocheng Yang, Christopher M Yip, Dietmar Appelhans, Stefan Zschoche, Karina Grundke, Michael L Hair, and A Wilhelm Neumann. Stick- slip of the three-phase line in measurements of dynamic contact angles. *Langmuir*, 22(2):628–636, 2006.

[49] Abraham Marmur. Contact angle hysteresis on heterogeneous smooth surfaces. *Journal of colloid and interface science*, 168(1):40–46, 1994.

[50] R Shuttleworth and GLJ Bailey. The spreading of a liquid over a rough solid. *Discussions of the Faraday Society*, 3:16–22, 1948.

[51] RE Johnson. Contact angle hysteresis i. study of an idealized rough surfaces, advances in chemistry. In *Ser.*, volume 43, page 112, 1964.

[52] R. E. Johnson and R. H. Dettre. Contact angle hysteresis. iii. Study of an idealized heterogeneous surface. *J. Phys. Chem.*, 68(7):1744–1750, 1964.

[53] Chun Huh and SG Mason. Effects of surface roughness on wetting (theoretical). *Journal of colloid and interface science*, 60(1):11–38, 1977.

[54] Abraham Marmur and Eyal Bittoun. When wenzel and cassie are right: reconciling local and global considerations. *Langmuir*, 25(3):1277–1281, 2009.

[55] A. Marmur and E. Bittoun. When wenzel and cassie are right: Reconciling local and global considerations. *Langmuir*, 25(3), 2009.

[56] Claire Andrieu, Cecile Sykes, and Francoise Brochard. Average spreading parameter on heterogeneous surfaces. *Langmuir*, 10(7):2077–2080, 1994.

[57] EL Decker and S Garoff. Using vibrational noise to probe energy barriers producing contact angle hysteresis. *langmuir*, 12(8):2100–2110, 1996.

[58] Tammar S Meiron, Abraham Marmur, and I Sam Saguy. Contact angle measurement on rough surfaces. *Journal of Colloid and Interface Science*, 274(2):637–644, 2004.

[59] F Li and Frieder Mugele. How to make sticky surfaces slippery: Contact angle hysteresis in electrowetting with alternating voltage. *Applied Physics Letters*, 92(24):244108, 2008.

[60] JP Oliver, Chun Huh, and SG Mason. An experimental study of some effects of solid surface roughness on wetting. *Colloids and surfaces*, 1(1):79–104, 1980.

[61] Erdal Bayramli, Theodore GM van de Ven, and Stanley G Mason. Tensiometric studies on wetting. i. some effects of surface roughness (theoretical). *Canadian Journal of Chemistry*, 59(13):1954–1961, 1981.

[62] Erdal Bayramli and Stanley G Mason. Tensiometric studies on wetting. ii. some effects of surface roughness (experimental). *Canadian Journal of Chemistry*, 59(13):1962–1968, 1981.

[63] Abraham Marmur. Contact-angle hysteresis on heterogeneous smooth surfaces: theoretical comparison of the captive bubble and drop methods. *Colloids and Surfaces A: Physicochemical and Engineering Aspects*, 136(1-2):209–215, 1998.

[64] Leonard W Schwartz and Stephen Garoff. Contact angle hysteresis on heterogeneous surfaces. *Langmuir*, 1(2):219–230, 1985.

[65] M. Pradas, N. Savva, J. B. Benziger, I. G. Kevrekidis, and S. Kalliadasis. Dynamics of fattening and thinning 2d sessile droplets. *Langmuir*, 32:4736–4745, 2016.

[66] Gary G Wells, Élfego Ruiz-Gutiérrez, Youen Le Lirzin, Anthony Nourry, Bethany V Orme, Marc Pradas, and Rodrigo Ledesma-Aguilar. Snap evaporation of droplets on smooth topographies. *Nature communications*, 9(1):1380, 2018.

[67] Abraham Marmur. Capillary rise and hysteresis in periodic porous media. *Journal of colloid and interface science*, 129(1):278–285, 1989.

[68] A. Marmur. Contact angle hysteresis on heterogeneous smooth surfaces. *J. Colloid Interface Sci.*, 168:40–46, 1994.

[69] S. Brandon and A. Marmur. Simulation of contact angle hysteresis on chemically heterogeneous surfaces. *J. Colloid Interface Sci.*, 183(Dec. 1996):351–355, 1996.

[70] M. Iwamatsu. Contact angle hysteresis of cylindrical drops on chemically heterogeneous striped surfaces. *J. Colloid Interface Sci.*, 297:772–777, 2006.

[71] MA Rodriguez-Valverde, FJ Montes Ruiz-Cabello, and MA Cabrerizo-Vilchez. Wetting on axially-patterned heterogeneous surfaces. *Advances in colloid and interface science*, 138(2):84–100, 2008.

[72] J. F. Joanny and P. G. de Gennes. A model for contact angle hysteresis. *J. Chem. Phys.*, 81(1):552, 1984.

[73] Jean-Pierre Hulin Etienne Guyon and Luc Petit. *Hydrodynamique Physique*. CNRS editions, 3 edition, 2012.

[74] Chun Huh and LE Scriven. Hydrodynamic model of steady movement of a solid/liquid/fluid contact line. *Journal of colloid and interface science*, 35(1):85–101, 1971.

[75] Alexey Rednikov and Pierre Colinet. Singularity-free description of moving contact lines for volatile liquids. *Physical Review E*, 87(1):010401, 2013.

[76] Marc Fermigier and Patrice Jenffer. An experimental investigation of the dynamic contact angle in liquid-liquid systems. *Journal of colloid and interface science*, 146(1):226–241, 1991.

[77] Andreas Nold, David Sibley, Benjamin Goddard, Serafim Kalliadasis, et al. *From the Nano-to the Macroscale: Bridging Scales for the Moving Contact Line Problem*. PhD thesis, Imperial College London, 2016.

[78] David N Sibley, Andreas Nold, and Serafim Kalliadasis. The asymptotics of the moving contact line: cracking an old nut. *Journal of Fluid Mechanics*, 764:445–462, 2015.

[79] BR Duffy and SK Wilson. A third-order differential equation arising in thin-film flows and relevant to tanner's law. *Applied Mathematics Letters*, 10(3):63–68, 1997.

[80] OV Voinov. Hydrodynamics of wetting. *Fluid dynamics*, 11(5):714–721, 1976.

[81] RG Cox. The dynamics of the spreading of liquids on a solid surface. part 1. viscous flow. *Journal of Fluid Mechanics*, 168:169–194, 1986.

[82] Jacco H Snoeijer. Free-surface flows with large slopes: Beyond lubrication theory. *Physics of Fluids*, 18(2):021701, 2006.

[83] Jens Eggers. Existence of receding and advancing contact lines. *Physics of Fluids*, 17(8):082106, 2005.

[84] Nolwenn Le Grand, Adrian Daerr, and Laurent Limat. Shape and motion of drops sliding down an inclined plane. *Journal of Fluid Mechanics*, 541:293–315, 2005.

[85] E. Raphael and P. G. de Gennes. Dynamics of wetting with nonideal surfaces. the single defect problem. *The Journal of Chemical Physics*, 90(12):7577–7584, 1989.

[86] TD Blake and JM Haynes. Kinetics of liquidliquid displacement. *Journal of colloid and interface science*, 30(3):421–423, 1969.

[87] Terence D Blake. The physics of moving wetting lines. *Journal of colloid and interface science*, 299(1):1–13, 2006.

[88] David Seveno, Alexandre Vaillant, Romain Rioboo, H Adao, J Conti, and Joël De Coninck. Dynamics of wetting revisited. *Langmuir*, 25(22):13034–13044, 2009.

[89] Yi Sui, Hang Ding, and Peter D.M. Spelt. Numerical simulations of flows with moving contact lines. *Annu. Rev. Fluid Mech*, 46(1):97–119, 2014.

[90] D. C. Pease. The significance of the contact angle in relation to the solid surface. *J. Phys. Chem.*, 49(3):107–110, 1945.

[91] E. B. Dussan. On the spreading of liquids on solid surfaces: Static and dynamic contact lines. *Ann. Rev. Fluid Mech.*, 11(1968):371–400, 1979.

[92] N. Savva and S. Kalliadasis. Two-dimensional droplet spreading over topographical substrates. *Phys. Fluids*, 21:092102, 2009.

[93] N N. Savva, S. Kalliadasis, and G. A. Pavliotis. Two-Dimensional Droplet Spreading over Random Topographical Substrates. *Phys. Rev. Lett.*, 104:084501, 2010.

[94] N. Savva, G. A. Pavliotis, and S. Kalliadasis. Contact lines over random topographical substrates. Part 2. Dynamics. *J. Fluid Mech.*, 672:384–410, 2011.

[95] R. Vellingiri, N. Savva, and S. Kalliadasis. Droplet spreading on chemically heterogeneous substrates. *Phys. Rev. E*, 84(3):1–14, 2011.

[96] C. Wylock, M. Pradas, B. Haut, P. Colinet, and S. Kalliadasis. Disorder-induced hysteresis and nonlocality of contact line motion in chemically heterogeneous microchannels. *Phys. Fluids*, 24:032108, 2012.

[97] N. Savva and S. Kalliadasis. Droplet motion on inclined heterogeneous substrates. *J. Fluid Mech.*, 725:462–491, 2013.

[98] N. Savva and S. Kalliadasis. Low-frequency vibrations of two-dimensional droplets on heterogeneous substrates. *J. Fluid Mech.*, 754:515–549, 2014.

[99] T. Cubaud and C. M. Ho. Transport of bubbles in square microchannels. *Phys. Fluids*, 16(12):4575–4585, 2004.

[100] E. Bittoun and A. Marmur. Chemical nano-heterogeneities detection by contact angle hysteresis: theoretical feasibility. *Langmuir*, 26(20):15933–15937, 2010.

[101] X. Xu and X. Wang. Analysis of wetting and contact angle hysteresis on chemically patterned surfaces. *SIAM J. Appl. Math.*, 71(5):1753–1779, 2011.

[102] V. De Jonghe and D. Chataint. Experimental study of wetting hysteresis on surfaces with controlled geometrical and/or chemical defects. *Acta metall. mater.*, 43, 1995.

[103] P. Collet, J. DeConinck, F. Dunlop, and A. Regnard. Dynamics of the contact line: Contact angle hysteresis. *Phys. Rev. Lett.*, 79(19):3704–3707, 1997.

[104] A. Giacomello, L. Schimmele, and S. Dietrich. Wetting hysteresis induced by nanodefects. *Proc. Natl. Acad. Sci. U.S.A.*, 113(3):E262–E271, 2016.

[105] H. Perrin, R. Lhermerout, K. Davitt, E. Rolley, and B. Andreotti. Defects at the nanoscale impact contact line motion at all scales. *Phys. Rev. Lett.*, 116(18):184502, 2016.

[106] J.-M. di Meglio and D. Quéré. Contact angle hysteresis: a first analysis of the noise of the creeping motion of the contact line. *Europhys. Lett.*, 11(2):163–168, 1990.

[107] S. M. M. Ramos, E. Charlaix, A. Benyagoub, and M. Toulemonde. Wetting on nanorough surfaces. *Phys. Rev. E*, 100(18):1–6, 2003.

[108] J. Crassous and E. Charlaix. Contact angle hysteresis on a heterogeneous surface: Solution in the limit of a weakly distorted contact line. *Europhys. Lett.*, 28:415–420, 1994.

[109] J.-M. di Meglio. Contact angle hysteresis and interacting surface defects. *Europhys. Lett.*, 17:607–612, 1992.

[110] A. Marmur. Thermodynamic aspects of contact angle hysteresis. *Adv. Colloid Interface Sci.*, 50:121–141, 1994.

[111] C. Priest, R. Sedev, and J. Ralston. A quantitative experimental study of wetting hysteresis on discrete and continuous chemical heterogeneities. *Colloid Polym. Sci.*, 291(2):271–277, 2013.

[112] Y. J. Wang, S. Guo, H. Y. Chen, and P. Tong. Understanding contact angle hysteresis on an ambient solid surface. *Phys. Rev. E*, 93(5):1–10, 2016.

[113] S. Brandon, N. Haimovich, E. Yeger, and A. Marmur. Partial wetting of chemically patterned surfaces: The effect of drop size. *J. Colloid Interface Sci.*, 263:237–243, 2003.

[114] C. Priest, R. Sedev, and J. Ralston. Asymmetric wetting hysteresis on chemical defects. *Phys. Rev. Lett.*, 99(2):1–4, 2007.

[115] M. Pradas, D. Tseluiko, S. Kalliadasis, D. T. Papageorgiou, and G. A. Pavliotis. Noise induced state transitions, intermittency, and universality in the noisy kuramoto-sivashinksy equation. *Phys. Rev. Lett.*, 106:060602, 2011.

[116] A. B. Duncan, S. Kalliadasis, G. A. Pavliotis, and M. Pradas. Noise-induced transitions in rugged energy landscapes. *Phys. Rev. E*, 94:032107, 2016.

[117] CA Fuentes, Le Quan Ngoc Tran, Maarten Van Hellemont, Van Janssens, C Dupont-Gillain, AW Van Vuure, and I Verpoest. Effect of physical adhesion on mechanical behaviour of bamboo fibre reinforced thermoplastic composites. *Colloids and surfaces A: physicochemical and engineering aspects*, 418:7–15, 2013.

[118] Daniel Hansen, Niels Bomholt, Jonas Camillus Jeppesen, and Adam Cohen Simonsen. Contact angle goniometry on single micron-scale fibers for composites. *Applied Surface Science*, 392:181–188, 2017.

[119] Si Qiu, Carlos A Fuentes, Dongxing Zhang, Aart Willem Van Vuure, and David Seveno. Wettability of a single carbon fiber. *Langmuir*, 32(38):9697–9705, 2016.

[120] You-Lo Hsieh and Bangling Yu. Liquid wetting, transport, and retention properties of fibrous assemblies: Part i: Water wetting properties of woven fabrics and their constituent single fibers. *Textile Research Journal*, 62(11):677–685, 1992.

[121] Ludwig Wilhelmy. Ueber die abhängigkeit der capillaritäts-constanten des alkohols von substanz und gestalt des benetzten festen körpers. *Annalen der Physik*, 195(6):177–217, 1863.

[122] AJG Allan. Wilhelmy's plate and young's equation. *Journal of Colloid Science*, 13(3):273–274, 1958.

[123] Lichao Gao and Thomas J McCarthy. Contact angle hysteresis explained. *Langmuir*, 22(14):6234–6237, 2006.

[124] Bharadwaj Prabhala, Mahesh Panchagnula, Venkat R Subramanian, and Srikanth Vedantam. Perturbation solution of the shape of a nonaxisymmetric sessile drop. *Langmuir*, 26(13):10717–10724, 2010.

[125] TD Blake. Dynamic contact angles and wetting kinetics. *Wettability*, 251, 1993.

[126] Mars M Alimov and Konstantin G Kornev. Meniscus on a shaped fibre: singularities and hodograph formulation. *Proceedings of the Royal Society A: Mathematical, Physical and Engineering Sciences*, 470(2168):20140113, 2014.

[127] FM Orr Jr, LE Scriven, and AP Rivas. Menisci in arrays of cylinders: numerical simulation by finite elements. *Journal of Colloid and Interface Science*, 52(3):602–610, 1975.

[128] CA Fuentes, Le Quan Ngoc Tran, C Dupont-Gillain, Willem Vanderlinden, Steven De Feyter, AW Van Vuure, and I Verpoest. Wetting behaviour and surface properties of technical bamboo fibres. *Colloids and Surfaces A: Physicochemical and Engineering Aspects*, 380(1-3):89–99, 2011.

[129] Martyn Hucker, Ian Bond, Andrew Foreman, and Jennifer Hudd. Optimisation of hollow glass fibres and their composites. *Advanced composites letters*, 8(4):096369359900800406, 1999.

[130] Ibon Aranberri-Askargorta, Thomas Lampke, and Alexander Bismarck. Wetting behavior of flax fibers as reinforcement for polypropylene. *Journal of colloid and interface science*, 263(2):580–589, 2003.

[131] Mars M Alimov and Konstantin G Kornev. Singularities of meniscus at the v-shaped edge. *Mechanics Research Communications*, 62:162–167, 2014.

[132] Michael Nosonovsky. Multiscale roughness and stability of superhydrophobic biomimetic interfaces. *Langmuir*, 23(6):3157–3161, 2007.

[133] Martin ER Shanahan. Simple theory of" stick-slip" wetting hysteresis. *Langmuir*, 11(3):1041–1043, 1995.

[134] MER Shanahan and K Sefiane. Kinetics of triple line motion during evaporation. *Contact angle, wettability and adhesion*, 6:19–31, 2009.

[135] David F James. The meniscus on the outside of a small circular cylinder. *Journal of Fluid Mechanics*, 63(4):657–664, 1974.

[136] CA Fuentes, Metin Hatipogullari, Sarah Van Hoof, Youen Vitry, Sam Dehaeck, V Du Bois, Pierre Lambert, Pierre Colinet, David Seveno, and AW Van Vuure. Contact line stick-slip motion and meniscus evolution on micrometer-size wavy fibres. *Journal of colloid and interface science*, 540:544–553, 2019.

[137] CA Fuentes, Kristel Beckers, Helge Pfeiffer, LQN Tran, C Dupont-Gillain, Ignace Verpoest, and AW Van Vuure. Equilibrium contact angle measurements of natural fibers by an acoustic vibration technique. *Colloids and Surfaces A: Physicochemical and Engineering Aspects*, 455:164–173, 2014.

[138] Julien Dupre de Baubigny, Michael Benzaquen, Laure Fabié, Mathieu Delmas, Jean-Pierre Aimé, Marc Legros, and Thierry Ondarçuhu. Shape and effective spring constant of liquid interfaces probed at the nanometer scale: Finite size effects. *Langmuir*, 31(36):9790–9798, 2015.

[139] Pierre Colinet and Alexey Rednikov. On integrable singularities and apparent contact angles within a classical paradigm. *The European Physical Journal Special Topics*, 197(1):89, 2011.

[140] Metin Hatipogullari, Christophe Wylock, Marc Pradas, Serafim Kalliadasis, and Pierre Colinet. Contact angle hysteresis in a microchannel: Statics. *Physical Review Fluids*, 4(4):044008, 2019.

[141] CA Fuentes, M Hatipogullari, S Van Hoof, Y Vitry, S Dehaeck, V Du Bois, P Lambert, P Colinet, D Seveno, and AW Van Vuure. Contact line stick-slip motion and meniscus evolution on micrometer-size wavy fibres. *Journal of colloid and interface science*, 2019.

[142] Uwe Thiele and Edgar Knobloch. Driven drops on heterogeneous substrates: Onset of sliding motion. *Physical review letters*, 97(20):204501, 2006.

[143] Weiqing Ren and E Weinan. Contact line dynamics on heterogeneous surfaces. *Physics of fluids*, 23(7):072103, 2011.

[144] Nikos Savva, Danny Groves, and Serafim Kalliadasis. Droplet dynamics on chemically heterogeneous substrates. *Journal of Fluid Mechanics*, 859:321–361, 2019.

[145] Göran Ström, Monica Fredriksson, Per Stenius, and Bovjan Radoev. Kinetics of steady-state wetting. *Journal of colloid and interface science*, 134(1):107–116, 1990.

[146] Erik Schäffer and Po-zen Wong. Contact line dynamics near the pinning threshold: A capillary rise and fall experiment. *Physical Review E*, 61(5):5257, 2000.

[147] L. D. Landau and E. M. Lifshitz. *Fluid Mechanics, Second Edition: Volume 6 (Course of Theoretical Physics)*. Course of theoretical physics / by L. D. Landau and E. M. Lifshitz, Vol. 6. Butterworth-Heinemann, 2 edition, January 1987.

[148] James O. Wilkes. Solution of viscous-flow problems. In Pearson, editor, *Fluid Mechanics for Chemical Engineers with Microfluidics and CFD*, chapter 6. Pearson, 2005.

[149] A. Marmur. Solid-surface characterization by wetting. *Annu. Rev. Mater. Res.*, 39:473–489, 2009.

[150] Frieder Mugele and Jean-Christophe Baret. Electrowetting: from basics to applications. *Journal of physics: condensed matter*, 17(28):R705, 2005.

[151] Ya-Pu Zhao and Ying Wang. Fundamentals and applications of electrowetting. *Reviews of Adhesion and Adhesives*, 1(1):114–174, 2013.

[152] Edward Bormashenko, Albina Musin, and Michael Zinigrad. Evaporation of droplets on strongly and weakly pinning surfaces and dynamics of the triple line. *Colloids and Surfaces A: Physicochemical and Engineering Aspects*, 385(1-3):235–240, 2011.

[153] COMSOL Multiphysics. Comsol multiphysics 4.3 user's guide, 2012.

LIST OF PUBLICATIONS

1. Hatipogullari, Metin, Christophe Wylock, Marc Pradas, Serafim Kalliadasis, and Pierre Colinet. ”Contact angle hysteresis in a microchannel: Statics.” Physical Review Fluids 4, no. 4 (2019): 044008.

2. Fuentes, C. A., Metin Hatipogullari, Sarah Van Hoof, Youen Vitry, Sam Dehaeck, V. Du Bois, Pierre Lambert, Pierre Colinet, David Seveno, and A. W. Van Vuure. ”Contact line stick-slip motion and meniscus evolution on micrometer-size wavy fibres.” Journal of colloid and interface science 540 (2019): 544-553.